Data Driven Acoustic Design

Achilleas Xydis

DISS. ETH NO. 29211

DISS. ETH NO. 29211

Data Driven Acoustic Design

A thesis submitted to attain the degree of

DOCTOR OF SCIENCES
(Dr. sc. ETH Zurich)

presented by

ACHILLEFS XYDIS

Diploma in Architectural Engineering, University of Patras

born on 10.06.1981

accepted on the recommendation of

Prof. Matthias Kohler
Dr Romana Rust
Prof. Fabio Gramazio
Prof. Dr Louena Shtrepi

2023

Abstract

Acoustics are rarely included as a design driver in the early phases of design due to the multi-faceted nature of sound and the complex and time-consuming analysis process of room acoustics software. Inevitably this results in architectural spaces with poor acoustics, where treatment is either disregarded or focuses only on noise prevention using absorbent materials. However, most commonly used construction materials have sound-reflecting properties and can be configured into sound-diffusive surfaces. These surfaces can help reduce unwanted flattered echoes, colourisation, and image shift and create a more pleasant and comfortable environment without needing additional elements (e.g. absorption panels). Faster and simpler analysis tools are required to harness the potential of diffusion in architectural design.

This dissertation presents a new data-driven approach to designing and evaluating the acoustic properties of architectural surfaces. It investigates the use of machine-learning techniques to study the mutual relationship between geometry and sound diffusion. It introduces a new acoustic dataset meant as a basis for training predictive machine-learning models. These models enable the creation of fast, less cumbersome, and reasonably accurate acoustics analysis tools. It proposes and implements a new automated multi-robotic data-acquisition method for collecting impulse responses from scale-modelled surfaces. It also develops computational tools to design and generate three-dimensional wall-like surface geometries. The geometrical characteristics of these surfaces are based on commonly used construction materials and techniques. A computational framework is developed in parallel to process the collected data and generate customisable and interactive visualisations for low- and high-dimensional data. This framework caters to both expert and non-expert users in acoustics, providing expert users with familiar descriptors and visualisations and introducing non-experts to simpler ones. Furthermore, to address users with no programming knowledge, it develops a web-based application enabling easy access to the collected dataset, the acoustic descriptors, and visualisations. It introduces a new workflow to the performance-driven acoustic design of sound-diffusing wall surfaces, allowing architects and designers to explore alternative wall designs with sound-diffusing properties, given a set of desired acoustic performance criteria.

The proposed workflow has the potential to bring acoustics closer to the early phases of architectural design and enable a more integrative acoustic and architectural design exploration. Providing architects and acousticians

with comprehensive and user-friendly tools for acoustics analysis can help integrate acoustics into the design process from the beginning rather than as an afterthought.

Zusammenfassung

Die Akustik wird aufgrund der vielfältigen Natur des Schalls und des komplexen und zeitaufwändigen Analyseprozesses von Raumakustik-Software selten in den frühen Phasen des Designs berücksichtigt. Dies führt zwangsläufig zu architektonischen Räumen mit schlechter Akustik, bei denen die Behandlung entweder vernachlässigt wird oder sich nur auf Lärmbekämpfung mit absorbierenden Materialien konzentriert. Die am häufigsten verwendeten Baumaterialien weisen jedoch schallreflektierende Eigenschaften auf und können zu schalldiffusiven Oberflächen konfiguriert werden. Diese Oberflächen können dazu beitragen, unerwünschte flache Echos, Klangverfärbungen und Bildverschiebungen zu reduzieren und eine angenehmere und komfortablere Umgebung zu schaffen, ohne zusätzliche Elemente (z. B. Absorptionspaneele) zu benötigen. Es sind schnellere und einfachere Analysetools erforderlich, um das Potenzial der Diffusion in der architektonischen Gestaltung nutzbar zu machen.

Diese Dissertation präsentiert einen neuen datengetriebenen Ansatz zur Gestaltung und Bewertung der akustischen Eigenschaften architektonischer Oberflächen. Sie untersucht den Einsatz von maschinellem Lernen, um die wechselseitige Beziehung zwischen Geometrie und Schalldiffusion hervorzuheben. Es wird ein neuer akustischer Datensatz vorgestellt, der als Grundlage für das Training prädiktiver maschineller Lernmodelle dient. Diese Modelle ermöglichen die Erstellung schneller, weniger umständlichen und angemessen genauen Akustikanalysetools. Eine neue automatisierte, multi-robotergesteuerte Datenakquisitionsmethode zur Erfassung von Impulsantworten maßstabsgetreu modellierter Oberflächen wird vorgeschlagen. Auch rechnergestützte Werkzeuge zur Gestaltung und Erzeugung dreidimensionaler, wandähnlicher Oberflächengeometrien werden entwickelt. Die geometrischen Eigenschaften dieser Oberflächen basieren auf häufig verwendeten Baumaterialien und Techniken. Parallel dazu wird ein rechnergestütztes Framework entwickelt, welches die gesammelten Daten verarbeitet und skalierbare und interaktive Visualisierungen für niedrig- und hochdimensionale Daten generiert. Dieses Framework richtet sich sowohl an Experten als auch an Nicht-Experten der Akustik. Es bietet Experten vertraute Beschreibungen und Visualisierungen und führt Nicht-Experten in einfachere ein. Darüber hinaus wird eine webbasierte Anwendung entwickelt, um Benutzer ohne Programmierkenntnisse anzusprechen und einen einfachen Zugriff auf den gesammelten Datensatz, die akustischen Beschreibungen und Visualisierungen zu ermöglichen. Es führt einen neuen Arbeitsablauf für die leistungsorientierte akustische Gestaltung von schalld-

iffusen Wandflächen ein, welcher Architekten und Designern ermöglicht, alternative Wandgestaltungen mit schalldiffusen Eigenschaften, basierend auf einer Reihe gewünschter akustischer Leistungskriterien, zu erforschen.

Der vorgeschlagene Arbeitsablauf hat das Potenzial, die Akustik näher in früheren Phasen der architektonischen Gestaltung anzusetzen und eine integrativere akustische und architektonische Gestaltungserkundung zu ermöglichen. Die Bereitstellung umfassender und benutzerfreundlicher Werkzeuge zur Akustikanalyse für Architekten und Akustiker kann dazu beitragen, die Akustik von Anfang an in den Gestaltungsprozess zu integrieren, anstatt sie als nachträgliche Überlegung zu behandeln.

Acknowledgement

I want to express my deepest gratitude to my supervisors, Prof Matthias Kohler and Prof Fabio Gramazio, for their guidance and support over the past years. This work would not have been possible without your dedication to pushing the boundaries of your research topics and perhaps your persistence in researching architectural acoustics.

I would also like to thank my co-supervisor Dr Romana Rust. You have been instrumental in shaping who I am now as a researcher. Thank you for supporting me when I needed help, pushing me when I was not feeling motivated, and pulling me back when I was going off track.

This research has its roots in the *Data Science Enabled Acoustic Design for Digital Fabrication in Architecture (AADS)*. The interdisciplinary nature of this research project brought me into contact with researchers from other fields, which have significantly contributed to the development of my research. I want to thank Jürgen Strauss from Strauss Elektroakustik GmbH for our technical but especially for the philosophical discussions on acoustics. Kurt Eggenschwiler from the Laboratory for Acoustics/Noise Control at EMPA and especially Dr Kurt Heutschi for all his help during and after our collaborative project. Thank you for always finding time to listen to all my questions, even the not-good ones. I would also like to thank Dr Fernando Perez-Cruz from the Swiss Data Science Center for his valuable input throughout the project. Most of all, I thank Dr Nathanaël Perraudin for his invaluable contribution to building the GIR Dataset and being a voice of reasoning when faced with challenging moments.

Gonzalo Casas, I cannot thank you enough for being there for me for the last four years. You have been an incredible collaborator in our AADS project. Thank you for always finding time to listen and find solutions to all my coding problems. Most of all, thank you for all the late-night talks. I would also like to thank Dr Beverly Lytle for her valuable coding help and especially for answering all my math questions in a way that an architect would understand. A big thank you to Chaoyu Du for being an exceptional student during her master's thesis and for all her help and contribution to the Geometry and Impulse Response Dataset (GIR Dataset) project.

Building up the data acquisition setup would not have been possible without the help and expertise of the Robotic Fabrication Lab's technicians and especially Mike Lyrenmann and Philippe Fleischmann. Mike, thank you

for all the technical and geeky talks and for always finding the time and enthusiasm to help find solutions to my technical challenges.

Many of the GIR Dataset's surfaces were printed with ITA's in-house 3D printer. Using the printer would not have been possible without the help of Dr Mathias Bernhard, Patrick Bedarf, and Pietro Odaglia from the Chair of Digital Building Technologies. Thank you for all your work and effort in keeping the printer working for as long as possible.

I want to thank all my colleagues at Raplab. You were a breath of fresh air and a ray of sunshine during the hard last part of my research. I especially would like to thank Alessandro Tellini. You supported me when I needed it and showed me a different way of working at Hönggerberg.

I would probably not have been where I am today without the help and support of Prof. Georgios Panetsos. Thank you for looking past my rushed-out entry exam drawings, unlocking and redefining my design language, and, lastly, for encouraging me to continue my academic path at ETH Zurich and supporting its every step.

Having done this research as part of the Chair of Architecture and Digital Fabrication (GKR) has brought me into contact with great people that contributed to the development of this research and my journey. I want to thank Anton Johansson, Liya Sunny Anthraper, Priyank Soni, Inés Ariza, and Joris Burger for helping me sleep a bit longer or go home at a reasonable time by taking shifts in the data acquisition process. Ryan, thank you for brainstorming ideas with me and for all the walks in the park with Waldo, Archie, and Sarah. Fabio, thank you for being a friendly and cheerful face every day at work and for all the laughs and countless conversations when not working. Victor, thank you for all the conversations we had inside and outside work and all the tasty food you fed me late at night after many hours of work.

Daniela, we started and finished this incredible journey together. We faced challenges and celebrated successes, and your presence and encouragement were invaluable. I am grateful for your support throughout the ups and downs of this journey. Your determination and dedication inspired me. I am happy to have witnessed your growth and the remarkable strides towards your goal. I do not doubt that you will continue to achieve greatness in all your endeavours.

I would not have made it here without my friends' mental, emotional, and sometimes physical support. Jess and Lisa, I am so glad I spent the lockdowns with you. Thank you for the countless conversations, the morning coffees, the delicious food, the movie nights, the time spent in our garden, making our place feel like home, and being there in times of need. Constantino, thank

you for all the long phone calls, the Sunday brunches in Graz, for never sugarcoating your criticism, and for being a stubborn advocate for equality and justice wherever you go. Dimitri, thank you for all the times you made fun of architects while explaining physics and electrical engineering to me, but above all, thank you for bringing music back into my life. Anna, you are the best flatmate one could have - twice. Thank you for opening your home to me and making it my home too. The last year of this journey was tough; thank you for supporting me as a friend and feeding me like a Greek mom.

A heartfelt and special thank you to Mariana Popescu for being an unwavering believer in my potential and wholeheartedly encouraging me to pursue this doctoral position. Your belief in me gave me the courage to take this leap; I am eternally grateful. Throughout these years, your support has been nothing short of extraordinary, and I cannot find the words to express how much it has meant to me. Your patience and willingness to listen and understand have been invaluable, especially during moments of uncertainty and challenges. I cannot thank you enough for your unwavering presence in my life.

Lastly, I would like to thank my loving family, Aspasia, Ioanni, and my sister Argiro for believing in me and supporting me all these years.
Δεν έχω λόγια να σας ευχαριστήσω για όλα όσα έχετε κάνει για ΄μένα. Σας ευχαριστώ για την υπομονή και την υποστήριξη που μου δείξατε όλα αυτά τα χρόνια.

Contents

1 Introduction

1.1 Motivation and background

Hearing is essential in our everyday life. It enables us to communicate with each other and perceive our environment. Every space, outdoor or indoor, exhibits different acoustical properties that may range from noisy to quiet or from very to dry. These properties depend on the space's shape, size, and material of its surfaces; therefore, how architects design these spaces influences their resulting acoustical signature. Nevertheless, architectural principles and styles change and evolve over time. During the Renaissance, Baroque, and up to the end of the Neoclassical period, sound-scattering surfaces were an integral part of the architectural form. While elements such as columns and coffered ceilings fulfilled a structural and aesthetical purpose (Figure 1.1), perhaps not always intentionally, they also had an acoustical function. These elements, combined with carved wooden doors and staircases, heavy curtains, thick carpets, and elaborate decorative wall elements and furniture, provided rooms with adequate acoustic treatment. Following the steps of the modernist movement of the early 1900s, contemporary architecture shifted to cleaner and simpler designs with flat smooth surfaces devoid of ornaments. Adolf Loos, an Austrian architect and theorist of modern Western architecture, was very critical of ornaments. In his essay *Ornament and Crime* [1], he explored the idea that cultural progress is linked to the omission of ornamentation from everyday objects. Forcing craftspeople and builders to squander their time on ornamentation represented wasted labour and ruined material, and it was not adequately remunerated. The lack of sound-scattering surfaces, combined with the often rectilinear room design - typical for modern western architecture - gave rise to multiple acoustical problems such as flutter echoes[1], colouration[2], and image shift[3]. In the 1950s, open-plan designs, such as Bürolandschaft, accentuated these problems by introducing large multi-functional spaces that were used by many people at the same time [3]. Their large size, high occupancy, and multi-functional character resulted in slower sound decay rates and increased noise exposure.

Poor acoustics and increased noise exposure have various auditory and non-auditory effects on our mental and physical health [4]. These effects range from simple annoyance, irritation, fatigue, loss of concentration, and decreased productivity to elevated stress levels, tension headaches, noise-induced hearing loss, or even cardiovascular diseases [5]. In our work environment, the acoustics are strongly linked to our productivity and well-being [3]. Struggling to understand the person speaking during a presentation, finding it hard to concentrate when working in an open-plan office, and feeling exhausted when coming out of a meeting room are things that many people have experienced more than once in their everyday lives.

Figure 1.1: Ernst August Saal in Burg Bentheim, Germany

According to the World Health Organisation [6], more than 1,5 million healthy years (DALYs[4]) are lost annually due to environmental noise exposure in the European A-member states.

4: DALYs are the sum of the potential years of life lost due to premature death and the equivalent years of "healthy" life lost by virtue of being in states of poor health or disability.

Room acoustic design can create good acoustic conditions, which in return help mitigate or even eliminate all mental and health-related problems caused by bad acoustics. One of the central topics in room acoustics is how to manipulate the sound reflections affecting the way sound propagates and is ultimately perceived [7]. The sound we hear combines the direct sound coming straight from the source and the indirect reflections from the surrounding surfaces. When a sound wave hits a surface is transmitted, absorbed, or reflected, and the ratio of sound energy that gets transmitted, absorbed, or reflected depends on the acoustic properties of the surface. With transmission, all or part of the sound energy passes through the surfaces and continues on the other side. With absorption, all or part of the sound energy dissipates inside the surface. There are two ways that sound is reflected, and it depends on the surface's texture and geometry. Large flat surfaces redirect sound (specular reflection), while rough or structured surfaces scatter a significant portion of the reflected sound spatially and temporarily (diffuse reflection) (see Figure 1.2).

Both absorptive and diffusive surfaces can be used to prevent - or fix if used retrospectively - acoustic distortions caused by the room's geometry and choice of surface materials. Whether absorptive or diffusive surfaces should be used depends on whether we wish to reduce the sound level or not while decreasing the Reverberation Time (RT). Absorptive surfaces can be used to reduce the sound level and lower the reverberation time,

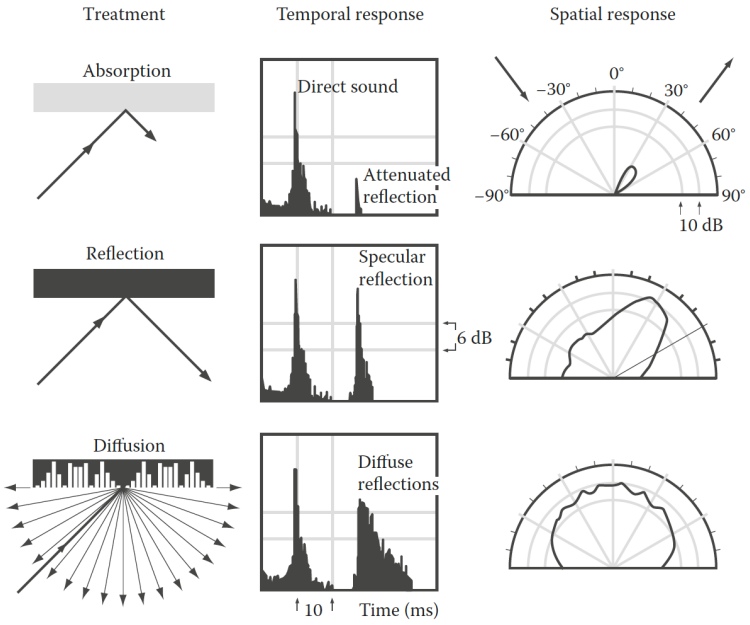

Figure 1.2: The temporal and spatial characteristics of absorbing, specularly reflecting and diffusing surfaces. After Trevor J. Cox and Peter D'Antonio.

whereas diffusive surfaces can reduce flutter echoes and image shifts while maintaining the sound energy inside the room. Absorption can create quieter working environments and increase intelligibility. However, a high increase of intelligibility in an open-plan office space inevitably decreases the level of privacy because all potentially masking background noises are now suppressed. Sound noises from printers or coffee machines, conversations between colleagues from other tables, or even phone calls are now clearer, making it more difficult to ignore them, thus, more difficult to concentrate. Furthermore, when only absorption is used as a sound treatment method, the room becomes unpleasant to stay in for an extended period, and people describe it as "dead". Therefore, a combination of absorptive and diffusive surfaces should be used to preserve some liveliness inside the room while reducing the sound levels and the reverberation time.

There are two general types of absorbers, porous absorbents and resonant devices [7]. The most common type is porous absorbents which are made of porous and fibrous materials such as mineral wool, fibreglass, open-cell expanded synthetic foam, wood chips, and more, making them difficult to maintain and clean. Over time their performance could degrade as their pores fill up with particulates from the air. Furthermore, they do not hold up well when used outdoors under rainy and windy conditions. Finally, absorptive materials are non-structural; therefore, they need to be installed

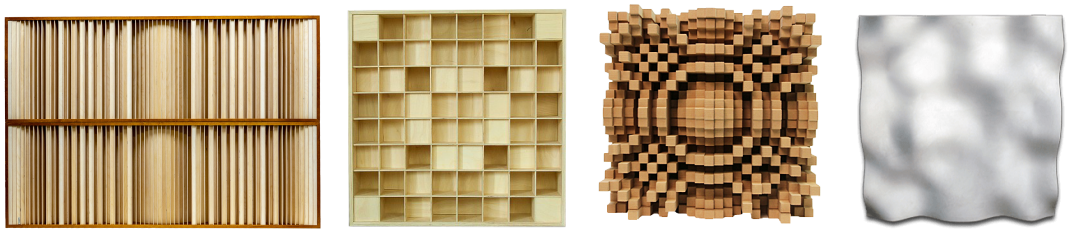

Figure 1.3: Commercially available acoustic diffusers based on Schroeder's quadratic residue diffuser. From left to right: 1D QRD diffuser, 2D QRD diffuser, Skyline diffuser, Harmonix K from RPG.Inc.

on another structural element. Diffusers, on the other hand, are rigid, non-porous articulated surfaces. Any reflective material can be used as a diffusive surface. Broadly used architectural materials such as concrete, brick, stone, plaster, clay, wood, and glass can be shaped or arranged to diffuse sound. Contrary to sound absorptive materials, these materials are easier to maintain and clean, and depending on their material or finishing treatment, they can stand up well in outdoor environments.

Many manufacturers offer standardised acoustic panels such as absorbers and diffusers for the acoustical treatment of rooms. Unfortunately, most architects are not keen on using such standardised acoustic panels in their designs, and the reason is twofold. First, standardised acoustic panels – and especially diffusers – have particular and limited geometries, a substantial thickness, and a dedicated placement according to acoustic criteria. These factors make them unattractive and difficult to integrate into an architectural design that is not purely focused on music performance. It becomes even harder to integrate when acoustic treatment is introduced later in the design process. Second, with the introduction of computational design and digital fabrication, architectural forms became expressive and complex. The regular and often rectilinear forms of standardised acoustic panels no longer fit with these complex and expressive architectural forms (see Figure 1.3).

Today, computational design, digital fabrication, and room acoustics simulation tools can be combined to provide custom acoustic treatment solutions. These solutions can either target the design of bespoke acoustic panels, the room's surfaces, or a combination of both. Despite the potential benefits of providing solutions that would integrate with the project's architectural aesthetics, such a combination has not yet been implemented in projects that do not focus mainly on sound or music.

1.2 Problem statement

The architectural design consists of several phases. During the early phases, architects explore various alternative design ideas. Early-stage decisions significantly impact the quality and performance of the final design. In contrast, late-stage design modifications can rarely compensate for poor early-stage choices [8]. Therefore, it is essential to consider all factors in the early-stage design to avoid potentially delaying the project, increasing the building cost, or impairing the overall design with retrospective changes. Design aspects such as the load-bearing structure and natural lighting are integral design drivers and are included early on in the design phase. This process has become a standard practice for most architectural projects because architects are trained to understand these topics (e.g., structural design) and acknowledge their importance for an aesthetical, performative, sustainable, and cost-effective design. Usually, this is done in close collaboration with experts in an iterative process where a design is analysed, evaluated, and adjusted to meet the desired performance criteria. Contrary, acoustics are rarely included as a performance criterion at an early design stage. Apart from cases where sound quality is critical (e.g., concert halls, auditoriums), the current acoustic design paradigm follows three possible paths: a) it focuses only on noise prevention, b) it applies simplified acoustic guidelines or c) it includes acoustic specialists only in the late design phase. The first two paths can result in the design of spaces with sub-nominal sound quality. The latter leads to the inevitable addition of previously unplanned elements, usually standardised acoustic panels, in the architectural design. Besides being difficult to incorporate these panels into an existing design, it is challenging to apply late-stage design modifications that will not also increase the project's budget.

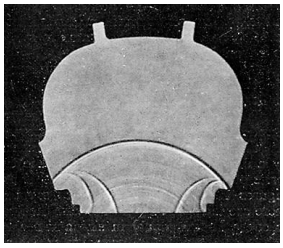

Figure 1.4: Schlieren photography experiment with a model of the New Theatre in New York by Wallace C. Sabine in 1913 [9].

The acoustic design does not have to weaken the intended architectural aesthetic. Custom acoustic treatments can be designed to match the architectural aesthetic, but this can only be achieved by including acoustic performance criteria early on in the design phase. The main factors hindering the inclusion of acoustics in the architectural workflow are a) the limitations and complexity of available acoustic assessment tools and b) a knowledge gap in evaluating their results. The following sections talk about these two limiting factors.

1.2.1 Tool limitations

In 1912 Wallace C. Sabine used a method called Schlieren photography [5] to visualise the sound propagation inside architectural models (see Figure

5: In his paper Theatre Acoustics [9] Sabine refers to it as *Toeppler-Boys-Foley method* after the inventor, physicist, August Toepler.

Figure 1.5: Interior view of the 1:10 physical scale model of the La Philharmonie de Paris. ©Nicolas Borel.

1.4) [10]. This technique allows the rendering of optical inhomogeneities in transparent media like air and water that otherwise are invisible to the naked eye [11]. Since then, many modelling techniques have been developed to analyse and study room acoustics. Today, to assess the acoustic quality of our designs, physical scale models or computer simulations are used. Physical scale models are usually constructed at scales ranging between 1:8 to 1:50 (see Figure 1.5). Although large-scale models can be accurate and adaptable, they pose several practical limitations as design tools. They are expensive and require larger-than-normal sized spaces to house the model (see Figure 1.6). most importantly, need a lot of time to construct, implying that they cannot be part of the design process [12, 13].

Computer simulations are generally faster than physical scale modelling and are based on two main approaches: wave-based modelling and Geometrical Acoustics (GA). Wave-based methods provide the most accurate results but are computationally intensive. These methods discretise the model or its boundary surfaces to small interconnected elements and calculate their interactions. The discretisation density increases relative to the frequency; therefore, time-consuming when simulating high frequencies [14, 15]. The long computing time makes it difficult for architects and acousticians to iterate quickly through several design variations[6]. GA techniques are faster because they are based on a simplified model where the wave properties of sound are neglected, and sound is assumed to propagate as rays[16]. This technique uses a simplified, low-polygon mesh representation of the space under study. Each surface is assigned two coefficients that describe how the surface interacts with the sound rays. The absorption coefficient is the ratio of incident sound that gets absorbed by the surface and not reflected back into the space. The scattering coefficient describes how much of the sound ray is reflected in a specular or diffuse way. A large number of rays is cast though out the space from the source position, and every time a ray intersects a

6: For a small 5x5x3m room and for frequencies up to 8kHz, an FDTD simulation takes around 10 hours. The computation time could reach several days for larger rooms or higher frequencies.

Figure 1.6: Exterior view of the 1:10 physical scale model of the La Philharmonie de Paris during an acoustic measurement. ©Nicolas Borel.

surface, the model calculates the energy losses and the type and direction of the reflected ray. The simplified assumptions of GA render them incapable of modelling diffraction and become equally slow as wave-based methods when simulating models with a high level of detail [17]. Therefore, diffusion – an important acoustic phenomenon that can promote spaciousness and prevent flutter echoes and colouration – cannot be accurately simulated [7], thus, not correctly evaluated.

1.2.2 User limitations

To employ acoustic performance as a design driver, we must be able to quantify and interpret the acoustic effects of our geometric design choices. In a classical design process, architects have no starting point for an acoustically performative design as they lack expert knowledge. Several computer simulation software (Odeon[7], Pachyderm[8], CATT-acoustics[9], EASE[10], and more) can simulate and characterise the acoustic performance of digitally designed geometries. Given a room and the material properties of each of its surfaces, they can calculate acoustic descriptors such as RT, Early Decay Time (EDT), Clarity (C50), Definition (D), and more. Nevertheless, this paradigm relies on the premise that the user is knowledgeable in room acoustics and knows what adjustments need to be made to achieve the desired goal. As a result, architects are discouraged from using such software to evaluate their designs, especially early on. Furthermore, no computer-aided design (CAD) or acoustic simulation software proposes a geometrical solution to an acoustical question.

7: www.odeon.dk (Odeon A/S 2020)

8: www.orase.org (ORASE 2022)

9: www.cate.se (CATT 2022)

10: www.afmg.eu/en/ease-enhanced-acoustic-simulator-engineers [18]

1.3 Research goal

As highlighted in sections 1.1 and 1.2, acoustic performance criteria are mainly considered in projects where spaces host music performances and heavily rely on expert knowledge in acoustics. Computational design and digital fabrication methods are opportunities to design and fabricate surfaces with complex geometries that can also be used as diffusers, enhancing the room's acoustic qualities. Contrary to standardised acoustic panels, these digitally designed and fabricated structures and surfaces could be an integral part of the room's surfaces. Custom acoustic treatments can be designed to match the architectural aesthetic, but further effort is needed to increase acoustic performance awareness in architectural design. A key ingredient to successful integration is providing architects with faster, simpler, and more accessible tools for including acoustics in their design workflows.

A possible approach to shorten the computation time and simplify the design workflow is to employ Machine Learning (ML) techniques. ML has enabled significant breakthroughs in automated data processing and pattern recognition within the field of computer vision [19]. Architecture and engineering have seen an increase in research on employing ML techniques in performance-based design [20], style transferring [21, 22], and clustering [23]. In acoustics research, ML has been used mainly as a predictive tool [24] focusing on information extraction, characterisation, and classification. Gamper et al. [25] extracted the RT and EDT from audio recordings, and Genovese et al. [26] the room's volume from music signals. Peters et al. [27] presented methods for identifying the room[11] in an audio file. They achieved an accuracy of 61% for musical signals and 85% for speech signals. Papayiannis et al. [28] used an Attention-Convolutional Recurrent Neural Network (CRNN) architecture to identify the room type[12] where a speech recording was captured. Their classification accuracy was 78% when using 5 hours of training data and 90% with 10 hours of data.

11: Bedroom, studio, classroom, church 1, church 2, great hall, and library.

12: Meeting room 1, Meeting room 2, building lobby 1, building lobby 2, office 1, office 2, lecture room 1, and lecture room 2.

Given the previous success of ML techniques in acoustics and other research fields, this doctoral thesis seeks to employ such techniques to provide faster and easy-to-use tools and workflows to study sound diffusion. This research aims to provide a dataset for acoustic research using machine learning applications and make this dataset and its content accessible to non-acoustics experts. It does it by developing novel visualisation methods for displaying complex and multi-dimensional acoustic data. Furthermore, it uses dimensionality reduction techniques to develop novel design methods that enable users to navigate and explore this large, high-dimensional dataset using acoustic performance criteria.

1.4 Research objectives

Diffusion occurs when sound waves hit a non-flat, articulated surface. These articulations scatter sound spatially and temporally [29] (see Figure 1.2). To predict the acoustic properties of such surfaces, we need to model the relationship between surface geometry and reflected sound. This model needs a dataset that contains both geometrical and acoustical data. Several datasets exist that contain acoustical data in the form of room Impulse Responses (IRs). AIR, BUT ReverbDB, RWCP, and DIRHA [30–33] are used for speech enhancement and speech recognition, the ACE Corpus [34] for acoustic environment characterisation. Nevertheless, these datasets do not address room acoustics applications and, most importantly, do not contain any three-dimensional geometrical data. As such, one of the primary objectives of this research is to:

- Create a dataset containing three-dimensional geometrical data of articulated surfaces and their corresponding physically measured impulse responses.

In ML techniques, the quality and size of the dataset heavily influence the final quality of the model [35]. Building a high-quality dataset mainly depends on a) defining the type of collected data based on the desired goals and b) defining an accurate collection, processing, and organisation pipeline. Having very few data points is problematic (Figure 1.7c); the same goes for a large dataset with insufficient diversity in its data points (Figure 1.7b). In both cases, although the predicted function accurately satisfies the training data, it does not accurately describe the real problem (represented with a dashed line in Figure 1.7). The dataset needs to have sufficient and diverse data to generalise the problem in question and achieve a high prediction accuracy (Figure 1.7d). Creating a new dataset can be challenging and time-consuming, especially with non-computer-generated data. The following objectives are set to ensure the creation of such a high-quality dataset.

- Define relevant diffusive geometries for architectural acoustics.
- Develop methods and tools to generate diffusive geometries for acoustic testing.
- Set up a data acquisition pipeline.

The objectives outlined above aim to provide the necessary dataset to develop ML methods for predicting the acoustical properties of diffusive surfaces. This alone does not address the need for intuitive and easy-to-use tools for non-expert users in acoustics or ML. This research aims to demonstrate that a dataset generated for predictive deep neural network applications can also be used as a knowledge base of known acoustic properties. Nevertheless,

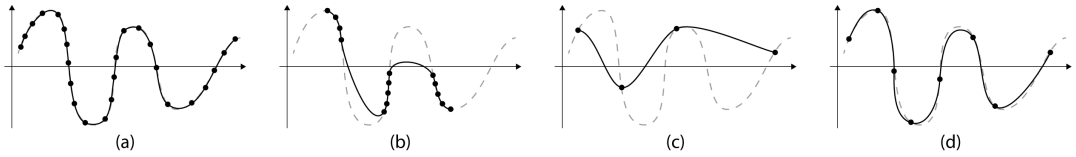

Figure 1.7: The relationship between training data and MLS's prediction quality. (a) Large, dense, and diverse training data set. (b) Large enough and dense but not diverse. (c) Small and diverse. (d) Large enough and diverse. – – –Function that perfectly describes the system. ——The predicted function that satisfies all input data points. • Data points.

the large number and multi-dimensional nature of its data points make it challenging to explore with conventional visualisation methods. ML techniques such as data clustering and dimensionality reduction can filter and organise large amounts and high-dimensional data. Visualisation tools based on these techniques can provide a more accessible and comprehensible data exploration, allowing architects and acousticians to study sound-diffusive surfaces and incorporate them in their designs easily.

- Develop data clustering and dimensionality reduction tools.
- Develop data visualisation tools

1.5 Research methodology

The methodology consists of quantitative and qualitative research to achieve the above research objectives. It addresses the challenges of creating a new dataset and developing easy-to-use data analysis and visualisation tools for large amounts and high-dimensional data. The methodology can be split into four main parts: a) the development of the data acquisition setup, b) the design, generation, and fabrication of diffuse surfaces, c) methods for processing and visualising the captured data, and finally, d) methods for analysing, exploring, and using the data within an architectural design process. Most of these parts are developed in parallel due to their high level of inter-dependency. The data acquisition requires the parallel use of surface design, data processing, data visualisation, and data analysis methods. It follows a closed-loop process (see Figure 1.8) consisting of the following steps:

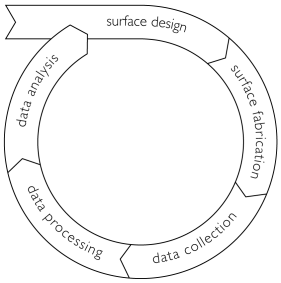

Figure 1.8: The closed-loop methodology of the data acquisition process.

1. Design an acoustic surface
2. Fabricate and post-process the surface
3. Collect acoustic data from the surface
4. Process the captured data
5. Analyse the processed data
6. Use the results of the analysis to inform the design of the next acoustic surface

Below is a description of the four methodological parts and how each one addresses the research objectives and tackles research challenges.

1.5.1 Data acquisition setup development

To study the spatiotemporal effects of diffusion, we need acoustic data from different positions and at different distances around the surface. A three-dimensional grid containing multiple measuring positions at different distances from the surface is introduced to address this challenge. Since every single measurement adds to the total time required to measure an entire surface, given the limited period of this research, the density and, consequently, the number of measurements per surface must be carefully defined. On the one hand, too many measurements per surface will result in a small number of surfaces. On the other hand, even though fewer measurements will result in a larger number of surfaces, the small number of measurements per surface will not be sufficient to characterise it adequately. To address this challenge, the measuring grid is defined using Fresnel zones[13][36]. A computational tool is developed to generate these Fresnel zones, and the generated zones are validated using empirical experiments. These tests help define the optimal grid density and the number of layers, which in return determines the total number of measurements per surface and the total time needed for each surface.

13: Fresnel zones are ellipsoidal shapes that, based on a predetermined source and receiver position, define the part of a sound reflector's surface that is mainly responsible for the reflected sound that arrives at the receiver's position.

The high number of measurements per surface and the imperative need for accuracy and repeatability in the measuring process dictates the use of automation. Two robotic arms are used to accurately reposition a microphone and a speaker on the measuring grid. The multi-robotic setup is integrated with audio equipment such as an audio interface, an audio amplifier, and environmental sensors to measure and document the temperature, humidity, and atmospheric pleasure during the measuring process.

1.5.2 Design and generation of diffuse surfaces

This part of the research focuses on developing a computational pipeline for designing and fabricating a large and diverse set of surfaces to be measured in the data-acquisition setup. To bring acoustics closer to the architecture practice, tools should be not only easy to use but also relatable and applicable to existing design workflows. Common architectural materials such as stone and brick and fabrication techniques such as ashlar masonry or stretcher-bond brick walls are included to create a link between past and current building systems. They are chosen based on their geometrical characteristics and ability to diffuse sound. Typologies help to organise the surfaces into groups

with distinct surface characteristics. During the data acquisition period, the data visualisation and data analysis methods described in the following sections are used to introduce geometrical variations in the typologies. This variation has the motivation to a) uncover new possibilities within the acoustics domain, possibly integrating diffusion and absorption within one surface, and b) diversify the acquired dataset.

1.5.3 Data processing and visualisation

The data captured with the acquisition setup are stored as IRs. Although an IR contains much information, this format type is not easily readable by a human[14]. For this reason, computational tools are developed to process an IR and compute multiple standard acoustic parameters such as Absorption Coefficient (α), energy, EDT, and more. Furthermore, several visualisation tools are developed to display these acoustical parameters and illustrate the complex nature of sound in relation to geometry. They provide a more detailed insight into the relationship between geometrical characteristics and the frequencies they influence. Simple and understandable data visualisations are key components for communicating these insights within interdisciplinary groups of experts and non-experts in acoustic.

14: An impulse response is the output or reaction of a dynamic system in response to an external change. It describes the system's reaction as a time function.

As mentioned in 1.5.2, these visualisations are also used to inform the design generation algorithm and vary the geometry of the acoustic surfaces. The design of these surfaces happens in several batches. For each batch, the measurements of the surfaces are visualised and compared with already measured surfaces. The results of this comparison inform the design of the next batch of acoustic surfaces. This process helps diversify the dataset with surfaces whose acoustic properties are not very similar but also not significantly different.

1.5.4 Data analysis

The captured data are complex and high in quantity, exceeding the number of dimensions humans can visualise or easily comprehend. Therefore, analytical strategies and machine learning techniques are employed for feature extraction and dimensionality reduction. Analytical tools such as Principal Component Analysis (PCA) [37] are used to analyse and extract correlations. PCA is a statistical procedure that emphasises variation and brings out strong patterns in a dataset, making data easy to explore and visualise. These results are then used to identify the most critical geometrical characteristics that influence specific acoustic properties. Self-Organising Map (SOM) [38], a dimensionality reduction technique, is a type of artificial neural network. It uses

unsupervised learning to produce a low-dimensional representation of the high-dimensional input space of the training samples in a two-dimensional graph. The dimensionality reduction helps arrange the data based on physical (i.e., fabrication technique, simulated material) or acoustical characteristics (i.e., absorption, scattering), allowing the identification of clusters in the generated data.

1.6 Interdisciplinary research

This dissertation is part of the AADS, an interdisciplinary research project between the Chair of Architecture and Digital Fabrication at ETH Zurich, the Swiss Data Science Center (SDSC), the Laboratory for Acoustics / Noise Control of Empa, and Strauss Elektroakustik. The scientific group of the AADS project includes architects, acousticians, data scientists, and software engineers. This project aims to investigate a novel application of ML techniques for predicting the acoustic properties of architectural surfaces. The data for training the ML models are collected using the data-acquisition setup described in 1.5.1. The data scientists of the SDSC would then use the data to implement predictive ML models using deep neural networks. These models would take new architectural geometries as input and provide acoustic performance information as output.

Each author's different collaborations and contributions are described in detail at the end of every paper.

1.7 Thesis structure

This cumulative, paper-based dissertation is built up of six chapters. Chapter 1 contains the introduction and contextualises the research. Chapters 2, 3, 4, and 5 contain the four papers that together with Chapter 6 form the body of the research. Chapter 6 describes the development of a web-based application that makes the entirety of this research available to users with no programming knowledge. Finally, chapter 7 contains the conclusions, outlining and discussing the contributions and the outlook of this research. These six chapters are followed by Appendices A, B, C, D, E, and F. Appendix F is a scientific publication describing a built project that used several methods developed in this thesis. Supplementary to this dissertation is an Annex that documents the content of the GIR Dataset.

Chapter 1
Introduction: forms the introduction to the subject matter, discussing the project background and research problem. It contextualises the research goal

and proceeds to describe the chosen methodology. The research objectives follow the problem statements. They are grouped into four parts consisting of setup development, digital design, data processing, and data analysis that are respectively developed in the body of this research in Chapters 2, 3, 4, and 5.

Chapter 2
Paper A - GIR Dataset: A Geometry and real Impulse Response Dataset for machine learning research in Acoustics: is a scientific publication in the journal of Applied Acoustics [39]. It introduces a new GIR Dataset, built within the scope of this research. The article details the dataset's content, how it is collected, and how it is structured. It continues by presenting a use-case ML application using the dataset and concludes by discussing the challenges of creating such a dataset, possible applications, limitations, and future work.

Chapter 3
Paper B - A data acquisition setup for data driven acoustic design: is a scientific publication in the journal of Building Acoustics [40]. It presents the automated data-acquisition setup, the data processing and the computational generation of diffusive surfaces. Finally, it describes initial comparative studies of measured surfaces.

Chapter 4
Paper C - Visualisation methods for big and high-dimensional acoustic data: is a peer-reviewed paper at the conference of the Association for Computer-Aided Design in Architecture (ACADIA) [41]. It presents novel methods for interactive visualisations of acoustic datasets for architects and non-acoustic experts. It introduces a series of simple acoustic properties for users with basic knowledge of acoustics and describes methods for low- and high-dimensional data visualisations. It describes the computational workflow and uses a design scenario to demonstrate the proposed visualisations. Finally, it discusses the challenges of developing such methods, their advantages, limitations, and future work.

Chapter 5
Paper D - Data-Driven Acoustic Design of Diffuse Soundfields: Self-Organising Maps as an Exploratory Design Tool for Big Data: is a peer-reviewed paper at the conference of the Association for Computer-Aided Design in Architecture (ACADIA) [42]. The paper demonstrates a novel approach to a performance-driven acoustic design of architectural diffusive surfaces using unsupervised machine learning techniques to analyse and explore the GIR Dataset described in Chapter 2. The paper introduces the computational pipeline, describes the methods used, and presents two use cases in the form of design experiments. Finally, the paper discusses the challenges of developing such a method, its advantages, limitations, and future work.

Chapter 6
Geometry and Impulse Responses web application: This chapter introduces the Geometry and Impulse Responses library, a web-based application allowing users without programming knowledge to explore the GIR Dataset. The chapter then describes two available visualisation modes and how to use them to analyse acoustic data. It concludes by demonstrating how it can be used and describes alternative methods to use developed visualisations to analyse the diffusivity of a surface.

Chapter 7
Conclusions: summarises the body of the research, discusses current limitations, and concludes on the implication of data-driven acoustic design in architecture. It lists the contributions of this dissertation and provides an outlook for future work in this field.

Appendix F
Paper E - Computational design and evaluation of acoustic diffusion panels for the Immersive Design Lab: An acoustic design case study: is a peer-reviewed paper in the proceedings of the eCAADe conference [43]. The paper presents a workflow for the computational design and evaluation of acoustic diffusive panels, developed and realised in a real building project - the Immersive Design Lab (IDL). This workflow includes a computational design system integrated with a rough acoustic evaluation method for fast performance feedback, assessing acoustic performance criteria using the data-acquisition setup described in Chapter 3, and the post-processing of a selected design instance for fabricability. Finally, the paper illustrates and discusses this workflow, its limitations, and future work.

Annex
Geometry and Impulse Response Dataset: is an overview of the GIR Dataset's content.

2 Paper A - GIR Dataset: A Geometry and real Impulse Response Dataset for machine learning research in Acoustics

Achilleas Xydis[*], *Nathanaël Perraudin*[†], *Romana Rust*[*], *Kurt Heutschi*[‡], *Gonzalo Casas*[*], *Oksana Riba Grognuz*[†], *Kurt Eggenschwiler*[‡], *Matthias Kohler*[*], *Fernando Perez-Cruz*[†]

[*] Gramazio Kohler Research, ETH Zurich, Zurich, Switzerland
[†] Swiss Data Science Center, Zurich, Switzerland
[‡] Laboratory for Acoustics / Noise Control, Empa, Duebendorf, Switzerland

Acoustics play a significant role in our everyday lives, influencing our communication, well-being, and perception of space. Fast and precise acoustics simulation is crucial for the accurate design of real spaces by architects and acousticians and maximises the user's immersion in virtual and augmented reality environments. Computer simulation techniques can help to simulate

and analyse acoustics. However, their cumbersome, computationally expensive, and often inaccurate results discourage most architecture practices from including acoustic evaluation in their design workflow and prevent real-time accurate audio synthesis in virtual reality. Recent advancements in ML and particularly Deep Learning offer compelling solutions to address the above problems. ML methods require large datasets for training, and existing datasets are either not large enough, contain synthetic data, or are not suitable for room acoustics research. This paper presents the GIR Dataset, a dataset of 920712 real IRs of 312 architectural geometries for the study of early reflections from diffusive surfaces. The paper provides a detailed description of the GIR Dataset's content and an ML use-case example. The dataset and the code described in this paper are open-sourced.

This version of the article has been published after peer review in the journal of *Applied Acoustics*, Volume 208, p. 109333, on June 15th 2023. The published version is available online at: `https://doi.org/10.1016/j.apacoust.2023.109333`.

2.1 Introduction

The sound we hear is a combination of the direct sound coming straight from the source and the indirect reflections from the surrounding surfaces. Sound hitting a surface is either transmitted, absorbed or reflected; the ratio depends on the surface's acoustic properties. Early reflections significantly affect the characteristics of the sound at the listening position. Furthermore, the directional aspects and the degree of diffusivity are most relevant in the early reflections [7, 44, 45]. Room acoustics combine room geometry and surface treatment by appropriately placing absorptive, reflective or diffusive surfaces to control sound propagation. In particular, diffuse surfaces can help to reduce flutter echoes and colouration and create a uniform sound field.

Today, to assess acoustic quality, we use physical scale models or computer simulations. Unfortunately, physical scale modelling is expensive both in cost and time, often requiring several months to fabricate and measure a single design. For these reasons, they are mainly used for projects where sound is the main protagonist, such as concert halls or auditoriums. On the other hand, computer simulations are generally faster and are based on two main approaches: wave-based modelling and GA. Wave-based modelling provides the most accurate results but with the expense of very long computation times [7, 14]. Techniques based on GA are faster but less accurate because sound wave properties are neglected, and sound is assumed to propagate as rays [16]. Both approaches create a bottleneck in the study of diffusion. Wave-based methods are time-intensive; therefore, architects and acousticians cannot iterate through several design variations. The simplified assumption of GA methods renders them incapable of modelling diffraction and are equally slow when used on high-level-of-detail models [17]. Except for projects that primarily focus on sound, these limitations, paired with their cumbersome-to-use nature, discourage most architectural practices from using them in their everyday design workflow to develop acoustically informed designs [8]. Thus, diffusion, an important acoustic phenomenon that can promote spaciousness, prevent flutter echoes, and improve speech intelligibility [7], is either neglected or inaccurately simulated, thus not properly evaluated.

Machine learning has enabled broad advances in automated data processing and pattern recognition capabilities in fields such as computer vision [19], reinforcement learning [46], audio processing, and (geo)physical science [47–49]. Sound event detection and source localisation are some of the tasks in acoustics and audio signal processing that have greatly benefited from deep-learning techniques [24]. One of the main limitations of data-driven ML methods is that they require large amounts of data for training and

validation. Furthermore, the quality of the training data has a big influence on the output quality and the prediction accuracy [35].

Therefore, a dataset containing a large number of high-quality real audio measurements taken from diffuse surfaces would aid the research on the mutual relationship between geometry and sound and the development of fast and easy-to-use acoustic tools using machine-learning methods.

2.1.1 Motivation

The motivation of this paper is to introduce the *Geometry and Impulse Response Dataset* GIR Dataset and describe the methodology of its collection. This unique dataset can be seen as the equivalent of COIL-100 [50] for audio. It comprises multiple real IR measurements taken from hundred surfaces that represent different architectural wall structures. The *GIR Dataset* was built to provide the scientific community with the first dataset of physically recorded IRs and their corresponding 3D geometries. The goal is to aid the research on diffusion and its relationship to geometrical characteristics. Knowledge of a surface's reflective properties could be translated into parameters such as absorption and scattering coefficient for use in room acoustic simulations. Furthermore, this dataset can be used as a basis to develop machine-learning models for predicting early reflections, or acoustic properties of 3D surfaces, thus omitting the need for a physical scale model. These models could enhance hybrid GA methods by including direction-specific diffusion as a replacement for global scattering coefficients while still keeping the computational effort low. The dataset is released under the GNU General Public License v3.0 and is available on Zenodo: `doi.org/10.5281/zenodo.5288743` [51]. Accompanying code is also distributed on Renku: `renkulab.io/projects/ddad/gir-dataset`.

2.1.2 Related work

This section focuses on three main topics. First, relevant datasets that contain audio information and have been used in acoustics research; second, ML applications on room acoustics; and finally, other research fields, besides architectural acoustics, that use audio and could benefit from the GIR Dataset.

Acoustic-based datasets. Several acoustic datasets containing real impulse responses exist, most of them addressing a specific application. AIR[1], BUT ReverbDB[2], and RWCP[3] [30–32] are used in speech enhancement and speech recognition. The ACE Corpus[4] [34] for acoustic environment characterisation and the DIRHA[5] [33] for smart-home applications. Nevertheless, these

1: `www.iks.rwth-aachen.de/fileadmin/user_upload/downloads/forschung/tools-downloads/air_database_release_1_4.zip`

2: `speech.fit.vutbr.cz/software/but-speech-fit-reverb-database`

3: `research.nii.ac.jp/src/en/RWCP-SSD.html`

4: `acecorpus.ee.ic.ac.uk`

5: `dirha.fbk.eu/English-PHdev`

datasets do not include geometric information; thus, they are not adapted to geometrical sound applications.

Room acoustics. Despite a lack of appropriate datasets, ML techniques have been applied recently in room acoustics applications, mainly focusing on characterisation, information extraction, or classification. In the past, ML has been used to extract different indicators and properties of reverberant environments. Such properties were the RT and the EDT of a room from music signals [25, 52], and the room volume [26, 53]. Peters et al. [27] presented a system for identifying a room in an audio or video recording. The system was based on a Gaussian mixture model and used acoustical features extracted using Mel-frequency cepstral coefficient. With no common content between the training and testing data, they achieved an accuracy of 61% for musical signals and 85% for speech signals. More recently, Papayiannis et al. [28] used an attention Convolutional Recurrent Neural Network architecture to identify the room in which a speech recording was taken. They provided a classification accuracy of 78% when using 5 hours of training data and 90% when using 10 hours.

Audio sensing. So far, the field of audio sensing has shown promising results when a suitable algorithm is combined with high-quality data. For example, audio camera applications can extract geometrical information from sound using microphone arrays [54–57] or reconstruct the geometry of the surrounding environment by measuring a series of IRs at different spatial positions [58–60]. These techniques could be used in situations where visual cameras are not available such as in surveillance applications [61], or the desired information is out of the camera's line of sight [62]. Arrays of microphones are also widely used for source localisation, where the goal is to identify the position of one or multiple sound sources [63]. The GIR Dataset could help to study further the extraction of geometrical information from sound events or source localisation by providing multiple measurements of the same object from different physical positions. For example, identifying the source-receiver localisation from multiple GIR Datasets corresponds to the object localisation problem, whereas finding the source position from the GIR Datasets at multiple receiver positions corresponds to source localisation.

2.1.3 Paper structure

Section 2.1 introduces the research context, describes the research motivation, and presents related work in audio and acoustics, existing datasets, and their shortcomings. Section 2.2 introduces the GIR Dataset, detailing its content, how it was collected, and how it is structured. Section 2.3 presents a use-case ML application using the GIR Dataset and describes the Neural Network

(NN) architecture and its results. The presented use case is fully reproducible as the whole dataset, the code, and all training data are made available. Finally, section 2.4 concludes the paper by discussing the challenges of creating such a dataset, possible applications, limitations, and future work.

2.2 Dataset

The GIR Dataset is a library of 920712 physically measured impulse responses of 312 scale-modelled architectural wall-like surfaces (2951 per surface) to study early reflections from diffusive surfaces. The measurements were carried out in a frequency range from 2 kHz to 40 kHz on an orthogonal four-layered grid (see Figure 2.1). Layer_0 contains 36 measurement positions in a 6×6 grid, Layer_1 25 measurements in a 5×5 grid, and Layer_2 16 measurements in a 4×4 grid. The fourth layer, *Layer_3*, contains only a single measuring point, but no IR was captured in this location. Instead, this point was used as a source position. The layers are located 124, 214, 304, and 474 millimetres on average away from the surface, respectively. The measurement points are used both as receiver and source positions. The decision to use an orthogonal grid was twofold. On the one hand, an orthogonal grid (in contrast to the polar proposed in the ISO 17497-2 [64]) allows the use of symmetries in ML algorithms [65], which can significantly reduce the sample complexity of the learning process [66, 67]. On the other hand, measuring the reflected sound at different distances from the surface enables the exploration of spatiotemporal relationships between geometry and sound. Spatially, three reflection patterns are captured at close, medium, and far distances from the surface. Temporally, the change in the reflection pattern over time can be captured and visualised [41].

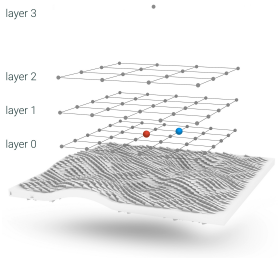

Figure 2.1: The measuring grid. The source is displayed in blue (0,3,3), and the receiver in red (0,2,2).

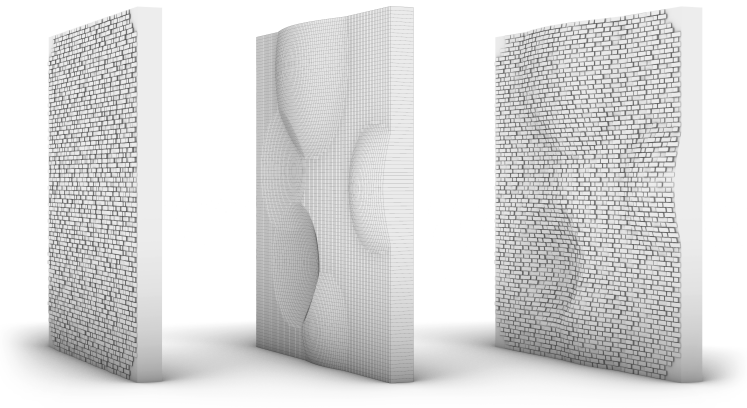

Figure 2.2: Micro- macro surface composition. Left: A surface with only the *Stretcher-bond bricks* microstructure. Middle: A surface with only a macrostructure. Right: The final surface combines the micro- and macrostructure.

Table 2.1: Number of surfaces per typology

Typology	Number of surfaces
Reference	16
Baseline flat	14
Baseline macro	6
Dutch-bond brick wall	68
Polygonal rubble stone wall	33
Ashlar masonry	16
stretcher-bond brick wall	81
IDL *(Gaussian noise & Spline lofting)*	10
Primitives	68
Total	312

The surfaces (referred to as *panels* in the dataset) were computationally designed to resemble 6×6 metres wide walls that are built using common fabrication techniques (referred to as *typologies* in the dataset) such as brick walls, stone walls, cast concrete, and more (See Table 2.1 for a list of surfaces per typology). The surfaces were 3D printed in a 1:10 scale using a binder-jet 3D printer and sprayed with two layers of paint to increase their sound reflectivity (see Appendix A.3). The varying geometry of each panel is composed of a macrostructure and a microstructure (see Figure 2.2) [40]. The first defines the overall shape of the panel, and the second its typology. Several material and construction parameters particular to each typology are coded in a geometry generation algorithm and utilised to generate various surfaces. For example, the brick typologies are defined by the brick size, rotation along the Z-axis, displacement along the macrostructure's normal vector, and the mortar's width and depth [42]. A big geometrical variety is achieved by combining different macro- and microstructures (see Figure 2.3).

The reflection properties of the panels depend on the ratio between geometric dimension and wavelength; therefore, the measurement results also remain valid for other frequencies or dimensions as long as the ratio mentioned remains the same. When interpreting the results in a scaled version, the time axis must also be stretched or compressed by the corresponding factor. This is particularly important in the analysis of time histories, such as the energy over time or the cumulative energy (see more in section 2.3 Use-case example).

2.2.1 Data acquisition setup

An automated robotic setup was used to capture all IR. The setup included two robotic arms inside an acoustically treated room. The room had a size of $5.70\text{m} \times 1.97\text{m} \times 2.55\text{m}$ (L, W, H), and all the surfaces around the measuring base were covered with 5cm thick *Basotect G+* melamine foam by *Vibraplast*.

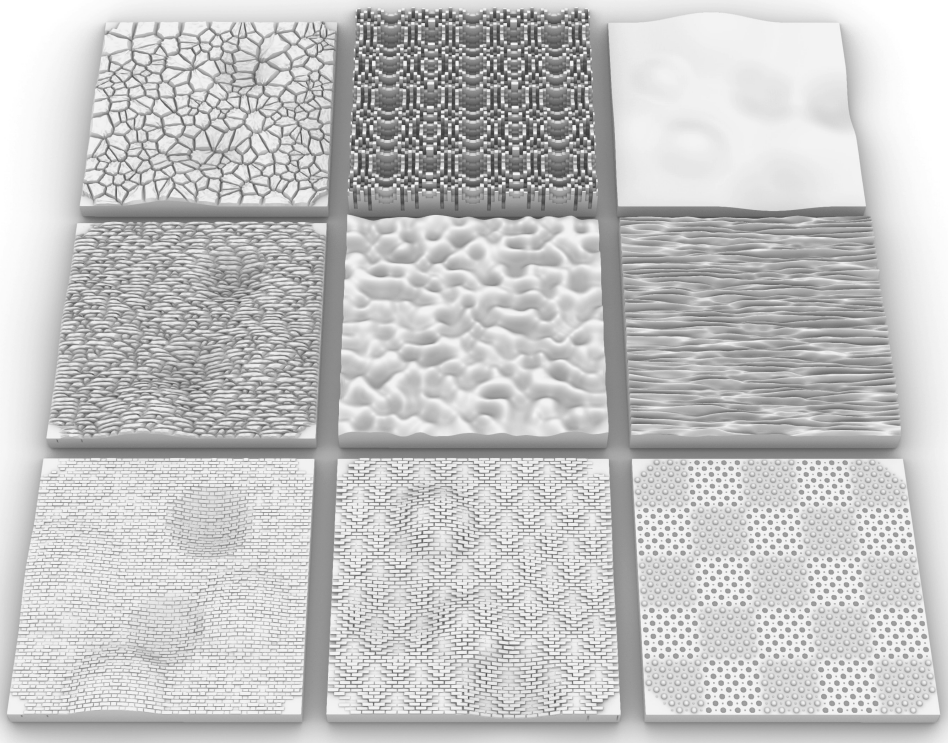

Figure 2.3: A sample of geometries included in the dataset illustrating the different typologies. From top left to bottom right: Polygonal Rubble Stones, Reference *(PRD diffuser)*, Baseline macro *(macrostructure)*, Ashlar masonry, IDL *(Gaussian noise)*, IDL *(spline lofting)*, Flemish-Bond Bricks, Stretcher-Bond Bricks, Primitives.

The first robot was equipped with a speaker (source) and the other with a microphone (receiver) (see Figure 2.4). The robotic arms acted as dynamic measuring devices, emitting a sound and recording the reflection from the 3D printed panel. They continuously re-positioned their end-effectors in a predefined three-dimensional measuring grid on top of the 3D printed panel (see Figure 2.1)[40].

The sound was a linear frequency sweep ranging from 2 kHz to 40 kHz. The frequency range is a direct consequence of the speaker's flat frequency response in this frequency range. The speaker's small membrane diameter produces a narrow sound radiation pattern, focusing sound radiation on-axis, especially at high-frequencies. To maintain its flat frequency response, we oriented the speaker in each measurement to directly point at the centre

Figure 2.4: A closeup view of the data acquisition setup. The microphone (left) and speaker (right) end-effectors attached to two Stäubli TX2-60L robots.

of that microphone-speaker combination's Fresnel Zone [36] on the 3D printed panel [40] (see Figure 2.5). Some microphone-speaker combinations are skipped because the end-effectors would collide with each other. All measured combinations are available by running the `all_combinations()` method of the `Grid` class from the accompanying code.

Figure 2.5: The Fresnel zone on the surface of the 3D-printed panel under test for a 2 kHz frequency.

After every recording, a post-processing pipeline performed automatic quality checks on the raw file before computing the IR. The system kept repeating the recording until all checks were passed. When all checks were successful, the pipeline was then converting the raw recordings to an IR using deconvolution, retaining only the first approximately 4ms. This step was used to filter out unwanted late room reflections and retain only the relevant part of the IR. In some geometries, the path lengths between direct sound and reflected sound were very similar; thus, direct sound suppression using a time-windowing separation was impossible. Instead, the IR of a highly absorbent acoustic foam panel, captured from the same source-receiver positions, was subtracted from the measured IR. This final step resulted in an IR containing only the reflected sound energy of the panel under test. The resulting IR can then be split up into five-octave bands using specifically designed band-pass filters.

Besides the two robotic arms, the data acquisition setup was comprised of several additional hardware components. Below we include a list of the most important components and a short description of how they were used. A more detailed description of the data acquisition setup can be found in [40].

- 2× *Staubli TX2-60L* robotic arms. The robotic arms were also covered with a custom-knitted cotton textile to reduce sound reflections. These robotic arms were chosen for their exceptional precision and repeatability (0.2mm and 0.02mm respectively). To remove any noise sources from the room, we placed their controllers in the adjacent room. Finally, their joint motors could be turned off and on through code, rendering them completely silent when recording.
- A microphone comprised of a *G.R.A.S. 40BE* capsule attached on a *Microtech Gefell MV 220* high impedance transducer.
- A *Berillyum Utopia Be* tweeter by *Focal* was used as a speaker.
- A *Dynavox ET-100* power amplifier drove the speaker.
- A *Scarlett 2i4* audio interface by *Focusrite* was used for playing the sweeping sound and recording the signal from the microphone.
- A *Gravity I2C BME680 Environmental Sensor* by *DFRobot* was used to capture the room's temperature, humidity, and atmospheric pressure in every recording. The temperature values were then used to compensate for the small changes in the speed of sound. All IRs in the dataset are re-sampled using the speed of sound at 20° Celsius.
- A *Gravity Analoge Sound Level Meter* by *DFRobot* was placed outside of the room to monitor the outside noise levels and pause the measurement process when the 60dB threshold was exceeded.
- A *DFRduino Mega2560* by *DFRobot* was used to control the environmental sensor and the sound level meter.

The measurement process per panel took approximately 11 hours, resulting in 16 months for the whole dataset. At the beginning of this research, we evaluated the use of acoustic simulations as a method of acquiring the desired IRs. Geometrical acoustic methods are not capable of modelling sound diffusion [17]; therefore, we looked into wave-based simulations using the Finite-Difference Time-Domain method (FDTD). For a maximum frequency of 40kHz, a domain of $585 \times 585 \times 45$ millimetres, and an FDTD solver performing 150 Million updates per second, a single source required approximately 75 minutes[6] to simulate 40ms. For the 75 sources we used, the FDTD solver would have needed almost 95 hours of continuous computing. This approach was rejected since it would have resulted in a very small dataset.

6: Running on a 2.9GHz 6-core i9 CPU, 32GB of 2400MHz DDR4 RAM.

2.2.2 Dataset content

A dataset sample is comprised of three items; a 3D geometry, a list of 2951 impulse responses, and a metadata file. The 1:10 scaled 3D geometry is stored as *3D Mesh* in an *OBJ* file and the IRs in a 2951×400[7] float32 matrix in an *.npz* file. Finally, the metadata file contains useful information about the geometry

7: $96000kHz \div 4ms = 384 \approx 400$ samples.

design, fabrication, and environmental conditions during the measuring process (Table 2.2). A list containing a detailed description of the metadata file's content can be found in Appendix A.1.

Table 2.2: Dataset sample content.

File type	Content
.obj	3D Mesh (1:10 scale)
.npz	2951 IRs
.json	panel_id, start_time, end_time, package_time, impulse_response_file, geometry_file, macrostructure, recording_sample_rate, reference_resample_temperature, print_provider, print_machine, print_sand_type, typology, print_binder_type, microphone_model, measurements

2.3 Use-case example

In this section, we demonstrate the use of the GIR Dataset to predict the acoustic properties of a surface. For architectural acoustics applications, the fast prediction of acoustic properties through ML could replace time-consuming physics-based acoustic simulations. This would allow designers more iterations on their design and evaluation workflow. Furthermore, since the dataset comprises real measurements, the ML model could provide a more accurate representation of reality than simulation.

Testing sets. The dataset is composed of a unique and highly diverse set of panels (see Figure 2.3 and Figure 2.6). Therefore, we manually defined six different testing sets[8] allowing us to evaluate different generalisation properties of our algorithms (A detailed description of the contents of each testing set can be found in Appendix A.2).

- *Random*: 19 different panels from all typologies. This testing set is informative of the general performance of the algorithm without distribution shift[9].
- *Micro-macro*: The training set contains panels that have either only a macrostructure or only a microstructure. Then, the testing set contains 16 panels that combine these macro and microstructures present in the training set. This set is informative of the model's ability to generalise by combining elements from the training set.
- *Brick-Printer-VJ*: All brick wall panels printed with the VJ[10] printer. This testing set allows evaluating the model's ability to generalise to different conditions, i.e. a different printer.
- *Brick-Printer-CG*: A random selection of brick wall panels from the CG printer.
- *Extrusion*: All *Flemish-Bond Brick* panels with a front extrusion distance of 3mm and a side extrusion distance of 5mm.

8: A testing set, also called test set or holdout data, consists of data that is held out of the training or parameters tuning. This data can then be used for the model evaluation without the risk of information leakage.

9: The term "distribution shift" is used to refer to the fact that samples from the training/validation set might be sampled from a different distribution than the one of the testing set.

10: *VJ* is an abbreviation of the printing service provider's name.

- *Macro*: Six panels composed of only a macrostructure (the flat panel is not included).

Problem details. The goal of this experiment is to predict the acoustic properties of a three-dimensional surface. The GIR Dataset contains a total of 312 panels, but some are reference panels that are used by the post-processing pipeline to clean and normalise the data. Therefore, for our training set, we used a subset consisting of 268 panels comprising a total of 743652 IRs. As

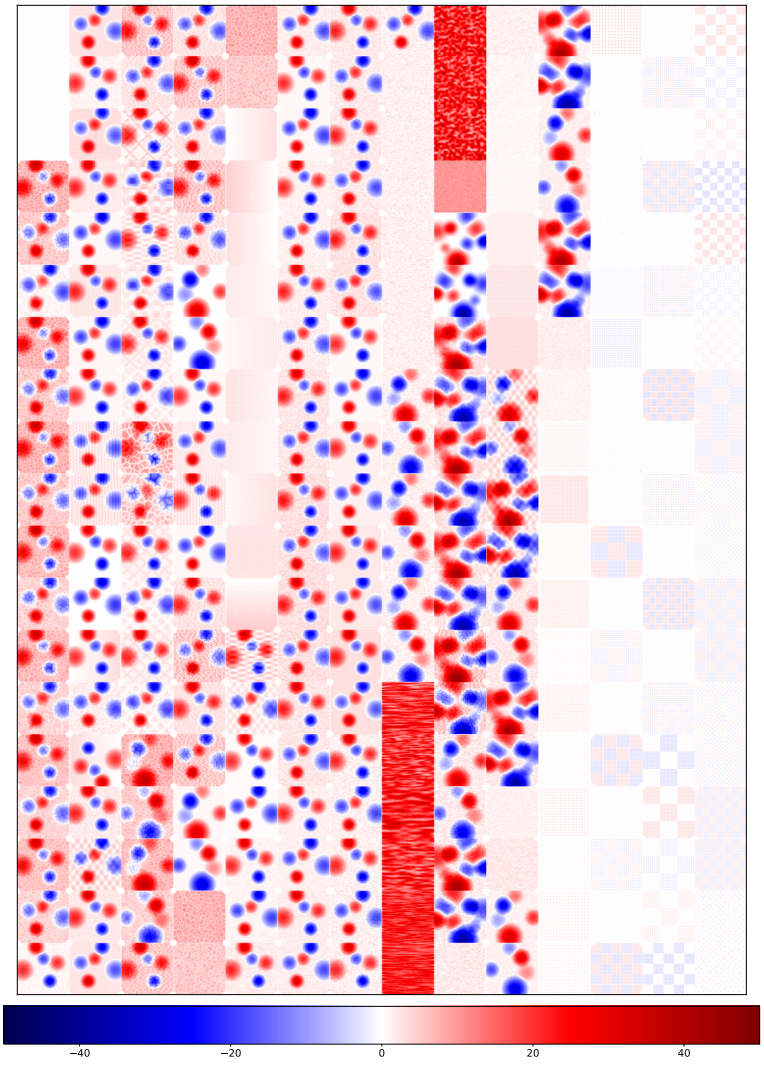

Figure 2.6: Top projection of 266 out of 268 panels used for the experiments. The legend represents the height values of each part of the panels (in millimetres). Panels with the same macrostructure are clearly visible.

a geometry input, we used the 2D projection of the panel's mesh and, as an output, the reflected Cumulative Energy (CE) for any source-receiver position. Our goal is to predict the CE for all available combinations of source-receiver positions on the grid. The cumulative energy is an essential feature as the steepness of the temporal increase maps the reflection characteristic. Moreover, this indicator is easier to predict, as it is evaluated based on the integration over time of sound pressure square and therefore does not contain any phase information. To allow for frequency-dependent predictions, we first split the IR into 5-octave bands using a band-pass filter bank as described in [40]. The first is a low-pass filter with a cutoff frequency of 3.5 kHz, then three band-pass filters with centre frequencies at 5 kHz, 10 kHz, and 20 kHz, and lastly, a high-pass filter with a cutoff frequency of 28 kHz. The filter bank is "tight", meaning that it conserves the signal energy. Then the 5 IRs are converted into CE and normalised using a corresponding reference panel. This panel is printed with the same 3D printer as the panel we wish to normalise, and its CE is used as a reference for the maximum specularly reflected energy. By summing up the CE time series, we obtain six numbers representing the Total Normalised Cumulative Energy (TNCE), five from the band-pass filter plus the total value. Assuming that there is negligible sound absorption by the surface, then TNCE values smaller than 1.0 indicate sound scattering, and values higher than 1.0 indicate sound focusing. Figure 2.7 shows the cumulative energy of an IR and the embedding of all panels using principal component analysis from their 17706 features vectors (6 TNCE numbers $\times$ 2951 positions).

As described in Section 2.2 Dataset, the dataset measurements remain valid for other sets of frequencies and dimensions as long as their ratio remains the same as the one that the GIR Dataset was created, and the time axis is also stretched or compressed by the corresponding factor. For an architectural acoustics application, a 10$\times$ factor can be used, resulting in panel dimensions of 5.85 $\times$ 5.85 meters and a frequency range between 200Hz and 4kHz. The time axis of the CE will also stretch by a factor of 10.

NN architecture and training information. We are in a very low sample regime as the dataset is composed of only 268 panels. Therefore, we use an encoder-decoder architecture that artificially multiplies the number of samples. The encoder comprises six convolutional layers and embeds the $512 \times 512 \times 1$ input geometry into a space of size $8 \times 8 \times 128$. The decoder takes the resulting code and the source positions $6 \times 6 \times 1$ as inputs and outputs the reflected energy for all receiver positions $6 \times 6 \times 1$. This artificially multiplies the number of samples by 36, at least for the decoder. The decoder is a fully convolutional NN with the addition of a trained resampler (a linear layer of size 64×36) that transforms the $8 \times 8 \times 128$ code into a $6 \times 6 \times 128$. Since some microphone-speaker combinations are not measured (see Data

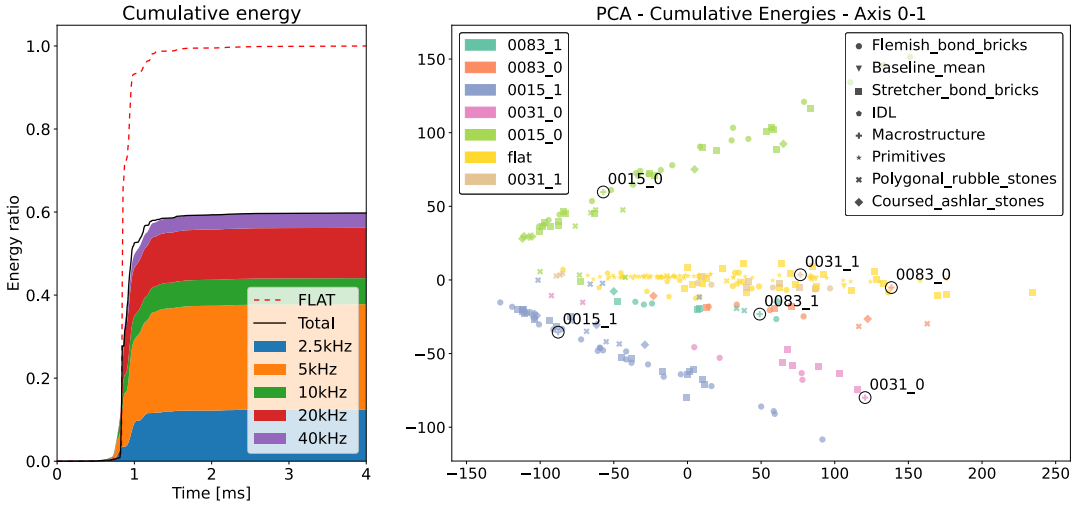

Figure 2.7: Left: Cumulative energy curves of an IR. Each colour represents the cumulative energy of each filter band. The red dashed line is the cumulative energy of the reference flat panel. Right: PCA embedding of the dataset with each dot corresponding to a panel. The colours represent the macrostructures and the symbols of the typologies. The macrostructure panels are marked with a circle.

acquisition setup), we ignore their unmeasured output using a mask. The network size (the number of convolutions and layers) gradually increased until the network would not improve in performance anymore. The overall architecture and the network parameters are illustrated in Appendix A.8.2 (see Figure A.1 and Tables A.4, A.5, and A.6).

We tried augmenting the training set by randomly performing one of four rotations (0°, 90°, 180°, 270°) and flipping the input/output pairs to increase the sample size. Unfortunately, this operation, instead of improving the results, increased the variance slightly. This could be the consequence of the dataset's non-reciprocal nature[11] (See Section 2.4).

11: A measurement with flipped source-receiver positions would not produce the same IR.

Optimisation parameters. We train the network using an Adam optimiser (learning rate of $5e-4$, $\beta_1 = 0.95$, $\beta_2 = 0.999$) [68] for 32 epochs with a batch size of 4. To find the best model, we randomly selected 10% of the training set for validation, computed the validation error at the end of each epoch and selected the model with the lowest validation error. To account for the randomisation error and to obtain an estimate of performance variance, we repeated the experiment 10 times with a different validation set for each repetition.

Results. To remove any possible positional/frequency bias in the dataset, we normalise the output data for the entire dataset. Each source-receiver-frequency band combination has a 0 mean and unit variance. Table 2.3

Table 2.3: Acoustic property prediction results. MSE values for the prediction of the cumulative energy in five energy bands. The output has been normalised with zero mean and unit variance for each band and each source-receiver combination.

	Testing set Variance	Testing MSE	Testing R^2	Validation MSE	Training MSE
Random	1.07	0.52 ± 0.06	0.51	0.60 ± 0.13	0.25 ± 0.03
Micro-Macro	1.59	0.99 ± 0.13	0.38	0.62 ± 0.12	0.24 ± 0.03
Brick-Printer-VJ	1.84	0.87 ± 0.05	0.53	0.61 ± 0.11	0.23 ± 0.01
Brick-Printer-CG	1.12	0.70 ± 0.09	0.37	0.57 ± 0.13	0.23 ± 0.01
Extrusion	1.19	0.39 ± 0.04	0.68	0.64 ± 0.15	0.23 ± 0.01
Macro	2.97	1.78 ± 0.09	0.40	0.56 ± 0.09	0.22 ± 0.01

shows the results acquired from the different testing sets. Due to their panel selection, the testing sets do not have a unit variance. We compare the testing set's variance with the prediction's MSE and compute the coefficient of determination:

$$R^2 = 1 - \frac{\mathrm{MSE}(Y_{\mathrm{pred}})}{\mathrm{var}(Y_{\mathrm{test}})} \tag{2.1}$$

R^2 represents the ratio of variance captured by the network, 0 is equivalent to predicting the mean, and 1 is a perfect prediction. Different testing sets vary the quality of the results with R^2 values ranging between 0.37 and 0.68. The performance differences of the different testing sets in Table 2.3 can be explained by the various distribution shifts between the testing and the training/validation sets. By design, the *Random* testing set has only a small random distribution shift, which explains why the validation and testing MSEs are similar. In fact, comparing the training and the validation MSEs, one can estimate how much of the error is caused by overfitting. The rest of the error can likely be associated with the various distribution shifts.

2.4 Discussion

We have created the GIR Dataset as the first publicly available dataset dedicated to the study of diffusion. The GIR Dataset consists of 920712 physically measured impulse responses and the three-dimensional information of 312 surfaces. We have demonstrated how it could be used in a use-case ML application.

2.4.1 Dataset limitations

Although the GIR Dataset is a unique and valuable dataset for studying acoustics, it comes with certain limitations. These limitations result from unforeseen events or because we underestimated the impact specific factors will have on the dataset. These events and factors are discussed below.

One of the biggest challenges of capturing this dataset was consistency. Computer simulations might not generate accurate IRs (depending on the technique), but they do so consistently. Real IRs, on the other hand, although they accurately represent reality, are sensitive to environmental factors.

A technical problem with the in-house 3D printer and the global pandemic forced us to use four different 3D printers (Table 2.4) from two manufacturers to meet the tight project timeline. We printed a flat reference panel with each printer to mitigate the surface quality differences between printers. We then used its data to normalise all other panels that were printed with the same printer. This solution brought all measurements to a comparable level.

Table 2.4: All the 3D printers that were used to print panels.

Printer	Binder
Voxeljet VX1000	Phenol
Voxeljet VX2000	Phenol
Voxeljet VX2000	Furan
ExOne S-Max	Furan

The 3D-printed panels were highly absorbent regardless of the printer they were printed with. To reduce their sound absorption, we applied two layers of spray paint to the surface of each 3D-printed panel. We used the same setup for all panels (paint, spray gun, spray booth, person spraying) to avoid possible surface variances. Although all panels exhibit the same surface quality when visually inspected, a slight variance can be detected from the recorded data. The only factor that could contribute to this effect is the person spraying. We also noticed that the printing and cleaning quality of one of the 3D printing companies was subpar. Several small and sharp surface features were not present on the final print, and the 3D printed panels had leftover sand stuck on them. These caused the panels to have a more smoothed-out appearance than their 3D model. We created a testing set with all the stone panels from *Printer-CG* for testing purposes. Evaluating the network on this particular testing set led to a negative coefficient of determination of -0.27.

Finally, we based the design of the measurement grid and, consequently, the source-receiver combinations on the reciprocity theorem [69, 70]. A data augmentation of up to 8× would have been possible if we could invert the source-receiver positions. We measured the same panel once in its standard orientation and once rotated 180 degrees around the Z-axis. We then compared the IRs of several symmetrical source-receiver combinations, but they did not match to a sufficient level to be used in our experiment. As an example, using this theoretical symmetry to augment the dataset in our use-case (see Section 2.3) did not improve the network's prediction accuracy. We suppose that the reciprocity principle was violated in our set-up by the non-strict omnidirectionality of the loudspeaker and the microphone at the upper end of the frequency range.

Despite these limitations, measurements are consistent within each panel and comparable across panels when looking at the same source-receiver combination. When looking at one panel, the dataset allows exploring the acoustical effects of microstructure variances or how that panel responds to the different incident and exit angles of sound. When comparing the

same source-receiver combinations on different panels, the dataset enables exploring the acoustical effects of different microstructures, macrostructures, and surface typologies.

2.4.2 Future work and potential applications

The results are very encouraging and suggest new questions to investigate using the GIR Dataset. a) How could we interpolate the measured IRs to other source-receiver spatial positions? Can we construct a high-resolution grid of IRs from just a few specific IR measurements? Some of our preliminary experiments suggest that this is possible. b) Can we perform audio sensing, i.e., recover the panel geometry from the raw IRs? Although it is possible to learn geometry from an IR, we can increase the resolution, thus making panel identification more accurate by combining the information of multiple IRs taken from several positions. c) We have shown in our experiment that we can predict some properties of an acoustic panel using a NN. Therefore, is it possible to construct a useful approximation of the IR only from the geometry? d) Finally, having a good predictor is the first step to tackling the reverse problem. Can we build an ML system that would propose new geometries that match certain given acoustic requirements? Such a system could have a two-fold benefit. On the one hand, it could be used as a design-exploration tool by architects and engineers. On the other hand, using reinforcement learning algorithms could help improve its accuracy by proposing new panel designs for areas with high uncertainty. The measured data will then be added to the dataset to decrease the system's uncertainty in these areas.

2.5 Credits and acknowledgements

2.5.1 Collaboration

The GIR Dataset is one of the research outputs of the collaborative and multidisciplinary research project Data Science Enabled Acoustic Design for Digital Fabrication in Architecture between the Chair of Architecture and Digital Fabrication at ETH Zurich, the Swiss Data Science Center, the Laboratory for Acoustics / Noise Control of Empa, and Strauss Elektroakustik. The data acquisition setup that enabled the GIR Dataset's collection was developed together with Dr Romana Rust, Gonzalo Casas, and Dr Kurt Heutschi. A detailed description of the individual contributions regarding the data-acquisition setup can be found in the Credits and acknowledgements section of chapter *Paper A - GIR Dataset: A Geometry and real Impulse Response*

Dataset for machine learning research in Acoustics (3.6). The data validation, processing, and packaging code were developed in collaboration with Gonzalo Casas. The ML models developed by Dr Nathanaël Perraudin at the Swiss Data Science Center. Oksana Riba Grognuz prepared the dataset for its open-source release on the Renku and Zenodo platforms.

2.5.2 Author's contribution

The author of this thesis conceptualised, generated, and collected the data of the GIR Dataset. The conceptualisation part included defining the relevant geometrical and acoustical data to be included in the GIR Dataset. The generation part included the development of the computational pipeline for designing the surfaces of the dataset, their digital fabrication, and post-processing. The collection part included the development of the data-acquisition setup together with Dr Romana Rust, Gonzalo Casas, and Kurt Heutschi (see 3.6 for more details). The author and Gonzalo Casas developed the computational methods for data validation, processing, and packaging. Lastly, the author developed the PCA tool to analyse and evaluate the GIR Dataset's content.

2.6 Authors contributions to the paper

The individual roles and contributions of each author in this paper are described using the standardised taxonomy CRediT[12][71].

12: Contributor Roles Taxonomy

Achilleas Xydis
Conceptualisation, Methodology, Software, Data Curation, Validation, Investigation, Writing – Original Draft, Writing – Review & Editing, Visualisation, Project administration

Nathanaël Perraudin
Methodology, Software, Data Curation, Validation, Formal analysis, Writing – Original Draft, Writing – Review & Editing, Visualisation

Romana Rust
Conceptualisation, Methodology, Software, Validation, Investigation, Writing – Review & Editing, Supervision, Project administration, Funding acquisition

Kurt Heutschi
Conceptualisation, Methodology, Validation, Writing – Review & Editing

Gonzalo Casas
Software, Validation, Investigation, Data Curation

Oksana Riba Grognuz
Data Curation, Validation, Writing – Review & Editing

Kurt Eggenschwiler
Conceptualisation

Matthias Kohler
Conceptualisation, Methodology, Writing – Review & Editing, Supervision

Fernando Perez-Cruz
Methodology, Writing – Review & Editing, Supervision

2.6.1 Acknowledgements

This research was jointly supported by the Swiss Data Science Center and the Chair of Architecture and Digital Fabrication, ETH Zurich and in collaboration with the Laboratory for Acoustics/Noise Control at EMPA and Strauss Elektoakustik GMBH. We would like to thank Liya Sunny Anthraper, Priyank Soni, Daniela Mitterberger, Inés Ariza, Pok Yin Victor Leung, Joris Burger, Fabio Scotto, Chaoyu Du, and Anton Johansson for their help in the measurement process and Dr Mariana Popescu for the custom-knitted sleeves.

3 Paper B - A data acquisition setup for data driven acoustic design

Romana Rust[*], *Achilleas Xydis*[*], *Kurt Heutschi*[†], *Nathanaël Perraudin*[‡], *Gonzalo Casas*[*], *Chaoyu Du*[*], *Jürgen Strauss*[∓], *Kurt Eggenschwiler*[†], *Fernando Perez-Cruz*[‡], *Fabio Gramazio*[*], *Matthias Kohler*[*]

[*] Gramazio Kohler Research, ETH Zurich, Zurich, Switzerland
[†] Swiss Data Science Center, Zurich, Switzerland
[‡] Laboratory for Acoustics / Noise Control, Empa, Duebendorf, Switzerland
[∓] Strauss Elektroakustik GmbH, Bern, Swizterland

In this paper, we present a novel interdisciplinary approach to studying the relationship between diffusive surface structures and their acoustic performance. Using computational design, surface structures are iteratively generated and 3D printed at a 1:10 model scale. They originate from different fabrication typologies and are designed to have acoustic diffusion and absorption effects. An automated robotic process measures the IRs of these surfaces by positioning a

microphone and a speaker at multiple locations. The collected data serves two purposes: first, as an exploratory catalogue of different spatiotemporal acoustic scenarios and second, as data set for predicting the acoustic response of digitally designed surface geometries using machine learning. In this paper, we present the automated data acquisition setup, the data processing and the computational generation of diffusive surface structures. We describe the first results of comparative studies of measured surface panels and conclude with steps for future research.

Romana Rust, Achilleas Xydis, Kurt Heutschi, Nathanaël Perraudin, Gonzalo Casas, Chaoyu Du, Jürgen Strauss, Kurt Eggenschwiler, Fernando Perez-Cruz, Fabio Gramazio, Matthias Kohler, *A data acquisition setup for data driven acoustic design*, Building Acoustics (Volume 28, Issue 4) pp. 345-360. The published version is available online at: https://doi.org/10.1177/1351010X20986901.

3.1 Introduction

The acoustic quality of a room is an important criterion for the perception and, subsequently, the sense of well-being of its inhabitants [72, 73]. However, today's architectural acoustic design is mainly focused on typologies that demand high-end acoustics, like concert halls or auditoriums. The acoustic design of the vast majority of the built environment is often overlooked, leading to reduced comfort, negative health effects from acoustic pollution, cost for noise abatement measures and unaesthetic retrofitting of built structures both indoors and outdoors.

One of the main reasons for this is the lack of accurate and easy-to-use simulation tools [74] that can be well integrated into computational design workflows, enabling the assessment of acoustic quality without the need for acoustic specialists. Thus, acoustics is only considered at a later stage of the architectural planning process (and often concerns only the installation of standard absorption panels). Still, computational room acoustics is a field that has been intensively studied over the past 50 years [16]. Fundamentally, there are two main approaches for computationally modelling the acoustics of a room, which are either based on numerically solving the wave equation or on the assumptions of GA. Wave-based modelling is able to provide the most accurate results but is too computationally expensive [14, 75] for an iterative design and evaluation workflow. GA is faster but less accurate. Here the sound is assumed to propagate as rays, and the wave nature of sound is neglected. Thus, all wave-based phenomena, such as diffraction and interference, are missing. Available room acoustic modelling software such as ODEON [76], CATT, EASE, Ramsete [77] or RAVEN [78] are offering hybrid GA methods, where the image source approach is combined with ray-tracing that allows to consider diffuse reflections [79]. The scattering properties of a surface are usually described by a simple one-parameter model that assumes Lambert's reflection directivity. This approach splits up the reflected power into a specular and a scattering part, whereas the ratio between the two contributions depends on the frequency and the structure depth. This coarse reflection model can not consider specific surface properties that can generate particular reflection patterns. In order to be able to work in room acoustic design with surfaces with specially designed reflective properties, other solutions are necessary.

Another method to validate room acoustics utilises physical scale models [80]. Here, sound sources are installed at predefined positions, emitting sound in a scaled frequency range while the corresponding audio signals are recorded. The resulting measurements can be used to analyse the acoustic performance [75] and improve the design [81]. However, this method is

extremely time- and resource-inefficient, as the number of design iterations is limited to the number of built models.

In this paper, we present a novel interdisciplinary approach to studying the mutual relationship between diffusive surface textures and their acoustic performance through data science methods. In order to leverage data gathered from physical scale models, we employ an automated robotic measurement setup to record the IRs in front of 3D printed acoustically diffusive surfaces at 1:10 scale. They represent surface structures created through certain fabrication typologies, such as brick or stone walls, for which we collect diverse acoustic scenarios. The recorded data set serves as a foundation to analyse relations between geometrical and acoustical configurations and to determine performance clusters. The final goal is to use the created data set as a basis for a data-driven acoustic simulation that will allow us to predict the acoustic properties of newly created 3D surfaces, thus omitting the need for a physical scale model.

The main challenge of building this data set arises from the need to define and collect sufficient, relevant, and reliable data in a short amount of time. Additionally, the post-processing of the input data needs to be identified since both geometric and acoustic information are high-dimensional. This is necessary for both the data visualisation and the future ML system. In the following sections, we describe the data acquisition setup, the parameters of the data set and the post-processing of the IR to extract meaningful measures, such as the reflected cumulative energy per frequency band. These evaluated indicators allow different panels to be compared. We introduce the computational generation of diffusive surface structures and conclude with strategies for shaping the data set and future work.

3.2 Acoustic data acquisition setup

The constituent parts of the multi-robotic setup were developed collaboratively by evaluating architectural and acoustic requirements, in addition to the requirements from the perspective of data science and the constraints of a physical setup. Several tests were performed to guide the development and validate the quality of the measured data. Some of these tests can be found in the project's open data repository [51].

The multi-robotic measurement setup consists of two 6-axis Staubli TX2-60L[1] robotic arms with a reach of 920mm each (see Figure 3.1). They are equipped with two different end-effectors: one with a speaker and the other one with a microphone. During the measurement process, they reconfigure from position to position in an irregular measurement grid above a 3D-printed acoustic panel. For each combination of microphone and speaker position,

1: These robotic arms are accurate (absolute positioning accuracy 0.2mm, repeatability 0.02mm), and they have the ability to programmatically turn the joint motors off and on, such that their operating noises do not affect acoustic measurements.

Figure 3.1: Acoustic data acquisition setup with two Staubli TX2-60L robots in an acoustically shielded and absorbent room.

a sweep signal in a scaled (1:10) frequency range of 2-40kHz is emitted, a recording is taken, and the corresponding IR is calculated. The sweep signal covers the frequency range that can be reproduced by the loudspeaker and determines the lower and upper-frequency limits of the data. The time spent on each measurement combination averages 12.3 seconds, and the measurement process per acoustic surface takes approximately 10 hours, during which the data of 2951 measurement combinations are stored. To avoid acoustic reflections, the robotic arms are covered with custom 3D knitted sound-absorbing cloths. The robot controllers are installed in the adjacent room to prevent their operating noise from affecting the measurement. The whole setup is installed inside a sound-insulated room, in which all surfaces are covered with 50mm melamine foam[2]. In the following paragraphs, the core components of the setup are described.

2: Basotect® G+ Melamine foam from Vibraplast AG.

3.2.1 3D printed acoustic panels

The goal of the research project is to produce a large and rich data set during the project's time span. However, the main constraints are the measurement time, the acoustic panel's size and its fabrication time. The print-bed of the in-house Voxeljet VX1000 3D sand printer and the defined operation hours constrain the acoustic panel's size to a bounding box measuring $585 \times 585 \times 100$mm (W x L x H), enabling the production of maximal five panels per week. To increase the number of measurable surfaces, we designed the panel with two sides (see Figure 3.2), thus two acoustic surfaces per panel. A square panel shape was selected for the possibility of applying

Figure 3.2: Double-sided 3D printed panel placed in a special fixture.

standard data augmentation techniques: based on the assumption that the measurements are symmetric, the data can be virtually mirrored and rotated four times (90 degrees each time), resulting in an overall increase of the collected data by a factor of eight.

A panel produced with a binder-jet 3D printer is porous and highly absorbing. To obtain a surface that represents rigid non-porous materials, the panel is coated. We evaluated different surface treatments and compared the respective normal incidence absorption coefficients obtained by impedance tube measurements. If left untreated or baked in an oven, the absorption coefficient is 0.47-0.58 for frequencies between 2-6kHz. If infiltrated with resin or coated with two layers of acrylic paint, the absorption coefficient is below 0.1 (see Figure E.2). We decided to proceed with the application of two layers of plant-based, water-borne paint using a compressed air spray gun. We compared the panel's surface reflectivity after coating by comparing the measurements from a coated flat 3D printed surface (referred to as *Flat*, see Table 3.1) with a flat MDF panel (referred to as *Wood*). Compared to *Wood*, *Flat* reflected on average 29.3% less energy. This unavoidable loss in reflected energy and the variations of the measurements is considered in the subsequent evaluations by normalisation (see Section 3.3.2); that is to say, all indicators are consequently calculated in relation to *Flat*.

3.2.2 Measurement grid

The measurement locations are set in an irregular point grid based on the defined dimensions of the 3D printed panel, the robots' working space, and acoustic considerations. The grid's dimensions are defined to avoid

measurements with edge diffraction as much as possible. The density of the measurement grid was calculated based on three criteria: a) to ensure a uniform surface coverage, b) to maximise the number of data points per panel, and c) to allow two acoustic surfaces to be measured within a 24-hour cycle. To do so, we calculated the first Fresnel zone[3][36] for each microphone and speaker combination for both the lowest and highest used frequencies, assuming a planar surface. By calculating all possible combinations of speaker and microphone positions (excluding some immeasurable cases), the final measurement grid contains 78 measurement points (see Figure 3.3) and a total of 2951 measurement combinations. The measurement points are placed on four planar layers, each with a different number of measurement points located at different offsets from the panel's surface. The first layer contains 6x6 measurement points, the second 5x5, and the third 4x4, with average offsets of 124, 214, and 304mm from the surface and respective distances of 75, 93.75 and 125mm between measurement points. The fourth layer has only one measurement point with an average offset of 474mm from the surface. Finally, the Fresnel zones for the lowest frequency (2kHz) have a minimum ellipse diameter of 195mm and a maximum of 560mm, and for the highest frequency (40kHz), 43mm and 140mm, respectively.

3: Fresnel zones on a surface are the intersections of Fresnel spheroids with a flat surface between a source and the image of the receiver. The foci of the Fresnel spheroid are the source and the image of the receiver. The resulting intersections have the form of an ellipse.

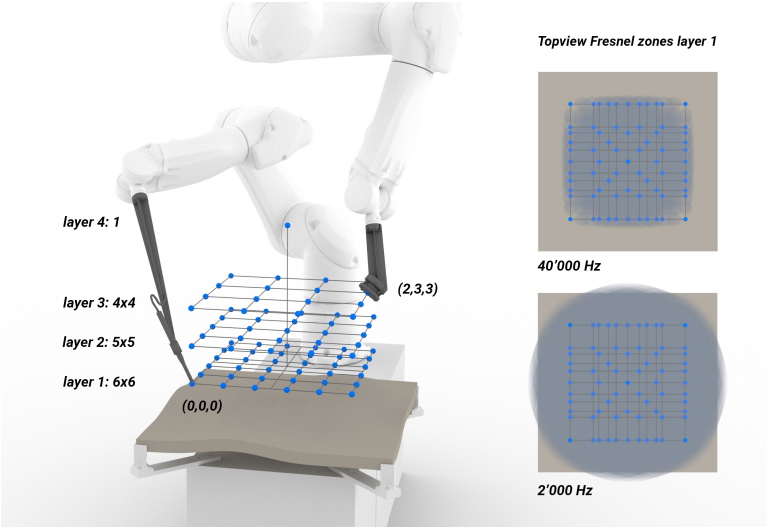

Figure 3.3: Left: Measurement grid with four layers in relation to robotic setup and 3D printed panel. Right: Panel top view with surface coverage in layer 1 at 40000Hz (top) and 2000Hz (bottom) calculated by Fresnel zones.

3.2.3 Microphone and speaker end-effector

To record clean audio responses, shielding and scattering from the robotic arms are avoided to the greatest possible extent. The microphone is positioned

Figure 3.4: Microphone (left) and speaker end-effector (right). The microphone is attached to an acoustically transparent steel mount, and the speaker is tilted to optimise directivity and ensure robot reachability.

such that it is far from the robot's flange (approx. 0.5m), and it is fixed on an acoustically transparent steel mount (see Figure 3.4). The precise tool manufacturing and the accuracy of the robotic arm allow us to achieve a positional accuracy of 0.17mm[4] for the microphone. The microphone consists of a *G.R.A.S. 40BE capsule* attached to a *Microtech Gefell MV 220* high-impedance transducer. The microphone is of free-field type and has a flat amplitude response up to 40kHz (-1dB) for sound incidence on-axis. For 30° and 60° off-axis, the sensitivity at 40kHz drops by 2 and 4dB, respectively.

4: After the absolute calibration of the robotic arms, we have a mean precision of 0.17mm and a max@90% of 0.28mm.

On the source side, a *Beryllium* tweeter was selected as a loudspeaker that is capable of exiting frequencies between 2 and 40kHz. As a direct consequence of the 20mm membrane diameter, the loudspeaker shows a directivity pattern with a tendency to focus sound radiation on-axis at high frequencies. Several tests with conical attachments and scattering objects in front of the membrane showed an improved (closer to omnidirectional) radiation pattern, however, with a degradation of the temporal signature. To maintain the excellent time response of the tweeter, it was decided to do without measures to optimise directivity but carefully orient the speaker in each measurement configuration. This is the reason for the 45° tilt of the steel mounting (see Figure 3.4), ensuring reachability by the robotic arm.

The microphone and speaker are connected to a *Focusrite Scarlett 2i4 2nd Gen* audio interface. We use two of the mono-balanced output channels. One is connected to an amplifier that drives the *Beryllium* tweeter, and the other is connected back to one of the audio interface's inputs and used as a loopback channel for computing the IR (See 3.3.2).

3.2.4 Automation, control setup and sensors

`COMPAS FAB` [82] and `MoveIt` [83] were used to calculate collision-free robot trajectories for each of the 2951 measurement configurations of microphone and speaker along a defined sequence. For the data acquisition phase, a workstation running texttttUbuntu 16.04, together with the audio interface and the two *Stäubli CS9* robot controllers, were installed in the adjacent control room. `ROS Kinetic` [84] is used as the base of a distributed system with the following nodes: main controller service, ambient measurement service, audio interface service, two VAL3 robot driver instances and `WebSockets ROS bridge` [85]. The main controller service was built using `COMPAS FAB` [82], and it coordinates all other services. After positioning, the controller powers the robots off so that their operating noises do not affect the measurement. Then it invokes the audio interface to start playback and recording while the ambient measurement service collects external sound level, temperature, relative humidity, and atmospheric pressure using an *Arduino* board. The external sound level values are employed to track exogenous sounds that can influence the quality of our measurements. After recording, the IR is calculated and validated to ensure that the measurement is not distorted by unwanted signals and repeated if needed.

Metrics of the process are continuously collected in an `InfluxDB` time-series database, and `Grafana` is used for monitoring. Tracked metrics include values from all ambient measurement sensors, system metrics based on `collectd`, and process metrics.

3.3 Dataset, post-processing and visualisation

The acoustic data acquisition setup collects different spatiotemporal acoustic scenarios, which are stored in a multivariable data set. One data point in the data set consists of the computationally generated geometry of the measured diffusive surface, plus 2951 IRs, supplemented by measured environmental data (temperature, humidity, atmospheric pressure). The geometric information of the data set includes input parameters of the geometry generation algorithm (see Diffusive surface structures), together with the algorithm itself, and the representation of the surface as a polygon mesh. The mesh data is directly used for the panel fabrication with the binder-jet 3D printer. Additionally, each 3D panel is labelled with a unique identifier and suffixed with 0 or 1, indicating the panel side (e.g. 0015_0). This identifier is used to determine the 3D-printed physical object with the data set entry.

Label	Material	Purpose
Wood	MDF plate	Reference for a surface of high reflection.
Flat	3D printed and coated	Reference for the surface of highest reflection possible with the used 3D printed and coated material. Used to normalise the measurements.
Foam	Acoustically absorbent melamine foam	Reference for a surface of high absorption. Used for subtracting the direct sound signal from the measurement.
2D-PRD	3D printed and coated	2D Primitive Root Diffuser. Reference for a surface of high and uniform diffusion.
0015_0	3D printed and coated	Reference for a specific macrostructure with no meso- and microstructure.

Table 3.1: Reference panels

3.3.1 Reference panels

Some data points in the data set are baseline measurements obtained from special reference panels with the same dimensions as our 3D-printed acoustic surfaces. These serve to put the measurements of the 3D-printed acoustic panels in relation to other materials or panels with different surface geometry. Table 3.1 lists the baseline measurements with their respective label, material and purpose. Two of these baseline panels (*Flat* and *Foam*) are also used in the post-processing of the data, which is part of both the ML processing pipeline and the data visualisation.

3.3.2 Impulse response and data post-processing

The primary measurement result for a specific surface and speaker/microphone combination is the IR. The IR is the richest representation possible as it contains all of the acoustic information linking the source and the receiver. Furthermore, one advantage of the IR is the fact that different contributions appear lined up on the time axis. As a result, the 2951 IRs offer a very precise and relatively complete representation of the acoustic response of a panel surface. Nevertheless, the IRs presents some challenges as well. First, IRs are not easily interpretable with respect to perceptional aspects, especially because the phase information is very complex. Second, for human data analysis, it is necessary to compress the information contained in the 2951 IRs such that it can be comprehensibly visualised per acoustic surface. Third, for the future ML system, the direct modelling of the IRs might be challenging or even impossible, given the low amount of available samples at the end of the research project. In consequence, we identified other indicators that represent the desired acoustic information of a surface from an acoustic design perspective.

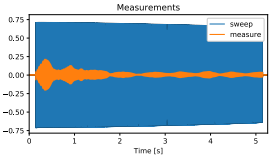

Figure 3.5: Captured IRs. Blue: the sweep signal Orange: the microphone measurement.

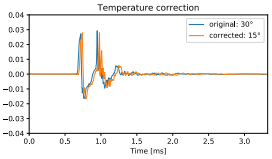

Figure 3.6: After deconvolution, the temperature correction is applied. In this figure, we used 30°C and 15°C to emphasise the resampling effect.

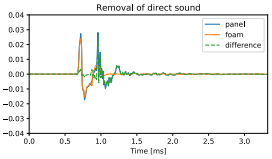

Figure 3.7: Direct sound removal.

Information extraction

First, to obtain the IR, we play a linear frequency sweep ranging from 2 to 40kHz and record the microphone signal as raw data. The IR is then computed by deconvolution, and temperature compensation is applied. The deconvolution operation is carried out using a simple division in the Fourier domain. Given $\hat{x} = Fx$ the Fourier transform of x and $x = F^{-1}\hat{x}$ its inverse operation, the deconvolution of the signal x with the sweep s is given by

$$x_d = F^{-1}\left(Fx/Fs\right) \tag{3.1}$$

where s is the sweep, and the division is performed element-wise. Note that $\mathcal{F}s$ is never close to 0 because the sweep contains all frequencies (see Figure 3.5). To adjust for the room temperature change, we estimate the speed of sound at temperature T (in $°C$)

$$c = c_0\sqrt{1 + (T/273.15)} \tag{3.2}$$

where c_0 is the temperature at $0°C$ [86]. The IR is then resampled at the frequency $c/c_{ref}f_s$, where c_{ref} is the speed of sound at $20°C$ and $f_s = 96kHz$ the sampling frequency. We use the polyphase filtering method (`resample_poly`) from the `SciPy` python package (see Figure 3.6). Afterwards, we crop the IR after 4 ms and suppress the direct sound. Due to small path length differences between direct and reflected sound in some geometries, a time-windowing-based separation is not applicable. For that reason, the direct sound time signal obtained from an IR measurement with an absorbing panel (referred to as *Foam*) is subtracted (see Figure 3.7). Third, the IR is band-pass filtered with the help of the filter bank described below (see Figure 3.8). This allows the derivation of frequency-dependent reflection properties of the surface. Fourth, the filtered IRs are converted to cumulative energy curves (see Figure 3.9) that display, on one hand, total reflected energy and its distribution among the different filter bands and, on the other hand, the temporal pattern of energy arrival. The cumulative energy curves are then put in relation to the measurements obtained from a reference flat panel (referred to as *Flat*) by normalisation. For simplification, we refer to the resulting curves as *Normalised Cumulative Energy (NCE)* curves and the resulting total value as *TNCE* in the following. The *TNCE* measure allows comparing different panels with each other. For example, if we contrast the stacked cumulative energy plots of Figure 3.9 and Figure 3.10 and refer to Table 3.2 for the *TNCE* values, the following information can be extracted: First, we see that panel *0072_0* reflects 14.1% less energy than the *Flat* panel. Second, the energy distribution among the different frequency bands changes. The 2.5kHz and 5kHz bands are exhibiting an energy increase, the 10kHz band has almost no difference ($< 0.2\%$), and the two higher bands have a significant decrease. Additionally, the slope of the *NCE* curve relates to the

Panel ID	2.5 kHz	5 kHz	10 kHz	20 kHz	40 kHz	Total
Flat	0.092	0.216	0.169	0.309	0.213	1.000
0072_0	0.136	0.291	0.169	0.157	0.106	0.859
energy difference	47.4%	34.5%	0.18%	-49.2%	-50.3%	-14.1%

Table 3.2: *TNCE* values for *Flat* and panel *0072_0*. The values relate to Figure 3.9 and Figure 3.10

degree of diffusiveness where a steep gradient indicates a rather specular reflection and a slow increase represents a diffuse reflection. In this case, panel *0072_0* has a slightly less steep slope.

Filterbank design

The signal is separated into different frequency bands using an "itersine" wavelet construction. Formally, we use the mother function:

$$c(\omega) = \sin\left(\frac{\pi}{2}\cos(\pi\omega)\right) \tag{3.3}$$

and scale, warp, and translate it as in [87]. Selecting the right parameters, we construct the set of five filters shown in Figure 3.8. The filters are centred at 5, 10, and 20kHz and are logarithmically stretched (warped). The blue and green filters correspond to the remaining low and high-frequency bands. Note that because everything is 1:10 scaled, the three band-pass filters correspond to 0.5, 1, and 2kHz bands. Note that this set of filters forms a unitary tight frame, meaning that the total energy of the signal is conserved after the application of the filters. The proposed construction does not satisfy a particular norm for octave-based filter banks such as IEC 61260.1:2019 [88]. However, it is tailored to our application because it conserves energy and has good localisation properties both in the time and the frequency domain.

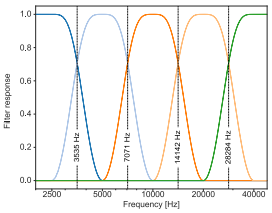

Figure 3.8: Constructed filters to separate the content of the IR in frequency

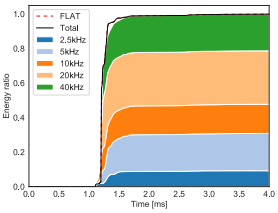

Figure 3.9: Stacked cumulative energy curves of panel *Flat*

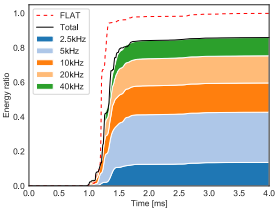

Figure 3.10: Stacked cumulative energy curves of panel *0072_0*

3.3.3 Data visualisation

For 150 measured surfaces, the *TNCE* values range between 0.02 and 24.32. However, the value of the 95th percentile is 1.67. To represent those values in a compact way and not clip high numbers, we map them on a logarithmic dB scale by applying the function:

$$f(x) = \frac{10}{log_{10}(x)} \tag{3.4}$$

Figure 3.11 shows all data that relate to a given microphone index at the corresponding location in the measurement grid for three of the reference panels. The *TNCE* values are first mapped on the logarithmic dB scale, then converted to colour, and finally grouped based on measurement grid layers

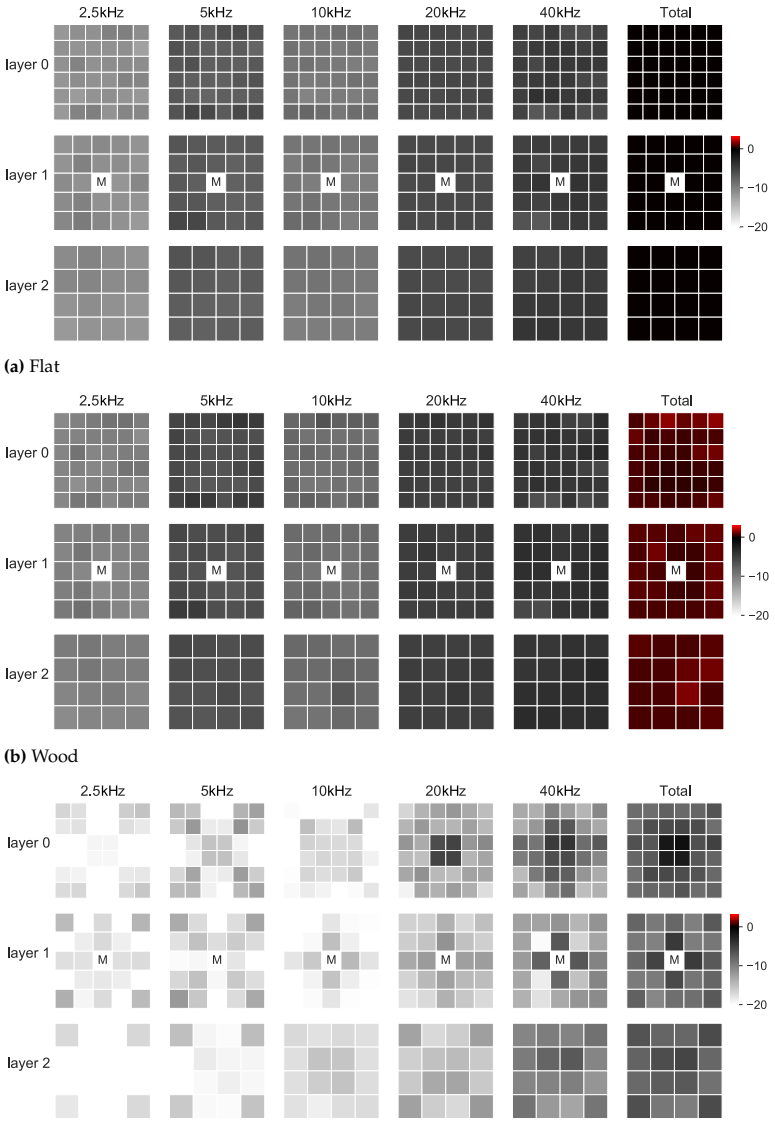

(a) Flat

(b) Wood

(c) 2D-PRD

Figure 3.11: Layered grid plot of band-separated *TNCE*. Layer 0 is the closest to the surface, and layer 2 is the furthest away. "M" indicates the microphone's position.

(horizontally) and filter bands (vertically). The data is always read relative to the *Flat* panel: white indicates less cumulative energy (minimum -20dB) and black an equal amount (0dB). In situations where amplification occurs due to focusing, they are represented with red (maximum +6dB). In this way, the

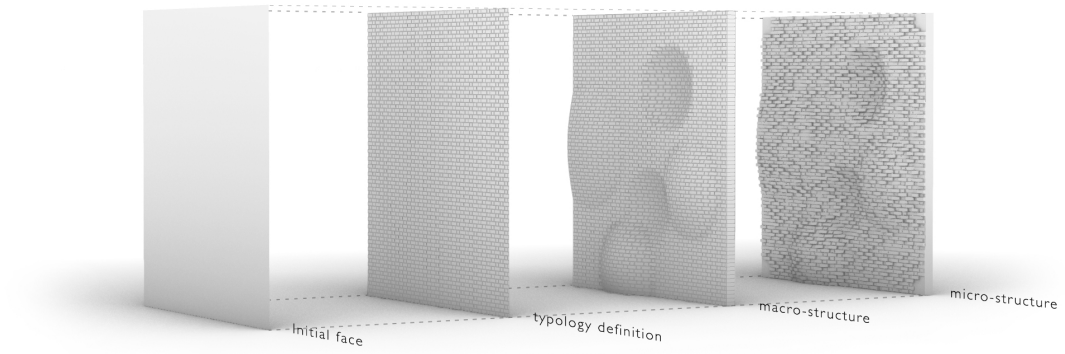

Figure 3.12: Geometry generation steps for a Flemish bond brick wall. From left to right: initial single-faced flat mesh, flat mesh subdivided according to typology, thickened mesh with macrostructure deformation, and final mesh with microstructure deformation.

high dimensional information of the panel measurements can be visually compared and evaluated (see section 3.4.2).

3.4 Diffusive surface structures

Surface articulations play a significant role in the resulting acoustic response. When a sound wave is incident on a surface, the shape and size of these articulations define which frequencies will be specularly reflected and which will be scattered [89]. Diffusion is an important acoustic phenomenon that can promote spaciousness, prevent flutter echoes, and improve speech intelligibility. Although a reasonably big library of absorption coefficients for different materials is available, the same is not true for scattering coefficients [75]. With the goal of investigating diffuse surface properties, we generate geometric typologies stemming from architectural fabrication techniques, ensuring compatibility with past and current building systems (rubble stone walls, river rock walls, slated stone walls, brick walls). These are chosen based on their ability to diffuse sound within a broadband or a selective frequency range. The typologies vary with the motivation to a) uncover new possibilities within the domain of acoustics, possibly integrating diffusion and absorption within one surface, and b) diversify the acquired dataset. To ensure the latter, data acquisition and the generation of new surface geometries are performed in parallel. In this way, results from a measured panel can be used to inform the generation of new ones.

3.4.1 Computational generation of diffusive surface structures

For each fabrication typology, the essential geometric characteristics were extracted and implemented in a geometry generation algorithm that controls the surface geometry represented by a polygon mesh with a set of functions. These functions generate macro-, meso-, and microstructures based on specific criteria by applying operations such as mesh subdivision and mesh face translation. The macrostructures are targeting the low-frequencies, the mesostructures the mid frequencies, and the microstructures the high frequencies. For example, for a stone wall (see Figure 3.12), its general shape (depth, straight or wavy) is controlled by the macrostructure, the overall size and placement of stones by the meso-structure, and finally, the surface roughness of each stone, and the shape of the joint between them, by the microstructure. Through this modular surface generation process, panels of the same macrostructure but different microstructure or similar combinations can be compared and analysed.

Due to the limited time span of this research project, there is a limited amount of surface variations per typology that can be explored. At the beginning of each typology exploration, the value ranges of all surface articulation parameters are defined. Then, random step sizes to sample these value ranges are chosen, and a first group with a certain number of panels is generated and produced. After this group has been measured, the acoustic data are compared against each other, and the step sizes for the next group of panels are adjusted. If the compared data are very similar, the step sizes need to be increased. If the data are significantly different, the step sizes need to be decreased. This allows for diversity in the data set while avoiding unexplored areas.

3.4.2 Comparative experiments

Comparative studies are used to investigate the relationship between geometry and resulting acoustical properties. These studies serve two main purposes: first, they help to verify certain acoustic assumptions and thus validate the data set; and second, they serve to develop quantitative design guidelines for acoustic planners and architects, which can be used in their design workflow. For each typology, experiments are designed to test how the size, rotation, spacing, protrusion and roughness of the base element (e.g. brick, stone) influence the acoustic response. This section describes three of these studies, comparing the captured acoustic data of several panels to determine how a chosen geometrical characteristic influences acoustic performance.

Brick wall joints

Panel ID	Mortar height	Frequency band					
		2.5 kHz	5 kHz	10 kHz	20 kHz	40 kHz	Total
0015_1	0	-7.66	-3.66	-9.18	-7.02	-5.54	-0.4
0012_1	0.6mm	-7.8	-4.14	-9.58	-8.06	-7.38	-1.02
0011_1	1.2mm	-7.86	-3.89	-9.19	-9.62	-8.55	-0.86

Table 3.3: Mortar on brick walls experiment. Mean *TNCE* values of the 90th percentile per filter band. Mortar height in mm (1:10) and energy values in dB. For every frequency band, red indicates the value with the smallest difference to the reference *Flat*, and green is the one with the highest.

This experiment investigates brick walls and the acoustic effect of different mortar joint heights and depths. Considering building parameters for brick walls, an average joint height ranges between 5 to 10mm (0.5 to 1.0mm in 1:10 scale). The mortar can be either flush with the surface of the bricks or recessed by a few millimetres. Given the small size of the joint in relation to the overall surface, we only expect an influence on the high frequencies. To test this assumption, we compare three panels with the same macrostructure: two of them feature a Flemish-bond brick wall typology, with a raked joint type and an average height of 0.6 mm (*0012_1*), and 1.2mm (*0011_1*) respectively; both with a joint depth of 1mm. The third panel features only the macrostructure (*0015_1*), representing a brick wall with a joint height of 0.6mm and a joint depth of 0mm. Table 3.3 shows the mean *TNCE* of the 90th percentile[5] for each filter band. As expected, the joint height does not affect the first three filter bands (2.5, 5, and 10kHz). For the two higher ones, panel *0012_1* shows 1.04 and 1.84dB less energy compared to the reference panel *0015_1*, and panel *0011_1* 2.6 and 3.01dB respectively. Therefore, a small but noticeable reduction in the high-frequency energy can be achieved just by recessing the mortar joint and by increasing the mortar height. It is important to note that if we look at the mean *TNCE* for the full spectrum, the difference is very small. Both panel *0011_1* and panel *0012_1* have very similar values and are only 0.68 and 0.46dB, respectively less than the one from panel *0015_1*.

5: The 90th percentile was chosen to exclude outliers.

Macrostructure

In this experiment, we compare panels *Flat*, *0015_0*, and *0031_0* and focus solely on the effect of the macrostructure. Each panel has a different macrostructure but no microstructure. Compared to *Flat* (see Figure 3.11a), an apparent disruption in the homogeneity of the energy distribution is visible (see Figure 3.14). Microphone-speaker combinations where their Fresnel zone falls in a convex shape exhibit less energy. Contrary, combinations in which their Fresnel zone falls in a concave part of the surface exhibit increased energy due to the focusing effect (see red squares in Figure 3.14b). When comparing two panels that share the same macrostructure but have different microstructures (see Figure 3.13), the cumulative energy plots show that the macrostructure influences all frequency bands and the microstructures start having an influence only after 10kHz.

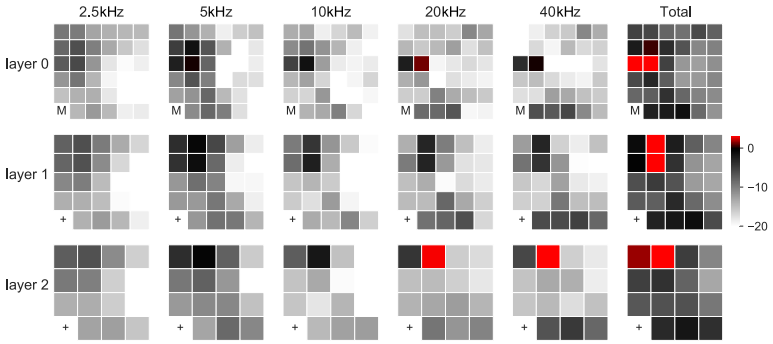

(a) Panel *0015_1*

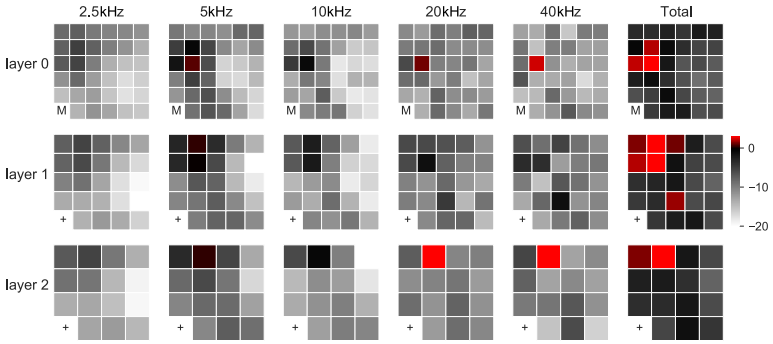

(b) Panel *0005_1*

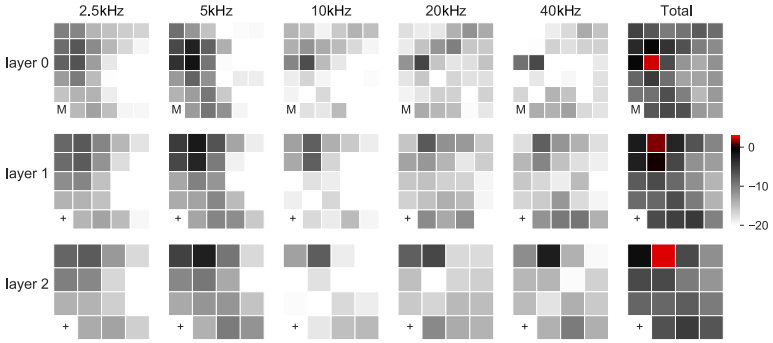

(c) Panel *0013_1*

Figure 3.13: *TNCE* values for stone vs brick walls - experiment. a) Panel with only the macrostructure, b) Stone wall typology panel with the same macrostructure as panel *0015_1*, c) Brick wall typology panel with the same macrostructure as panel *0015_1*

Stone vs brick walls

This experiment aims to determine whether stone walls or brick walls are better at diffusing sound. We generated and measured 46 stone and 92 brick walls. Our analysis shows that brick walls diffuse sound more

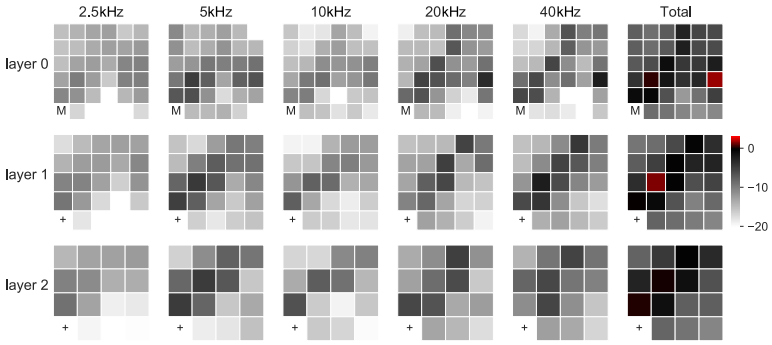

(a) Panel_0015_0

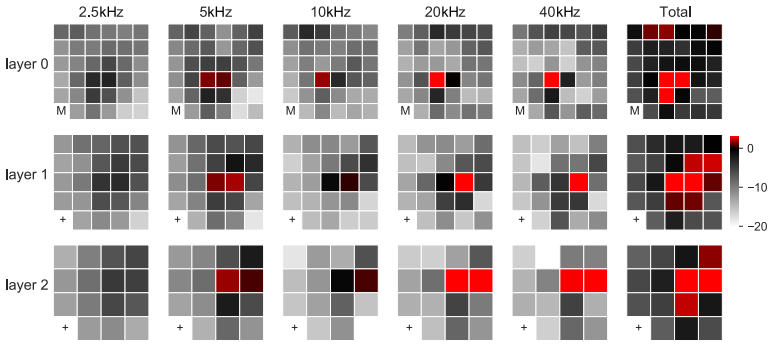

(b) Panel_0031_0

Figure 3.14: *TNCE* values for macrostructure comparative experiment with varying macrostructures. "M" indicates the microphone's position, and "+" is a point with no data.

consistently. Polygonal rubble stone walls generally diffuse less energy in the lower frequencies, but the results were inconclusive for the mid and high frequencies. To illustrate the findings, we present two extreme cases (see Figure 3.15).

Panel *0005_1* is from the polygonal rubble stone wall typology. It features, on average, nine stones per square meter, a joint width between 20-30mm, a joint depth between 50-80mm, and a stone surface roughness of ±30mm (numbers in 1:1). Panel *0013_1* is from the brick typology and resembles a standard stretcher-bond brick wall. It features standard bricks measuring 215 × 65 × 102.5mm (W x H x D) and a raked joint around 15mm wide (±1mm) and 10mm deep (±1mm) (numbers in 1:1). Both panels *0005_1* and *0013_1* share the same macrostructure with panel *0015_1*. Compared to panel *0015_1* (Figure 3.13a), panel *0005_1* (Figure 3.13b) exhibits higher *TNCE* values across all filter bands (see Table 3.4), with the exception of 40kHz, but only by 0.4dB. On the contrary, panel *0013_1* (Figure 3.13c) exhibits less cumulative energy across all filter bands. The difference is smaller in the two

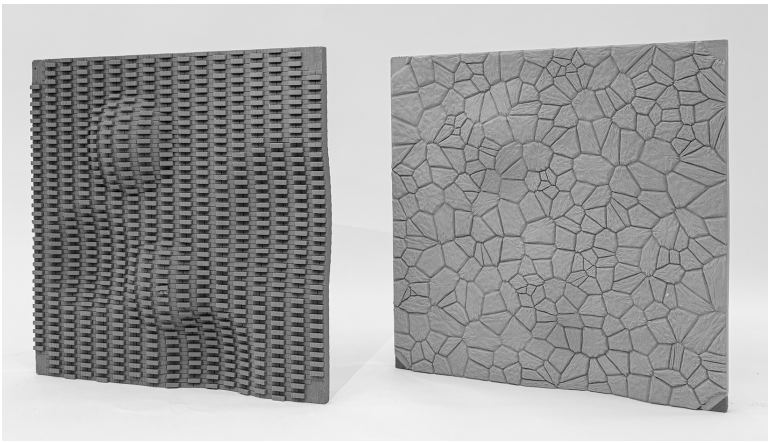

Figure 3.15: 3D printed and coated panels. Left: Surface *0013_1* from the brick typology. Right: Surface *0005_1* from the polygonal rubble stone wall typology.

lower filter bands (-0.49, -1.6dB), in which the effect of the macrostructure is more dominant, but more present in the upper three bands (-3.6, -4.03, -5.03dB). In comparison to panel *0015_1*, the *TNCE* of panel *0005_1* is higher by 2.03dB, and of panel *0013_1* lower by -1.88dB.

Table 3.4: Stone vs brick walls. Mean TNCE of the 90th percentile per filter band. All values are relative to the reference *Flat*.

Panel ID	Frequency band					
	2.5 kHz	5 kHz	10 kHz	20 kHz	40 kHz	Total
0015_1	-7.66	-3.66	-9.18	-7.02	-5.54	-0.4
0005_1	-7.44	-3.09	-6.96	-5.96	-5.94	1.63
0013_1	-8.15	-5.26	-12.78	-11.05	-10.57	-2.28

3.5 Conclusions and future work

In this paper, we presented a novel approach to studying the mutual relationship between diffusive surface structures and their acoustic performance through data science methods. We described the post-processing of the measured data and the evaluated indicators and showed that they can be used for the quantitative assessment of different surface structures, thus providing a valid evaluation system.

By the end of this research project, we target to measure 350 acoustic surfaces; this amounts to approximately 1 million IRs in total. To create high diversity, the data set is continuously shaped through analysis and subsequent surface generation. This approach should enable the future ML model to generalise as well as possible. Analytical tools, for example, PCA [37] and PCC [90], will be evaluated to identify the most important geometrical

characteristics that influence certain acoustic responses. SOM [38] are also tested for clustering the surfaces based on geometrical (fabrication typology) and acoustical characteristics (i.e. absorption, scattering). This will help to identify unexplored areas in the design and data space and test new hypotheses that emerge during analysis.

Currently, we can only speculate on the output and accuracy of the ML system. However, it is foreseeable that the limited number of data set samples will be critical. This limitation can be mitigated by leveraging the large number of IRs present in each sample and by the data augmentation naturally emerging from the setup symmetries. From our preliminary testing on 100 acoustic surfaces, we believe that an exact prediction of the IR is likely impossible. Hence, we will focus our efforts on predicting the compressed information obtained from the post-processing step presented in this paper. Our preliminary ML architecture is able to predict the energy reflected (more precisely, the TNCE) in every measured position for geometries that present similarities with the training set.

Our future ML model shall be used as a fast acoustic evaluation tool for diffusive surfaces, which facilitates acoustic-driven form-finding in early design phases. Together with the developed design guidelines for certain fabrication typologies, this will enable more acoustic-aware designs, thus bringing acoustics closer to the architectural practice.

3.6 Credits and acknowledgements

3.6.1 Collaboration

This project was part of the collaborative and multidisciplinary research project Data Science Enabled Acoustic Design for Digital Fabrication in Architecture between the Chair of Architecture and Digital Fabrication at ETH Zurich, the SDSC, the Laboratory for Acoustics / Noise Control of Empa, and Strauss Elektroakustik. All the authors of this paper contributed to the conceptualisation and methodological approach of the presented work.

The data-acquisition setup was developed together with Dr Romana Rust, Gonzalo Casas, and Dr Kurt Heutschi. Dr Romana Rust developed the robotic tool paths and their end-effectors. Gonzalo Casas developed the ROS-based communication between the computer and the two robotic arms, developed and implemented the computational methods for recording, validating, and storing the audio measurements, and collecting and storing the environmental conditions during the data-acquisition process. Lastly, he implemented the web application for monitoring the data-acquisition process.

Dr Kurt Heutschi developed the sweep signal generation and the method for converting the raw recording into an impulse response. Furthermore, he advised and validated all sound-related research methods. Dr Nathanaël Perraudin developed the methods for the multi-band audio filtering and the direct sound removal at the SDSC. Chaoyu Du developed the layered grid plot during her internship with the Gramazio Kohler Research group under the supervision of the author of this thesis.

3.6.2 Author's contribution

The author of this thesis conceptualised and developed the generation of diffuse surfaces. This included defining the relevant surface typologies and the necessary geometrical features of each typology that had to be implemented in the geometry generation pipeline. The author developed the computational method for fabricating the diffusive surfaces and their post-processing treatment. Additionally, the author developed and validated the computational method based on the Fresnel zones used to define the measuring grid using empirical testing. Furthermore, the author implemented the entire data acquisition setup. The implementation included performing and applying the acoustic treatment of the room and implementing and validating all the used hardware such as computer, audio interface, sound amplifier, microphone, speaker, environmental sensors, robotic arms, robotic controller, safety sensors, and more. Lastly, the author of this thesis collected and analysed the data presented in this paper.

3.7 Authors contributions to the paper

6: Contributor Roles Taxonomy

The individual roles and contributions of each author in this paper are described using the standardised taxonomy CRediT[6][71].

Romana Rust
Conceptualisation, Methodology, Software, Validation, Investigation, Writing – Original Draft, Writing – Review & Editing, Visualisation, Supervision, Project administration, Funding acquisition

Achilleas Xydis
Conceptualisation, Methodology, Software, Data Curation, Validation, Investigation, Writing – Original Draft, Writing – Review & Editing, Visualisation

Kurt Heutschi
Conceptualisation, Methodology, Validation, Writing – Original Draft, Writing – Review & Editing

Nathanaël Perraudin
Methodology, Software, Data Curation, Validation, Formal analysis, Writing – Original Draft, Writing – Review & Editing, Visualisation

Gonzalo Casas
Software, Validation, Investigation, Data Curation, Writing – Original Draft

Chaoyu Du
Software, Investigation

Jürgen Strauss
Conceptualisation

Kurt Eggenschwiler
Conceptualisation

Fernando Perez-Cruz
Conceptualisation, Methodology, Writing – Review & Editing, Supervision

Fabio Gramazio
Conceptualisation, Methodology, Writing – Review & Editing, Supervision

Matthias Kohler
Conceptualisation, Methodology, Writing – Review & Editing, Supervision

3.7.1 Acknowledgements

This research is jointly supported by the Swiss Data Science Center and the Chair of Architecture and Digital Fabrication, ETH Zurich. The authors would like to thank Michael Lyrenmann and Philippe Fleischmann from the NCCR Digital Fabrication, ETH Zurich, for their help with building the multi-robotic measurement setup, Dr Mariana A. Popescu for her assistance in producing the 3D knitted sleeves for the robots, and Anton Johansson for his help in the measurement process. Furthermore, Dr Mathias Bernhard, Patrick Bedarf, and Pietro Odaglia from the Chair of Digital Building Technologies, ETH Zurich, for their support with the in-house 3D printer and Alessandro Tellini from Raplab, ETH Zurich, for his help and support using the digital workshop, and finally, a sincere thank you to Dr Lauren Vasey for her diligent proofreading of this manuscript.

4 Paper C - Visualisation methods for big and high-dimensional acoustic data

Achilleas Xydis[*], *Chaoyu Du*[*], *Romana Rust*[*], *Fabio Gramazio*[*], *Matthias Kohler*[*]

[*] Gramazio Kohler Research, ETH Zurich, Zurich, Switzerland

Acoustics are rarely included in architectural design because available acoustic analysis tools are cumbersome and require expert knowledge of acoustics. This exclusion from the design phase could lead to late-stage design modifications, potential delays, and increased building costs. On the contrary, their inclusion can improve the acoustic properties of spaces and ensure seamless design integration. This can be achieved by providing architects with easy-to-use visualisation tools to study the relationship between geometry and sound

without expert knowledge in acoustics. Available acoustic datasets can enable the development of such visualisations, but recent technological advances have increased their complexity and size. Although existing data-science methods can process and analyse them, it remains challenging to develop easy-to-use and informative visualisations for architects and non-acoustic experts.

This research proposes a novel approach for interactive visualisations of acoustic datasets for architects and non-acoustic experts. It introduces a series of simple acoustic properties for users with basic knowledge of acoustics and describes methods for low- and high-dimensional data visualisations. It describes the computational workflow and uses a design scenario to demonstrate the proposed visualisations. Finally, it discusses the challenges of developing such methods, their advantages, limitations, and future work.

This version of the article has been accepted for publication after peer review in *ACADIA 2022: Hybrids & Haecceities - Proceedings of the 42nd Annual Conference of the Association for Computer Aided Design in Architecture (ACADIA)*, 2022.

4.2 Introduction

Sound visualisations are an integral part of the study of room acoustics. Since the introduction of Ultrasonic-Schlieren photography by Wallace C. Sabine in 1912 [10], acousticians have developed multiple methods to visualise the invisible to the naked eye propagation of sound and its interaction with surfaces. Advancements in measurement techniques and computer simulations make it easier today to measure and simulate sound propagation. However, our display mediums are still two-dimensional, and visualisation tools face the challenge of projecting high-dimensional data on flat screens or paper. This challenge becomes apparent when we try to display even the most essential acoustical features (frequencies, amplitude, phase, direction) simultaneously, making the visualisation unreadable or overwhelming. Looking at recent developments in acoustic measurement technology and advances in computing power and storage capabilities, acoustic data collection has the tendency to increase in complexity and size rather than simplify. Large and often heterogeneous data sets make it challenging to develop informative visualisations [91] because such datasets have surpassed human cognitive capabilities when explored through simple data analysis tools [92]. Therefore, the challenge of visualising large acoustic datasets to make them accessible and readable to humans becomes more and more pressing.

Data visualisation can facilitate meaningful analysis, accessibility, and interpretation of large datasets because it relies on the human's cognitive capabilities to process visual information [93]. Furthermore, it can support unanticipated discoveries by visually exploring and analysing the data [94]. These discoveries could be a valuable resource in steering the creative process within architectural design. One reason for the necessity of data visualisation in architecture is the potential to include acoustics in the early design stages. Although architects already include performance as an early-on design driver for building components such as the building structure or façades, room acoustics are rarely included in the early design process [8, 95]. The reason for this is twofold. On the one hand, there is a lack of acoustic visualisations for architects and users with basic knowledge of acoustics. On the other hand, available visualisations are decoupled from the geometry that influences the sound. Nevertheless, geometry is essential for architects to understand the relationship between sound and geometry. This understanding would enable them to develop design workflows where they can manipulate the design and intuitively understand how this manipulation affects the room's acoustics.

Therefore, this research focuses on developing acoustic visualisations for big acoustic datasets for architects and non-acoustic experts that can be

integrated into the early design processes to enable acoustically informed design explorations.

4.3 Background

As big data becomes more prevalent in acoustic research, data visualisations have become increasingly important to interpret it. Lowe and Matthee describe that dimensionality reduction, interactivity, readability, and user assistance are key requirements of data visualisation tools to interpret big data [94]. Building upon the key requirements introduced by them, we focus on four points to develop novel acoustic visualisation for architectural applications: low- and high-dimensional visualisations, interactive visualisations, and usability of acoustic visualisations in architectural applications.

4.3.1 Low-dimensional visualisations

From a data science perspective, an Impulse Response (IR) is a time series of float numbers that describe the sound's energy and phase over time. All acoustic parameters (called descriptors) that derive from it can be grouped into a) single-value descriptors and b) series-of-numbers descriptors. Single value descriptors include Reverberation Time (RT), Clarity (C50), Strength (G), Definition (D), Centre Time (TS), and more. Series-of-numbers descriptors include frequency response and energy over time. Although acoustic analysis software such as Odeon and CATT-acoustics [96, 97] provides methods to calculate these acoustic descriptors, it requires expert knowledge in acoustics to decode their meaning.

4.3.2 High-dimensional visualisations

High-dimensional data pose another challenge for accurate and readable visualisation methods. Humans can only visually perceive three dimensions. Traditional data science visualisation techniques, such as scatter plots and heat maps, can represent small or intermediate datasets in two or three dimensions. Although these visualisations are intuitive and may be used to identify bivariate correlations between variables, they require dimensionality reduction to arrange the data points in a lower-dimensional space. Dimensionality reduction methods such as Principal Component Analysis [98] and t-distributed stochastic neighbour embedding [99] can compress attributes and reduce complexity. Although this compression is necessary to lower the dimensions down to two or three dimensions, it could lead to projection losses [94]. Projection loss describes a scenario where well-spread

points in high-dimensional space appear falsely close in the low-dimensional projection [94]. Other limitations of dimensionality reduction methods are that they treat the values as pure numbers, completely decoupled by the geometry that influenced them. This makes it especially difficult to include these methods in architectural applications as geometry is one of the key design components.

4.3.3 Interactive visualisations

Interactive visualisations combine human and machine intelligence [100] to explore and uncover unexpected patterns in datasets [101]. This visual analysis benefits *"visual perception, interactive exploration, improved understanding, informed steering and intuitive interpretation"* [102]. Furthermore, this type of analysis can have two approaches; a bottom-up approach that can potentially uncover patterns in the data [103] and a top-down approach to test theories and search for evidence in the data [91, 104].

4.3.4 Usability of acoustic visualisations in architectural applications

During the design phase, architects explore various alternative design ideas. Early-stage design decisions have a significant impact on the final design's quality and performance [8]. In contrast, late-stage design modifications can rarely compensate for poor early-stage choices. Therefore, it is essential to consider all factors early on to avoid potentially delaying the project, increasing the building cost, or impairing the overall design. To employ acoustic performance as a design driver, we must be able to quantify and interpret the acoustic effects of our geometric design choices. Currently, most of the visual analytics are performed by acousticians equipped with the necessary knowledge and specialised acoustic analysis software. The reason for this is that this type of software is cumbersome to use and requires expert knowledge in acoustics. As a result, architects are discouraged from using them to evaluate their designs, especially early on.

Commercially available acoustic analysis and visualisation software are black boxes, providing insufficient feedback to the user and often no description of how the results were calculated [105]. Furthermore, most commercial software do not provide APIs[1] or ways for external software to interface with them. This limitation, for example, hinders form-finding studies using computational design because each design must be exported from the design software and imported into the acoustic analysis software for analysis. Therefore, acoustic visualisation tools should be flexible for customisation

1: API stands for application programming interface, which is a set of definitions and protocols for building and integrating application software.

and easily expandable to accommodate study-specific requirements. The increased popularity of web-based Python programming allows the development of visualisation tools that are easily accessible and easy to use. Furthermore, their open-source nature allows users to customise them and extend their capabilities according to their needs.

This research proposes a novel approach for interactive visualisations of acoustic datasets for architects and non-acoustic experts. It introduces a series of simpler descriptors for users with basic knowledge of acoustics and describes methods for low- and high-dimensional data visualisations. It introduces visualisation methods that incorporate the geometry that influenced the sound under study. The inclusion of influential geometry provides a more detailed insight into the relationship between geometrical characteristics and the sound properties they influence. Moreover, this research proposes methods for interactive visualisations that allow users to explore the data from different angles and zoom closer to reveal more details. Interactivity also allows animated content to display how sound properties change over time. Furthermore, it describes methods that allow the simultaneous display of multiple data points, enabling the user to compare data within the same visualisation. Lastly, all visualisations are customisable and extendable, and the entire code is open-sourced and available at `https://github.com/gramaziokohler/sdsc_data_driven_acoustic_design`.

4.4 Methods

Based on the topics described in the background, this section describes the computational workflow of the proposed visualisation pipeline and demonstrates its use through a design scenario. For the design scenario, we used the open-source Geometry and Impulse Response Dataset (GIR Dataset) [51]. The dataset contains 920712 physically measured IRs from 312 surfaces (2951 per surface). More details about how the dataset was collected can be found in [40].

4.4.1 Computational workflow

The visualisation pipeline is written in Python and contains two main classes, the `DataConverter` and the `DataPlotter`. The `DataConverter` handles the data retrieval from the dataset and can convert the IR data to the desired acoustic descriptors, and the `DataPlotter` handles all the visualisation computing. Open-source libraries are used to extend the core code. The `Numpy` library handles the mathematical operation, and the `Scipy` library manages the audio-related computation, such as Fast Fourier Transform

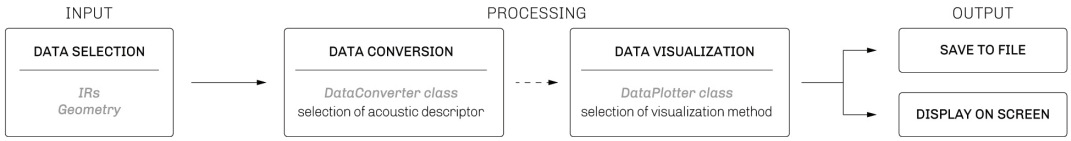

Figure 4.1: Computational pipeline.

(FFT) analysis and resampling. The visualisation part of the code uses `Seaborn` for computing heat maps, `Matplotlib` for constructing all the static visualisations, and `pythreejs` for interactive visualisations. `Ipywidgets` is used to generate graphic widgets such as number sliders, buttons, and text inputs. The computational pipeline comprises of three main steps (see Figure 4.1). First, the input step, where the data selection takes place; second, the processing step with data conversion and data visualisation; and finally, the output step, where the visualisation is displayed or saved to a file.

4.4.2 Visualisation types

There are two types of visualisations possible with the computational workflow, explanatory visualisations and comparative visualisations.

Explanatory visualisations. The acoustic data visualisation process begins with the selection of an input. For low-dimensional data, the input refers to an IR measurement; in high-dimensional visualisations, the input refers to several IRs. Afterwards, the user selects the desired acoustic descriptor, and the `DataConverter` class returns the converted data. This data then can be passed to the `DataPlotter` for visualisation. Table 4.1 shows all the available acoustic descriptors that `DataConverter` class can compute. Besides the standard output, each of these descriptors can also be normalised (from $0.0 - 1.0$ or $0\% - 100\%$ depending on the descriptor) or scaled using a scale factor. Table 4.2 shows all the available visualisations the `DataPlotter` class can generate. All visualisations have the option to display the output for the entire audio spectrum or per user-defined frequency bands (see Figures 4.4 and 4.5). This option, for example, allows the user to analyse the relationship between a geometrical design and groups of frequencies. This enables them to adjust their design to target specific frequencies. Finally, the output of the visualisation can be either saved directly to a file, displayed on the screen, or both.

All visualisations follow the same principle. A sound is emitted at the source position, then the sound wave hits the room's surfaces and finally arrives at the receiver position. The visualisations show how these surfaces influenced

Descriptor	Value type
Reverberation time	float
Clarity	float
Definition	float
Energy over time	list of floats
Cumulative energy over time	list of floats
Total cumulative energy	float
Frequency response	list of floats
Absorption coefficient	list of floats
Scattering coefficient	list of floats

Table 4.1: Available acoustic descriptors inside `DataConverter` class.

Visualisation method	Interactive	Comparative
2D IR	no	yes
Energy over time	no	yes
Cumulative energy over time	no	yes
Frequency response	no	yes
Absorption coefficient	no	yes
Scattering coefficient	no	yes
2D grid	yes	yes
3D grid	yes	yes
3D polar	yes	yes

Table 4.2: Available visualisations inside `DataPlotter` class.

the sound wave when the wave came in contact with them. Except for IR, Absorption coefficient, Scattering coefficient, and Frequency response, all visualisations can display absolute and relative values. For relative values, the values of a flat and smooth surface are taken as a baseline, and all values of the chosen surface relate to them. This way, the visualisations enable the evaluation of acoustic properties without professional assistance.

Comparative visualisations. Several low- and high-dimensional descriptors can be used in comparative visualisations. The process is similar to the one described in the computational workflow section, except that for low-dimensional data (see Figure 4.2 top), users select two or more IRs and for high-dimensional data, two sets of multiple IRs. Then, they select the desired acoustic descriptor and generate the comparative visualisation.

4.4.3 Interactivity

All high-dimensional data visualisations, explanatory and comparative, are displayed in a three-dimensional interactive window and include the surface geometry (see Figure 4.3). They allow the user to pan, zoom, and rotate around the displayed data, breaking the barrier of a static data representation and enabling users to intuitively study the relationship between geometry and sound. Furthermore, these visualisations support animated content.

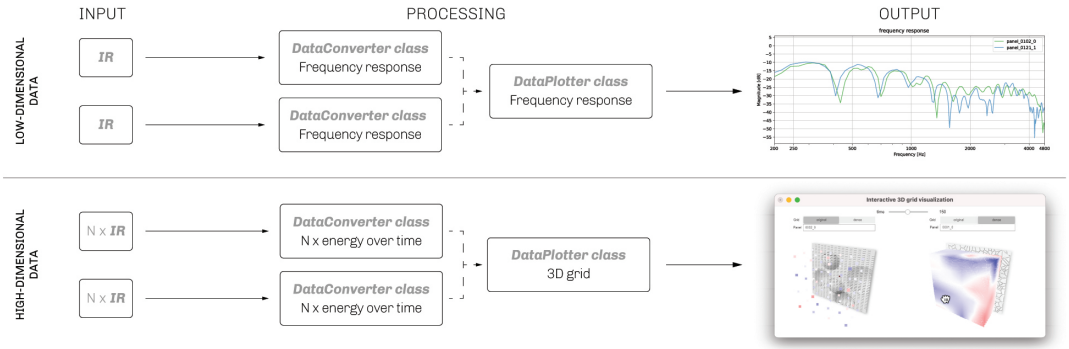

Figure 4.2: Computational workflow for comparative visualisations. To illustrate both output options, the low-dimensional visualisation outputs a file, and the high-dimensional visualisation opens a window where users can interact with the data.

If a specific acoustic descriptor is selected, it can display the descriptor's value over time, adding an extra dimension to the visualisation. When the comparative mode is active, the user can apply the same transformation to both visualisations and see the animated data simultaneously for both surfaces.

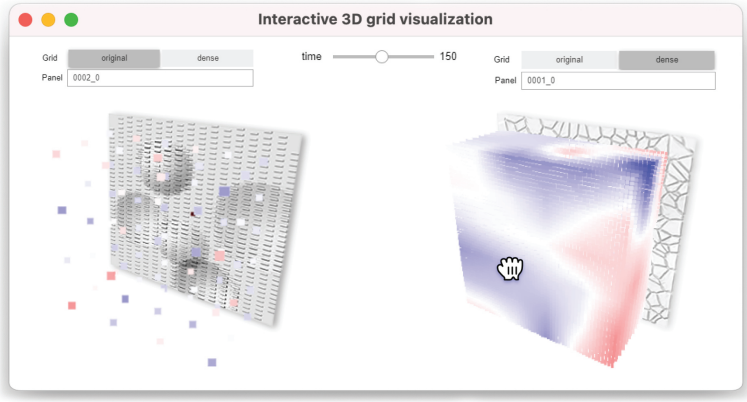

Figure 4.3: Interactive comparative visualisation of the energy over time. The left surface has the original density of the measuring grid, and the right surface has the denser interpolated grid. The time slider can be changed to show the energy for a specific time.

4.5 Design scenario

To show the entire workflow of the presented research, we are converting an existing room into an open-plan office space as an example. This section goes through several architectural design phases and demonstrates how the proposed visualisations enable a more acoustically informed design outcome. The design scenario has the architect as a user, and it consists of two main steps a) analysis and evaluation of the existing acoustic conditions and b) exploration of acoustic design interventions.

4.5.1 Analysis and evaluation

The process starts by analysing the existing acoustic conditions of the room to understand the design actions necessary to improve the acoustic properties of the room for our open-plan office. After acquiring the impulse response measurements of the existing room, the user is ready to start the analysis. The computational workflow supports single IR measurements or multiple IR measurements recorded at several positions inside a room. Multiple IR measurements can be arranged in orthogonal two-dimensional or three-dimensional grids. Below we describe the three different arrangement options.

Single IR measurements. Figure 4.4 shows explanatory two-dimensional visualisations of the Cumulative energy over time of single IRs. In this case, the user defines five filter bands, with a centre frequency of 250Hz, 500Hz, 1kHz, 2kHz, and 4kHz. The 250Hz band is a Low-pass Filter (LPF), and the 4kHz is a High-pass Filter (HPF). The values are normalised from 0.0 to 1.0, with 0.0 representing no energy at the receiver position and 1.0 that all the energy emitted by the source arrived at the receiver position. The Cumulative energy inside the room (see Figure 4.4 left) goes up quickly

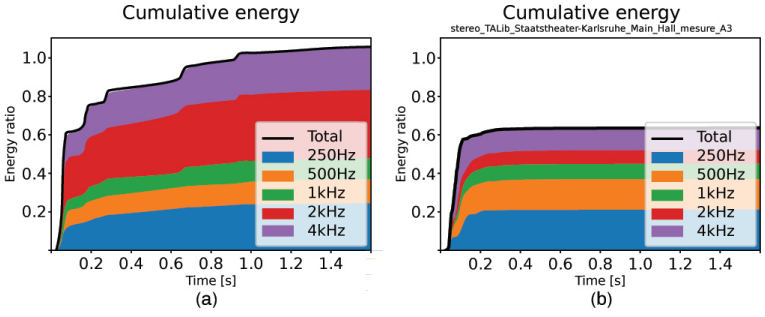

Figure 4.4: Cumulative energy over time visualisation. Left: The current acoustic conditions of the scenario's room. The room is highly reverberant and has an unbalanced frequency response. The 2kHz and 4kHz bands contain more energy than the other bands. Right: The Staatstheater in Karlsruhe is a reference of an acoustically treated space. The black line represents the cumulative energy of the entire audio spectrum in the IR and the coloured sections for each filter band.

when the direct sound arrives, but because the room is very reverberant due to its big volume and the lack of absorptive surfaces, the energy continues to rise for another 1.5 seconds. The small "steps" in the plot indicate when strong reflections arrive at the receiver position. These reflections can cause colouration, image shift, and flutter echoes, all negative characteristics for meeting rooms, lecture halls, and offices where speech clarity is important. Comparing it to the Cumulative energy of the Staatstheater in Karlsruhe[2], we see that the energy rises quickly and then remains stable. This shows that there are no more reflections arriving at the receiver position. Furthermore, the total energy is lower because a portion of it (around 40%) was absorbed by the room's surfaces. Rooms with Cumulative energies like Figure 4.4 right will have a clearer sound and be more relaxing working environments.

2: The IR is taken from the "Théâtre Acoustique Room Impulse Response Library" `https://www.lieuxperdus.com/convolver/download/`.

Multiple IR measurements: 2D measurement grids. Multiple IR measurements of the same room enable a higher-resolution analysis of the existing acoustic conditions. The visualisation in Figure 4.5 can be used when the measurement positions are arranged in a two-dimensional grid. For this visualisation, we chose the total energy as a descriptor, and each square represents one total energy value. This value defines the total amount of sound energy that arrived at that location for the duration of the measurement. Looking at the entire spectrum grid, we can clearly see the high sound energy concentrated at the corner of the room.

Multiple IR measurements: 3D measurement grids. The visualisation in Figure 4.6 can display values that were measured using a three-dimensional grid. The values are colour-coded and displayed inside the room's geometry. Users can pan and rotate the geometry to look at the values from a different angle or zoom in to take a closer look when the data is too dense. The grid's density can be increased to make patterns more visible or decreased to reduce the visual complexity. Because this visualisation also supports animated content, the energy values over time can be displayed by moving a time slider.

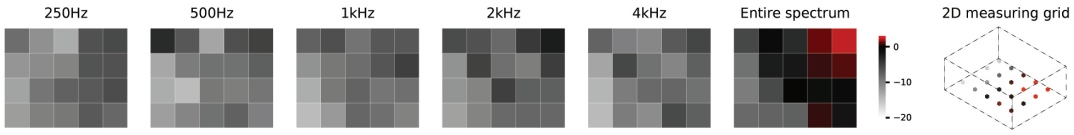

Figure 4.5: 2D grid. Total energy per filter band and for the entire audio spectrum. Black represents energy values similar to the transmitted energy, and white 20dB less energy (equivalent to 100 times less energy). Red squares are positions where the received energy is higher, indicating a local focusing effect.

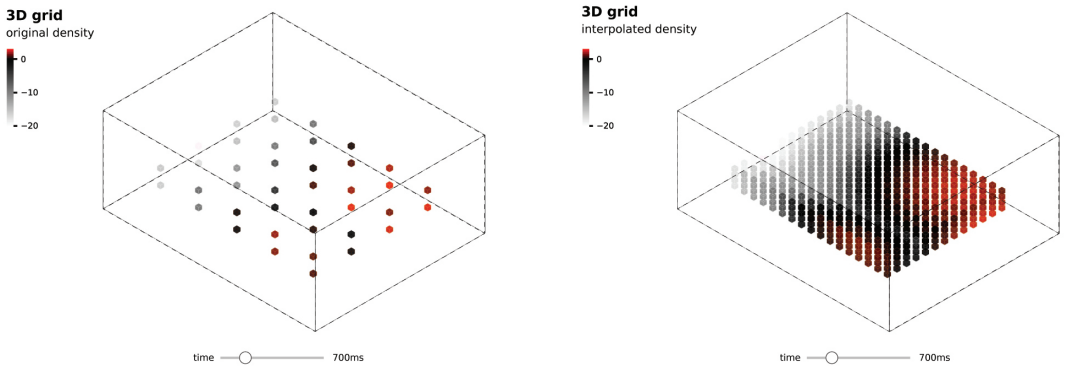

Figure 4.6: Interactive 3D grid visualisation. Left: The original density grid with 40 measuring positions. Right: higher-density linear interpolated grid with 884 positions. In the interpolated grid, the energy pattern is more visible.

The analysis and evaluation show us clearly that the existing acoustic conditions are not suitable for a comfortable working environment. More precisely, some of the energy needs to be removed by means of absorptive materials. The ceiling and the floor are ideal locations for installing such materials. To balance the sound energy inside the room, limit disturbing flutter echoes, and prevent the room from becoming very unnatural from excess absorption, the walls can be designed in such a way that they will diffuse sound. Bellow, we introduce different design explorations that the user can use to address the acoustic problems.

4.5.2 Design explorations

This part of the scenario focuses on design interventions that can improve the acoustic conditions of the room. This part consists of two main steps, a) general acoustic treatment through proper surface material selection and b) design and adjustment of the wall's geometry to maximise the acoustic performance.

General acoustic treatment. The sound we hear is a combination of the direct sound coming straight from the source and indirect reflections from the surrounding surfaces. Sound hitting a surface is either transmitted, absorbed, or reflected; the ratio depends on the surface's acoustic properties. Based on the analysis of Figure 4.4, the user needs to lower the sound energy inside the room, emphasising the mid and high frequencies. This issue can be addressed by choosing appropriate materials that absorb the sound energy of mid- and high frequencies. Figure 4.7 shows three comparative two-dimensional visualisations of absorption coefficients for

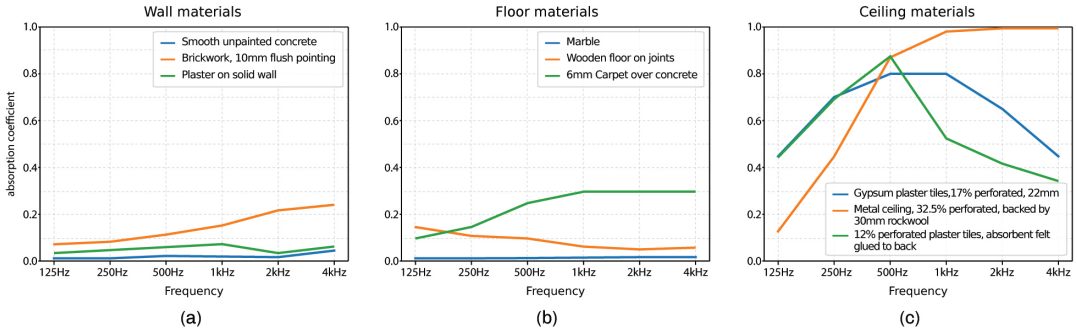

Figure 4.7: Comparative visualisations of absorption coefficients of different materials for the wall surfaces, the floor, and the ceiling of the room. Values close to 0.0 represent no sound absorption; therefore, all energy is reflected, and values close to 1.0 complete absorption.

common architectural materials that can be used on the walls, floor, and ceiling of the room. The algorithm either receives the coefficients as a list of floats or computes them from IRs measured according to the ISO 354:2003 standard [106]. In this case, the coefficient values for these visualisations are taken from a dataset that was created using data from `www.akistik.ua`. Analysing the three visualisation reveals that Brickwork would be preferable for the walls of the room (Figure 4.7 left, in orange), a thin carpet for the floor (Figure 4.7 middle, in green), and 32.5% perforated thin metal sheets, backed by 30mm rock wool for the ceiling (Figure 4.7 right, in orange).

Design and adjustment of architectural geometries After deciding on brickwork as a wall material, the exact design of its geometry must be defined. Brickwork has a structured surface texture. Parts of the texture diffuse sound, and other parts reflect sound in a specular way (Figure 4.8). The brickwork geometry can be optimised to redirect the reflected energy towards the ceiling (Figure 4.9). This way, more sound is reflected towards the ceiling, where it gets absorbed.

Recent research introduced a computational workflow to generate various acoustically informed diffusive surfaces, including brickworks [42]. The research uses Self-Organising Map (SOM) to arrange sound-diffusive architectural surfaces based on chosen acoustic properties. Using its design workflow, the SOM cell with the best matching unit contains two surfaces, a flat and textured brickwork. To decide which of the two surfaces addresses better our acoustic requirements, the user can evaluate the direction of the reflected energy. Figures 4.10, 4.11, and 4.12 show interactive visualisations that display the direction and intensity of the reflected sound energy. The direction is represented as a ray leaving the surface, and the intensity by the length and colour of the line. Users can pan, zoom, or rotate to explore the

sound directivity from different angles. Furthermore, the descriptors can be displayed for the entire audio spectrum or per user-defined frequency bands (see Figure 4.12). By comparing the two visualisations in Figure 4.10 and Figure 4.11 we can clearly see that the surface on the right redirects more energy upwards, making it an ideal option for the design scenario.

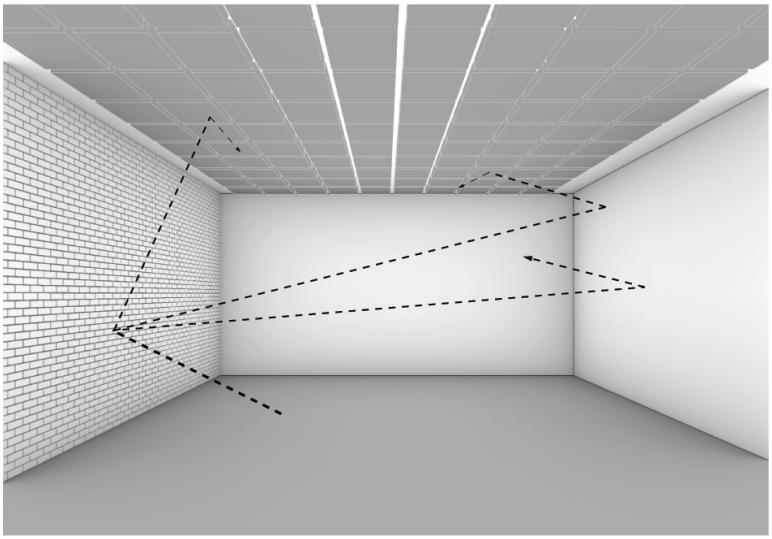

Figure 4.8: The room from the design scenario with the flat brickwork. The black dashed lines illustrate the direction and intensity of the reflected sound according to the data from Figure 4.10. Most of the sound energy bounces back into the working area.

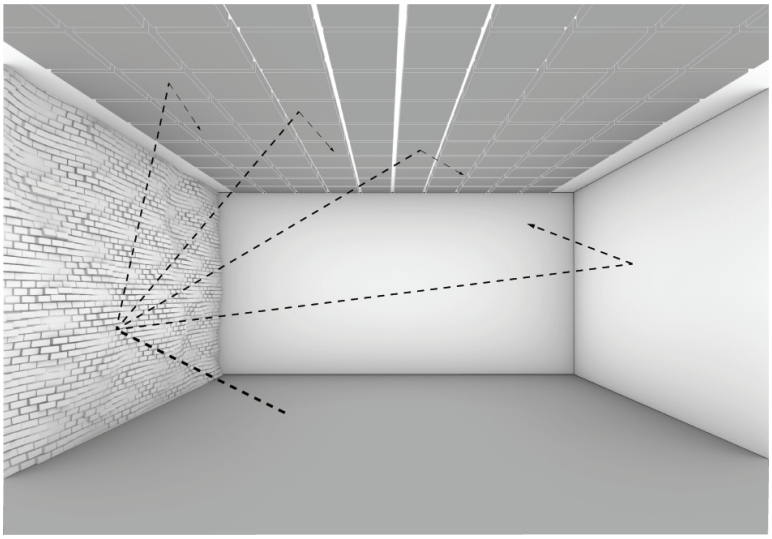

Figure 4.9: The room from the design scenario with the optimised brickwork. The black dashed lines illustrate the direction and intensity of the reflected sound according to the data from Figure 4.11. Here a significant portion of the sound energy gets reflected towards the absorbent ceiling.

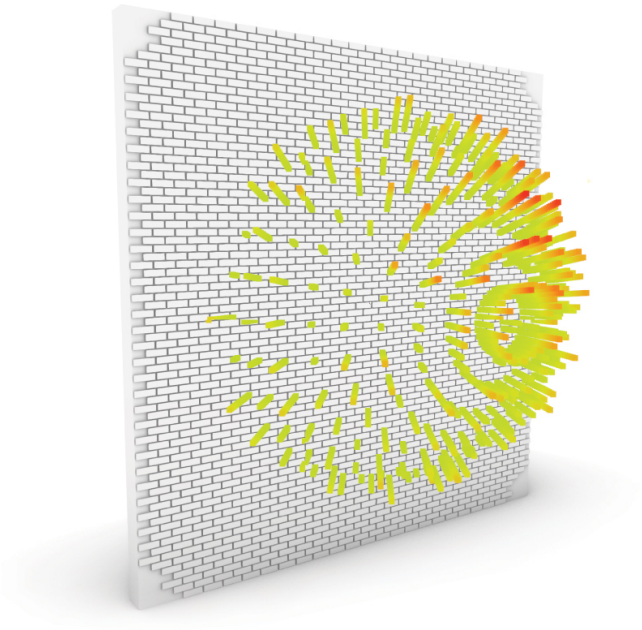

Figure 4.10: 3D polar sound directivity visualisation of the total energy of the entire audio spectrum for the flat brickwork.

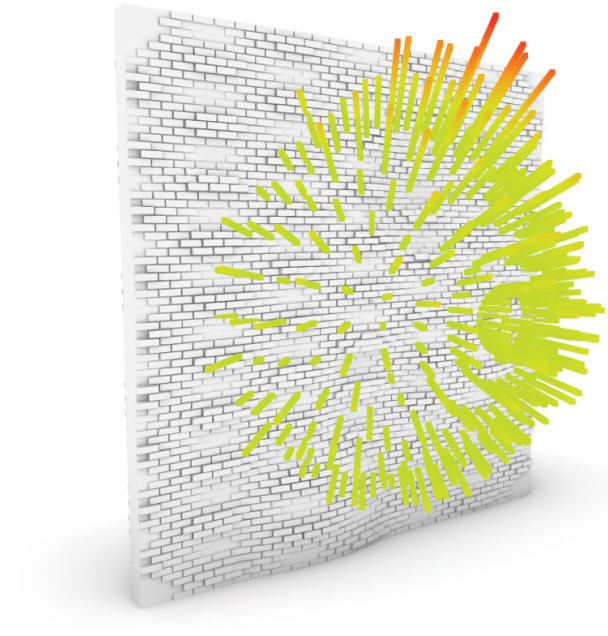

Figure 4.11: 3D polar sound directivity visualisation of the total energy of the entire audio spectrum for the textured brickwork.

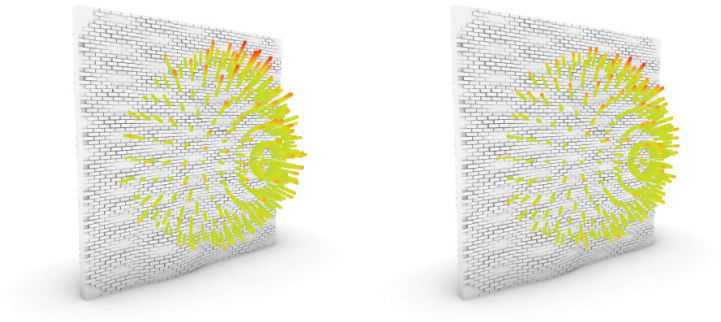

Figure 4.12: 3D polar sound directivity visualisation of the total energy of two frequency bands for the textured brickwork, left: 4kHz, right: 1kHz.

4.6 Results and Discussion

We have presented a novel approach to visualising low and high-dimensional acoustic data. We described the computational workflow to produce these visualisations, its components, and how each of them contributes to the entire workflow. We demonstrated a series of visualisations and described how they could be used for acoustic studies. These visualisations show that thanks to their intuitive visual implementation, they can be used both by expert and non-expert users in acoustics. The proposed workflow addresses both experts and non-experts in acoustics users. Expert users can use standard and familiar acoustic descriptors and visualisations, while non-expert users are presented with a range of newly proposed and simplified descriptors and visualisations. Furthermore, both users benefit from the intuitive layout of the visualisations, especially from the interactivity of the high-dimensional visualisations. Finally, including the geometry that influenced the sound in the visualisations allows for a deeper analysis of the mutual relationship between geometry and sound. We believe that these visualisations will help bring acoustics closer to the early phases of architectural design and enable a more integrative acoustic and architectural design exploration.

4.6.1 Limitations and future work

Despite the intuitive workflow, users still required basic knowledge of Python to run the scripts. That is also true for extending and further customising the visualisations. However, this visualisation pipeline could be turned into a plugin for CAD software, eliminating the need for programming knowledge. In future steps, we are committed to continuing extending the visualisation pipeline by adding more acoustic descriptors and visualisation methods to it. Finally, we are confident that the proposed visualisation methods will

encourage researchers to create more open-source high-dimensional acoustic datasets.

4.7 Credits and acknowledgements

4.7.1 Collaboration

Part of this research was executed within the collaborative and multidisciplinary project Data Science Enabled Acoustic Design for Digital Fabrication in Architecture. Several of the presented visualisations were developed during the collaborative project to communicate data and findings within the research group. The initial version of the IR and CE visualisations was developed by Dr Nathanaël Perraudin. Chaoyu Du developed the initial versions of the 2D-grid and 3D-grid visualisations as part of her MAS[3] internship program, supervised by the author of this paper. Lastly, Dr Kurt Heutschi provided valuable input by validating the correctness of the computational methods that generate these visualisations.

3: Master of Advance Studies in Architecture and Digital Fabrication at ETH Zurich

4.7.2 Author's contribution

The author of this thesis conceptualised, investigated, and developed the presented approach for visualising low and high-dimensional acoustical data. The investigative part of this research included developing and testing several iterations of the presented visualisations. The author further developed and optimised the visualisations that Dr Nathanaël Perraudin and Chaoyu Du had initially developed.

4.8 Authors contributions to the paper

4: Contributor Roles Taxonomy

The individual roles and contributions of each author in this paper are described using the standardised taxonomy CRediT[4][71].

Achilleas Xydis
Conceptualisation, Methodology, Software, Validation, Investigation, Writing – Original Draft, Writing – Review & Editing, Visualisation

Chaoyu Du
Software, Validation, Investigation, Visualisation

Romana Rust
Writing – Review & Editing, Supervision

Fabio Gramazio
Writing – Review & Editing, Supervision

Matthias Kohler
Writing – Review & Editing, Supervision

4.8.1 Acknowledgements

This research steamed out of a collaborative and multidisciplinary project between Gramazio Kohler Research at ETH Zurich, the Swiss Data Science Center, the Laboratory for Acoustics/Noise Control at EMPA, and STRAUSS ELEKTROAKUSTIK GMBH. Therefore, the authors would like to thank Dr Fernando Perez-Cruz, Dr Nathanaël Perraudin, Dr Kurt Heutschi, Kurt Eggenschwiler, and Jurgen Strauss for their input. Furthermore, we would like to thank Daniela Mitterberger for her valuable help and support in preparing this paper.

5 Paper D - Data-Driven Acoustic Design of Diffuse Soundfields: Self-Organising Maps as an Exploratory Design Tool for Big Data

Achilleas Xydis[*], *Nathanaël Perraudin*[†], *Romana Rust*[*], *Beverly Ann Lytle*[*], *Fabio Gramazio*[*], *Matthias Kohler*[*]

[*] Gramazio Kohler Research, ETH Zurich, Zurich, Switzerland
[†] Swiss Data Science Center, Zurich, Switzerland

The paper demonstrates a novel approach to a performance-driven acoustic design of architectural diffusive surfaces. It uses unsupervised machine learning techniques to analyse and explore the GIR Dataset, an extensive collection of physically measured impulse responses and acoustically diffusive surfaces. The presented approach enables designers to

explore many alternative acoustically-informed material patterns with various diffusive properties without requiring expert knowledge in acoustics. The paper introduces the computational pipeline, describes the methods used and presents two use cases in the form of design experiments. Finally, the paper discusses the challenges of developing such a method, its advantages, limitations, and future work.

This version of the article has been published after peer review in *ACADIA 2021: Realignments: Toward Critical Computation - Proceedings of the 41st Annual Conference of the Association of Computer Aided Design in Architecture (ACADIA)*, pp. 170-181, in November 2021. The published version is available online at `https://papers.cumincad.org/cgi-bin/works/paper/acadia21_170`.

5.1 Introduction

During the design phase, architects examine a wide range of alternative design ideas. Early-stage design decisions significantly impact the final design's performance, whereas late-stage design modifications can rarely compensate for poor early-stage choices. In fundamental building components such as the building structure or façade, performance is an integral design driver, which is included early on. Usually, this is done in close collaboration with experts in an iterative process where a design is analysed, evaluated, and adjusted to meet the desired performance criteria. This process has become a standard practice for most architectural projects because architects are trained to understand these topics (e.g., structural design). However, room acoustics are rarely included in the early design process, even though they significantly impact our perception of space and well-being. Apart from cases where sound quality is critical (e.g., concert halls, auditoriums), acoustics are either not included in the design process or come as an afterthought relying on standardised solutions in the form of absorbent or diffusive panels.

The acoustic quality of a room is determined by its geometry and the structure or pattern of its surfaces. Slight manipulations of the surface geometry could yield significant gains in acoustic quality [75]. Currently, through computational design and digital fabrication, architects already design, visualise, and fabricate surfaces with complex geometries. While these geometries are not designed with acoustics in mind, they could act as sound diffusers, enhancing the room's acoustic qualities. Diffusive surfaces reflect sound in multiple directions and, by doing so, reduce echoes, standing waves, and sound colouration while promoting spaciousness. Suppose acoustics were included as a design criterion. In that case, these complex geometries could be an integral part of architectural elements and combine multiple acoustic properties, targeting the acoustic needs of their immediate surrounding.

To employ acoustic performance as a design driver, we must be able to quantify and interpret the acoustic effects of our geometric design choices. In a classical design process, architects have no starting point for an acoustically performative design of surfaces as they lack expert knowledge. Different computer simulation software (Odeon [96], Pachyderm [107], CATT-acoustics [97]) can be used to analyse and characterise the acoustic performance of digitally designed geometries. Nevertheless, this paradigm relies on the premise that the user is knowledgeable in room acoustics and knows what adjustments need to be made to achieve the desired goal. As a result, architects are discouraged from using such software to evaluate their designs, especially early on. Furthermore, no CAD[1] nor acoustic simulation software exists that proposes a geometrical solution to an acoustical question. Further

1: Computer Aided Design

effort is needed to increase acoustic performance awareness in architecture and provide architects with simple and accessible workflows for designing diffusive surfaces.

ML has enabled significant breakthroughs in automated data processing and pattern recognition within various fields [19, 46, 47]. Architecture and engineering have also seen an increase in research on how to employ ML techniques in performance-based design [20], style transferring [21, 22], and clustering [23]. In ML techniques, the quality and size of the dataset heavily influence the ML model's final quality [35]. Although a larger dataset is desirable as it makes for a more confident prediction, the larger the dataset, the more challenging it is to navigate, especially for non-expert users. Given its success in other fields, ML is also used in acoustics research, mainly as a predictive tool. Datasets built for this purpose could also be explored as a knowledge base of known acoustic properties. This paper combines data clustering techniques with a large dataset of geometries and IRs. It provides an exploratory design tool for diffusive surfaces, bringing acoustic performance-based evaluation earlier into the design stage.

5.2 Background

5.2.1 Acoustics

In recent years, significant research has been carried out on acoustic performance-based design. Shtrepi et al. [15] presented a design process that provides architects and designers with rapid visual feedback on the acoustic performance of diffusive surfaces. Peters [108, 109] demonstrated methods that allow tuning acoustic performance while geometry and materials change. Badino et al. [8] presented the state-of-the-art of acoustic performance-based design application in practice using 19 built projects. Most of these projects were conducted by big architectural firms in collaboration with expert acoustic consulting groups but were only geared towards spaces intended for music performance. Several computational tools exist that enable the design and optimisation of acoustically diffusive surfaces. However, their primary focus is phase grating surfaces (stepped diffusers, quadratic residue diffusers, primitive root diffusers) [110], based on sound diffusers introduced by Schroeder [111]. Although these tools simplify the acoustic design process, the generated diffusers have particular and limited geometries, a substantial thickness, and a dedicated placement according to acoustic criteria. These factors make them unattractive and difficult to integrate into an architectural design that is not purely focused on music performance.

5.2.2 Machine Learning

The main ML applications in room acoustics have focused on characterisation, information extraction, or classification. For example, ML has been used to extract the RT and the EDT of a room from music signals [25], and the room volume [26]. Peters et al. and Papayiannis et al. [27, 28] presented methods to identify the room type from an audio recording.

Most of the contributions above used supervised learning, which generally requires large amounts of labelled data. Data such as IR, absorption and scattering coefficient, early decay time, and many more are primarily quantitative in nature; therefore, they are hard to evaluate by non-acousticians. Moreover, architectural design is often focused on qualitative measures that depend on the application context and the designer's personal preferences. Alternately, unsupervised learning allows the extraction of information from data even when no labels are available. For example, dimensionality reduction organises high-dimensional data samples in a lower-dimensional space, also known as embedding, by clustering similar samples together. A high-dimensional space contains data samples with multiple attributes; for example, an image with a resolution of just 100 by 100 pixels is a 10000-dimensional sample if we view each pixel within the image as an attribute. Classical dimensionality-reduction techniques include PCA [98], t-SNE [99], or SOMs [38]. SOMs have been successfully employed in several fields such as environmental studies [112], cancer research [113], chemistry [114], structural design [23], and architectural design [115]. SOMs are particularly useful in this context. They use unsupervised training to create a nonlinear data transformation of a high-dimensional space to a low-dimensional space (usually a two-dimensional map) while preserving the topological relationships of the original high-dimensional space [116]. Topology preservation implies that if two data points are close in the high-dimensional space, they must also be near each other in the new low-dimensional space and therefore belong to the same cluster. This reduction in complexity makes it possible for designers to associate a qualitative measure with the embedding.

5.2.3 Dataset

As mentioned in the Introduction, the success of ML techniques relies heavily on the quality and size of the dataset they use. Several acoustic datasets exist containing room IRs, but their main application is in the field of speech enhancement and speech recognition (AIR[2], BUT ReverbDB[3], RWCP[4] [30–32]), acoustic environment characterisation (ACE Corpus[5] [34]), or for smart-home applications (DIRHA[6] [33]). Furthermore, these datasets do not contain any three-dimensional geometrical data. The open-sourced GIR Dataset[7] [51], an

2: www.iks.rwth-aachen.de/fileadmin/user_upload/downloads/forschung/tools-downloads/air_database_release_1_4.zip

3: speech.fit.vutbr.cz/software/but-speech-fit-reverb-database

4: research.nii.ac.jp/src/en/RWCP-SSD.html

5: acecorpus.ee.ic.ac.uk/

6: dirha.fbk.eu/English-PHdev

7: renkulab.io/projects/ddad/gir-dataset/

extensive collection of three-dimensional diffuse surfaces and their corresponding real IRs, was recently released. It can be used for ML applications to predict the acoustic properties of three-dimensional surfaces.

5.3 Methods

As highlighted in sections 5.1 and 5.2, acoustic performance criteria are mainly considered in projects where spaces host music performances. Furthermore, current methods mainly focus on design optimisation and heavily rely on expert knowledge in acoustics. This research presents a workflow that enables architects to explore several possible design solutions, given specific acoustic performance criteria (energy per frequency band). It uses the GIR Dataset for its unique set of three-dimensional surfaces and the high number of real IRs per surface. Machine learning techniques and specifically SOMs are used to cluster the surfaces based on acoustic performance criteria.

5.3.1 The GIR Dataset

The GIR Dataset contains 873496 real IRs from 296 surfaces (2951 per surface), spread in three layers (see Figure 5.4). Layer_0 contains 36 measurements in a 6×6 grid and is the closest to the surface at a distance of 1 meter. Layer_1 and layer_2 contain 25 and 16 measurements in a 5×5 and 4×4 grid at a distance of 1,9 meters and 2,8 meters, respectively. The IRs were captured inside a semi-anechoic room and time-windowed only to contain the first reflections. The surfaces of the dataset resemble architectural material systems and are arranged in nine typologies, such as brick walls, stone walls, and more (see Figure 5.1). The geometry of each surface is composed of a microstructure and a macrostructure. The first defines the typology, and the second its overall

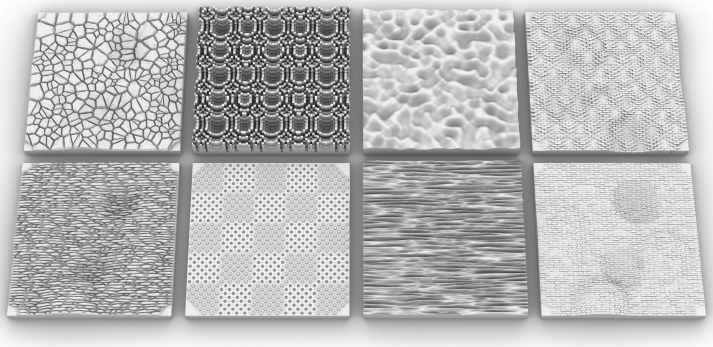

Figure 5.1: A sample of different surface typologies. From top left to bottom right: Polygonal rubble stones, PRD diffuser, IDL, Stretcher-bond bricks, Coursed ashlar stones, Primitives, IDL, Flemish-bond bricks.

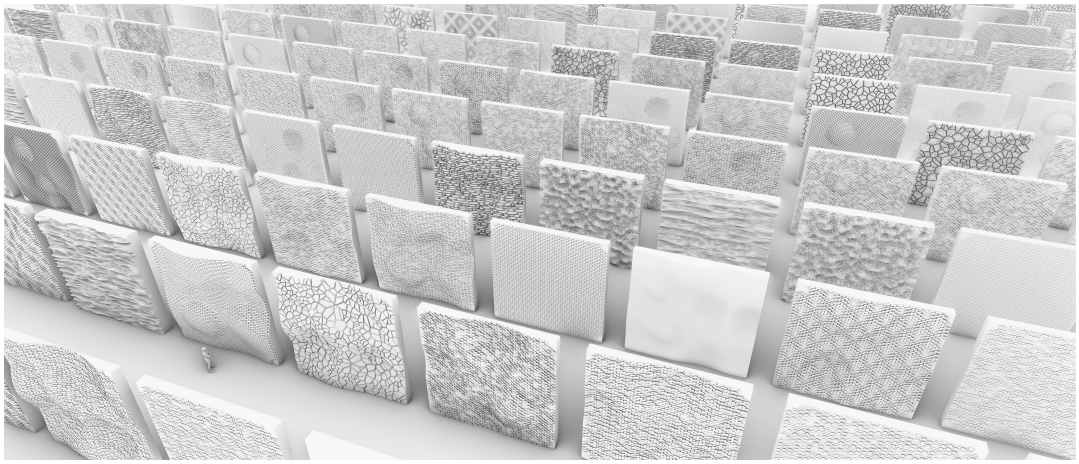

Figure 5.2: 3D visualisation of a portion of GIR Dataset's diffusive surfaces demonstrating possible geometric variations. For scale reference, a human is placed at the bottom left part of the image.

shape. Several typology-specific material and construction characteristics are coded in the geometry generation algorithm and used to create different material patterns (see Figure 5.2). The brick dimensions, its rotation along the Z-axis, its shift along the macrostructure's normal vector, and the width and depth of the mortar are used for the brick typologies. The number of stones per square meter is used for the stone typologies, along with the surface roughness and the joint depth between them. The macrostructure enhances the low-frequency diffusion by significantly increasing the depth variation (see Figure 5.3).

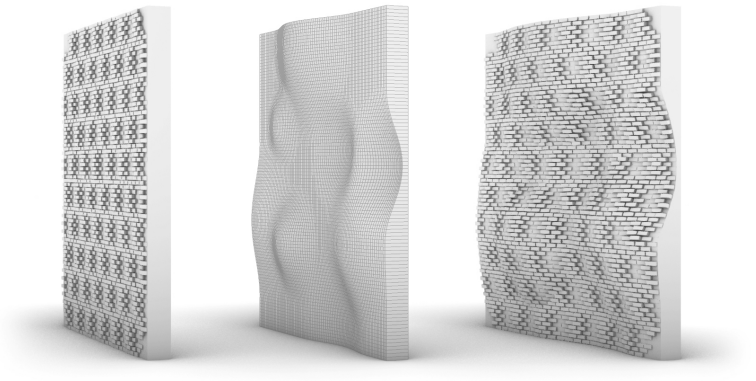

Figure 5.3: Micro-macrostructure. Left: A surface with only a microstructure (Stretcher-bond bricks). Middle: A surface with only a macrostructure. Right: A surface that combines the micro- and macrostructure.

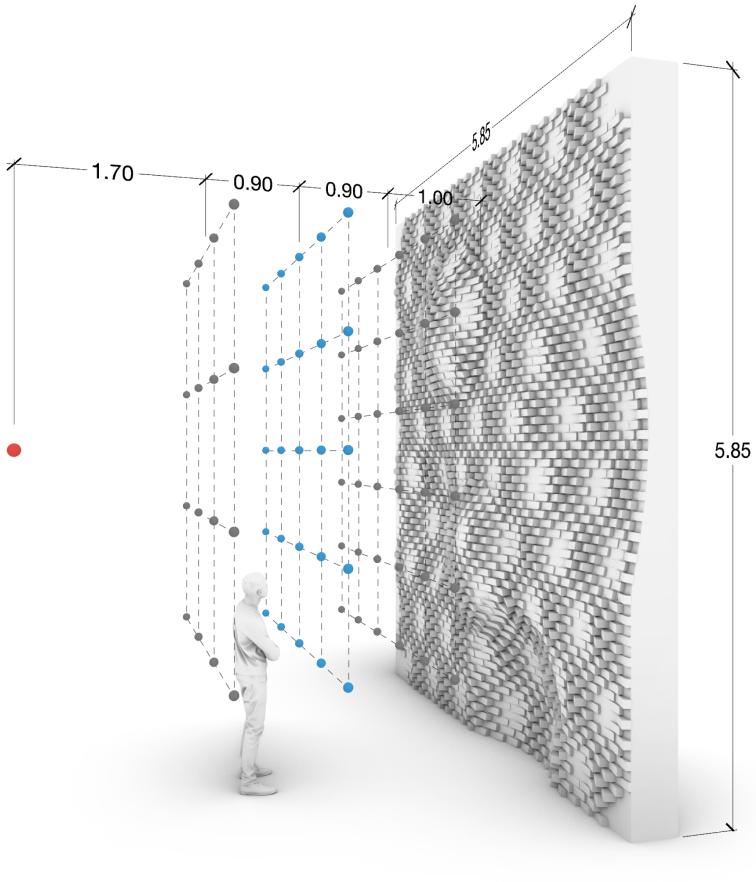

Figure 5.4: The measuring grid in front of a surface. Red represents the source position, and blue is the selected receivers' layer. The source is located in the centre of the surface and 4,5 meters away from it. The receivers' layer (layer_1) is approximately 1,9 meters away from the surface.

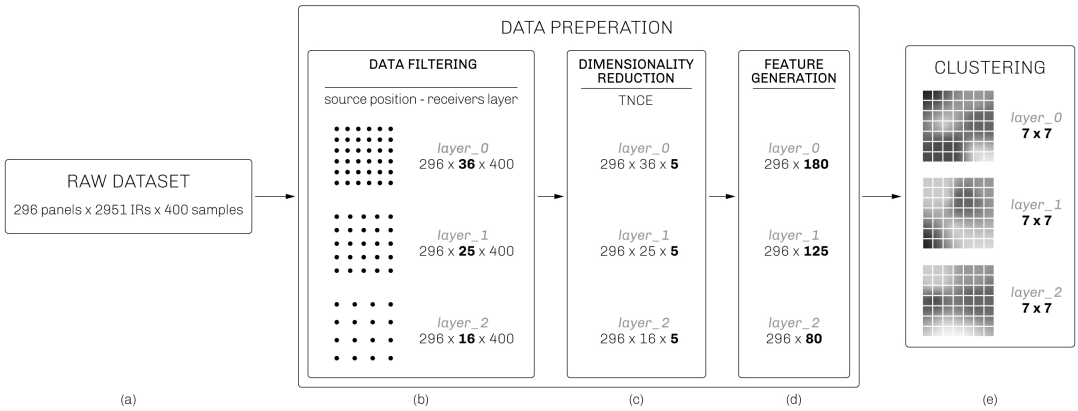

Figure 5.5: Data preparation pipeline.

5.4 Proposed Design Workflow

The proposed design workflow contains three main steps: data preparation, clustering, and design exploration (see Figure 5.5). We use the IRs of the GIR Dataset to compute the primary performance criteria for our method. The large size of the dataset dictated the need for data reduction strategies. We use the open-sourced `MiniSom`[8] python library [117] and create several custom data visualisation algorithms for the clustering step. These algorithms provide an easy and understandable way to visualise complex and high-dimensional data and validate the quality and performance of several steps of our workflow. Finally, we describe using the trained SOM to explore design options based on given acoustic criteria.

8: `https://github.com/JustGlowing/minisom`

5.4.1 Data Preparation

The principal challenge when constructing a low-dimensional embedding using a SOM is the size of a sample. Given that each of the patterns contains 2951 IRs of 400 float numbers, the total size of the raw feature vector is 1180400 (see Figure 5.5a). We use three steps to reduce this large dimension. First, a source position is selected from the measuring grid, which yields 83 measurements spread across the three grid layers (see Figure 5.5b). In the second step, we use the post-processing pipeline from Rust et al. [40] to build low-dimensional feature vectors from the selected IRs. This pipeline removes the direct sound from the IR, retaining only the reflected sound coming from the surface. A custom-designed band-pass filter is used to split the above-mentioned acoustic descriptors into five frequency bands, with centre

frequencies at 250Hz, 500Hz, 1kHz, 2kHz, and 4kHz[9]. As a last step, we use the provided functions to convert the IR into TNCE[10]. This step effectively reduces each IR's 400 samples to 5 numbers (see Figure 5.5c). Finally, we concatenate the features of each pattern and obtain feature vectors of size 36×5, 25×5, and 16×5 for layers 0, 1, and 2, respectively (see Figure 5.5d).

9: The dataset's geometries and frequencies are in 1:10 scale.

10: The TNCE is the last value from the NCE list, representing the total energy arrived at the receiver position.

5.4.2 Clustering

Clustering operations aim to group various design options into sets with similar features (in this case, TNCE). Analogous to the clustering methods used by [23, 118], this paper proposes a method to cluster multiple design options based on their acoustic performance. Therefore, one can expect similar acoustic performance for all the designs of the same cluster. Such clustering can be used as a data-driven catalogue that enables designers to explore the available design space based on acoustic criteria. The SOM algorithm organises all the patterns on a two-dimensional plane. Figure 5.6 shows the embedding of 296 patterns based on TNCE values. As highlighted with the coloured outline, the macrostructure is one of the most discriminative features for the SOM.

5.4.3 Design Exploration

Using the two-dimensional SOM described in the previous subsection, designers can get a fast and precise overview of possible design options. Each cell of the SOM contains a group of design options clustered based on the acoustic performance feature selected by the designer (e.g., TNCE). The hypothetical examples described below are used to illustrate the proposed design workflow. We imagine a generic meeting room where one of its walls may be freely designed to improve the room's acoustical properties. For our performance criterion, we choose the TNCE values of layer_1 because they are located very close to the centre of the room. Because the IRs contain only early reflection information (See The GIR Dataset in chapter 5.3.1), the TNCE values also contain only the energy from these early reflections. Although the form of the room does not influence our method, for simplicity, the meeting room has a shoe-box shape measuring 5 meters wide, 6 meters long, and 4 meters high. We consider the reflected energy of a flat surface as our 100 per cent reference (maximum specular reflection). The criterion is the reflected energy of the desired surface, represented as a ratio of the flat surface's energy. Values higher than 100 per cent represent amplification, and lower values energy reduction.

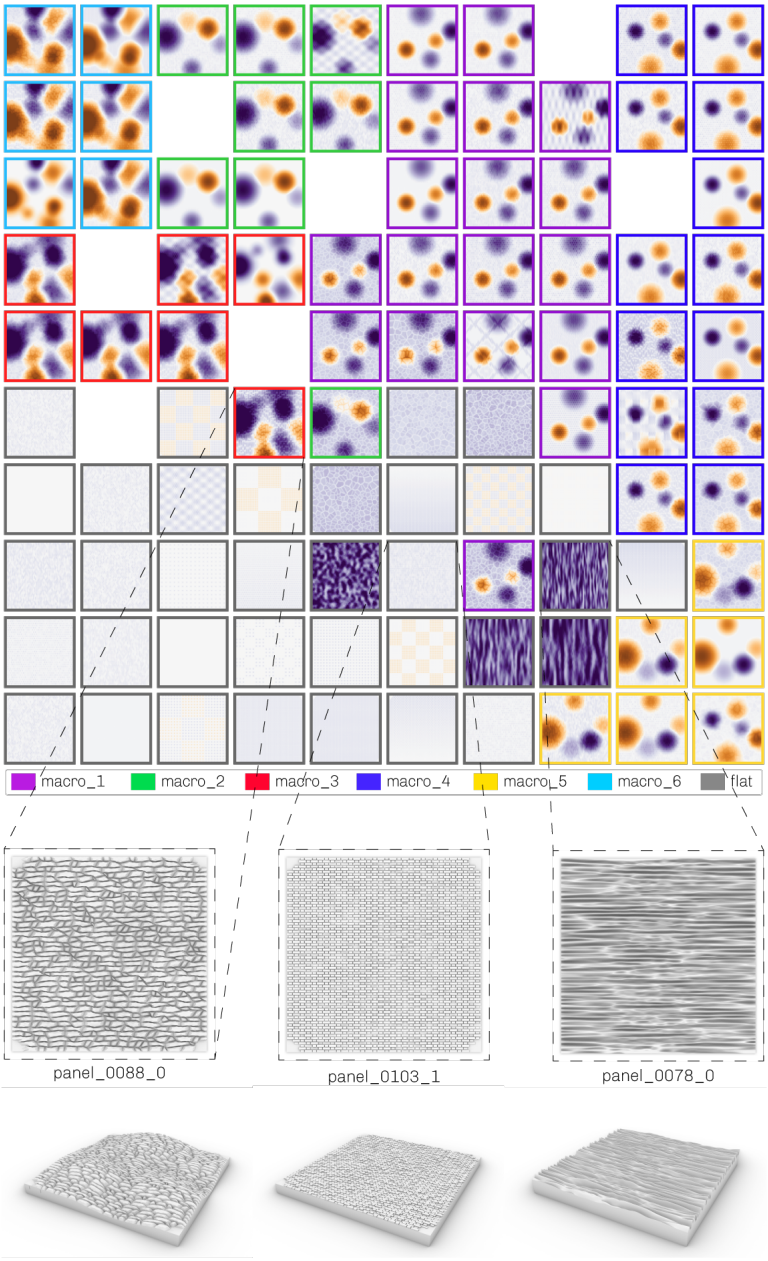

Figure 5.6: An SOM of 296 surfaces based on the TNCE values of layer_1. The displayed surfaces are coloured from violet to orange to represent their depth, and the coloured outline indicates their macrostructure.*

**This figure has been modified from the published version. Its content has been rearranged to fit the thesis layout.*

	neurons		iterations	neighbourhood function	sigma	learning rate	training time
	x	y					
scenario A	10	10	100000	Gaussian	0.8	1.5	28 sec
scenario B	7	7	100000	Gaussian	1.0	2.5	22 sec

Table 5.1: SOM training values.

Scenario A does not have a specific material system in mind, but scenario B assumes designers have already decided on a material system, specifically, a brick wall. These different decisions result in two different sets of panels for the SOM training. Scenario A uses all the dataset typologies, resulting in 279 surfaces, and scenario B uses only the brick wall typologies, resulting in 146 surfaces. For the SOM training, the MiniSom library requires us to provide values for the following arguments: map dimensions (x, y number of neurons), training iterations, the neighbourhood function, the sigma, and the learning rate[11] (see Table 5.1). Sigma defines the spread of the neighbourhood function in number-of-neighbours. The appropriate value for sigma varies by map dimensions. When the sigma value is too small, the samples cluster near the centre of the map; When it is too large, the map exhibits several large empty areas towards the centre [119]. The learning rate defines only the initial value of the learning rate for the SOM. With every training iteration, the learning rate adjusts according to the following function:

11: Further documentation can be found on MiniSom's Github repository. `github.com/JustGlowing/minisom`

$$learning\ rate(t) = \frac{learning\ rate}{\frac{1+t}{0.5 * iterations}} \tag{5.1}$$

We iterated over different training values to achieve an optimum embedding (Figures 5.9 and 5.12). A SOM with many neurons has enough space to arrange the data samples. When multiple very similar samples exist, the SOM algorithm places these samples in the same cell; thus, the resulting embedding can have several empty cells. On the other hand, a SOM with a very small number of neurons may not have enough space to arrange the samples. This constraint will force the algorithm to place less similar samples on the same cell, resulting in a less representative data embedding.

5.4.4 Scenario A

This scenario aims to design a surface that, compared to a flat reflective surface, lowers the specularly reflected energy in the whole spectrum, emphasising the mid and high-frequency bands. This emphasis will make the room sound softer by reducing the often harsh high-frequency specular reflections. Combined with the overall reduction in reflected energy, the person speaking will sound more clear. To achieve the desired energy goal, we input the following values: [80, 80, 70, 60, 60], and the SOM cell with the closest matching values is displayed (see Figure 5.9). Selecting the cell reveals all the surfaces with similar values in descending order, from the closest to the least matching option. Nevertheless, because of how the SOM clustering algorithm works, even the least matching option is very close to our desired acoustic criterion. Figure 5.9 shows the energy ratios of all matching surfaces compared to the desired energies and their close-up views. Option 1 (panel_0100_0) and option 3 (panel_0082_0) are also visualised inside the room to evaluate them based on aesthetic qualities (see Figures 5.7 and 5.8). At this point, the architect decides which surface best suits their design idea.

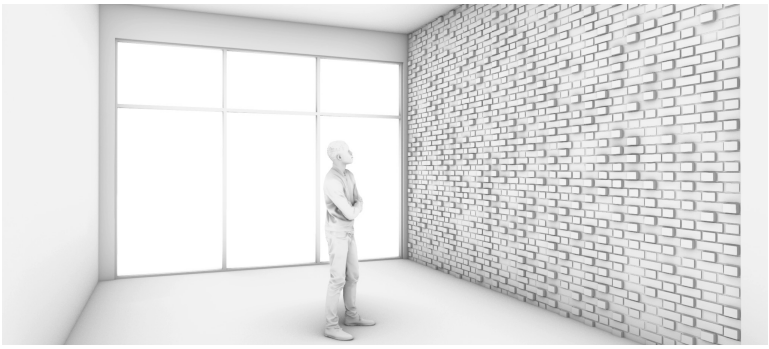

Figure 5.7: 3D Visualisation of option 1 from scenario A (panel_0100_-0).

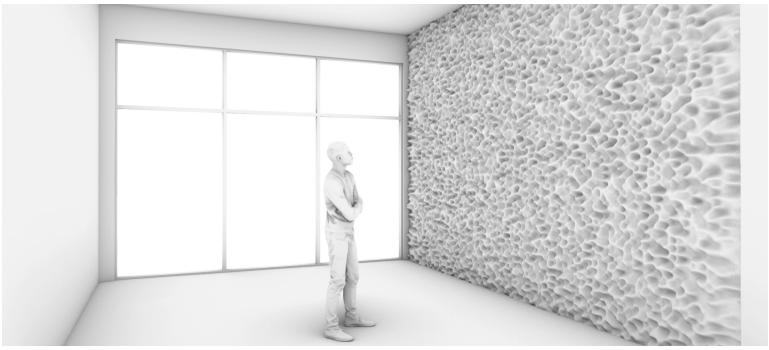

Figure 5.8: 3D Visualisation of option 3 from scenario A (panel_-0082_0).

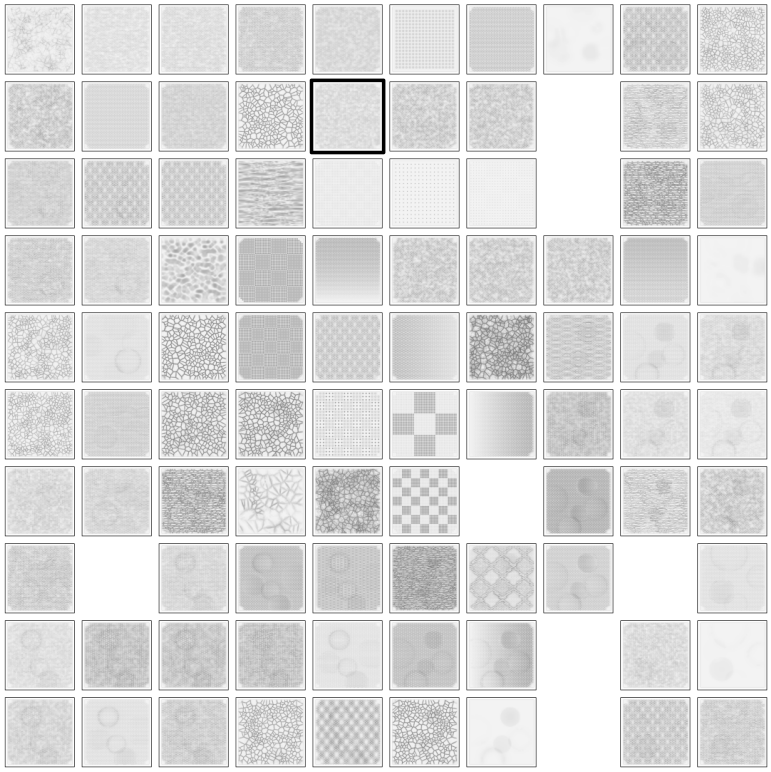

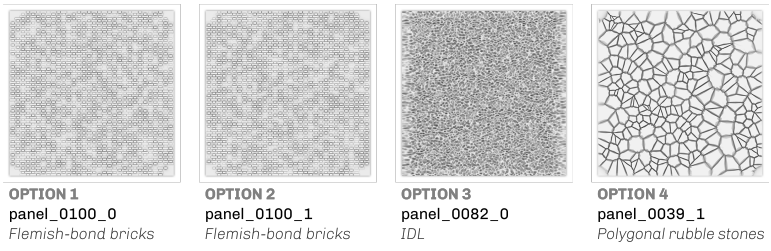

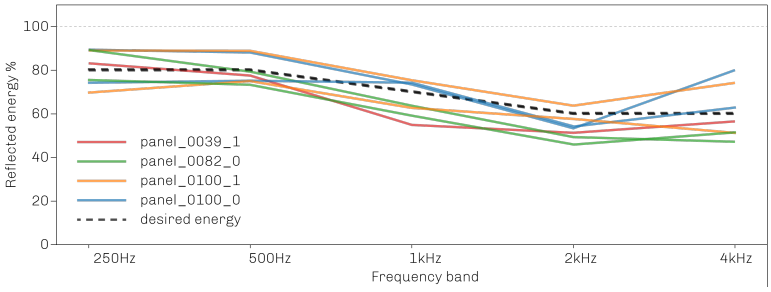

Figure 5.9: Top: The 10x10 SOM for Scenario A. The black outline indicates the best-matching cell according to the desired energy values. Middle: The surfaces of the best matching cell. Bottom: Energy ratios of all matching surfaces.

5.4.5 Scenario B

Like the previous scenario, the performance criterion is again the TNCE values of layer_1. Figure 5.12 shows the cell with the best matching values, the close-up views of the associated surfaces and their energy ratios. In this case, the SOM cell contains only three surfaces. Contrary to scenario A, these surfaces happen to have a macrostructure, making them more spatially expressive. Options 1 and 3 are from the same typology and have very similar designs and energy values; therefore, we focus on options 1 and 2. Panel_0036_1 lowers the energy by five to ten per cent more than the desired energy goal in all frequency bands. Although panel_0104_1 also lowers the energy a little more than the set goal in the two lowest frequency bands (250Hz, 500Hz), it matches the desired goal in the 1kHz and 4kHz frequency bands (see Figure 5.12 bottom). Therefore, option 1 better matches our desired acoustic performance criteria. A visualisation of these two options can be seen in Figures 5.10 and 5.11.

Figure 5.10: 3D visualisation of option 1 from scenario B (panel_0104_-1).

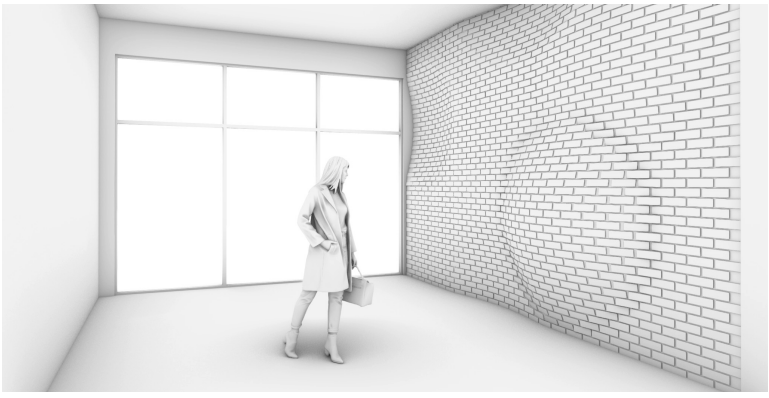

Figure 5.11: 3D Visualisation of option 2 from scenario B (panel_0036_-1).

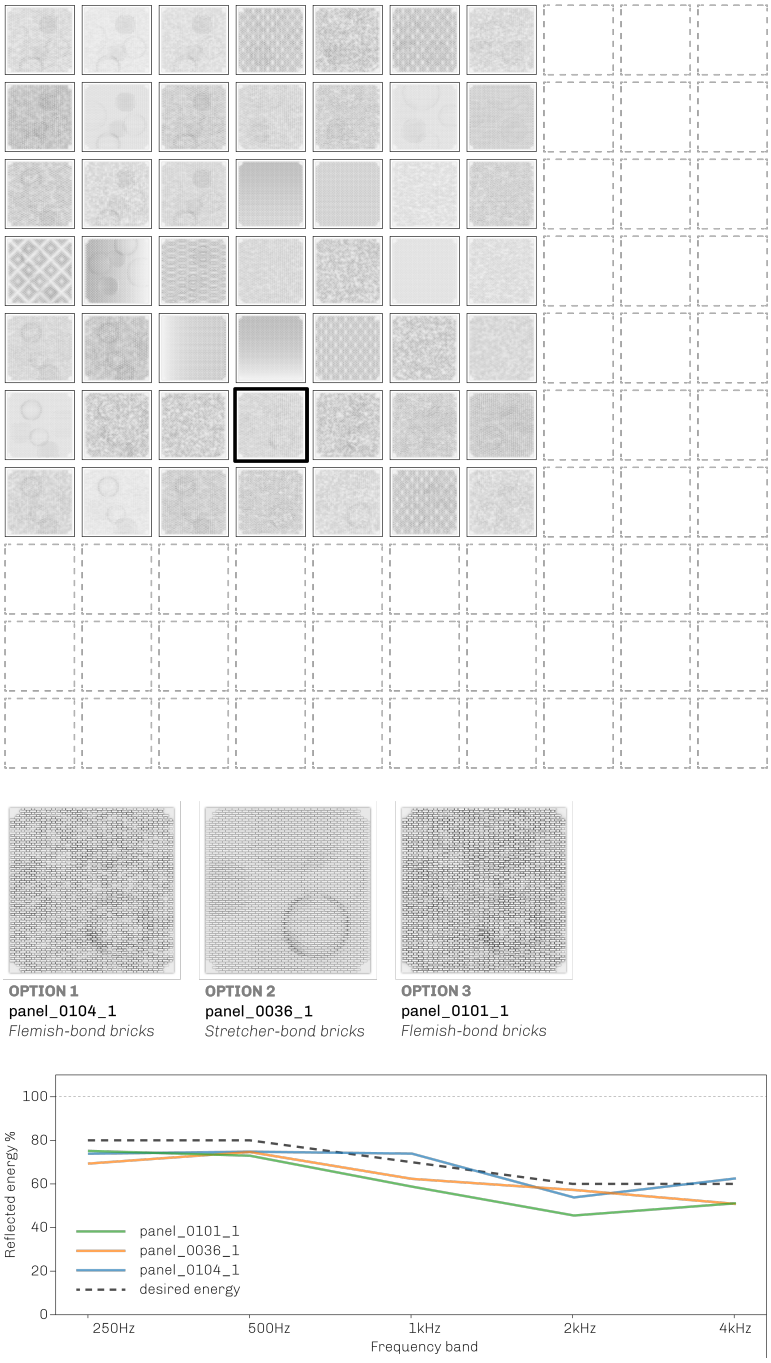

Figure 5.12: Top: The 7x7 SOM for Scenario B. The black outline indicates the best-matching cell according to the desired energy values. Middle: The surfaces of the best matching cell. Bottom: Energy ratios of all matching surfaces.

5.5 Results and Discussion

We have proposed a novel and fast workflow for a performance-driven acoustic design of diffusive surfaces. We described its components and how each of them contributes to the entire workflow. We have demonstrated its application with two design experiments. These experiments showed that thanks to its visual and intuitive implementation, users need little acoustic expert knowledge to specify and explore early design options compared to traditional room acoustic surface design processes. When no predefined typology is chosen, the design proposals could include several different typologies. This approach could inspire or drive the designer's choices and could also be used as a base for discussion and further refinement with acoustic experts. Compared to sometimes days of computing time when using numerical modelling algorithms [108], our method needs only 20 to 30 seconds[12] to train the SOM depending on the dataset size (see Table 5.1). Then, computing the closest matching designs requires less than a second. Although the presented workflow is based on the GIR Dataset and precisely a panel's TNCE values, one could use any other acoustical descriptor from the GIR Dataset (impulse response, frequency response, cumulative energy, and more). Furthermore, the presented methodology is not limited to the GIR Dataset. It can be adapted and applied to any other acoustic dataset.

12: On a 2.9GHz 6-core Intel i9 CPU and 32GB 2400MHz DDR4 RAM.

The two design scenarios have shown that both flat-like (scenario A) and spatially varied surfaces (scenario B) are considered options. Flat-like surfaces are more likely to have uniform TNCE values across points of the same layer; therefore, they are more likely to be the closest matching sample in the SOM. Nevertheless, the design workflow is not limited to a single set of desired energy values. We can assign different values to each layer, assign individual values to each grid point of a specific layer, and finally, assign a few values at desired locations and let the algorithm interpolate the in-between values. The fewer sets of energy values one uses as a performance criterion, the more likely it will result in a flat-like design.

5.5.1 Limitations

Although the presented design workflow proposes material patterns based on desired acoustic performance criteria, these patterns can only be from the GIR Dataset. Nevertheless, the dataset can be expanded to include more patterns for a specific typology or introduce an entirely new typology. Furthermore, because the measurements were not according to the ISO standard, they cannot be used to derive standard acoustical descriptors such as absorption and scattering coefficients. Therefore, the clustering can only be done using the descriptors provided by Rust et al. [40] (e.g., cumulative

energy, normalised cumulative energy, total normalised cumulative energy). Nevertheless, we believe that energy values (NCE, TNCE) split into five filter bands are metrics most users can understand or quickly get familiar with.

5.5.2 Future Work

The proposed design workflow provides initial ideas or inspiration for a more acoustically informed design direction. However, choosing the desired acoustical parameters for the different frequency bands may still require some basic understanding of acoustics or initial consultation with an acoustics expert. Therefore, predefined acoustic use cases should be implemented. These cases will translate qualitative intentions into quantitative parameters. Currently, the design workflow can be used via a `Jupyter notebook`, and it is available as an open-source code at `https://renkulab.io/gitlab/ddad/ddad-renku/`. The interface can be further streamlined and possibly integrated as a tool within existing CAD software or a stand-alone web-based application.

5.6 Credits and acknowledgements

5.6.1 Collaboration

Dr Nathanaël Perraduin developed the code to select the SOM cell with the best matching acoustical criteria. Dr Beverly Ann Lytle optimised the SOM code making it run in multiple processes, thus reducing the computation time.

5.6.2 Author's contribution

The author of this thesis undertook the conception, development, testing, and validation of the presented design workflow. This included developing the code for generating the SOMs, translating and structuring the GIR Dataset's data for use with the SOM, and visualising the output of the SOM.

5.6.3 Authors contributions to the paper

13: Contributor Roles Taxonomy

The individual roles and contributions of each author in this paper are described using the standardised taxonomy CRediT[13][71].

Achilleas Xydis
Conceptualisation, Methodology, Software, Validation, Investigation, Writing – Original Draft, Writing – Review & Editing, Visualisation

Nathanaël Perraudin
Software, Validation, Writing – Review & Editing

Romana Rust
Writing – Review & Editing, Supervision

Beverly Ann Lytle
Software, Writing – Review & Editing

Fabio Gramazio
Writing – Review & Editing, Supervision

Matthias Kohler
Writing – Review & Editing, Supervision

5.6.4 Acknowledgements

This research steamed out of a collaborative and multidisciplinary project between Gramazio Kohler Research at ETH Zurich, the Swiss Data Science Center, the Laboratory for Acoustics/Noise Control at EMPA, and STRAUSS ELEKTROAKUSTIK GMBH. Therefore, the authors would like to thank Dr Fernando Perez-Cruz, Dr Kurt Heutschi, Kurt Eggenschwiler, and Jurgen Strauss for their input. Furthermore, we would like to thank Dr Nikola Marinčić for his valuable inputs on self-organising maps and Gonzalo Casas for always being keen (hopefully) on helping on Python-related topics.

6 Geometry and Impulse Responses web application

Chapters 2, 3, 4, and 5 describe design workflows that enable acoustic-aware design using the GIR Dataset. Even though these workflows provide visualisation methods enabling users to explore the differences in reflected sound energy, the scattered sound's direction, the frequency response, and more, they require programming knowledge to set up, execute, and even more customise and further develop them. This requirement could exclude the usability of this research from users with limited or no programming knowledge. One of the research objectives is to increase the impact of this research by developing easy-to-use tools and open-sourcing the dataset and

all the developed code. A web-based application was developed, allowing users with no programming knowledge to access the dataset. The application uses all the visualisations described in chapter 4 to enable architects and acousticians with no prior programming knowledge to explore, visualise, and study the interaction between sound and diffusive surfaces.

The following sections describe the web app's user interface, the two available visualisation modes, and how it can be used to explore the content of the GIR Dataset. Lastly, it describes visualisation methods not covered in the previous chapters to study a surface's diffusivity.

6.1 User Interface

Users are presented with a simple one-page - two-column design containing all available information and eliminating unnecessary navigation to other pages (see Figure 6.1). Users can filter out the surfaces of the GIR Dataset based on their typology and then select a surface while being presented with a close-up rendering of its geometry (see Figures 6.2 and 6.3). This action loads the 3D geometry of the selected surface in the 3D view window. Users can interact with the surface by panning around it or zooming in to get a closer look at its structure. A list of all available metadata is displayed below, containing information such as measured date, printer model, binder type, air temperature and atmospheric pressure during the measuring process, and many more. The measuring grid is superimposed in front of the surface's 3D geometry, making it easy to select the right source-receiver combination. By choosing a source[1] and a receiver[2] position, all acoustic descriptors are calculated and displayed in a series of visualisations in the right column.

1: blue sphere

2: red sphere

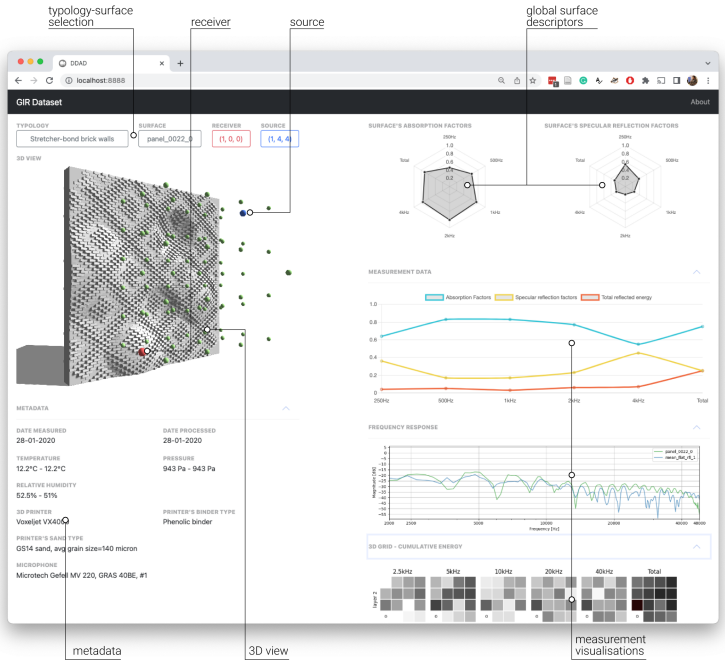

Figure 6.1: A screenshot of the web-based application.

All visualisations provide an absolute and relative mode. In the absolute mode, the mathematical results are output without any alteration. In the relative mode, before visualising, the results are first normalised using the values of a reference flat surface. The flat surface is a reference for the

maximum specularly reflected energy. It allows for a direct comparison with some of the most commonly used flat architectural surfaces, such as drywalls, smooth concrete, or plastered brick walls. The importance of reference surfaces in the computational pipeline and their usefulness in comparative studies can be found in Appendix E.

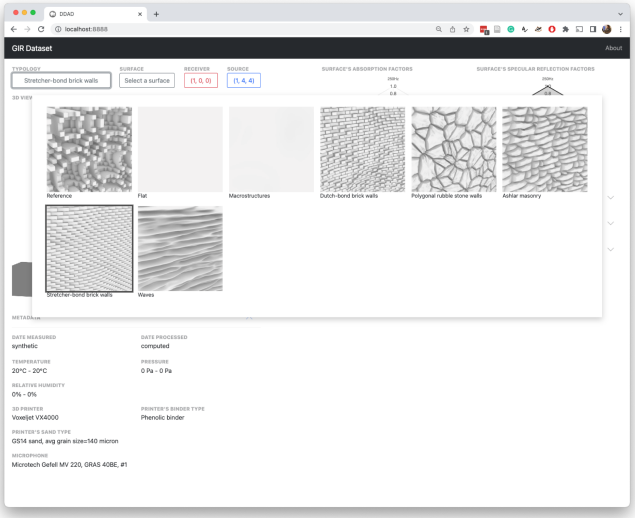

Figure 6.2: Typology selection process.

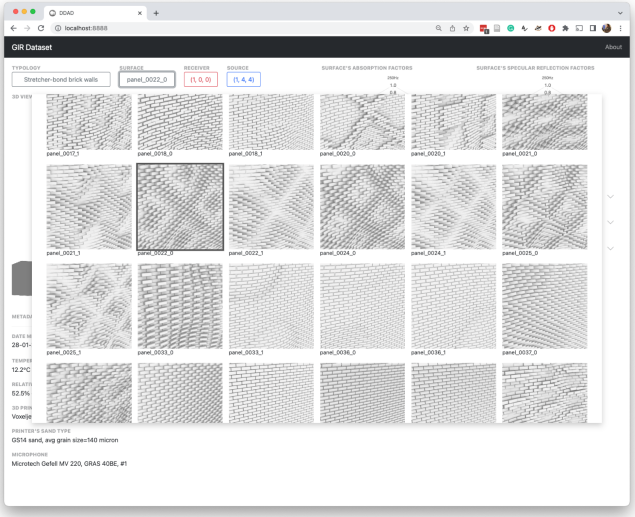

Figure 6.3: Surface selection process.

6.2 Absolute - relative modes

3: microphone at (0,1,0) and speaker at (0,3,0)

Figure 6.4 shows cumulative energy over time plots for the same microphone-speaker combination[3]. Figure 6.4a shows the absolute energy values of the reflected energy for a flat surface. The maximum value is the Total Cumulative Energy (TCE) and is always located at the end of the plot. When normalising the plots, that value is scaled to 1.0 and becomes the TNCE value (see Figure 6.4b). Even though, for specific applications, absolute values are helpful, it is also convenient to display energy values relatively. Users can easily and quickly compare a structured surface's cumulative energy to a flat surface's energy. Figure 6.4c shows the absolute cumulative energy values of a Primitive Root Diffuser (PRD Diffuser). Although this plot provides an insight on the speed that energy accumulates at the receiver position, the energy distribution per frequency bands, and the TNCE, only in figure 6.4d it becomes evident how much less energy is reflected from a PRD Diffuser compared to a flat surface[4].

4: The energy of a flat surface is shown with a red dashed line

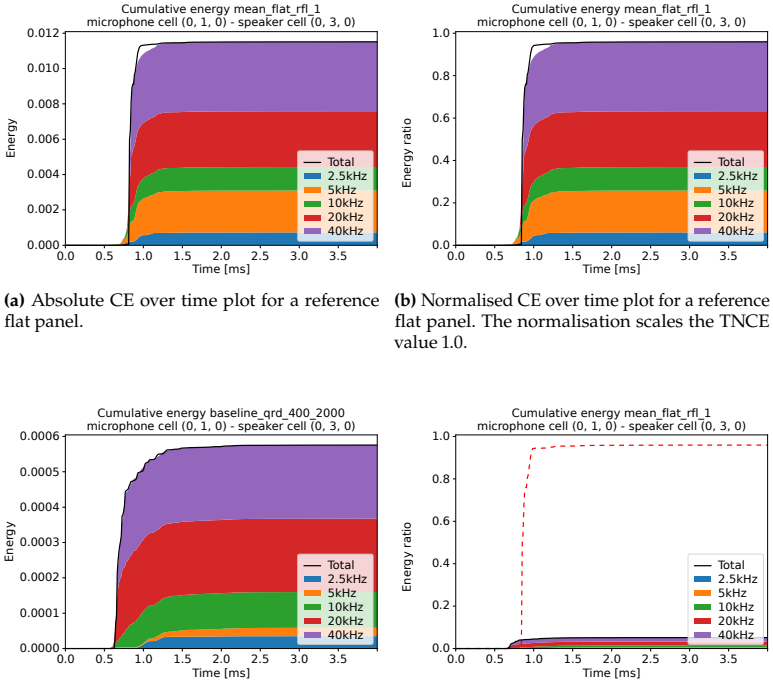

(a) Absolute CE over time plot for a reference flat panel.

(b) Normalised CE over time plot for a reference flat panel. The normalisation scales the TNCE value 1.0.

(c) Absolute CE over time plot for a Primitive Root Diffuser (`baseline_prd_400_2000`).

(d) Normalised CE over time plot for a Primitive Root Diffuser (`baseline_prd_400_2000`).

Figure 6.4: Absolute and relative cumulative energy CE over time plots.

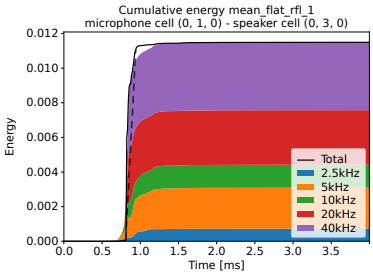

(a) The CE slope of a flat surface. It takes 0.15 ms for the energy to go from 5% to 95%.

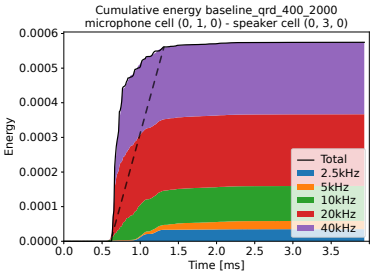

(b) The CE slope of a PRD Diffuser. It takes 0.7 ms for the energy to go from 5% to 95%.

Figure 6.5: Diffusivity slope.

6.3 Usability

Similar to the comparative studies possible using the `DataPloter` class from the computational pipeline, such studies are also possible via the web app. Users can open two browser windows and select two different surfaces on each one. Using one of the flat surfaces on the one window and a PRD Diffuser on the other, users can compare their diffusivity by looking at the CE over time plot. The flat reflector produces specular reflections that almost instantaneously redirect most incident sound at the receiver's location. On the contrary, the highly diffusive surface of the PRD Diffuser produces many smaller amplitude reflections spread over a more extended period. Looking at figures 6.5a and 6.5b[5] the dotted line marks the steepness of the CE curve indicating the time it took for the reflected energy to arrive at the receiver's location. It takes 0.15 ms with a flat surface and 0.7 ms with a PRD Diffuser for the CE to go from 5% to 95%[6], a 4.6× increase in time.

Another way to study a surface's diffusivity is by looking at the *3D Grid - Cumulative Energy* plot, visible at the bottom of the right column on Figure 6.1 (A detailed view of this plot can be seen in Figures 6.6 and 6.7). This visualisation provides a detailed overview of the reflected energy, with each square representing the TCE value at a position on the measuring grid. The values are normalised based on the TCE values of the entire audio spectrum of a flat surface (flat reflector) and range from -20dB to +3dB. Values equal to 0 are shown in black, indicating the same energy as a flat surface. Values smaller than 0 are shown in white and indicate sound reduction. Lastly, values above 0 are shown in red and indicate sound amplification[7]. The energy values are grouped column-wise per frequency band and row-wise per measuring grid layer[8].

Figure 6.6[9] shows the TCE values of a flat surface. It is evident and expected that this surface has a uniform energy distribution in every measuring position. On the contrary, looking at Figure 6.7, we can see how much less

5: The figures are isolated from the web app for better readability.

6: The 5% offset from 0% and 100% is chosen to exclude any possible leftover energy from imperfect removal of the direct sound and possible late reflections originating from the acquisition setup and not the surface.

7: Sound focusing

8: Layer 0 is the closest to the surface and layer 2 the furthest.

9: The plot is isolated from the web page for better readability.

energy is reflected in a specular way from a PRD Diffuser. Furthermore, close to the surface, the energy distribution is not as uniform, but it becomes more uniform in layer 2, which is the furthest away from it. This is expected, considering that some distance is required for the destructive interferences to create a uniform diffuse sound field. The repeating structural pattern of this diffuser is also expressed as an energy pattern, especially at layer 0 for the 20kHz, 40kHz, and Total frequency bands.

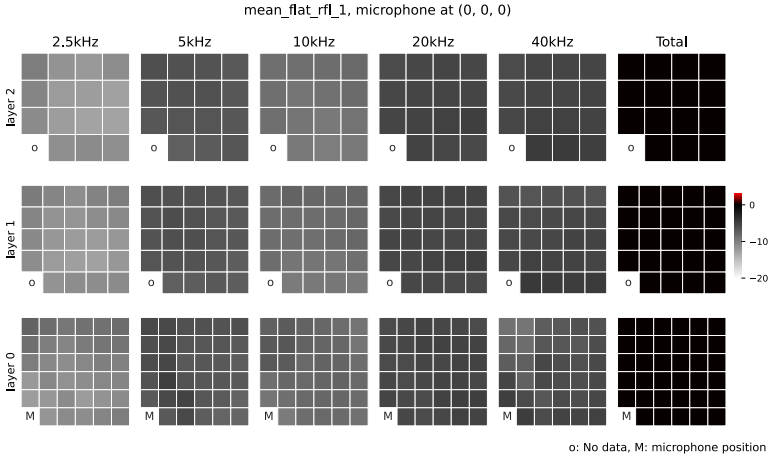

Figure 6.6: The TNCE value on every point on the measuring grid for a flat surface.

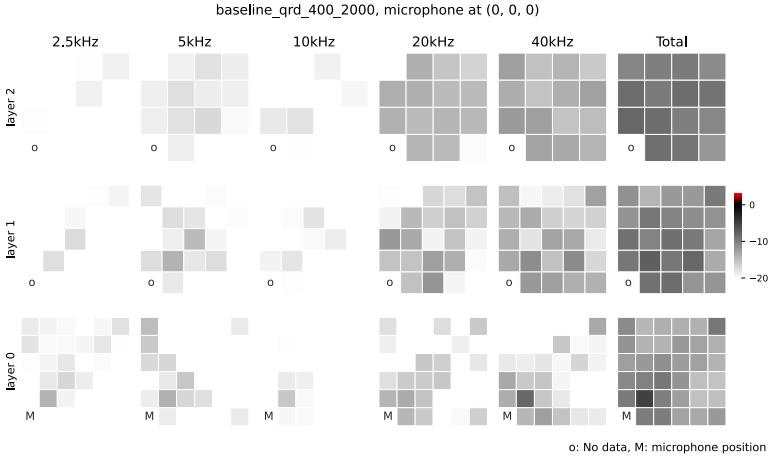

Figure 6.7: The TNCE value on every point on the measuring grid for a PRD Diffuser.

7 Conclusions

This doctoral thesis focused on architectural acoustics and sound diffusion in particular and presented a novel approach to studying the mutual relationship between geometry and sound diffusion. Instead of simulating the interaction between diffusive surfaces and sound, it opens the possibility of predicting acoustical properties using machine learning techniques. These techniques address the two main reasons that currently discourage architects from including acoustics evaluation in the early design stages, computation time and ease of use. By focusing on developing faster and simpler to use acoustic evaluation methods, this research created a new dataset, developed data analysis and visualisation tools, and proposed new methods for a data-driven acoustic design. Chapter 1 provided the motivation, context, and problem statement

supporting the need for an alternative approach to including acoustics evaluation in the early design stages. Chapters 2 to 6 presented the main body of this research. This chapter provides an overview of the work presented in the previous chapters consolidating the contributions made throughout this cumulative thesis. It continues by discussing the results and limitations of the work presented in chapters 2 to 6 and concludes with an outlook and recommendations for future work.

7.1 Contributions

This research promotes the importance of interdisciplinary collaboration in scientific discourse by bridging different disciplines, such as architecture, acoustics, and data science. It contributes to the field of architectural acoustics and fosters the application of data science methods. It enables fast data-driven approaches for designing and evaluating the acoustics properties of digitally designed architectural surfaces. It simplifies the current design-simulation-evaluation process, thus bringing acoustics closer to the architecture practice and enabling acoustics-aware designs. The following paragraphs summarise the main contributions of this research.

7.1.1 Dataset

The basis of ML applications is high-quality datasets. A new acoustic dataset was collected to aid the development of ML applications on sound diffusion. The dataset is the basis for machine learning algorithms that will help create tools that are faster, less cumbersome, and have reasonable accuracy. It can also be explored as a library of surfaces and known acoustic properties. It is the first dataset containing both acoustical and geometrical data. The GIR Dataset includes 312 scale-modelled[1] architectural wall-like surfaces. The surfaces resemble commonly used fabrication methods and construction materials. For each surface, 2951 measurements were taken from multiple source and receiver positions, resulting in a total of 920712 impulse responses. The dataset is made available open-source and can be downloaded from `https://doi.org/10.5281/zenodo.5500519`. A detailed documentation is published describing its content, how it can be accessed, the data-acquisition setup with all the hardware specifications, the data collection protocol, data post-processing, and data storing (see chapters 3 and 2). Several ML examples are made available showcasing the potential benefit of the GIR Dataset in ML applications (see chapters 2.3, 5, and C).

1: In 1:10 scale.

7.1.2 Data-acquisition method

An automated multi-robotic data-acquisition method was developed for collecting impulse responses from scale-modelled 3D-printed surfaces. The method uses two industrial robotic arms inside an acoustically treated and sound-insulated room. The robotic arms have as end-effectors a microphone and a speaker, and they reposition them along a three-dimensional orthogonal grid over the surface under test. The three-dimensional grid enables the measurement of surfaces with non-uniform material properties, such as diffusive texture combinations and gradients, or combinations of diffusive

and absorptive areas. Furthermore, it captures the acoustic responses at three distinct distances (layers) from the surface, allowing the study of distance-related acoustical effects. Lastly, the entire process - robotic movement, audio playback and recording, data processing, and data storing - is fully automated and does not require human presence or supervision. On the one hand, this automation provides the necessary accuracy and repeatability required for such a precision-sensitive task. On the other hand, similar to measurement processes such as the one described in ISO 17497 standard, it is extremely time-consuming, thus human-resource consuming.

7.1.3 Data analysis and visualisation

This research introduced a large and high-dimensional acoustic dataset. Three approaches were developed, addressing the complex and multi-dimensional nature of the data. First, a series of new acoustic descriptors tailored for users with basic knowledge of acoustics. Second, a computational framework that generates customisable and interactive visualisations for low- and high-dimensional data. These visualisations include the geometry of the studied surface, coupling it with the acoustic data, and providing a detailed way to study the mutual relationship between geometrical characteristics and sound scattering. The interactive nature of these visualisations enables users to explore the data from different perspectives and use animated content to display how sound properties change over time. Lastly, the visualisations are available in absolute and relative modes. Even though the first mode visualises the absolute mathematical results of the selected acoustical descriptor, the latter normalises the results based on a reference flat surface. This mode makes comparative studies easier for users with limited knowledge of acoustics since the data are presented in comparison to a familiar flat surface.

7.1.4 Data-driven acoustic design

A novel approach to acoustically performance-driven design of sound-diffusing wall surfaces was introduced. The computational workflow allows architects and designers to explore alternative wall designs, given a set of desired acoustic performance criteria. The design tool uses unsupervised machine learning and data clustering techniques[2] to analyse and arrange the GIR Dataset. To allow architects and acousticians with no programming knowledge to explore the dataset, all the visualisations are made available through an online web-based application. Users can filter surfaces based on typology, explore a 3D view of their geometry, and access associated metadata such as measuring date, printer model, binder type, temperature, atmospheric

2: Principal component analysis, Self-organising maps

pressure, and more. By selecting a source and receiver combination, the application visualises all available acoustic descriptors. The website is publicly accessible at `www.ddad.ethz.ch`.

7.1.5 Computational design of sound diffusive surfaces

A computational tool was developed that generates highly customisable three-dimensional wall-like geometries. It combines macro and microstructures to create unique architectural surfaces. The macrostructure adds low-frequency wave deformations that break the flatness of the surface, while the microstructure adds fine geometrical features that resemble common architectural materials and construction techniques. The tool includes functions to generate various types of stone and brick walls, concrete walls, and surfaces with primitive shapes. The tool is fully parametric, allowing the user to adjust various geometrical properties such as stone type, surface roughness, brick dimensions, mortar height and depth, and more. Additionally, the tool outputs a ready-to-3D-print file that combines two surfaces in one three-dimensional mesh, reducing material use and printing time. The tool is open-sourced and available for download at `github.com/gramaziokohler/sdsc_data_driven_acoustic_design`.

7.2 Discussion

This research investigated the spatiotemporal relationship between geometry and reflected sound using data-science methods and ML applications, focusing on early reflections and sound diffusion. The lack of a dataset containing geometrical and acoustical data was seen as an opportunity to define the relevant data, its collection, post-processing, and use within ML applications targeting architectural design. Two topics are discussed in the following sections, the collected dataset and acquisition setup and the usability of the developed visualisations and design workflows.

7.2.1 Dataset - Acquisition setup

The generated dataset is the foundation for ML algorithms to develop efficient, easy-to-use design and analysis tools with reasonable precision. The dataset contains only first-reflection acoustical information. Although this is not sufficient for a room acoustics analysis, it provides much information for the direction, amplitude, frequency response, and more of the reflected sound. This information is beneficial for designing and optimising sound diffusers. Additionally, it can be utilised as a library of surfaces and their associated

acoustic characteristics. The geometrical data are organised in typologies that resemble commonly used architectural materials and construction techniques. Designing a dataset around these commonly used materials and construction techniques increases the likelihood of the data being used in an architectural context. The dataset is open-source; therefore, anyone can extend it by contributing to it if more surfaces or typologies are needed. This can be achieved by physically reproducing the data-acquisition setup described in chapters 2 and 3 or digitally reproducing its conditions within a numerical, wave-based simulation[3]. Measuring the impulse responses at three different distances from the surface captures the evolution of the reflected wavefront over space and time. Having spatial information on the sound propagation gives information not only on the far field but also on the near-field behaviour of a surface. Such spatiotemporal investigation is not possible with a measurement method based on the ISO 17497 standard [64, 120]. That method, even though it captures the reflected sound from multiple angles around a surface, it does it from a single fixed distance. The implication of not following the ISO standard is that the absorption, scattering, and diffusion coefficients can not be properly computed. Nevertheless, computational methods have been developed to translate the captured data to ISO-equivalent absorption and scattering coefficients (see chapters D and F). Calculating the diffusion coefficient requires the surface's polar response. Although a portion of the polar response can be computed, it is insufficient to develop a method that translates the captured data to an AES-4id-2001 [89] equivalent diffusion coefficient with acceptable accuracy.

3: Finite Element Method (FEM), Boundary Element Method (BEM), FDTD

The design of the dataset and the data-acquisition setup makes it possible to collect acoustical data from surfaces with heterogeneous textures. The three-dimensional measuring allows the collection of IRs not only at a global surface level but also from a focused, localised part of the surface. This made it possible to combine multiple geometrical textures on a single surface. Working with the hypothesis that ML models could learn these features and extract their geometrical information will allow testing and predicting how gradient geometrical transitions and alternations between diffusive and absorptive areas on the same surface affect the reflected sound. These are essential design questions from an architectural perspective because they investigate the extent of architectural expression in an acoustically informed design, but these ML models are still under development.

The GIR Dataset stores the raw data captured with the data acquisition setup. The only post-processing applied to the data is a time-window of around $4ms$[4] which filters out unwanted reflections from the room (see chapters 2 and 3). The decision to store the raw data was twofold. First, it allows other researchers to apply different post-processing methods directly to the raw data. Second, there is always a possibility for errors or mistakes in a code.

4: 400 samples at a 96kHz sampling rate.

By storing the processed data, these errors would have been permanently embedded in the dataset.

7.2.2 Usability

The GIR Dataset is large and high-dimensional; therefore, highly complex to explore with conventional data analysis and visualisation methods. To make the data easily available, computational tools were developed to process the data and compute simple-to-understand acoustic descriptors. Additionally, interactive visualisation methods enable users to display and explore high-dimensional data, and lastly, dimensionality reduction techniques allow users to filter out and organise the surfaces based on acoustic characteristics. The usability of the developed computational pipeline, design workflow, and web application are discussed below.

Computational pipeline

The developed pipeline handles all computational needs from data retrieval, data processing, and data visualisation. First, given a surface name[5], the data-retrieval part provides several methods to get the correct measurement data from the dataset. The data of a single measurement can be returned given a source-receiver combination[6] or a combination number[7]. For multiple measurements, other methods return the data of an entire measurement-grid layer or all the combinations of a single source position. Second, the data-processing part handles data sanitation and data conversion. The data-sanitation part cleans up the recording by removing the direct sound, and the data-conversion part computes all the acoustical descriptors. Lastly, the data visualisation ensures that all the acoustical descriptors are properly displayed using two or three-dimensional interactive visualisations. These visualisations address the needs of both expert and non-expert users of acoustics. Experts can use standard and familiar acoustic descriptors and visualisations, while non-experts are presented with a range of newly proposed and simplified descriptors and visualisations. This approach allows for a more inclusive design process, where different design team members can contribute their expertise to the acoustics analysis. The intuitive layout of the visualisations and the interactivity provided in the high-dimensional visualisations make the workflow more accessible, improving communication among the design team. Including surface geometry in the visualisations allows for a deeper analysis of the relationship between geometry and sound. Overlaying the acoustical data onto the geometry enables users to couple geometrical characteristics with certain acoustical responses. Furthermore, it helps architects and acousticians to understand how different design

5: `panel_name` in the code

6: The source and receiver positions are given based on their measurement grid coordinates (z,x,y).

7: A number between 1 and 2951.

decisions affect the acoustic response and make informed design choices. Currently, the computational pipeline is set to work with the data structure of the GIR Dataset. However, the code's architecture, and it being open-source, allows adjusting and extending it to accommodate different data structures from other datasets.

Design Workflow

The design workflow presented in chapter 5 combines several computational tools developed in this research to introduce an alternative method for including acoustics as a performance driver in architectural design. It evaluates all or a subset of surfaces based on desired acoustic performance criteria set by the user to filter and organise all surfaces on an easily readable two-dimensional map. The process can be a single-criterion or multi-criterion evaluation.

The output of this workflow is a single surface or a set of them that match the desired criteria. Although it outputs existing surfaces from the dataset and does not generate new ones, its computational speed allows for bespoke multi-criterion searches containing arrays of acoustic descriptor values at multiple receiver positions.

This workflow does not substitute room acoustics simulations, which are still required to study the sound field inside the designed space. Nevertheless, the architectural design process does not always include acousticians. In those cases, the proposed workflow still improves the acoustic quality of the design by enabling architects to make informed decisions that influence early reflections. These reflections significantly affect how sound is perceived in the listening position as directional aspects and the degree of diffusivity are most relevant in early reflections. Furthermore, strong early reflections can cause image shifts and sound colouration. [7, 44, 45].

When acousticians are involved in the design process, the developed workflow is still valuable and beneficial because acousticians are presented with an acoustically better starting point by the architects. When an accurate acoustics evaluation is needed, GA simulation software can be used. Even though the acoustic descriptors developed in this research cannot be directly used with GA software, the computational pipeline offers methods to translate the GIR Dataset's descriptors into data usable by GA simulation software. Appendix D describes these translation methods that compute ISO-equivalent absorption and scattering coefficients.

Web application

Using or extending the computational pipeline and the design workflows presented in this thesis requires programming knowledge in Python. The developed web-based application described in Chapter 6 addresses this usability limitation by enabling users with no prior knowledge of programming to use the GIR Dataset as a library of architectural wall-like surfaces with sound-diffusive properties. The interface provides an overview of all available surfaces, pre-filtered based on their typology, an interactive three-dimensional view of the surface, metadata, and the visualisations of all available acoustic descriptors. By increasing the accessibility of this research, exploring and studying sound diffusion becomes easier to integrate into an architectural design workflow and in the educational curriculum of architectural studies.

7.2.3 Machine Learning applications

One of the goals of this dissertation is to aid research in sound diffusion by enabling the development of ML applications. Chapter 2.3 describes such an application that predicts a surface's acoustic properties. Even though, in that case, the property is the TNCE value, any other acoustic descriptor that derives from an IR can be predicted.

Predicting acoustical properties is not the only useful ML application for the GIR Dataset. Measuring or simulating an IR is a time-consuming and computationally expensive process. Furthermore, the auralisation of dynamic virtual environments with a moving listener or moving sources and possibly changing geometries is still challenging. Although a plausible but not physically correct auralisation can be achieved in real-time, several approximations must be made [78]. Alternatively, one could extrapolate the IR corresponding to the desired position in real-time by using existing surrounding IRs. These existing IRs can be pre-recorded or simulated in advance. The benefit of this method is the significantly smaller number of IRs that need to be pre-recorded or simulated in advance. A case study that acted as a feasibility study can be found in Appendix C.1.

The GIR Dataset dataset and the computational framework developed in this research can be used to create ML models to reconstruct or generate surfaces from acoustic data. Such models can then be used as generative design tools for designing and optimising sound-diffusive surfaces. The input criterion can be a desired IR, a scattering or absorption coefficient, a sound energy value, or any acoustic descriptor that can derive from an IR. Appendix C.2 describes such a classification model where the surface or its typology can be identified given a single IR as an input.

7.3 Outlook

Existing data-acquisitions methods have certain limitations. Even though developing a new method can address these limitations, it is crucial to ensure that it is compatible with established and widely used methods to facilitate its adoption. This can be done by providing data translation options between the new and existing data-acquisition methods, ensuring future compatibility. Additionally, comparing the new method to the standards could also provide an accuracy validation for the new method and a quality benchmark for the collected data. As a future recommendation, the developed data acquisition method and the structure of the GIR Dataset should be extended to also include measurements according to the ISO 17497 standard[64, 120].

User testing and feedback are needed to further facilitate the adoption of such computational and design workflows. This feedback can be used to identify usability or workflow issues which will guide required adjustments. Additionally, it can provide valuable insights into how users employ the workflow, leading to more informed decisions about future development and design.

This research provides access to object-oriented computational tools, enabling complete customisation of the computational workflow based on user needs. Providing the choice for a graphical programming interface would be an advantage; users without coding skills would have access to the entire computational pipeline. A start has been made to translate the Data-Driven Acoustic Design (DDAD) code to a Grasshopper plugin for Rhino3D[121]. This will enable users to develop bespoke workflows. Currently, the DDAD code is heavily linked to the GIR Dataset. Several computational tools and visualisations are developed to accept and work with the data structure of the GIR Dataset. Nevertheless, several of the tools and visualisations could easily be generalised and decoupled from it. These generalised computational tools could be up-streamed as a Python library to the COMPAS framework[122]. COMPAS is an open-source framework for research and collaboration in Architecture, Engineering, Fabrication, and Construction. Distributing the code through the COMPAS framework will make it more visible, increasing its usage and impact.

This research investigated only a fraction of potential ML applications for the GIR Dataset. Based on the promising results of the ML model described in Appendix C.2, one could develop a ML model that generates new geometries based on desired acoustic properties. Form-finding design studies can couple the geometrical output of this model with optimisation algorithms to design new acoustically performative surfaces.

The three ML applications demonstrated in this dissertation (see chapter 2.3, and Appendix C.1 and C.2) could be combined to develop a hybrid ray-tracing room acoustics simulation. The simulation will be able to classify the surfaces inside the model, interpolate the source position to match the direction of the incident sound, and finally predict the direction and amplitude of the reflected sound. A lower accuracy compared to existing GA simulations is expected from such an application, but the very short computational time will make it a valuable exploratory design tool.

7.4 Last remarks

As a last remark, new datasets, computational tools, and design workflows are promising steps towards making acoustic design more accessible to architects. Nevertheless, these tools on their own are not enough and should be complemented within the education of future generations of architects. These potential educational methods and curricula should not mimic the ones from electrical engineering or physics. Architects cannot and should not become expert acousticians but should become aware of the importance of acoustics and build a vocabulary allowing them to include acoustics as a design driver.

Appendix

A Paper A

A.1 Dataset content

At the time of publication, the dataset is composed of 312 samples, and each sample contains the following metadata:

- A `3D Mesh` geometry saved as an *.obj* file
- 2951 IRs in a 2951×400 *float32* matrix, saved in an *.npz* file.
- A metadata file saves as a *.json* file. The content of this file is outlined in Table A.1.

Table A.1: The content of the metadata file.

Variable	Data type	Description
panel_id	`string`	The ID of the panel
start_time	`string`	The date and time the measuring process started in `ISO 8601` format, `YYYY-MM-DDTHH:MM:SS.mmmmmm`
end_time	`string`	The date and time the measuring process ended in `ISO 8601` format, `YYYY-MM-DDTHH:MM:SS.mmmmmm`
package_time	`string`	The date and time all recordings were processed and stored in `ISO 8601` format, `YYYY-MM-DDTHH:MM:SS.mmmmmm`
impulse_responses_file	`string`	The name of the *.npz* file containing all IRs
geometry_file	`string`	The name of the *.obj* file containing the panel geometry
recording_sample_rate	`integer`	The sample rate of the recording in `Hz/sec`
reference_resampling_temperature	`integer`	The temperature in `Celsius` that was used to resample the IRs
print_provider	`string`	The name of the printing service
print_machine	`string`	The name of the printer
print_sand_type	`string`	The type of sand used in the 3D printer
print_binder_type	`string`	The type of binder used in the 3D printer
microphone_model	`string`	The model of the microphone use in the recording
typology	`string`	The typology of the panel
macrostructure	`string`	The macrostructure that was used to generate the panel's geometry. It corresponds to the `panel_id` of a panel that was created using only that macrostructure. When `flat`, no macrostructure was used
measurements		extra metadata info for each of the 2951 measurements
combination	`integer`	The microphone-speaker combination number. It starts from 1 and goes up to 2952
fluid_pressure	`float`	Air pressure inside the room in `Pa`
relative_humidity	`float`	Air humidity inside the room in `%`
sound_level	`float`	The sound level outside the room in `dB`
temperature	`float`	The temperature inside the room in `C`
distance	`float`	The distance between microphone and speaker frame in `mm`
end_time	`string`	The date and time of the successful recording in `ISO 8601` format, `YYYY-MM-DDTHH:MM:SS.mmmmmm`

Table A.2: Testing sets.

Testing set	Panel names			
Random	panel_0001_1,	panel_0009_1,	panel_0010_0,	panel_0011_1,
	panel_0014_1,	panel_0021_1,	panel_0023_1,	panel_0024_1,
	panel_0049_1,	panel_0054_1,	panel_0058_1,	panel_0066_0,
	panel_0071_0,	panel_0073_0,	panel_0085_1,	panel_0087_1,
	panel_0089_0,	panel_0090_1,	panel_0094_0	
Micro-Macro	panel_0099_0,	panel_0105_0,	panel_0105_1,	panel_0016_1,
	panel_0064_0,	panel_0064_1,	panel_0065_0,	panel_0066_0,
	panel_0066_1,	panel_0070_1,	panel_0071_0,	panel_0072_0,
	panel_0072_1,	panel_0013_0,	panel_0013_1,	panel_0036_1
Brick-Printer-VJ	panel_0101_1,	panel_0107_1,	panel_0092_0,	panel_0092_1,
	panel_0089_0,	panel_0072_1,	panel_0108_1,	panel_0070_0,
	panel_0091_0,	panel_0095_1,	panel_0090_0,	panel_0093_1,
	panel_0107_0,	panel_0094_0,	panel_0072_0,	panel_0094_1,
	panel_0096_1,	panel_0071_0,	panel_0090_1,	panel_0070_1,
	panel_0071_1,	panel_0105_0,	panel_0095_0,	panel_0089_1,
	panel_0096_0,	panel_0108_0,	panel_0101_0,	panel_0091_1,
	panel_0093_0,	panel_0105_1		
Brick-Printer-CG	panel_0036_0,	panel_0037_1,	panel_0043_1,	panel_0044_0,
	panel_0046_1,	panel_0049_0,	panel_0049_1,	panel_0051_0,
	panel_0053_0,	panel_0054_1,	panel_0055_1,	panel_0056_0,
	panel_0057_0,	panel_0057_1,	panel_0058_1,	panel_0061_0,
	panel_0063_1,	panel_0066_1,	panel_0068_0,	panel_0068_1
Extrusion	panel_0056_0,	panel_0056_1,	panel_0106_0,	panel_0106_1,
	panel_0107_0,	panel_0107_1,	panel_0108_0,	panel_0108_1
Macro	panel_0015_1,	panel_0015_0,	panel_0031_0,	panel_0031_1,
	panel_0083_0,	panel_0083_1		

A.2 Testing set details

In the following table, we list the panels we selected for each testing set. The entire list of panels is available through the code.

A.3 Panel diffusivity

To evaluate the diffusivity of each panel in the dataset, we can look at the amount of reflected energy. A flat reflector produces a specular reflection, redirecting most of the energy to a specific narrow direction. A highly diffusive surface redirects the energy at a large solid angle. Similar to [43], by comparing the two energy values, we can calculate how much energy was not reflected specularly. Table A.3 shows the mean reflected energy values of each typology compared to a flat surface. If close to 1, the panels perform similarly to a flat reflector (high specular reflections). If close to 0, the panel diffuses or absorbs all the energy. Indeed, the Primitive root diffuser (panel_id: *baseline_qrd_400_4000*) that was designed to diffuse frequencies between 400Hz and 4000Hz has values very close to 0.

Typology		200Hz	500Hz	1kHz	2kHz	4kHz	Total
Stretcher bond bricks	mean	0.82	0.77	0.66	0.59	0.68	0.68
Flemish bond bricks	mean	0.83	0.80	0.65	0.51	0.59	0.65
IDL	mean	0.61	0.45	0.46	0.37	0.50	0.47
Polygonal rubble stones	mean	0.61	0.50	0.46	0.46	0.49	0.49
Coursed ashlar stones	mean	0.64	0.53	0.43	0.36	0.39	0.45
Primitives	mean	0.87	0.78	0.62	0.52	0.59	0.65
Macrostructure	mean	0.83	0.84	0.71	0.71	0.76	0.77
Primitive root diffuser		0.15	0.06	0.03	0.06	0.09	0.07
Reference Flat		1.00	1.00	1.00	1.00	1.00	1.00
Reference Foam		0.00	0.00	0.00	0.00	0.00	0.00

Table A.3: Specular reflection factors

A.4 Extra information

A.5 Dataset documentation and intended uses

GIR Dataset is intended for research in computational acoustics and, in particular, the studies of the relationship between geometry and diffusion. We describe the data organisation and provide rich metadata with contextual documentation. With the *Renku* platform[1], we automatically capture the lineage and metadata. The latter is further enriched with the additional attributes recommended in the framework dataset nutrition labels[2] and Schema.org note on data and datasets[3]. This enriched metadata is provided in a standard *JSON-LD* format on *Renku*[4] and on *Zenodo* as part of the published dataset.

1: `https://renkulab.io/`

2: `https://arxiv.org/abs/1805.03677`

3: `https://schema.org/docs/data-and-datasets.html`

4: `https://renkulab.io/projects/ddad/gir-dataset/files/blob/dataset.json`

A.6 Links to access the dataset, its metadata, and the code

We provide open and easy access to the *GIR dataset* through two publicly available resources: *Zenodo*: `doi.org/10.5281/zenodo.5288743` and *Renku*: `renkulab.io/projects/ddad/gir-dataset/datasets/gir/`. Both *Zenodo* and *Renku* provide unrestricted access to the dataset without the need for authentication, including a free interactive computational environment to explore the dataset directly on the *Renku* platform `https://renkulab.io/projects/ddad/gir-dataset/sessions/new`. The code and the instructions needed to reproduce the main experimental results are available on *RenkuLab* in the `https://renkulab.io/projects/ddad/gir-dataset` repository.

A.7 Author statement

The dataset and all the code can be downloaded freely for research purposes. The dataset is released under the GNU General Public License v3.0: `https://renkulab.io/projects/ddad/gir-dataset/files/blob/LICENSE`. The authors bear all responsibility in case of violation of rights regarding the created dataset.

A.8 Hosting, licensing, and maintenance plan

To guarantee data access and retention we opted for two publicly available resources: *Zenodo* and *Renku*, with *Zenodo* ensuring the long-term preservation of data and *Renku* providing the long-term availability of the code. The integration of *Renku* with *Zenodo* streamlines data maintenance by automating the export of new data releases along with the lineage and rich metadata automatically captured on *Renku*.

A.8.1 Ensuring accessibility

To ensure that the *GIR dataset* can be easily found and accessed, we use *Zenodo* to assign a persistent unique Digital Object Identifier (DOI) and index metadata enriched with descriptions, keywords, and author information at *Zenodo* and *DataCite* servers. *Zenodo* guarantees a 20-year retention period and implements the DCAT metadata standard. We further enhance the accessibility of the *GIR dataset* with the *Renku* platform, where data can be accessed through a curated reproducible run time environment. Metadata captured on *Renku* follow *Schema.org* standards. Files constituting the dataset are in standard, widely accepted formats and documented in the metadata.

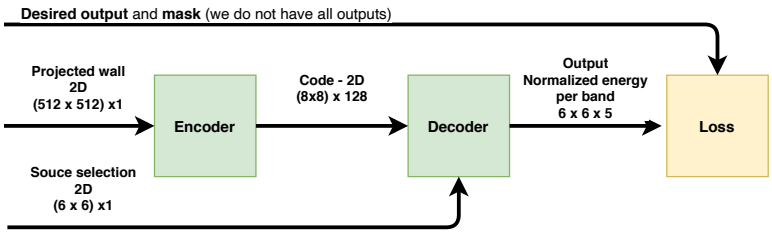

Figure A.1: General structure of the network. The network is made of an encoder that transforms the input wall (a 512×512 image) into a code ($8 \times 8 \times 128$). The decoder takes the code as well as the source position and produces the energy level for the 5 bands and the 6 receiver positions.

A.8.2 Network architecture details

Figure A.1 describes the overall architecture of the NN used to predict acoustic properties from a geometry. The NN takes as inputs a 512×512 image (the 2D projection of the geometry) as well as the position of the source in the form of a 6×6 matrix (zero everywhere except for the source position). The NN outputs a $6 \times 6 \times 5 = 36 \times 5$ tensor consisting of the reflected energy in 5 frequency bands for the $6 \times 6 = 36$ receiver positions. As some source-receiver positions are not measured, we apply a mask before computing the loss. The NN is composed of an encoder and a decoder. The encoder embeds the wall geometry into a space of size $6 \times 6 \times 128$. It is a conventional 6 layer Convolutional Neural Network (CNN) with leaky ReLu non-linearity (See Table A.5). The decoder is made of three different blocks. First, the resampling block is a learned linear layer with a weight matrix of size $8^2 \times 6^2$ (See Table A.4). The same function is applied for all 128 channels. Second, a three-layer CNN transforms the source position into a positional encoding that is multiplied by the resampled code. Finally, a three-layer CNN decodes the result into the energy per band. The parameters of the decoder are given in Table A.6.

Layer	Operation	Activation	Dimension
Input code c			$b \times 8 \times 8 \times 128$
d_0	Reshape		$b \cdot 128 \times 64$
d_1	Linear (64×36)		$b \cdot 128 \times 36$
d_2	Reshape		$b \times 6 \times 6 \times 128$
Resampled code c'			$b \times 6 \times 6 \times 128$

Table A.4: Resampler.

Layer	Operation	Activation	Dimension
Input image$X$			$b \times 512 \times 512 \times 1$
h_0	Conv($k = 5 \times 5, s = 2$)	LeakyRelu	$b \times 256 \times 256 \times 8$
h_1	Conv($k = 5 \times 5, s = 2$)	LeakyRelu	$b \times 128 \times 128 \times 16$
h_2	Conv($k = 5 \times 5, s = 2$)	LeakyRelu	$b \times 64 \times 64 \times 32$
h_3	Conv($k = 5 \times 5, s = 2$)	LeakyRelu	$b \times 32 \times 32 \times 64$
h_4	Conv($k = 3 \times 3, s = 2$)	LeakyRelu	$b \times 16 \times 16 \times 128$
h_5	Conv($k = 3 \times 3, s = 2$)	LeakyRelu	$b \times 8 \times 8 \times 128$
Output code c			$b \times 8 \times 8 \times 128$

Table A.5: Encoder for acoustic property prediction. Here b is the batch size, k the convolutional kernel size and s the stride. The number of filters (convolution layer) is shown in blue. The LeakyRelu activation uses the parameter $\alpha = 0.2$.

Table A.6: Decoder for acoustic property prediction. Here b is the batch size, k the convolutional kernel size and s the stride. The number of filters (convolution layer) is shown in blue. The LeakyRelu activation uses the parameter $\alpha = 0.2$.

Layer	Operation	Activation	Dimension
Source position s			$b \times 6 \times 6 \times 1$
d_3	Conv ($k = 5 \times 5$, $s = 1$)	LeakyRelu	$b \times 6 \times 6 \times 128$
d_4	Conv ($k = 5 \times 5$, $s = 1$)	LeakyRelu	$b \times 6 \times 6 \times 128$
d_5	Conv ($k = 5 \times 5$, $s = 1$)	LeakyRelu	$b \times 6 \times 6 \times 128$
d_6	Multiply with c'		$b \times 6 \times 6 \times 128$
d_7	Conv ($k = 3 \times 3$, $s = 1$)	LeakyRelu	$b \times 6 \times 6 \times 128$
d_8	Conv ($k = 3 \times 3$, $s = 1$)	LeakyRelu	$b \times 6 \times 6 \times 256$
d_9	Conv ($k = 3 \times 3$, $s = 1$)	LeakyRelu	$b \times 6 \times 6 \times 5$
Predictions			$b \times 6 \times 6 \times 5$

B Paper B

B.1 Impulse response post-processing details

The post-processing of the impulse response consists of the following three steps, which are illustrated in Figures 3.5, 3.6, and 3.7.

B.1.1 Deconvolution

The deconvolution operation is carried out using a simple division in the Fourier domain. Given $\hat{x} = Fx$ the Fourier transform of x and $x = F^{-1}\hat{x}$ its inverse operation, the deconvolution of the signal x with the sweep s is given by

$$x_d = F^{-1}\left(Fx/Fs\right) \tag{B.1}$$

where s is the sweep, and the division is performed element-wise. Note that Fs is never close to 0 because the sweep contains all frequencies.

B.1.2 Temperature correction

To adjust for the room temperature change, we estimate the speed of sound at temperature T (in $°C$)

$$c = c_0\sqrt{1 + (T/273.15)} \tag{B.2}$$

where c_0 is the temperature at $0°C$ [86]. The impulse response is then resampled at the frequency

$$\frac{c}{c_{ref} f_s} \tag{B.3}$$

where c_{ref} is the speed of sound at $20°C$ and $f_s = 96kHz$ the sampling frequency. We use the polyphase filtering method (`resample_poly`) from the `SciPy` python package.

B.1.3 Removal of direct sound

The direct sound removal is performed by subtracting the impulse response of the absence of a wall (an absorbent foam inserted instead of the panel; see Table 3.1, *Foam*).

C Machine Learning Applications

C.1 Impulse response interpolation model

Given 4 IRs in a specific position, this model aims to infer the IRs of 5 new positions. The model takes as an input (I) 4 receiver positions and a single source position (S) and outputs the IR of 5 new receiver positions (O) seen in Figure C.1. This method results in 144 samples per panel for a total dataset size of $144 \times 268 = 38592$[1]. For the validation set, a random selection of 10 panels is made (1440 samples).

1: The testing set is the same as the one defined in chapter 2.3.

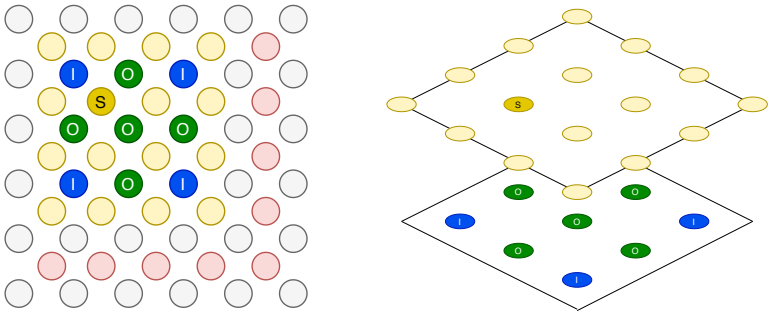

Figure C.1: Source-receiver positions for the interpolation experiment. Left: top view. Right: isometric view. On the top level, a single source is selected among the yellow positions (red positions are not allowed). On the bottom level, the blue dots correspond to the 4 input receiver positions and the 5 green dots to the output receiver positions.

C.1.1 Neural Network architecture

Since the 4 inputs and the 5 outputs are IRs in the form of a time series, a one-dimensional convolutional encoder/decoder architecture is chosen. The encoder contains three convolutional layers with a stride of 2, `BatchNorm` [123] and `LeakyRelu` [124] activation functions. At the end of the encoder, we add a linear layer with 512 neurons. The decoder is the reversed architecture where the convolution is replaced with deconvolution. The network size[2] was gradually increased until the network would not increase in performance anymore. Table C.1 describes the NN's architecture, essentially a convolutions encoder-decoder architecture.

2: number of convolutions/neurons per layer and number of layers

Table C.1: Encoder-decoder architecture. Here b is the batch size, k the convolutional kernel size and s the stride. The number of filters (convolution layer) and the number of neurons (linear layers) are shown in blue. The `LeakyRelu` activation uses the parameter $\alpha = 0.2$.

Layer	Operation	Activation	Dimension
X			$b \times 256 \times 4$
h_0	Conv ($k = 11, s = 1$)	BatchNorm / LeakyRelu	$b \times 256 \times 16$
h_1	Conv ($k = 11, s = 2$)	BatchNorm /LeakyRelu	$b \times 128 \times 32$
h_2	Conv ($k = 11, s = 2$)	BatchNorm /LeakyRelu	$b \times 64 \times 64$
h_3	Reshape		$b \times 4096$
h_4	Linear	LeakyRelu	$b \times 512$
h_5	Linear	LeakyRelu	$b \times 4096$
h_6	Reshape		$b \times 64 \times 64$
h_7	Deconv ($k = 11, s = 2$)	BatchNorm /LeakyRelu	$b \times 128 \times 64$
h_8	Deconv ($k = 11, s = 2$)	BatchNorm /LeakyRelu	$b \times 256 \times 32$
h_9	Deconv ($k = 11, s = 1$)	BatchNorm / LeakyRelu	$b \times 256 \times 5$

C.1.2 Optimisation parameters

We train the network using an Adam optimiser (learning rate of $5e-4, \beta_1 = 0.95, \beta_2 = 0.999$ [68]) for 200 epochs with a batch size of 32. To find the best model, we randomly selected 10% of the training set for validation, computed the validation error at the end of each epoch and selected the model with the lowest validation error. To account for the randomisation error and to obtain an estimate of performance variance, we repeated the experiment 5 times with a different validation set for each repetition.

Results

Table C.2 reports the Mean Square Errors (MSEs) for the interpolation problem on the different testing sets presented in chapter 2.3. The outputs (IRs) have been normalised with a zero mean and unit variance over the full dataset. In this setting, the testing set variance corresponds to the MSE of a predictor predicting the mean (i.e. 0). For a human-friendly measure of the performance, the coefficient of determination is also computed:

$$R^2 = 1 - \frac{\text{MS}(Y_{\text{pred}})}{\text{MSE}(Y_{\text{test}})} \tag{C.1}$$

MS signifies *Mean Square* and is equivalent to the variance since Y_{test} has a zero mean[3]. R^2 represents the ratio of variance captured by the network[4]. There is an important variation of this coefficient depending on the testing set (between 0.37 and 0.64), signifying that some panels or testing sets are significantly harder to predict than others. From an ML perspective, these performance differences are explained by the various distribution shifts between the testing and the training/validation sets. Comparing the training and the validation MSEs, one can estimate how much of the error is caused by overfitting. The rest of the error can likely be associated with the various distribution shifts. The large variation of error can also be observed directly

3: IRs always have a zero mean.

4: 0 is equivalent to predicting the mean, and 1 is a perfect prediction

Testing set	Testing set mean square	Testing MSE	Testing R^2	Validation MSE	Training MSE
Random	0.82	0.47 ± 0.00	0.43	0.40 ± 0.11	0.10 ± 0.00
Micro-Macro	0.92	0.43 ± 0.01	0.53	0.37 ± 0.05	0.11 ± 0.00
Brick-Printer-VJ	1.04	0.66 ± 0.00	0.37	0.39 ± 0.10	0.10 ± 0.00
Brick-Printer-CG	0.79	0.28 ± 0.00	0.64	0.40 ± 0.04	0.11 ± 0.00
Extrusion	0.87	0.34 ± 0.01	0.61	0.44 ± 0.13	0.11 ± 0.00
Macro	1.19	0.69 ± 0.01	0.42	0.34 ± 0.05	0.08 ± 0.00

Table C.2: IR interpolation results. The output has been normalised with a variance of 1 over the full dataset. As all IRs have a mean of 0, the testing set variance/mean square correspond to the MSE of a predictor predicting 0.

by looking at the IRs. In Figure C.2, the prediction almost perfectly matches the measurement. In this case, we can conclude that there would be no audible difference between the measured and predicted reflection patterns. In Figure C.3, the prediction underestimates the positive peak and loses some of the fine structure in the negative peak. Finally, in Figure C.4, the prediction cannot trace the IR details. As a consequence of the significant local variation, the prediction seems to average out the oscillating curve. This is comparable to a low-pass filtering process that attenuates the high frequencies.

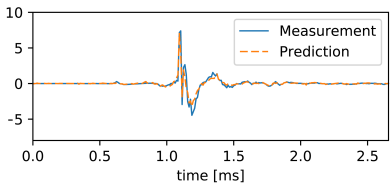

Figure C.2: IR interpolation results for receiver-source combination (0,4,3)-(1,2,4) from `panel_-0011_1`.

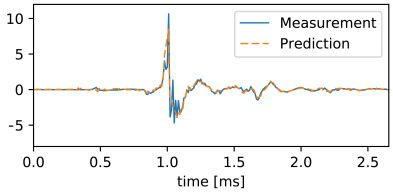

Figure C.3: IR interpolation results for receiver-source combination (0,1,3)-(1,2,2) from `panel_-0011_1`.

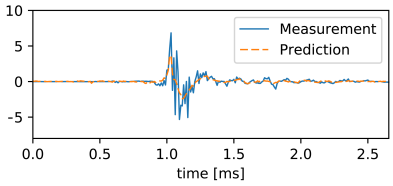

Figure C.4: IR interpolation results for receiver-source combination (0,2,4)-(1,3,2) from `panel_-0089_0`.

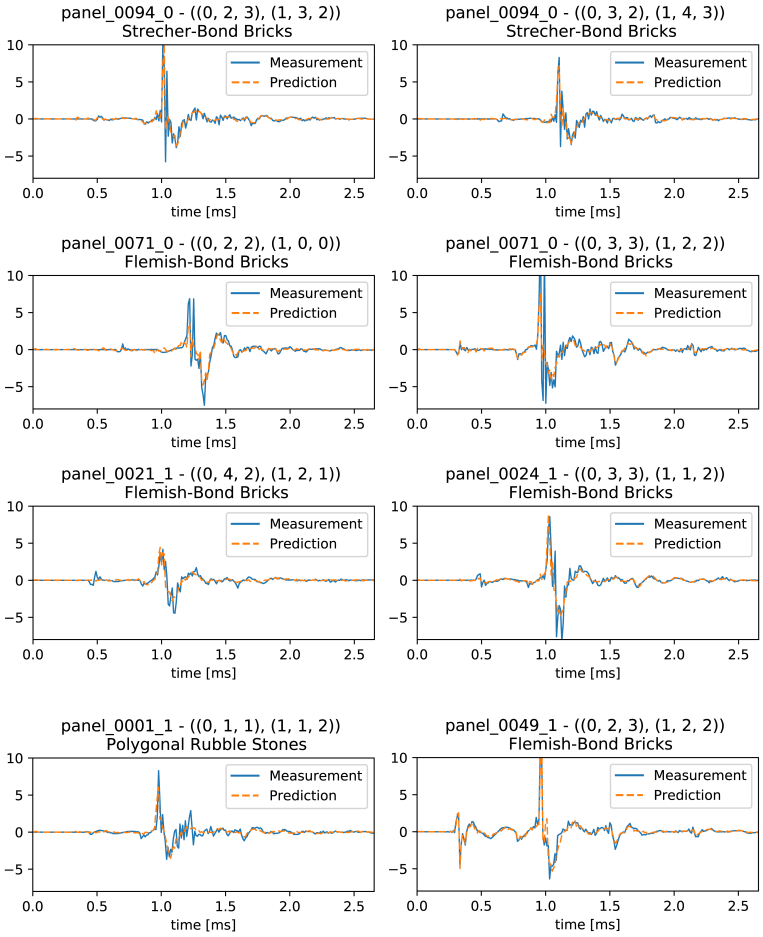

Figure C.5: IR interpolation results for various panels and source-receiver positions.

C.2 Geometry reconstruction model

This can be seen as a classification problem, where given a single IR as an input, the surface or typology can be identified. For this model, each typology is a class (8 classes), each surface is also a class (268 classes), and each IR forms a sample (790868 samples[5]). The same testing set is used as the one described in chapter 2.3. It is interesting to investigate how many IRs are necessary to correctly classify a surface or a typology. For this reason, different training set sizes are formed, from 50 to 2800 IRs per surface. The validation set contains 10 IRs per surface, and the testing set all the remaining IRs. Furthermore, two different types of IR selection for the testing sets are investigated; First, *random*, where the IRs assignment to either the testing or the training set is entirely random, and second, *position*, where the IRs used in the testing set are not present in the training set.

5: 268 classes × 2951 IR per surface = 790868 samples.

C.2.1 NN architecture and training information.

As the input is a time series, a traditional 1D CNN is proposed. It contains 4 convolutional layers with a stride of 2, `BatchNorm` [123], and `LeakyRelu` [124] activation functions. A final linear layer is added that outputs the correct number of classes. The network size (the number of convolutions and the number of layers) was gradually increased until the network would not increase in performance anymore. Table C.3 shows the parameters for the geometrical classifier with the IR as input, consisting of a simple convolutional architecture. The same optimisation parameters are used as the ones in the IR interpolation model in Appendix C.1.

Layer	Operation	Activation	Dimension
X			$b \times 400 \times 1$
h_0	conv ($k = 11, s = 2$)	BatchNorm/LeakyRelu	$b \times 200 \times 64$
h_1	conv ($k = 11, s = 2$)	BatchNorm/LeakyRelu	$b \times 100 \times 128$
h_2	conv ($k = 11, s = 2$)	BatchNorm/LeakyRelu	$b \times 50 \times 256$
h_3	conv ($k = 11, s = 2$)	BatchNorm/LeakyRelu	$b \times 25 \times 16$
h_4	reshape		$b \times 400$
h_5	linear	linear	$b \times c$

Table C.3: Architecture of the classifier. Here b is the batch size, k the convolutional kernel size and s the stride. The number of filters (convolution layer) and the number of neurons (linear layers) are shown in blue. The `LeakyRelu` activation uses the parameter $\alpha = 0.2$. c is the number of classes which is 268 for surface classification and 8 for typology classification.

Results

Figure C.6 shows the classification accuracy on the testing set based on the number of IRs per surface. Around 500 IR are needed to correctly identify 60% of the surfaces in the setup. If only the panel's typology is desired, 200

IR provide an accuracy of 80%. These results show that the CNNs can learn the geometrical property of the panel directly from the IRs.

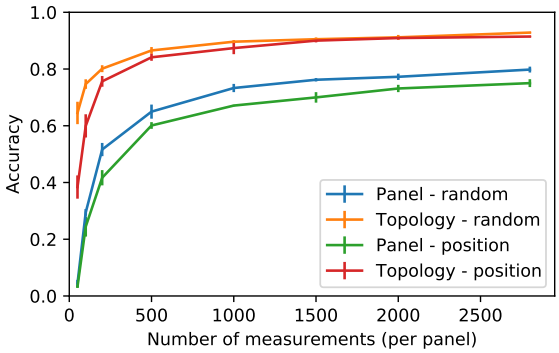

Figure C.6: Classification accuracy compared to the training set size. The reported classification results are averaged over 5 trials corresponding to 5 different (random) testing sets.

D Compatibility with Geometrical Acoustics simulations

Geometrical acoustics simulations are the most common methods to study room acoustics. Even though a direct use of the acoustic descriptors developed in this research cannot be used with GA software, the following method proposes a translation of the GIR Dataset's descriptors into data usable in GA simulation software.

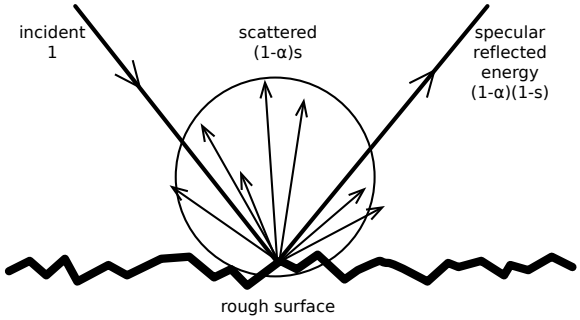

Figure D.1: Sound scattering from a rough surface illustrating the separation of reflected energy into scattered and specular components (After Vorländer and Mommertz [125]).

According to Vorländer and Mommertz [125], the energies[1] seen in Figure D.1 can be expressed as:

1: The energies are normalised with respect to the reflection from a reference flat plane.

$$E_{spec} = (1-\alpha)(1-s) = (1-\alpha_{spec}) \tag{D.1}$$

$$E_{total} = 1-\alpha \tag{D.2}$$

with s being the scattering coefficient, α the absorption coefficient, E_{spec} representing the specularly reflected energy, and E_{total} the total reflected energy. The coefficient α_{spec}, also called the "specular absorption coefficient", is an apparent absorption coefficient, as energy may be scattered away from the specular reflection direction rather than being absorbed by the surface material and converted into non-acoustical energy.

The goal is to obtain the E_{spec}. From equations D.1 and D.2, the scattering

coefficient can be expressed as:

$$s = \frac{\alpha_{spec} - \alpha}{1 - \alpha} = 1 - \frac{E_{spec}}{E_{total}} \tag{D.3}$$

To compute the E_{spec}, we first compute the Complex Reflection Factor (R). The R can be expressed as the sum of a specular and a diffuse component:

$$R = R_{spec} + S \tag{D.4}$$

The specular complex reflection factor is calculated by coherently adding n complex reflection coefficients from different incident angles. Although the energy of the specular component ($|R_{spec}|^2$) adds up coherently, the scattering component (S) does so incoherently. With a large number of measurements, the R_{spec} energy increases proportionally to n^2, and the incoherent S part becomes comparatively significantly smaller. To phase align the IRs, the time of arrival of the reflected sound is computed for each measurement using the `estimated_time_of_arrival` functions from the `Grid` class. This value describes the time it takes for the sound wave to reach the receiver position through the surface. Using this value, the IRs are shifted along the time axis, bringing the start of the pulse at the 0 position. Then the specular reflection factor can be calculated as follows:

$$R_{spec} = \frac{1}{n} \sum_{i=1}^{n} R_i \qquad \text{for } n > 1 \tag{D.5}$$

The specular absorption coefficient can now be calculated using the following:

$$\alpha_{spec} = 1 - |R_{spec}|^2 \tag{D.6}$$

Finally, the scattering coefficient s can be calculated from equation D.3 using the α_{spec} from equation D.6 and the absorption coefficient α of the spray-painted 3D-printed panels (see Flat surface in Appendix E.1).

The specular absorption coefficient α_{spec} can be retrieved by calling the `specular_absorption_coefficient` function from the `PanelData` class and the scattering coefficient s by calling `scattering_coefficient`.

E Reference surfaces

The GIR Dataset includes several reference surfaces (panels) such as Flat[1], Foam[2], and 2D-PRD Diffuser[3]. These surfaces can be used to clean impulse response data and establish reference baselines for data normalisation by the computational pipeline, and they also serve as a common point of comparison in studies. The following sections describe their purpose within the computational pipeline and how they can be used in comparative studies.

1: e.g. `mean_flat_rfl_1`

2: e.g. `mean_foam_1`

3: e.g. `baseline_prd_400_2000`

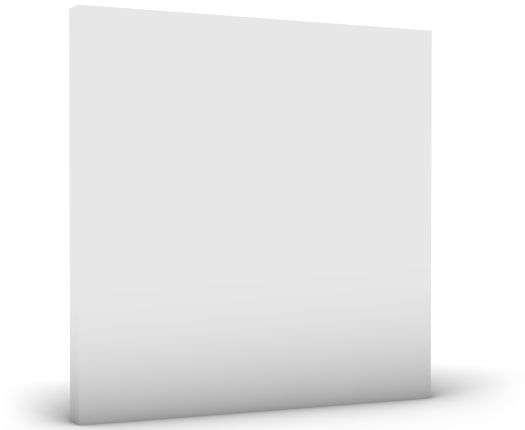

Figure E.1: 3D rendering of a flat panel (e.g `mean_flat_rfl_1`). The foam panel has the same geometry (e.g. `mean_foam_1`).

E.1 Flat surface

The flat surface (see Figure E.1) resembles hard and smooth architectural surfaces like plasterboard and smooth concrete. The values of this surface are used to normalise the values of all other surfaces in the dataset and to act as a baseline for the maximum specularly reflected energy. Three different 3D printers and two different binders were used to produce the panels for the data-acquisition setup (see 2.4.1). Because each printer uses sand with different grain sizes and has different printing quality, four versions of this surface are included in the GIR Dataset. This is done to match the material properties and printing quality of each printer. Each version corresponds to

Table E.1: Specular reflection factors of two reference flat panels compared to a wooden panel.

panel name	specular reflection factors					
	2.5kHz	5kHz	10kHz	20kHz	40kHz	Total
mean_flat_rfl_1	0.85	1.04	0.81	0.95	0.72	0.86
mean_flat_rfl_2	0.90	0.95	0.87	0.90	0.75	0.85
baseline_wood_2	1.00	1.00	1.00	1.00	1.00	1.00

one 3D printer and the binder that was used. The 3D printer's model and the binder are stored in the metadata file of each surface. These data are used by the computational pipeline to select the appropriate flat surface to normalise the values as described in section 6.2.

The GIR Dataset also contains a flat wooden surface. Although this surface should not be used for comparative studies since it has not the same material properties as all other surfaces, it is used to validate the reflectivity of the 3D-printed panels and ensure that enough energy is reflected and not absorbed by the highly absorbent fine-grain sand used by the 3D printers. The values of the wooden panel act as a reference of the maximum specularly reflected energy possible with the data-acquisition setup described in chapter 3. Table E.1 shows that the flat 3D-printed panels absorb only around 15% of incident energy with the exception of the 40kHz frequency band, where they absorb around 25%. These values are analogous to the ones obtained by measuring a 3D-printed sample in an impedance tube [126]. The absorption coefficient of an untreated 3D-printed sample and one coated with two layers of spray paint are shown in Figure E.2.

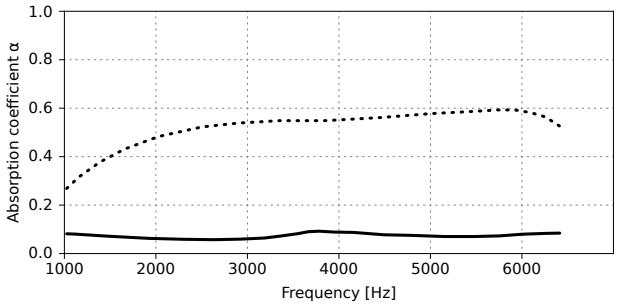

Figure E.2: The absorption coefficients of the 3D-printed panels used in the data-acquisition setup. - - -: Untreated 3D-printed sand with 140-micron average grain size. ——: 3D-printed sand with two layers of spray paint.

E.2 Foam surface

The foam surface represents highly absorbent surfaces like acoustic foam, stone wool, or glass fibre. Its usefulness is threefold. First, it can be used like any other surface in a comparative study as a highly absorbent surface. Second, it acts as a baseline for the minimum reflected energy, representing

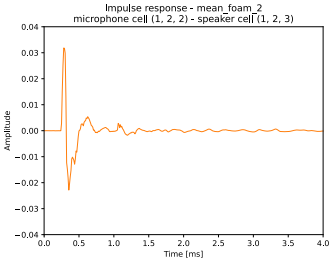

(a) The raw IR of the Foam panel containing only the direct sound.

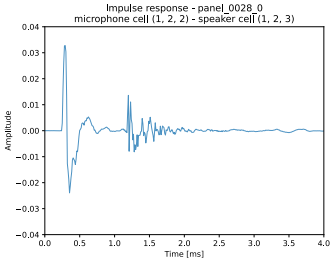

(b) The raw IR of `panel_0028_0` containing the direct and the reflection from the surface.

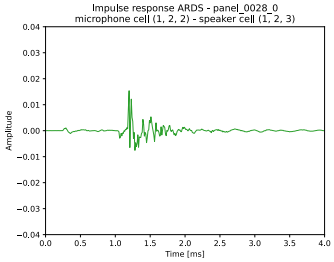

(c) The IR of `panel_0028_0` after removing the direct sound.

Figure E.4: Direct sound removal steps.

the maximum possible absorption level. This representation is useful when evaluating the performance of other surfaces, as it provides a baseline against which their performance can be measured. Lastly, this material absorbs over 95% of incident sound for frequencies above 1kHz (see Figure E.3); therefore, all recordings from the 2951 source-receiver combination contain only direct sound information. As described in 3.3.2, the computational pipeline uses this information to remove the direct sound from all recordings (see Figure E.4). The geometry of this surface is the same as the geometry of a flat surface (see Figure E.1).

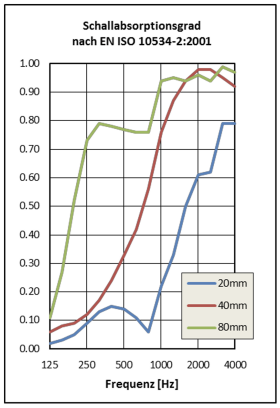

Figure E.3: The absorption coefficient of the Basotect©G+ melamine foam. A thickness of 100mm is used in the GIR Dataset.
Image source: `www.vibraplast.ch`

E.2.1 Primitive Root Diffuser

The GIR Dataset includes two two-dimensional phase grating diffusers (one of them can be seen in Figure E.6). The diffusers are modelled after D'Antonio and Konnert's two-dimensional primitive root diffusor [127] (see Figure E.5). They represent highly diffusive surfaces and act as a baseline for minimum specularly reflected energy, representing the maximum possible sound scattering level.

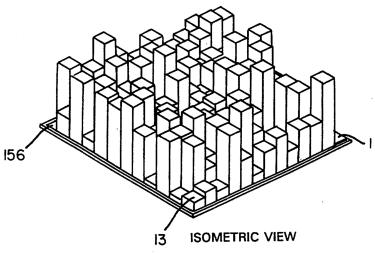

Figure E.5: Isometric view of a 2D PRD Diffuser after D'Antonio and Konnert[127].

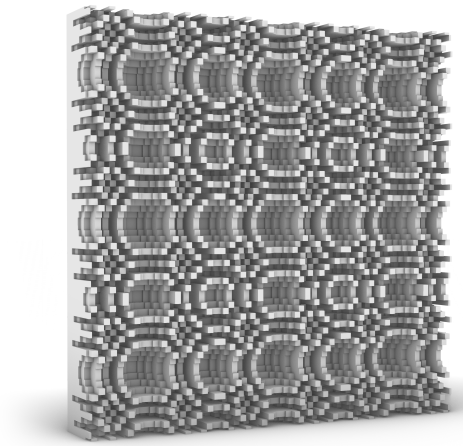

Figure E.6: 2D-PRD Diffuser included in the GIR Dataset with design frequency 2000kHz, Prime number N=23, and well width 8.6mm (1:10 scale).

F Paper E - Computational design and evaluation of acoustic diffusion panels for the Immersive Design Lab: An acoustic design case study

Romana Rust[*], *Achilleas Xydis*[*], *Christian Frick*[†], *Jürgen Strauss*[‡], *Christoph Junk*[*], *Jelle Feringa*[∓], *Fabio Gramazio*[*], *Matthias Kohler*[*]

[*] Gramazio Kohler Research, ETH Zurich, Zurich, Switzerland
[†] Rocket Science AG, Zurich, Swizterland
[‡] Strauss Elektroakustik GmbH, Bern, Swizterland
[∓] Aectual, Amsterdam, The Netherlands

Acoustic performance is an important criterion for architectural design. Much is known about sound absorption but little about sound scattering, although it is equally important for improving the acoustic quality of built spaces. This paper presents an alternative workflow for the

computational design and evaluation of acoustic diffusion panels, which have been developed and realised in a real building project - the IDL. This workflow includes a computational design system, which is integrated with a rough acoustic evaluation method for fast performance feedback, as well as the assessment of acoustic performance with an experimental measurement setup and the post-processing of a selected design instance for fabricability. The paper illustrates and discusses this workflow on the basis of the presented design study.

This version of the article has been published after peer review in *Towards a new, configurable architecture - Proceedings of the 39th eCAADe conference*, Volume 1, pp. 515-524, in September 2021. The published version is available online at: https://doi.org/10.52842/conf.ecaade.2021.1.515.

F.1 Introduction

In performance-based design, building performance is the guiding factor from early design phases, benefiting both design workflow and outcome. The final design emerges as the design is constantly being evaluated and the computational model is adjusted [128, 129]. Using this design approach, evaluative simulation processes and analysis tools are integrated with digital form generation processes. In the field of architectural acoustics, the application of such an approach would allow the designer to better combine acoustic performance objectives with architectural goals [8, 95], since they are strictly interlinked: the emitted sound is altered by the architectural space within which it is deployed. The constellation and material of surfaces within that space evoke sound reflection, absorption, and diffusion phenomena. While most architectural acoustics is concerned with sound absorption, sound diffusion is just as important for obtaining an even distribution of sound. It helps to promote spaciousness, prevent flutter echoes, and improve speech intelligibility [75]. Computer simulation software such as e.g. Odeon and Pachyderm Acoustics, which are based on GA, can predict the acoustic performance of architectural spaces before construction with sufficient accuracy. However, despite significant research over the past decades on methods to design, predict, and measure diffusing surfaces, GA methods still lack the ability to accurately model their behaviour [17, 130, 131]. To predict the scattering of sound caused by these diffusive surfaces, wave-based acoustic simulations must be used, or physical models must be tested. Both of these methods are time-consuming, which is why they cannot be used in an iterative design and evaluation workflow common to performance-based design. Therefore, in architectural practice, design rules for sound scattering [132] are often applied, or geometries are designed that are similar to tested ones. By using certain mathematical formulae [111], the scattering performance for a certain type of geometries can also be predicted.

This paper presents an alternative workflow for the evaluation of acoustic diffusion panels, which have been specifically developed for the IDL. The lab is an interdisciplinary laboratory at ETH Zurich for future design, architecture, and engineering using Extended Reality (XR) technologies[1]. It offers 3D spatial auralisation, which is enabled by a total of 75 speakers in an 80 m^2 space (10.6 × 7.6 m) with a height of six meters. Consequently, the room has high acoustic requirements, which had to be taken into account during the planning of the lab. A homogeneous, acoustically isotropic room was to be realised. The acoustics of the laboratory was planned in a 3D model calibrated from a measurement of the existing room using ray-tracing methods. A combination of sound-diffusing and sound-absorbing surfaces was chosen, the area proportion of which was determined in the 3D CAD

1: www.gramaziokohler.arch.ethz.ch/web/projekte/e/0/0/0/417.html

simulation. Absorbers were installed on the walls, floor and ceiling, and a sound-absorbing curtain was chosen to prevent specular reflections from the glass façade. The selected proportion of diffusive surfaces is to prevent specular reflections in the listening area. Their staggered mounting also creates a phase grid, which extends the diffusion into lower frequency ranges.

The particular challenges for the development of the acoustic diffusion panels were to a) improve the acoustic quality of a given space within selected frequency bands, b) fit the aesthetic considerations of the overall design concept of the lab and c) be fabricatable within a tight timeframe using 3D printing. This paper presents the design of sound scattering surfaces through the use of parametric design tools, the integration with a rough acoustic evaluation method (FFT analysis), and measured results obtained from an experimental measurement setup. Additionally, the post-processing of adapting the panels for fabrication, taking the fabrication constraints for a 3D contour printer and the panel mounting into account, is explained. The project presented in this paper builds upon previous and ongoing research projects conducted together with acoustic experts at the chair of Gramazio Kohler Research. Fields of study have been the design, fabrication, and analysis of wall panels with differentiated spatial and sound-aesthetic properties[2] and an acoustic wall system for office spaces [132] specifically tailored to sound diffusion. In the ongoing research project Data-Driven Acoustic Design, an acoustic measurement setup for data collection was developed with the goal of studying diffusive surfaces with machine learning [40]. This experimental measurement setup is also utilised in the presented project.

2: www.gramaziokohler.arch.ethz.ch/web/forschung/e/0/0/0/85.html

F.2 Background

Currently, different acoustic simulation tools are available (e.g. Odeon[3], CATT-Acoustic[4], Pachyderm Acoustics[5], etc.), to estimate the performance of design proposals using the GA method. In GA, sound is assumed to propagate as rays, and the wave nature of sound is neglected [16]. Thus, all wave-based phenomena, such as diffraction and interference, are absent. This drawback is usually circumvented by using hybrid GA, which combines ray-tracing with the image source approach that allows for the consideration of diffuse reflections [79]. GA techniques require that absorption and scattering coefficients are assigned to all surfaces in the model in order to calculate the energy loss and the direction of the reflected sound. While the sound absorption properties of many materials are available through acoustic analysis software [133] or can be obtained from material manufacturers, the same is not true for sound scattering properties. Although a number of

3: www.odeon.dk

4: www.catt.se

5: www.food4rhino.com/app/pachyderm-acoustical-simulation

Figure F.1: Acoustic data acquisition setup from the DDAD project with two Stäubli TX2-60L robots in an acoustically shielded and absorbent room. The double-sided 3D printed panel of dimensions 585x585 mm is placed in a special fixture [40]

commercially available diffusers from different manufacturers with known scattering coefficients exist (e.g. RPG, GIK Acoustics, Auralex), for most architectural surfaces, these coefficients are unknown. If new surface geometries are developed to be performative as a sound scattering device, their performance will be difficult to predict. There are standards for measuring directional diffusion coefficient [64] and random incidence scattering coefficient [120]. These processes, though, require the fabrication of a prototype surface, a highly specialised setup, are time-consuming, labour-intensive, and expensive. Therefore, the very limited dataset of scattering coefficients that can be assigned to surfaces in GA models forces room modellers to rely on empirical guidelines and intuition when assigning scattering coefficients [134]. Unlike GA simulations, wave-based simulation methods (e.g. BEM, ISM, FDTD) can accurately simulate the scattering of sound caused by diffusing surfaces. However, these methods are computationally heavy, require long simulation times, and are currently not supported in any commercial acoustic simulation tool [8]. The FabPod [108, 135] is an example of a research project in which BEM was successfully used to compute the scattering coefficients of different surface proposals and FDTD to visualise the sound waves in order to evaluate different surface geometries. Two different methods had to be used because their FDTD tool lacked the ability to provide a measure of scattering performance. Peters [108] concluded that the applied workflows are still cumbersome due to the lack of available tools for architects to evaluate the acoustic performance of complex surfaces.

The research project Data-Driven Acoustic Design (DDAD) proposes another approach for studying the relationship between diffusive surface structures and their acoustic performance using data science methods [40]. To this end, a robotic data acquisition setup (see Figure F.1) was developed that measures

3D-printed surface textures at a 1:10 model scale on a daily basis. The setup records 2951 impulse responses in front of these surfaces by repeatedly positioning a microphone and a speaker within a predefined measurement grid of 78 positions. The collected data serves both as an exploratory catalogue of different spatiotemporal acoustic scenarios and as a data set for predicting the acoustic response of digitally designed surface geometries using machine learning. As part of the project, a post-processing method was developed to extract meaningful indicators from the 2951 impulse responses per panel. One of these indicators is the DDAD absorption coefficient, which is used in the presented project to assess diffusion properties.

F.3 Workflow and design system

The acoustic panels were developed using a computational design system that generates variable geometric patterns for doubly-curved, undulated surfaces. This design system integrates a rough acoustic assessment method (FFT analysis), which is used to quickly analyse the surface's acoustic performance. It also integrates fabricability analysis and optimisation for a 3D contour printing process. In the beginning, it was necessary to identify the combination of parameters that would generate a particular surface structure which both fulfils aesthetic and acoustic requirements. This was conducted in a two-step process: First, the geometry generation parameters were manually adjusted, and the result of the FFT analysis was observed until a selection of six design instances was found. These designs were then selected for a second, more in-depth acoustic evaluation, for which they were 3D printed at 1:10 scale and measured using the acoustic measurement setup from the DDAD project. A final design selection was then made based on the measurement results. These geometry generation parameters, together with other design-relevant settings, were used to create the 29 individual acoustic diffuser panels for the Immersive Design Lab. In a post-processing step, the geometry of these panels was adapted considering the fabrication constraints for a 3D contour printer and the panel mounting.

F.3.1 DDAD conformity

In order to conform to the DDAD measurement setup (see Figure F.1) and the inclusion of the recorded data into the DDAD dataset, two conditions had to be fulfilled. First, the dimensions of the surface, which is evaluated by both acoustic analysis methods, had to be in a rectangular size of 5.85×5.85m, such that it would fit into the measurement fixture at 1:10 scale (585×585mm). Secondly, the geometry generation algorithm had to be reproducible without

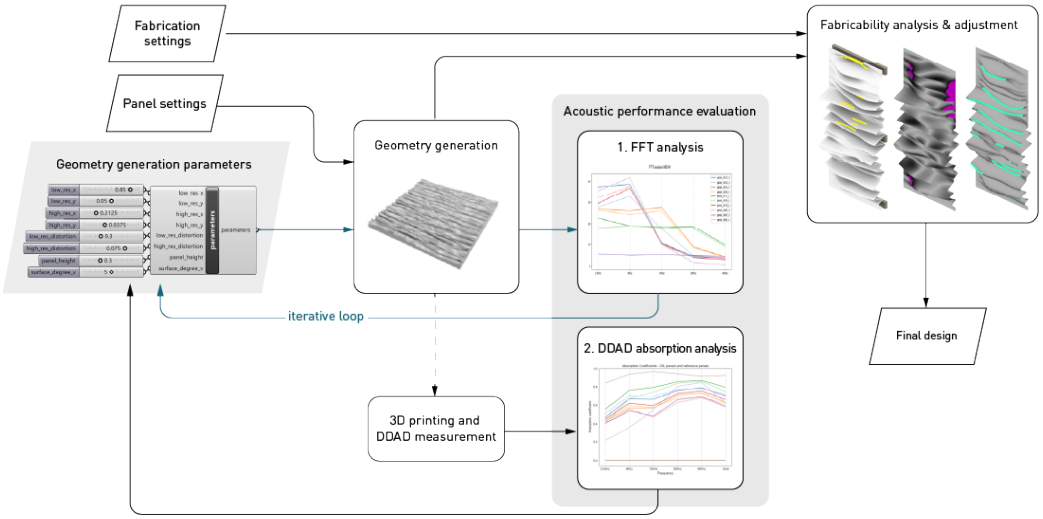

Figure F.2: The workflow elements and information flows of the design system

proprietary software. For this reason, the algorithm was written in Python and only builds upon open-source Python libraries such as `numpy`, `scipy` and `compas_nurbs`[6]. Via the `COMPAS` Remote Procedure Call (RPC), the algorithm can be executed from within the Rhinoceros/Grasshopper environment, from which also the remaining components of the computational design system are accessible.

6: `www.pypi.org/project/compas-nurbs/`

F.3.2 Geometry Generation

The custom geometry generation algorithm creates a NURBS surface that is lofted through planar NURBS curves arranged along the x-axis of a defined frame. It is loosely based on deducted design rules from the research of Cox and D'Antonio [75] [132], focusing on differentiated and aperiodic surface depth. It was also conceptualised with one defined direction, i.e. exhibiting the highest undulation along the v-direction (=y-axis of the surface's frame), due to the selected layer-based fabrication method of 3D printing. Apart from project-specific settings, the main parameters controlling the surface undulation are resolution values in u- and v-direction, distortion values u- and v-direction, the panel height, and the degree of the surface in v-direction. The degree in u-direction is set to three. These parameters, together with a random seed value, define the variable location of the surface's control points. The z-value of the control points (in relation to the surface's frame)

can be controlled by an additional input, for example, to achieve a flattening at the edges of the surface.

F.4 Acoustic performance evaluation

F.4.1 Fast Fourier Transform (FFT) analysis

To quickly and roughly assess the acoustic performance of such a generated surface, FFT analysis was integrated into the design tool. For this purpose, a certain number of linear sections (iso-curves) of the surface in both u- and v-directions are analysed by Fourier transform, and the spectral characteristics are RMS-averaged and translated into octave band diffusion values. These values are a measure for the 'roughness' of the given surface structure and allow for an estimate of how the surface performs in six-octave bands (250, 500, 1000, 2000, and 4000Hz) (see Figure F.3).

F.4.2 Panel selection and reference panels for measurement

In order to make an initial selection of both aesthetically pleasing and acoustically performing designs, the design parameters were manually adjusted, and the result of the FFT analysis was observed. This was done until a selection of six design instances was found (see Figure F.4a). Note that the labelling of the design instances stems from the GIR Dataset dataset (each surface is labelled successively with a unique identifier and suffixed with 0 or 1 indicating the panel side). Apart from the six selected design instances (panels 0073-0078), another six panels have been chosen as reference panels (see Figure F.4b) to compare the measurement results. Four of which (0079-0082) were generated with the same geometry generation algorithm as the

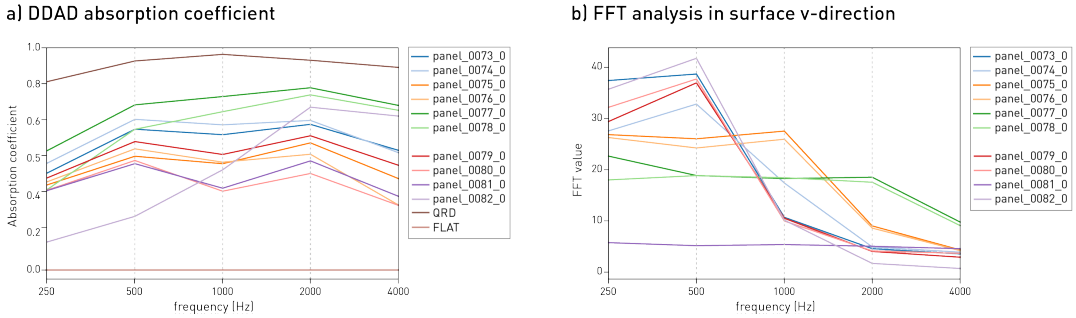

Figure F.3: Comparison between DDAD absorption coefficient calculated from measurements (left) and FFT analysis (right)

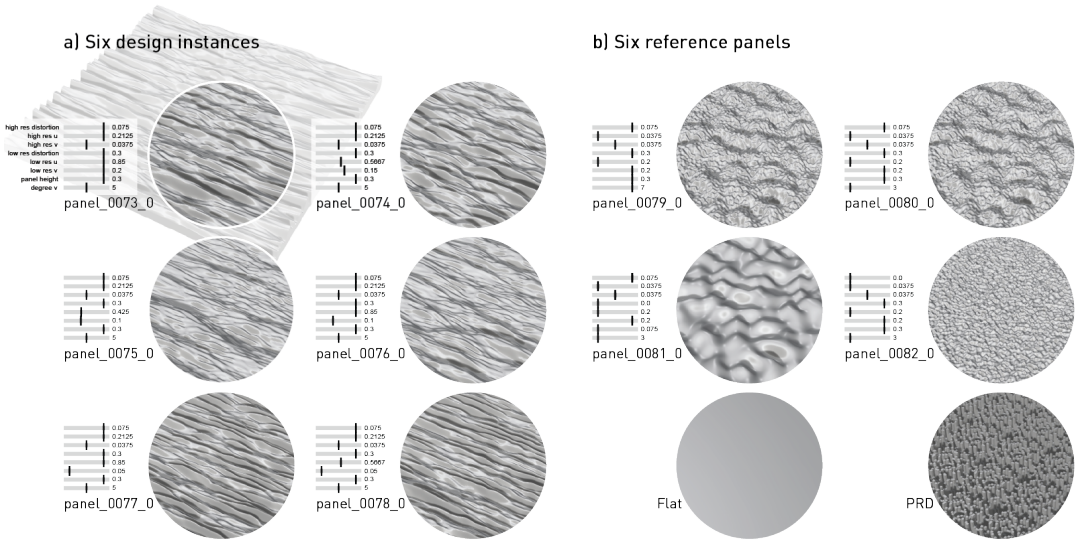

Figure F.4: a) Selection of design instances and their parameter settings, b) Six reference panels for comparison

selected panel designs and resemble commonly known diffusers (e.g. RPG Harmonix[7]). The two panels, Flat and PRD Diffuser, are reference panels from the DDAD dataset. The flat is the reference for the surface of the highest possible reflection within the dataset, and PRD Diffuser is the reference for a surface of high and uniform diffusion.

7: `www.rpgeurope.com/de/products/product/harmonixk.html`

F.4.3 DDAD absorption coefficient

During the AADS project, we developed several methods to compress the information contained in the 2951 captured impulse responses and extract meaningful descriptors therefrom, such that different surfaces can be visually compared to one another and their performances can be analysed at different frequency bands. One of these descriptors is the DDAD absorption coefficient[8]. To evaluate the diffusivity of each panel, we observe the amount of reflected energy. For example, a flat reflector produces a specular reflection, redirecting the majority of the energy to a specific direction, and a highly diffusive surface redirects the energy in multiple directions. By comparing the two energy values, it can be calculated how much energy was not reflected in a specular way, therefore diffused or absorbed.

8: In the main body of this dissertation and the released open-sourced code; this coefficient is referred to as specular absorption coefficient α_{spec}

We evaluate a reflection factor

$$Rj = \sqrt{E_j / E_{ref_j}} \tag{F.1}$$

for every source-receiver combination j that describes the ratio of sound pressure of the reflected energy with respect to a reference. E_j is the TCE [40] of the reflected sound for the diffusive panel and E_{ref_j} is the corresponding TCE of the reflected sound for the reference Flat panel. To obtain a global descriptor, we calculate the arithmetic mean $\overline{R}$ of all R_j, and from this, the DDAD absorption coefficient

$$\alpha = 1 - \overline{R}^2 \tag{F.2}$$

for the whole panel. The same process can be applied for each octave band, providing a more detailed view of the panel's diffusivity over different frequency bands. Panels that perform similarly to the flat panel would exhibit values close to 0, and panels with values close to 1 diffuse almost all energy. Note that the final values slightly overestimate the diffusivity of our panels because a portion of that energy gets absorbed by the panel's material.

F.4.4 Results

The graph in Figure F.3a shows the result of the calculated DDAD absorption coefficients for different frequency bands (250, 500, 1000, 2000 and 4000Hz). The reference panel Flat clearly marks the lower line and the reference panel PRD Diffuser the uppermost, such that panels with values on the top can be assumed with higher diffusion. As identified by the acoustic room measurement in the IDL before the installation of acoustic treatment, it is desirable that these curves are as flat as possible, i.e. that they behave similarly at the chosen frequencies. For this reason, panel 0077_0 was identified as the best performing panel, and 0074_0 as the second best, although panel 0078_0 is higher on average, but it performs worse than 0074_0 in the lower frequencies of 200 and 500 Hz. Comparing the measurement result with the FFT analysis in Figure F.3b, one can discover parallels. The two green curves (panels 0077_0 and 0078_0) stand out clearly, and one could already identify the two as best performing in all selected frequency bands after the FFT analysis. This was, however, done with caution because the FFT only analyses one surface direction and does not take the acoustic response of the full 3D surface into account. Therefore, the measuring of several different design proposals was still essential in order to validate the results.

F.5 Fabrication adjustments

Once the geometry generation parameters for the geometry generation were identified, the next step was to generate 29 individual surfaces: nine,

Figure F.5: Visualisation of the Immersive Design Lab before construction. It shows some of the 75 speakers integrated at different heights in the columns and the ceiling rack. The diffuser panels are planned to create a visually continuous diffusion belt that extends across three walls of the lab. The fourth wall is a glass façade that can be covered with a sound-absorbing curtain to prevent specular reflections.

eleven, and nine, respectively, for three walls of the room, creating a visually continuous diffusion belt that extends across the three walls (see F.5). For this, design-specific considerations were taken into account, such as panel arrangements and areas in which the surface depth was reduced, for example, in the corners or at the belt's ends. The individual NURBS surfaces were then further processed such that they 1) do not collide with the panel mounting and 2) can be fabricated using a robotic 3D contour printing process. In both cases, an iterative method was implemented in which surface analysis is followed by surface adaptation until the surface fulfils requirements defined for 1) and 2).

The requirement for 1) is simply that there is no intersection between the surface and the mounting elements (see Figure F.6b). For 2), two sub-conditions need to be fulfilled. First, the 3D printing overhang angle should not exceed 45°. This is to ensure that each successive printing layer has sufficient support and to avoid droopy filament strands. Another identified 3D printing constraint is the maximum allowed curvature along the printing direction, which constraint derives from the used robotic setup and control. During tests, it was found that surface areas with a curvature radius smaller than 0.0028 m could lead to filament artefacts. A characteristic of the generated surface is that its undulation expands from the surface's frame only along the negative and the positive z-axis (see Figure F.6a). To fulfil the identified requirements, a similar strategy of surface adaptation could be applied, namely to make the surface smoother or flatter by moving its control points along the z-axis towards the surface frame. For requirement 1), since the panel mounts are along the negative z-axis of the surface's frame, the control points move incrementally along the positive z-axis. For 2) a smoothing strategy similar to Laplacian smoothing was chosen that proved to be stable, i.e. the error could

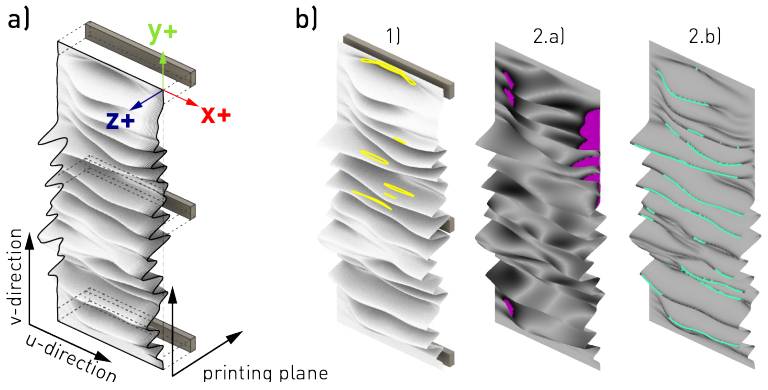

Figure F.6: a) Panel build-up, b) Fabrication adjustments: 1) intersection with mounting elements, 2.a) coloured areas with 3D printing overhang and 2.b) coloured areas with curvature radius < 0.028m

continuously be reduced: The surface analysis identifies uv point locations that do not fulfil requirements defined for 2). Then, the corresponding control points of the NURBS surface are calculated and grouped per problem area. In each group of N control points P, a new z-value z_i for each control point P_i is calculated as follows:

$$z_i = z_i + \lambda \frac{1}{N} \sum_{j=1}^{N} z_j \tag{F.3}$$

Where z_j is the z-value of the j-th control point P_j in the group and λ a factor that controls the amount of displacement per iteration, which was chosen at 0.05. The process would terminate if less than 0.001% of evaluated uv points would have overhang or curvature problems. This incremental adjustment with a small λ was particularly chosen to avoid unnecessarily smoothing the surface and losing too much surface depth; otherwise, the effect of diffusion would have been altered. We compared all surfaces before and after the adjustment. Overall, only 5% of all control points moved more than 10mm along the z-axis. On the most adjusted surface, there was only one area (3% of the total surface) that had larger adjustments of up to 90mm. This was due to the fact that the bottom peak of the surface wave collided with the mounting part. The adjustments due to 3D printing amounted to a maximum of 4mm, thus negligible.

F.6 Results

Once the surfaces were processed for production, they were passed on to the fabrication partner Aectual[9], who generated the geometry of the panels' support structure considering the panel mounting and for introducing

9: www.aectual.com

additional stiffness. From this geometry, 3D printing paths were generated, and the final product was fabricated using a robotic 3D printing process.

F.6.1 Validation of the acoustic performance

The performance of the diffuser panels was determined by impulse response analysis of acquired gun-shot decay sound samples. For this purpose, impulse responses before and after installation of the inhere-described diffuser panels were compared using multiple different analysis methods (e.g. cumulative spectral decays, spectrograms with high temporal resolutions). All methods focused on the characteristics of the reverberation time decay slope and did not per se determine panel diffusion parameters. The graphs in Figure F.7 visualise the cumulative spectral decay plots using GNU octave. Both impulses were filtered with a digital brick wall high pass filter at 200Hz, with the initial rising edge being an artefact. During the measurements, the room was empty, and the sound-absorbing curtains were closed. Overall, the results show that the set goals were successfully achieved, and the room is within the identified specifications. Due to the geometric arrangement of the diffusers and absorbers on the walls, the reverberation time was not significantly reduced by the introduction of the diffusers. Subjective evaluation by carefully listening to the room response validated the measurement results in Figure F.7, no flutter echoes or other types of artefacts resulting from specular reflections could be identified.

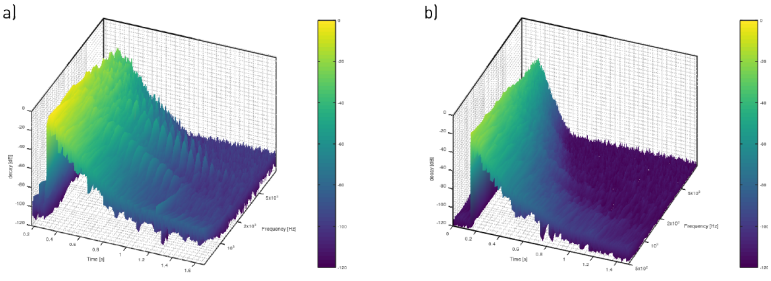

Figure F.7: a) Before the installation of the diffusers: Flutter echoes are significantly level-determining and clearly audible towards the end of the impulse decay at mid frequencies and can be seen as spikes towards the tail of the impulse response (dual slope decay). b) After installation of the diffusers: The impulse decays very densely and smoothly. No disturbing spatial artefacts can be measured or heard.

F.7 Discussion and Conclusion

Empowered through digital communication and new tools, the way how architects, experts, engineers, and fabricators work is dramatically altered. Autonomous processes can be replaced by collective workflows supported by a common digital infrastructure. Especially for non-standard design projects,

such as curated digital workflows that span from design, over performance analysis to production are paramount.

This paper presented a design system which has been successfully validated in a real building project. It integrates acoustic evaluation and fabrication constraints, allowing for a successful collaboration amongst all involved experts from the fields of architecture, acoustics and fabrication. The result is embodied in the feature-rich, full-scale and permanent acoustic panels that adorn the walls of the Immersive Design Lab and have thus become an essential part of its architecture. The development of acoustic diffuser panels has created a synthesis with ongoing research projects and produced new findings in a number of aspects. However, a number of limitations were also uncovered during the realisation, highlighting opportunities for improvement and further research:

- While the fast FFT analysis allowed for a good selection of design proposals, thus providing an initial evaluation, it is not suitable as a sole acoustic assessment and needs to be complemented with acoustic measurements or wave-based acoustic simulations. Ideally, only wave-based simulations could be used for the purpose presented, but they are too computationally intensive for an iterative design and evaluation process. However, for a specific design system like the one presented, machine learning could be applied by replacing the wave-based simulation with a surrogate simulation and thus decrease the response time for evaluation.
- Another improvement to the presented workflow would be the earlier consideration of fabrication constraints. Rather than trying to adapt the surface in a post-processing step, the acoustic evaluation should be applied to geometries that are fabricatable in the first place.

Projects like the one presented are exemplary of how converging interests in academia and start-ups like Aectual can bring academic research and product development in closer continuation of one another: The developed design system provides a lean computational pipeline from design to fabrication and allows the adaptation of surfaces to individual room shapes and custom designs. As a result of this successful partnership, Aectual is launching mass-customisable acoustic diffusion panels that are 3D printed on demand.

Acknowledgements The acoustic diffusion panels have been developed by Gramazio Kohler Research in collaboration with acoustic partners Rocket Science AG and Strauss Elektroakustik GmbH and the fabrication partner Aectual. We thank the extended team of industry partners for inspiring discussions and help. Further, the authors want to thank Beat Jäggli for planning the execution on behalf of ETH Real Estate and Michael Lyrenmann

for making beautiful images. Kurt Heutschi developed the DDAD absorption coefficient. The realisation of the Immersive Design Laboratory has been made possible as part of the Design++ initiative funded by ETH Zurich through an ETH+ Grant.

Figure F.8: Acoustic panels installed in the Immersive Design Lab.

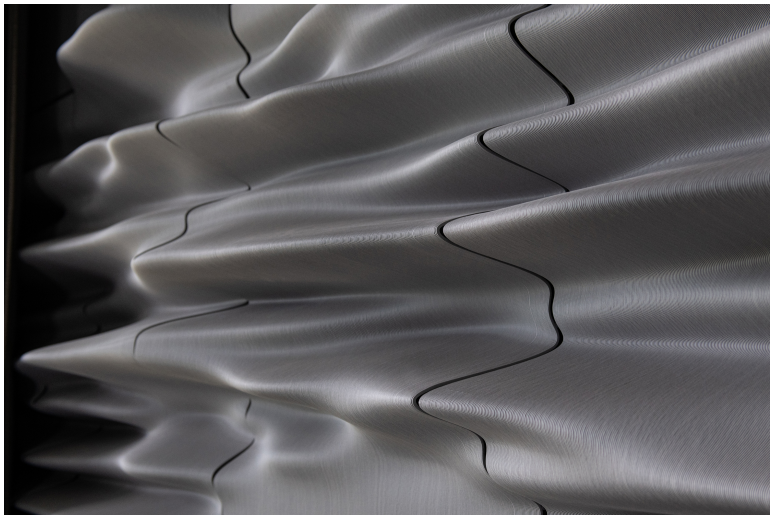

Figure F.9: Close up of the acoustic diffusor panel.

F.8 Authors contributions to the paper

The individual roles and contributions of each author in this paper are described using the standardised taxonomy CRediT[10][71].

10: Contributor Roles Taxonomy

Romana Rust
Visualisation, Writing - Review & Editing, Writing - Original Draft, Data Curation, Investigation, Formal analysis, Validation, Software, Methodology

Achilleas Xydis
Visualisation, Writing - Review & Editing, Writing - Original Draft, Data Curation, Investigation, Formal analysis, Software, Validation

Christian Frick
Resources, Investigation, Validation, Writing - Review & Editing, Software, Conceptualisation

Jürgen Strauss
Conceptualisation, Validation, Writing - Review & Editing

Christoph Junk
Conceptualisation, Project administration, Visualisation, Writing - Review & Editing

Jelle Feringa
Resources, Validation, Writing - Review & Editing

Fabio Gramazio
Conceptualization, Supervision, Writing - Review & Editing

Matthias Kohler
Investigation, Conceptualization, Supervision, Writing - Review & Editing, Software, Methodology

Bibliography

References in citation order.

[1] Adolf Loos. *Ornament and Crime*. Penguin Books Limited, 2019 (cited on page 4).

[2] Toshiyuki Okano. 'Image shift caused by strong lateral reflections, and its relation to inter-aural cross correlation'. In: *The Journal of the Acoustical Society of America* 108.5 (Nov. 2000), pp. 2219–2230. DOI: 10.1121/1.1311775 (cited on page 4).

[3] A. Kaarlela-Tuomaala et al. 'Effects of acoustic environment on work in private office rooms and open-plan offices – longitudinal study during relocation'. In: *Ergonomics* 52.11 (Nov. 2009). Publisher: Taylor & Francis _eprint: https://doi.org/10.1080/00140130903154579, pp. 1423–1444. DOI: 10.1080/00140130903154579 (cited on page 4).

[4] Mathias Basner et al. 'Auditory and non-auditory effects of noise on health'. In: *The Lancet* 383.9925 (Apr. 2014). Publisher: Elsevier, pp. 1325–1332. DOI: 10.1016/S0140-6736(13)61613-X (cited on page 4).

[5] Wolfgang Babisch. 'Cardiovascular effects of noise'. In: *Noise and Health* 13.52 (May 2011). Company: Medknow Publications and Media Pvt. Ltd. Distributor: Medknow Publications and Media Pvt. Ltd. Institution: Medknow Publications and Media Pvt. Ltd. Label: Medknow Publications and Media Pvt. Ltd. Publisher: Medknow Publications, p. 201. DOI: 10.4103/1463-1741.80148 (cited on page 4).

[6] World Health Organisation and others. *Burden of disease from environmental noise: quantification of healthy life years lost in Europe*. OCLC: 779684347. Copenhagen: World Health Organization, Regional Office for Europe, 2011 (cited on page 5).

[7] Trevor Cox and Peter D'Antonio. *Acoustic Absorbers and Diffusers: Theory, Design and Application*. 3rd ed. Boca Raton: CRC Press, Aug. 2016 (cited on pages 5, 6, 10, 22, 115).

[8] Elena Badino, Louena Shtrepi, and Arianna Astolfi. 'Acoustic Performance-Based Design: A Brief Overview of the Opportunities and Limits in Current Practice'. In: *Acoustics* 2.2 (May 2020), pp. 246–278. DOI: 10.3390/acoustics2020016 (cited on pages 8, 22, 64, 66, 83, 144, 146).

[9] Wallace Clement Sabine. *Theatre acoustics*. American Architect, Incorporated, 1913 (cited on page 8).

[10] Wallace Clement Sabine. *Collected papers on acoustics*. Open Library ID: OL7190039M. Cambridge: Harvard University Press, 1922 (cited on pages 9, 64).

[11] G. S. Settles. *Schlieren and Shadowgraph Techniques: Visualizing Phenomena in Transparent Media*. Experimental Fluid Mechanics. Berlin Heidelberg: Springer-Verlag, 2001 (cited on page 9).

[12] Mike Barron. 'Acoustic scale model testing over 21 years'. In: *Acoustics Bulletin* 22 (May 1997), p. 5 (cited on page 9).

[13] Jens Holger Rindel. 'Modelling in auditorium acoustics. From ripple tank and scale models to computer simulations'. In: *Revista de Acustica* XXXIII (2002), pp. 31–35 (cited on page 9).

[14] Samuel Siltanen, Tapio Lokki, and Lauri Savioja. 'Rays or waves? Understanding the strengths and weaknesses of computational room acoustics modeling techniques'. In: *Proc. Int. Symposium on Room Acoustics*. 2010 (cited on pages 9, 22, 42).

[15] Louena Shtrepi et al. 'A performance-based optimization approach for diffusive surface topology design'. In: *Building Acoustics* (Oct. 2020). Publisher: SAGE Publications Ltd STM, p. 1351010X20967821. DOI: 10.1177/1351010X20967821 (cited on pages 9, 83).

[16] Lauri Savioja and U. Peter Svensson. 'Overview of geometrical room acoustic modeling techniques'. In: *The Journal of the Acoustical Society of America* 138.2 (2015), pp. 708–730. DOI: 10.1121/1.4926438 (cited on pages 9, 22, 42, 145).

[17] Fabian Brinkmann et al. 'A round robin on room acoustical simulation and auralization'. In: *The Journal of the Acoustical Society of America* 145.4 (2019), pp. 2746–2760. DOI: 10.1121/1.5096178 (cited on pages 10, 22, 29, 144).

[18] Ahnert Feistel Media Group. *EASE®*. Jan. 2022. URL: www.afmg.eu/en/ease-enhanced-acoustic-simulator-engineers (cited on page 10).

[19] Athanasios Voulodimos et al. 'Deep Learning for Computer Vision: A Brief Review'. In: *Computational Intelligence and Neuroscience* 2018 (Feb. 2018). Publisher: Hindawi, e7068349. DOI: 10.1155/2018/7068349 (cited on pages 11, 22, 83).

[20] Martin Tamke, Paul Nicholas, and Mateusz Zwierzycki. 'Machine learning for architectural design: Practices and infrastructure'. In: *International Journal of Architectural Computing* 16 (June 2018), pp. 123–143. DOI: 10.1177/1478077118778580 (cited on pages 11, 83).

[21] Kyle Steinfeld. 'Dreams May Come'. In: *ACADIA 2017: DISCIPLINES & DISRUPTION [Proceedings of the 37th Annual Conference of the Association for Computer Aided Design in Architecture (ACADIA)*. Cambridge, MA: CUMINCAD, Nov. 2017, pp. 590–599 (cited on pages 11, 83).

[22] Leon A. Gatys, Alexander S. Ecker, and Matthias Bethge. 'A Neural Algorithm of Artistic Style'. In: *arXiv:1508.06576 [cs, q-bio]* (Sept. 2015). arXiv: 1508.06576 (cited on pages 11, 83).

[23] Karla Saldana Ochoa et al. 'Beyond typologies, beyond optimization: Exploring novel structural forms at the interface of human and machine intelligence'. In: *International Journal of Architectural Computing* (July 2020). Publisher: SAGE Publications, p. 1478077120943062. DOI: 10.1177/1478077120943062 (cited on pages 11, 83, 84, 89).

[24] Michael J. Bianco et al. 'Machine learning in acoustics: Theory and applications'. In: *The Journal of the Acoustical Society of America* 146.5 (Nov. 2019). Publisher: Acoustical Society of America, pp. 3590–3628. DOI: 10.1121/1.5133944 (cited on pages 11, 22).

[25] Hannes Gamper and Ivan J. Tashev. 'Blind Reverberation Time Estimation Using a Convolutional Neural Network'. In: *2018 16th International Workshop on Acoustic Signal Enhancement (IWAENC)*. Sept. 2018, pp. 136–140. DOI: 10.1109/IWAENC.2018.8521241 (cited on pages 11, 24, 84).

[26] Andrea F. Genovese et al. 'Blind Room Volume Estimation from Single-channel Noisy Speech'. In: *ICASSP 2019 - 2019 IEEE International Conference on Acoustics, Speech and Signal Processing (ICASSP)*. ISSN: 2379-190X. May 2019, pp. 231–235. DOI: 10.1109/ICASSP.2019.8682951 (cited on pages 11, 24, 84).

[27] Nils Peters, Howard Lei, and Gerald Friedland. 'Name That Room: Room Identification Using Acoustic Features in a Recording'. In: *Proceedings of the 20th ACM International Conference on Multimedia*. MM '12. event-place: Nara, Japan. New York, NY, USA: ACM, 2012, pp. 841–844. DOI: 10.1145/2393347.2396326 (cited on pages 11, 24, 84).

[28] Constantinos Papayiannis, Christine Evers, and Patrick A. Naylor. 'End-to-End Classification of Reverberant Rooms Using DNNs'. In: *IEEE/ACM Transactions on Audio, Speech, and Language Processing* 28 (2020). Conference Name: IEEE/ACM Transactions on Audio, Speech, and Language Processing, pp. 3010–3017. DOI: 10.1109/TASLP.2020.3033628 (cited on pages 11, 24, 84).

[29] Stefan Weinzierl. *Handbuch der Audiotechnik*. Springer Science & Business Media, 2008 (cited on page 12).

[30] Marco Jeub, Magnus Schafer, and Peter Vary. 'A binaural room impulse response database for the evaluation of dereverberation algorithms'. In: *2009 16th International Conference on Digital Signal Processing*. ISSN: 2165-3577. July 2009, pp. 1–5. DOI: 10.1109/ICDSP.2009.5201259 (cited on pages 12, 23, 84).

[31] Igor Szoke et al. 'Building and Evaluation of a Real Room Impulse Response Dataset'. In: *IEEE Journal of Selected Topics in Signal Processing* 13.4 (Aug. 2019). arXiv: 1811.06795, pp. 863–876. DOI: 10.1109/JSTSP.2019.2917582 (cited on pages 12, 23, 84).

[32] Satoshi Nakamura et al. 'Acoustical Sound Database in Real Environments for Sound Scene Understanding and Hands-Free Speech Recognition'. In: *Proceedings of the Second International Conference on Language Resources and Evaluation (LREC'00)*. Athens, Greece: European Language Resources Association (ELRA), May 2000 (cited on pages 12, 23, 84).

[33] Mirco Ravanelli et al. 'The DIRHA-ENGLISH corpus and related tasks for distant-speech recognition in domestic environments'. In: *2015 IEEE Workshop on Automatic Speech Recognition and Understanding (ASRU)*. Dec. 2015, pp. 275–282. DOI: 10.1109/ASRU.2015.7404805 (cited on pages 12, 23, 84).

[34] James Eaton et al. 'Acoustic Characterization of Environments (ACE) Challenge Results Technical Report'. In: *arXiv:1606.03365 [cs]* (June 2017). arXiv: 1606.03365 (cited on pages 12, 23, 84).

[35] Stuart E. Mirvis. 'Garbage in, garbage out (How purportedly great ML models can be screwed up by bad data)'. In: *Applied Radiology* 31.2 (2002). ISBN: 0036-861X, p. 5. DOI: 10.1037/e475262008-002 (cited on pages 12, 23, 83).

[36] James Heddle. 'Fresnel Zones and Spheroids for Room Acoustics'. In: November (2016), pp. 1–10 (cited on pages 14, 28, 46).

[37] Karl Pearson F.R.S. 'LIII. On lines and planes of closest fit to systems of points in space'. In: *The London, Edinburgh, and Dublin Philosophical Magazine and Journal of Science* 2.11 (Nov. 1901), pp. 559–572. DOI: 10.1080/14786440109462720 (cited on pages 15, 58).

[38] Teuvo Kohonen. 'Self-organized formation of topologically correct feature maps'. In: *Biological Cybernetics* 43.1 (Jan. 1982), pp. 59–69. DOI: 10.1007/BF00337288 (cited on pages 15, 59, 84).

[39] Achilleas Xydis et al. 'GIR dataset: A geometry and real impulse response dataset for machine learning research in acoustics'. In: *Applied Acoustics* 208 (June 2023), p. 109333. DOI: 10.1016/j.apacoust.2023.109333 (cited on pages 17, 185).

[40] Romana Rust et al. 'A data acquisition setup for data driven acoustic design'. In: *Building Acoustics* 28.4 (2021), pp. 345–360. DOI: 10.1177/1351010X20986901 (cited on pages 17, 26–28, 32, 67, 88, 96, 145, 146, 151, 185).

[41] Achilleas Xydis et al. 'Visualization methods for big and high-dimensional acoustic data'. In: *ACADIA 2022: Hybrids & Haecceities [Proceedings of the 42st Annual Conference of the Association for Computer Aided Design in Architecture (ACADIA)]*. 2022 (cited on pages 17, 25, 185).

[42] Achilleas Xydis et al. 'Data-Driven Acoustic Design of Diffuse Soundfields: Self-Organising Maps as an Exploratory Design Tool for Big Data'. English. In: *ACADIA 2021: Realignments: Toward Critical Computation [Proceedings of the 41st Annual Conference of the Association of Computer Aided Design in Architecture (ACADIA)]. edited by B. Bogosian, K. Dörfler, B. Farahi, J. Garcia del Castillo y López, J. Grant, V. Noel, S. Parascho, and J. Scott.* ACADIA. Nov. 2021, pp. 170–181 (cited on pages 17, 26, 74, 185).

[43] Romana Rust et al. 'Computational Design and Evaluation of Acoustic Diffusion Panels for the Immersive Design Lab'. In: *Towards a new, configurable architecture - Proceedings of the 39th eCAADe Conference*. Vol. 1. University of Novi Sad, Novi Sad, Serbia, Sept. 2021, pp. 515–524. DOI: https://doi.org/10.52842/conf.ecaade.2021.1.515 (cited on pages 18, 122, 185).

[44] Jens Blauert. *Spatial hearing: the psychophysics of human sound localization*. MIT press, 1997 (cited on pages 22, 115).

[45] Sean E Olive and Floyd E Toole. 'The detection of reflections in typical rooms'. In: *Audio Engineering Society Convention 85*. Audio Engineering Society, 1988 (cited on pages 22, 115).

[46] Kai Arulkumaran et al. 'Deep Reinforcement Learning: A Brief Survey'. In: *IEEE Signal Processing Magazine* 34.6 (Nov. 2017). Conference Name: IEEE Signal Processing Magazine, pp. 26–38. DOI: 10.1109/MSP.2017.2743240 (cited on pages 22, 83).

[47] Haiqiang Niu et al. 'Deep-learning source localization using multi-frequency magnitude-only data'. In: *The Journal of the Acoustical Society of America* 146.1 (July 2019). Publisher: Acoustical Society of America, pp. 211–222. DOI: 10.1121/1.5116016 (cited on pages 22, 83).

[48] Kaiming He et al. 'Deep Residual Learning for Image Recognition'. In: 2016, pp. 770–778 (cited on page 22).

[49] Yun Wang and Hua Peng. 'Underwater acoustic source localization using generalized regression neural network'. In: *The Journal of the Acoustical Society of America* 143.4 (Apr. 2018). Publisher: Acoustical Society of America, pp. 2321–2331. DOI: 10.1121/1.5032311 (cited on page 22).

[50] Samer A. Nene, Shree K. Nayar, and Hiroshi Murase. *Columbia Object Image Library (COIL-20)*. Tech. rep. CUCS-005-96. Department of Computer Science, Columbia University, Feb. 1996 (cited on page 23).

[51] Achilleas Xydis et al. *GIR Dataset: A Geometry and real Impulse Response Dataset*. Aug. 2021. DOI: 10.5281/zenodo.5288743. URL: https://doi.org/10.5281/zenodo.5288743 (cited on pages 23, 43, 67, 84).

[52] P. Kendrick et al. 'Room Acoustic Parameter Extraction from Music Signals'. In: *2006 IEEE International Conference on Acoustics Speech and Signal Processing Proceedings*. Vol. 5. May 2006, pp. V–V. DOI: 10.1109/ICASSP.2006.1661397 (cited on page 24).

[53] Noam Shabtai, B Rafaely, and Yaniv Zigel. *Room Volume Classification from Reverberant Speech*. Jan. 2010 (cited on page 24).

[54] Adam O'Donovan, Ramani Duraiswami, and Dmitry Zotkin. 'Imaging concert hall acoustics using visual and audio cameras'. In: *2008 IEEE International Conference on Acoustics, Speech and Signal Processing*. ISSN: 2379-190X. Mar. 2008, pp. 5284–5287. DOI: 10.1109/ICASSP.2008.4518852 (cited on page 24).

[55] Charles Vanwynsberghe et al. 'Design and implementation of a multi-octave-band audio camera for realtime diagnosis'. In: *Applied Acoustics* 89 (2015). Publisher: Elsevier, pp. 281–287 (cited on page 24).

[56] Adam O'Donovan, Ramani Duraiswami, and Nail A Gumerov. 'Real time capture of audio images and their use with video'. In: *2007 IEEE Workshop on Applications of Signal Processing to Audio and Acoustics*. IEEE, 2007, pp. 10–13 (cited on page 24).

[57] Adam O'Donovan, Ramani Duraiswami, and Jan Neumann. 'Microphone arrays as generalized cameras for integrated audio visual processing'. In: *2007 IEEE Conference on Computer Vision and Pattern Recognition*. IEEE, 2007, pp. 1–8 (cited on page 24).

[58] F. Antonacci, A. Sarti, and S. Tubaro. 'Geometric reconstruction of the environment from its response to multiple acoustic emissions'. In: *2010 IEEE International Conference on Acoustics, Speech and Signal Processing*. ISSN: 2379-190X. Mar. 2010, pp. 2822–2825. DOI: 10.1109/ICASSP.2010.5496186 (cited on page 24).

[59] David B. Lindell, Gordon Wetzstein, and Vladlen Koltun. 'Acoustic Non-Line-Of-Sight Imaging'. In: 2019, pp. 6780–6789 (cited on page 24).

[60] David B. Lindell, Gordon Wetzstein, and Matthew O'Toole. 'Wave-based non-line-of-sight imaging using fast *f-k* migration'. In: *ACM Transactions on Graphics* 38.4 (July 2019), 116:1–116:13. DOI: 10.1145/3306346.3322937 (cited on page 24).

[61] Marco Crocco et al. 'Audio surveillance: A systematic review'. In: *ACM Computing Surveys (CSUR)* 48.4 (2016). Publisher: ACM New York, NY, USA, pp. 1–46 (cited on page 24).

[62] Peter Haubrick and Juan Ye. 'Robust audio sensing with multi-sound classification'. In: *2019 IEEE International Conference on Pervasive Computing and Communications (PerCom*. IEEE, 2019, pp. 1–7 (cited on page 24).

[63] Maximo Cobos et al. 'A survey of sound source localization methods in wireless acoustic sensor networks'. In: *Wireless Communications and Mobile Computing* 2017 (2017). Publisher: Hindawi (cited on page 24).

[64] ISO. *ISO 17497-2 Acoustics - Sound-scattering properties of surfaces - Part 2: Measurement of the directional diffusion coefficient in a free field*. ISBN: 0471297836. 2012 (cited on pages 25, 113, 117, 146).

[65] Michael M Bronstein et al. 'Geometric deep learning: Grids, groups, graphs, geodesics, and gauges'. In: *arXiv preprint arXiv:2104.13478* (2021) (cited on page 25).

[66] Song Mei, Theodor Misiakiewicz, and Andrea Montanari. 'Learning with invariances in random features and kernel models'. In: *Proceedings of Thirty Fourth Conference on Learning Theory*. ISSN: 2640-3498. PMLR, July 2021, pp. 3351–3418 (cited on page 25).

[67] Alberto Bietti, Luca Venturi, and Joan Bruna. 'On the sample complexity of learning with geometric stability'. In: *arXiv preprint arXiv:2106.07148* (2021) (cited on page 25).

[68] Diederik P Kingma and Jimmy Ba. 'Adam: A method for stochastic optimization'. In: *arXiv preprint arXiv:1412.6980* (2014) (cited on pages 33, 130).

[69] 'Reciprocity in acoustics'. In: *Reciprocity in Elastodynamics*. Ed. by J. D. Achenbach. Cambridge Monographs on Mechanics. Cambridge: Cambridge University Press, 2004, pp. 55–69. DOI: 10.1017/CBO9780511550485.005 (cited on page 35).

[70] Prasanga Samarasinghe, Thushara D. Abhayapala, and Walter Kellermann. 'Acoustic reciprocity: An extension to spherical harmonics domain'. In: *The Journal of the Acoustical Society of America* 142.4 (Oct. 2017). Publisher: Acoustical Society of America, EL337–EL343. DOI: 10.1121/1.5002078 (cited on page 35).

[71] Liz Allen, Alison O'Connell, and Veronique Kiermer. 'How can we ensure visibility and diversity in research contributions? How the Contributor Role Taxonomy (CRediT) is helping the shift from authorship to contributorship'. In: *Learned Publishing* 32.1 (2019). _eprint: https://onlinelibrary.wiley.com/doi/pdf/10.1002/leap.1210, pp. 71–74. DOI: 10.1002/leap.1210 (cited on pages 37, 60, 78, 97, 157).

[72] Stephen Handel. *Listening: An Introduction to the Perception of Auditory Events*. Cambridge, Massachusetts: MIT Press, 1993 (cited on page 42).

[73] Wonyoung Yang and Jin Yong Jeon. 'Design strategies and elements of building envelope for urban acoustic environment'. In: *Building and Environment* 182 (Sept. 2020), p. 107121. DOI: 10.1016/j.buildenv.2020.107121 (cited on page 42).

[74] Sönke Pelzer et al. 'Integrating Real-Time Room Acoustics Simulation into a CAD Modeling Software to Enhance the Architectural Design Process'. In: *Buildings* 4.2 (June 2014). Number: 2 Publisher: Multidisciplinary Digital Publishing Institute, pp. 113–138. DOI: 10.3390/buildings4020113 (cited on page 42).

[75] Trevor J. Cox and Peter D'Antonio. *Acoustic Absorbers and Diffusers: Theory, Design and Application*. CRC Press, 2004 (cited on pages 42, 53, 82, 144, 148).

[76] G. M. Naylor. 'ODEON—Another hybrid room acoustical model'. In: *Applied Acoustics* 38.2 (Jan. 1993), pp. 131–143. DOI: 10.1016/0003-682X(93)90047-A (cited on page 42).

[77] Angelo Farina, Paolo Galaverna, and Guido Truffelli. *RAMSETE : Room Acoustics modeling on PC*. URL: http://www.ramsete.com (cited on page 42).

[78] Dirk Schröder and Michael Vorländer. 'RAVEN: A Real-Time Framework for the Auralization of Interactive Virtual Environments'. In: *Forum Acusticum* c (2011). ISBN: 9788469415207, pp. 1541–1546 (cited on pages 42, 116).

[79] Michael Vorländer. 'Computer simulations in room acoustics: Concepts and uncertainties'. In: *The Journal of the Acoustical Society of America* 133.3 (2013), pp. 1203–1213. DOI: 10.1121/1.4788978 (cited on pages 42, 145).

[80] Brian Katz et al. *La Philharmonie de Paris - Acoustic scale model study*. Oct. 2015 (cited on page 42).

[81] Benjamin S. Koren. 'The Grand Hall of the Elbphilharmonie Hamburg: Development of Parametric and Digital Fabrication Tools in Architectural and Acoustical Design'. In: *Humanizing Digital Reality: Design Modelling Symposium Paris 2017*. Ed. by Klaas De Rycke et al. Singapore: Springer, 2018, pp. 141–151. DOI: 10.1007/978-981-10-6611-5_13 (cited on page 42).

[82] R. Rust et al. *COMPAS FAB: Robotic fabrication package for the COMPAS Framework*. 2018. URL: https://doi.org/10.5281/zenodo.3469478 (cited on page 48).

[83] David Coleman et al. *Reducing the Barrier to Entry of Complex Robotic Software: a MoveIt! Case Study*. arXiv:1404.3785 [cs]. Apr. 2014. DOI: 10.48550/arXiv.1404.3785. URL: http://arxiv.org/abs/1404.3785 (cited on page 48).

[84] Morgan Quigley et al. 'ROS: an open-source Robot Operating System'. In: *ICRA workshop on open source software*. Vol. 3. Issue: 3.2. Kobe, Japan, 2009, p. 5 (cited on page 48).

[85] Russell Toris et al. 'Robot Web Tools: Efficient messaging for cloud robotics'. In: *2015 IEEE/RSJ International Conference on Intelligent Robots and Systems (IROS)*. Sept. 2015, pp. 4530–4537. DOI: 10.1109/IROS.2015.7354021 (cited on page 48).

[86] Owen Cramer. 'The variation of the specific heat ratio and the speed of sound in air with temperature, pressure, humidity, and CO2 concentration'. In: *The Journal of the Acoustical Society of America* 93.5 (May 1993). Publisher: Acoustical Society of America, pp. 2510–2516. DOI: 10.1121/1.405827 (cited on pages 50, 127).

[87] Nicki Holighaus, Christoph Wiesmeyr, and Zdeněk Průša. 'A Class of Warped Filter Bank Frames Tailored to Non-linear Frequency Scales'. In: *Journal of Fourier Analysis and Applications* 26.1 (Jan. 2020), p. 22. DOI: 10.1007/s00041-020-09726-w (cited on page 51).

[88] IEC. *Electroacoustics–Octave-Band and Fractional-Octave-Band Filters*. IEC 61260-1:1995. Backup Publisher: International Electrotechnical Commission. Geneva, Switzerland: International Electrotechnical Commission, 1995 (cited on page 51).

[89] Trevor John Cox et al. 'A Tutorial on Scattering and Diffusion Coefficients for Room Acoustic Surfaces'. In: *Acta Acustica united with Acustica* 92.1 (Jan. 2006). ISBN: 1436-7947, pp. 1–15 (cited on pages 53, 113).

[90] Jacob Benesty et al. 'Pearson correlation coefficient'. In: *Noise reduction in speech processing*. Springer, 2009, pp. 1–4 (cited on page 58).

[91] Amy Genender Feltheimer. 'Visualizing High Dimensional and Big Data'. In: *Procedia Computer Science*. Cyber Physical Systems and Deep Learning Chicago, Illinois November 5-7, 2018 140 (Jan. 2018), pp. 112–121. DOI: 10.1016/j.procs.2018.10.308 (cited on pages 64, 66).

[92] Tran Van Long and Lars Linsen. 'Visualizing high density clusters in multidimensional data using optimized star coordinates'. In: *Computational Statistics* 26.4 (July 2011), p. 655. DOI: 10.1007/s00180-011-0271-3 (cited on page 64).

[93] Andrej Gisbrecht. 'Advances in dissimilarity-based data visualisation'. PhD thesis. Germany: Bielefeld University, 2015 (cited on page 64).

[94] Joy Lowe and Machdel Matthee. 'Requirements of Data Visualisation Tools to Analyse Big Data: A Structured Literature Review'. In: *Responsible Design, Implementation and Use of Information and Communication Technology*. Ed. by Marié Hattingh et al. Lecture Notes in Computer Science. Cham: Springer International Publishing, 2020, pp. 469–480. DOI: 10.1007/978-3-030-44999-5_39 (cited on pages 64–66).

[95] Brady Peters. 'Acoustic Performance as a Design Driver: Sound Simulation and Parametric Modeling Using SmartGeometry'. In: *International Journal of Architectural Computing* 8.3 (Sept. 2010), pp. 337–358. DOI: 10.1260/1478-0771.8.3.337 (cited on pages 64, 144).

[96] Odeon A/S. *https://odeon.dk*. May 2022. URL: https://odeon.dk/ (cited on pages 65, 82).

[97] CATT-Acoustic. *https://www.catt.se/*. May 2022. URL: https://www.catt.se/ (cited on pages 65, 82).

[98] Svante Wold, Kim Esbensen, and Paul Geladi. 'Principal component analysis'. In: *Chemometrics and Intelligent Laboratory Systems*. Proceedings of the Multivariate Statistical Workshop for Geologists and Geochemists 2.1 (Aug. 1987), pp. 37–52. DOI: 10.1016/0169-7439(87)80084-9 (cited on pages 65, 84).

[99] Laurens Van der Maaten and Geoffrey Hinton. 'Visualizing data using t-SNE.' In: *Journal of machine learning research* 9.11 (2008) (cited on pages 65, 84).

[100] Yi Chen et al. 'A survey on visualization approaches for exploring association relationships in graph data'. In: *Journal of Visualization* 22.3 (June 2019), pp. 625–639. DOI: 10.1007/s12650-019-00551-y (cited on page 66).

[101] Wonhee Cho et al. 'Big Data Analysis with Interactive Visualization using R packages'. In: *Proceedings of the 2014 International Conference on Big Data Science and Computing*. BigDataScience '14. New York, NY, USA: Association for Computing Machinery, Aug. 2014, pp. 1–6. DOI: 10.1145/2640087.2644168 (cited on page 66).

[102] Zhanping Liu. 'A prototype framework for parallel visualization of large flow data'. In: *Advances in Engineering Software* 130 (Apr. 2019), pp. 14–23. DOI: 10.1016/j.advengsoft.2019.02.004 (cited on page 66).

[103] Guangchen Ruan and Hui Zhang. 'Closed-loop Big Data Analysis with Visualization and Scalable Computing'. In: *Big Data Research*. Tutorials on Tools and Methods using High Performance Computing resources for Big Data 8 (July 2017), pp. 12–26. DOI: 10.1016/j.bdr.2017.01.002 (cited on page 66).

[104] Benson Mwangi, Jair C. Soares, and Khader M. Hasan. 'Visualization and unsupervised predictive clustering of high-dimensional multimodal neuroimaging data'. In: *Journal of Neuroscience Methods* 236 (Oct. 2014), pp. 19–25. DOI: 10.1016/j.jneumeth.2014.08.001 (cited on page 66).

[105] Seokyeon Kim et al. 'Big Data Visual Analytics System for Disease Pattern Analysis'. In: *Proceedings of the 2015 International Conference on Big Data Applications and Services*. BigDAS '15. New York, NY, USA: Association for Computing Machinery, Oct. 2015, pp. 175–179. DOI: 10.1145/2837060.2837089 (cited on page 66).

[106] ISO. *ISO 354:2003 Acoustics — Measurement of sound absorption in a reverberation room*. 2003. URL: https://www.iso.org/cms/render/live/en/sites/isoorg/contents/data/standard/03/45/34545.html (cited on page 74).

[107] ORASE. *oraser.org*. Jan. 2022. URL: https://www.orase.org/resources (cited on page 82).

[108] Brady Peters. 'Integrating acoustic simulation in architectural design workflows: the FabPod meeting room prototype'. In: *SIMULATION* 91.9 (2015), pp. 787–808. DOI: 10.1177/0037549715603480 (cited on pages 83, 96, 146).

[109] Anke Pasold and Mads Brath Jensen Isak Worre Foged. 'Evolution of an Instrumental Architecture'. In: *Thompson, Emine Mine (ed.), Fusion - Proceedings of the 32nd eCAADe Conference - Volume 2, Department of Architecture and Built Environment, Faculty of Engineering and Environment, Newcastle upon Tyne, England, UK, 10-12 September 2014, pp. 365-372*. CUMINCAD, 2014 (cited on page 83).

[110] Trevor J. Cox and Peter D'Antonio. 'Acoustic phase gratings for reduced specular reflection'. In: *Applied Acoustics* 60.2 (June 2000), pp. 167–186. DOI: 10.1016/S0003-682X(99)00055-9 (cited on page 83).

[111] Manfred R. Schroeder. 'Diffuse sound reflection by maximum-length sequences'. In: *The Journal of the Acoustical Society of America* 57.1 (1975), p. 149. DOI: 10.1121/1.380425 (cited on pages 83, 144).

[112] Angela Gorgoglione et al. 'A Comparison of Linear and Non-Linear Machine Learning Techniques (PCA and SOM) for Characterizing Urban Nutrient Runoff'. In: *Sustainability* 13.4 (Jan. 2021). Number: 4 Publisher: Multidisciplinary Digital Publishing Institute, p. 2054. DOI: 10.3390/su13042054 (cited on page 84).

[113] Asim Mazin et al. 'Identification of sarcomatoid differentiation in renal cell carcinoma by machine learning on multiparametric MRI'. In: *Scientific Reports* 11.1 (Feb. 2021). Bandiera_abtest: a Cc_license_type: cc_by Cg_type: Nature Research Journals Number: 1 Primary_atype: Research Publisher: Nature Publishing Group Subject_term: Cancer imaging;Diagnostic markers;Renal cancer Subject_term_id: cancer-imaging;diagnostic-markers;renal-cancer, p. 3785. DOI: 10.1038/s41598-021-83271-4 (cited on page 84).

[114] Benyamin Motevalli, Baichuan Sun, and Amanda S. Barnard. 'Understanding and Predicting the Cause of Defects in Graphene Oxide Nanostructures Using Machine Learning'. In: *The Journal of Physical Chemistry C* 124.13 (Apr. 2020). Publisher: American Chemical Society, pp. 7404–7413. DOI: 10.1021/acs.jpcc.9b10615 (cited on page 84).

[115] Yosihiro Kobayashi. 'Self-Organizing Map and Axial Spatial Arrangement: Topological Mapping of Alternative Designs'. In: *Synthetic Landscapes [Proceedings of the 25th Annual Conference of the Association for Computer-Aided Design in Architecture] pp. 342-355*. CUMINCAD, 2006 (cited on page 84).

[116] Vahid Moosavi. 'Contextual mapping: Visualization of high-dimensional spatial patterns in a single geo-map'. In: *Computers, Environment and Urban Systems* 61 (Jan. 2017), pp. 1–12. DOI: 10.1016/j.compenvurbsys.2016.08.005 (cited on page 84).

[117] Giuseppe Vettigli. *MiniSom: minimalistic and NumPy-based implementation of the Self Organizing Map*. 2018 (cited on page 88).

[118] Lukas Fuhrimann et al. 'Data-Driven Design: Exploring new Structural Forms using Machine Learning and Graphic Statics'. In: *Proceedings of IASS Annual Symposia* 2018.2 (July 2018), pp. 1–8 (cited on page 89).

[119] John Hearty. *Advanced Machine Learning with Python*. Packt Publishing Ltd, 2016 (cited on page 91).

[120] ISO. *ISO 17497-1 Acoustics – Sound-scattering properties of surfaces – Part 1: Measurement of the random-incidence scattering coefficient in a reverberation room*. 2004. URL: http://www.iso.org/cms/render/live/en/sites/isoorg/contents/data/standard/03/13/31397.html (cited on pages 113, 117, 146).

[121] McNeel Robert and Associates. *Rhinoceros 3D*. 2023. URL: https://www.rhino3d.com/ (cited on page 117).

[122] Tom Van Mele and many others. *COMPAS: A framework for computational research in architecture and structures.* 2017 (cited on page 117).

[123] Sergey Ioffe and Christian Szegedy. 'Batch normalization: Accelerating deep network training by reducing internal covariate shift'. In: *International conference on machine learning*. PMLR, 2015, pp. 448–456 (cited on pages 129, 133).

[124] Andrew L Maas, Awni Y Hannun, and Andrew Y Ng. 'Rectifier nonlinearities improve neural network acoustic models'. In: *Proc. icml*. Vol. 30. Citeseer, 2013, p. 3 (cited on pages 129, 133).

[125] Michael Vorländer and Eckard Mommertz. 'Definition and measurement of random-incidence scattering coefficients'. In: *Applied Acoustics* 60.2 (June 2000), pp. 187–199. DOI: 10.1016/S0003-682X(99)00056-0 (cited on page 135).

[126] ISO. *ISO 10534-2 Acoustics - Determination of sound absorption coefficient and impedance in impedance tubes - Part 2: Transfer-function method*. Nov. 1998. URL: http://www.iso.org/cms/render/live/en/sites/isoorg/contents/data/standard/02/28/22851.html (cited on page 138).

[127] Peter D'Antonio and John H. Konnert. 'Two-Dimensional Primitive Root Diffuror'. Pat. Issue: 19 ISBN: 1312013125. 1995 (cited on page 139).

[128] Branko Kolarevic. 'Back to the future: performative architecture'. In: *International Journal of Architectural Computing* 2.1 (2004). Publisher: SAGE Publications Sage UK: London, England, pp. 43–50 (cited on page 144).

[129] Rivka Oxman. 'Performance-based design: current practices and research issues'. In: *International journal of architectural computing* 6.1 (2008). Publisher: SAGE Publications Sage UK: London, England, pp. 1–17 (cited on page 144).

[130] Ingolf Bork. 'Report on the 3rd round robin on room acoustical computer simulation–Part I: Measurements'. In: *Acta Acustica united with Acustica* 91.4 (2005), pp. 740–752 (cited on page 144).

[131] Ingolf Bork. 'Report on the 3rd round robin on room acoustical computer simulation–Part II: Calculations'. In: *Acta Acustica united with Acustica* 91.4 (2005), pp. 753–763 (cited on page 144).

[132] Maximilian Vomhof et al. 'Robotic Fabrication of Acoustic Brick Walls'. In: *ACADIA 14: Design Agency [Proceedings of the 34th Annual Conference of the Association for Computer Aided Design in Architecture (ACADIA)] Los Angeles 23-25 October, 2014*. CUMINCAD, 2014, pp. 555–564 (cited on pages 144, 145, 148).

[133] Claus Lynge Christensen and Jens Holger Rindel. 'A new scattering method that combines roughness and diffraction effects Geometrical model The Reflection Based Scattering coefficient'. In: *Forum Acusticum, Budapest, Hungary* (2005). ISBN: 9638241683, pp. 2159–2164. DOI: 10.1121/1.4788035 (cited on page 145).

[134] Lily M. Wang and Jonathan Rathsam. 'The influence of absorption factors on the sensitivity of a virtual room's sound field to scattering coefficients'. In: *Applied Acoustics* 69.12 (Dec. 2008), pp. 1249–1257. DOI: 10.1016/j.apacoust.2007.09.007 (cited on page 146).

[135] Nicholas Williams et al. 'FabPod: Designing with temporal flexibility & relationships to mass-customisation'. In: *Automation in Construction* 51 (2015). Publisher: Elsevier, pp. 124–131 (cited on page 146).

List of Figures

List of Tables

List of Abbreviations

A

AADS Data Science Enabled Acoustic Design for Digital Fabrication in Architecture. 16, 36, 59, 78, 150

α Absorption Coefficient. 15

B

BEM Boundary Element Method. 113

C

C50 Clarity. 10, 65

CE Cumulative Energy. 32, 78, 104, 105, 177

CNN Convolutional Neural Network. 125, 133, 134

CRNN Convolutional Recurrent Neural Network. 11

D

D Definition. 10, 65

DDAD Data-Driven Acoustic Design. 117, 146, 147, 149–151, 156, 178

E

EDT Early Decay Time. 10, 11, 15, 24, 84

F

FDTD Finite-Difference Time-Domain method. 29, 113, 146

FEM Finite Element Method. 113

FFT Fast Fourier Transform. 67, 147, 149, 151, 155, 178

G

G Strength. 65

GA Geometrical Acoustics. 9, 10, 22, 42, 115, 118, 135, 144–146

GIR Dataset Geometry and Impulse Response Dataset. 16–18, 21, 23–25, 30–32, 34, 36, 37, 67, 80, 84–86, 88, 96, 97, 100–102, 110, 111, 113–117, 123, 135, 137–140, 149, 176, 178

H

HPF High-pass Filter. 71

I

IDL Immersive Design Lab. 18, 143, 144, 151

IR Impulse Response. 12, 15, 21, 23–26, 28–33, 35, 36, 40, 43, 44, 47–50, 58, 59, 65, 67, 69, 71, 78, 83–85, 88, 89, 113, 116, 121, 129–131, 133, 134, 136, 139, 174, 175, 182

L

LPF Low-pass Filter. 71

M

ML Machine Learning. 11–13, 16, 17, 21, 23–25, 30, 34, 36, 37, 49, 59, 83–85, 110, 112, 113, 116–118, 130

MSE Mean Square Error. 130, 131, 182

N

NCE Normalised Cumulative Energy. 50, 89, 97

NN Neural Network. 24, 32, 36, 125, 129

P

PCA Principal Component Analysis. 15, 33, 37, 58, 84, 174

PRD Diffuser Primitive Root Diffuser. 104–106, 137, 139, 140, 150, 151, 177, 178

R

R Complex Reflection Factor. 136

RT Reverberation Time. 5, 10, 11, 24, 65, 84

S

SDSC Swiss Data Science Center. 16, 36, 37, 59, 60

SOM Self-Organising Map. 15, 59, 74, 84, 85, 88–97, 176, 177, 181

T

TCE Total Cumulative Energy. 104, 105, 151

TNCE Total Normalised Cumulative Energy. 32, 50–52, 55–59, 89, 90, 94, 96, 97, 104, 106, 116, 174–177, 181

TS Centre Time. 65

X

XR Extended Reality. 144

This dissertation is designed and typeset by the author using LaTeX and the kaobook template. All images by the authors, unless stated otherwise.

Acoustics are rarely included as a design driver in the early phases of design due to the multi-faceted nature of sound and the complex and time-consuming analysis process of room acoustics software. Inevitably this results in architectural spaces with poor acoustics, where treatment is either disregarded or focuses only on noise prevention using absorbent materials. However, most commonly used construction materials have sound-reflecting properties and can be configured into sound-diffusive surfaces. These surfaces can help reduce unwanted flattered echoes, colourisation, and image shift and create a more pleasant and comfortable environment without needing additional elements (e.g. absorption panels). Faster and simpler analysis tools are required to harness the potential of diffusion in architectural design.

This dissertation presents a new data-driven approach to designing and evaluating the acoustic properties of architectural surfaces. It investigates the use of machine-learning techniques to study the mutual relationship between geometry and sound diffusion. It introduces a new acoustic dataset meant as a basis for training predictive machine-learning models. These models enable the creation of fast, less cumbersome, and reasonably accurate acoustics analysis tools. It proposes and implements a new automated multi-robotic data-acquisition method for collecting impulse responses from scale-modelled surfaces. It also develops computational tools to design and generate three-dimensional wall-like surface geometries. The geometrical characteristics of these surfaces are based on commonly used construction materials and techniques. A computational framework is developed in parallel to process the collected data and generate customisable and interactive visualisations for low- and high-dimensional data. This framework caters to both expert and non-expert users in acoustics, providing expert users with familiar descriptors and visualisations and introducing non-experts to simpler ones. Furthermore, to address users with no programming knowledge, it develops a web-based application enabling easy access to the collected dataset, the acoustic descriptors, and visualisations. It introduces a new workflow to the performance-driven acoustic design of sound-diffusing wall surfaces, allowing architects and designers to explore alternative wall designs with sound-diffusing properties, given a set of desired acoustic performance criteria.

The proposed workflow has the potential to bring acoustics closer to the early phases of architectural design and enable a more integrative acoustic and architectural design exploration. Providing architects and acousticians with comprehensive and user-friendly tools for acoustics analysis can help integrate acoustics into the design process from the beginning rather than as an afterthought.

DISS. ETH NO. 29211

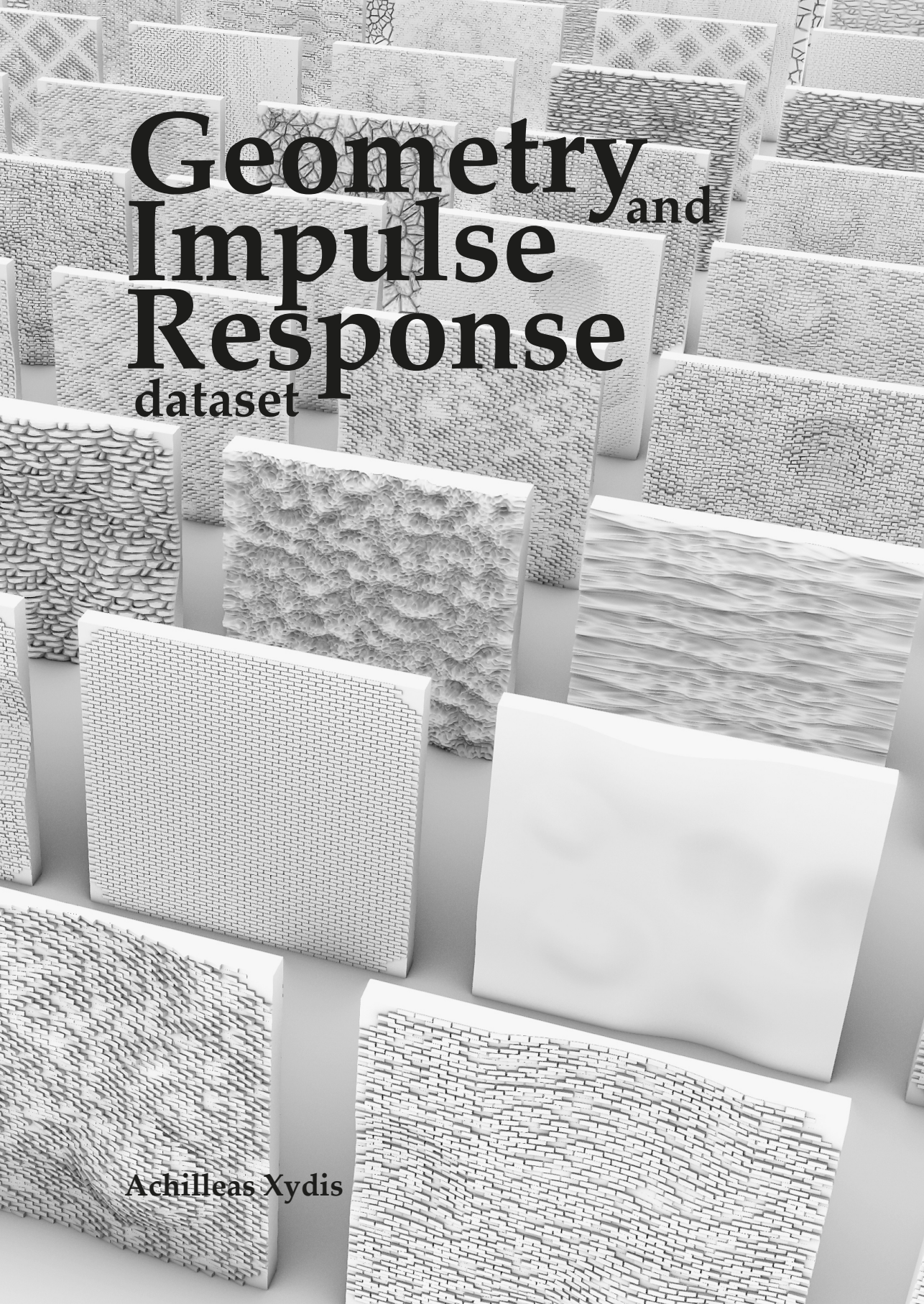

Geometry and Impulse Response dataset

Achilleas Xydis

The GIR Dataset can be downloaded freely for research purposes from Zenodo doi.org/10.5281/zenodo.5288743 and is released under the GNU General Public License v3.0[1]. The dataset contains 312 samples, and for each one, the following metadata is provided:

1: https://renkulab.io/projects/ddad/gir-dataset/files/blob/LICENSE

- A 3D Mesh geometry saved as an *.obj* file
- 2951 impulse responses in a 2951×400 $float32$ matrix, saved in an *.npz* file.
- A metadata file saves as a *.json* file. The content of this file is shown below in Table 1.

Table 1: The content of the metadata file.

Variable	Data type	Description
panel_id	string	The ID of the panel
start_time	string	The date and time the measuring process started in ISO 8601 format, YYYY-MM-DDTHH:MM:SS.mmmmmm
end_time	string	The date and time the measuring process ended in ISO 8601 format, YYYY-MM-DDTHH:MM:SS.mmmmmm
package_time	string	The date and time all recordings were processed and stored in ISO 8601 format, YYYY-MM-DDTHH:MM:SS.mmmmmm
impulse_responses_file	string	The name of the *.npz* file containing all IRs
geometry_file	string	The name of the *.obj* file containing the panel geometry
recording_sample_rate	integer	The sample rate of the recording in Hz/sec
reference_resampling_temperature	integer	The temperature in Celsius that was used to resample the IRs
print_provider	string	The name of the printing service
print_machine	string	The name of the printer
print_sand_type	string	The type of sand used in the 3D printer
print_binder_type	string	The type of binder used in the 3D printer
microphone_model	string	The model of the microphone use in the recording
typology	string	The typology of the panel
macrostructure	string	The macrostructure that was used to generate the panel's geometry. It corresponds to the panel_id of a panel that was created using only that macrostructure. When flat, no macrostructure was used
measurements		extra metadata info for each of the 2951 measurements
combination	integer	The microphone-speaker combination number. It starts from 1 and goes up to 2952
fluid_pressure	float	Air pressure inside the room in Pa
relative_humidity	float	Air humidity inside the room in %
sound_level	float	The sound level outside the room in dB
temperature	float	The temperature inside the room in C
distance	float	The distance between microphone and speaker frame in mm
end_time	string	The date and time of the successful recording in ISO 8601 format, YYYY-MM-DDTHH:MM:SS.mmmmmm

More information on its content, the collection setup, and methodology can be found in the main volume of this dissertation. The next section provides an overview of all dataset samples listing their main properties alongside a front view and a close-up rendering of their geometry.

baseline_3dprint_0

date_measured	date_processed
06-01-2020	06-01-2020
temperature	**humidity**
12.5 °C - 12.7 °C	50.4 % - 50.0 %
pressure	**macrostructure**
966.6 *Pa* - 966.6 *Pa*	flat
printer	**printer_binder**
Voxeljet VX4000	Phenolic binder

baseline_3dprint_1

date_measured	date_processed
07-01-2020	07-01-2020
temperature	**humidity**
12.6 °C - 12.8 °C	50.5 % - 50.7 %
pressure	**macrostructure**
969.3 *Pa* - 969.2 *Pa*	flat
printer	**printer_binder**
Voxeljet VX4000	Phenolic binder

baseline_flat1_0

date_measured	date_processed
22-10-2020	23-10-2020
temperature	**humidity**
18.1 °C - 18.3 °C	55.2 % - 56.1 %
pressure	**macrostructure**
959.1 *Pa* - 959.1 *Pa*	flat
printer	**printer_binder**
Voxeljet VX4000	Phenolic binder

baseline_flat1_1

date_measured	date_processed
23-10-2020	23-10-2020
temperature	**humidity**
18.2 °C - 18.4 °C	56.5 % - 57.6 %
pressure	**macrostructure**
956.4 *Pa* - 956.4 *Pa*	flat
printer	**printer_binder**
Voxeljet VX4000	Phenolic binder

baseline_flat_cg_0

date_measured	**date_processed**
14-08-2020	14-08-2020
temperature	**humidity**
23.1 °C - 23.3 °C	66.2 % - 66.1 %
pressure	**macrostructure**
957.9 *Pa* - 957.9 *Pa*	flat
printer	**printer_binder**
ExOne S-Max	Furan binder

baseline_flat_cg_1

date_measured	**date_processed**
16-08-2020	16-08-2020
temperature	**humidity**
23.2 °C - 23.4 °C	66.7 % - 65.1 %
pressure	**macrostructure**
953.4 *Pa* - 953.4 *Pa*	flat
printer	**printer_binder**
ExOne S-Max	Furan binder

baseline_flat_vj_0

date_measured	**date_processed**
09-08-2020	09-08-2020
temperature	**humidity**
22.8 °C - 22.9 °C	64.2 % - 63.1 %
pressure	**macrostructure**
960.5 *Pa* - 960.5 *Pa*	flat
printer	**printer_binder**
PDB	Phenolic binder

baseline_flat_vj_1

date_measured	**date_processed**
09-08-2020	10-08-2020
temperature	**humidity**
22.9 °C - 22.9 °C	63.2 % - 64.0 %
pressure	**macrostructure**
956.8 *Pa* - 956.8 *Pa*	flat
printer	**printer_binder**
PDB	Phenolic binder

baseline_foam_2

date_measured	date_processed
30-01-2020	31-01-2020
temperature	**humidity**
12.3 °C - 12.4 °C	51.9 % - 53.8 %
pressure	**macrostructure**
954.1 *Pa* - 954.1 *Pa*	flat
printer	**printer_binder**
None	None

baseline_foam_3

date_measured	date_processed
11-06-2020	12-06-2020
temperature	**humidity**
18.9 °C - 19.1 °C	61.5 % - 60.7 %
pressure	**macrostructure**
948.5 *Pa* - 948.5 *Pa*	flat
printer	**printer_binder**
None	None

baseline_foam_4

date_measured	date_processed
13-06-2020	14-06-2020
temperature	**humidity**
18.9 °C - 19.1 °C	62.5 % - 63.0 %
pressure	**macrostructure**
951.1 *Pa* - 951.1 *Pa*	flat
printer	**printer_binder**
None	None

baseline_foam_5

date_measured	date_processed
21-10-2020	22-10-2020
temperature	**humidity**
18.3 °C - 18.4 °C	50.4 % - 52.6 %
pressure	**macrostructure**
953.3 *Pa* - 953.3 *Pa*	flat
printer	**printer_binder**
None	None

baseline_foam_6

date_measured	date_processed
22-10-2020	22-10-2020
temperature	**humidity**
18.2 °C - 18.2 °C	53.3 % - 54.6 %
pressure	**macrostructure**
958.8 *Pa* - 958.8 *Pa*	flat
printer	**printer_binder**
None	None

baseline_qrd_400_2000

date_measured	date_processed
09-01-2020	13-01-2020
temperature	**humidity**
12.7 °C - 13.2 °C	50.2 % - 49.1 %
pressure	**macrostructure**
962.3 *Pa* - 962.3 *Pa*	flat
printer	**printer_binder**
Voxeljet VX4000	Phenolic binder

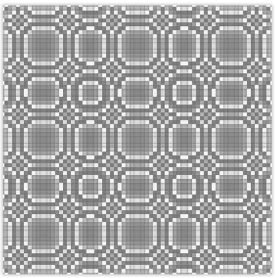

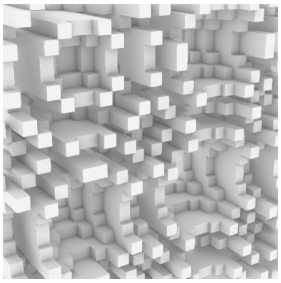

baseline_qrd_400_4000

date_measured	date_processed
14-01-2020	14-01-2020
temperature	**humidity**
13.0 °C - 13.1 °C	49.3 % - 48.4 %
pressure	**macrostructure**
958.1 *Pa* - 958.1 *Pa*	flat
printer	**printer_binder**
Voxeljet VX4000	Phenolic binder

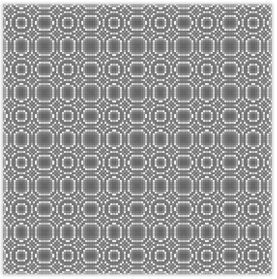

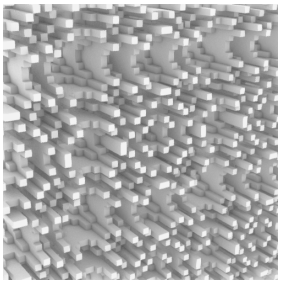

baseline_vj2_0

date_measured	date_processed
04-12-2020	05-12-2020
temperature	**humidity**
14.7 °C - 14.8 °C	41.8 % - 42.5 %
pressure	**macrostructure**
930.4 *Pa* - 930.4 *Pa*	flat
printer	**printer_binder**
FDB	Furan binder

baseline_vj2_1

date_measured	date_processed
07-12-2020	07-12-2020
temperature	**humidity**
14.1 °C - 14.3 °C	45.0 % - 45.0 %
pressure	**macrostructure**
941.3 *Pa* - 941.3 *Pa*	flat
printer	**printer_binder**
FDB	Furan binder

baseline_vj2_r180_0

date_measured	date_processed
04-02-2021	05-02-2021
temperature	**humidity**
11.9 °C - 12.0 °C	61.8 % - 61.4 %
pressure	**macrostructure**
953.8 *Pa* - 953.8 *Pa*	flat
printer	**printer_binder**
FDB	Furan binder

baseline_vj3_0

date_measured	date_processed
09-02-2021	09-02-2021
temperature	**humidity**
12.5 °C - 12.8 °C	56.5 % - 55.1 %
pressure	**macrostructure**
941.6 *Pa* - 941.6 *Pa*	flat
printer	**printer_binder**
FDB	Furan binder

baseline_vj3_1

date_measured	date_processed
10-02-2021	11-02-2021
temperature	**humidity**
12.8 °C - 12.8 °C	53.5 % - 52.1 %
pressure	**macrostructure**
945.9 *Pa* - 945.9 *Pa*	flat
printer	**printer_binder**
FDB	Furan binder

baseline_wood_1

date_measured	date_processed
27-04-2020	28-04-2020
temperature	**humidity**
16.7 °C - 17.0 °C	53.8 % - 56.7 %
pressure	**macrostructure**
949.7 *Pa* - 949.7 *Pa*	flat
printer	**printer_binder**
None	None

baseline_wood_2

date_measured	date_processed
29-08-2020	29-08-2020
temperature	**humidity**
23.1 °C - 23.3 °C	57.7 % - 57.5 %
pressure	**macrostructure**
948.8 *Pa* - 948.8 *Pa*	flat
printer	**printer_binder**
None	None

baseline_wood_3

date_measured	date_processed
29-08-2020	30-08-2020
temperature	**humidity**
23.2 °C - 23.3 °C	58.0 % - 56.3 %
pressure	**macrostructure**
948.1 *Pa* - 948.1 *Pa*	flat
printer	**printer_binder**
None	None

mean_flat_cg

date_measured	date_processed
synthetic	computed
temperature	**humidity**
20.0 °C - 20.0 °C	0 % - 0 %
pressure	**macrostructure**
0 *Pa* - 0 *Pa*	flat
printer	**printer_binder**
ExOne S-Max	Furan binder

mean_flat_rfl_1

date_measured	**date_processed**
synthetic	computed
temperature	**humidity**
20.0 °C - 20.0 °C	0 % - 0 %
pressure	**macrostructure**
0 *Pa* - 0 *Pa*	flat
printer	**printer_binder**
Voxeljet VX4000	Phenolic binder

mean_flat_rfl_2

date_measured	**date_processed**
synthetic	computed
temperature	**humidity**
20.0 °C - 20.0 °C	0 % - 0 %
pressure	**macrostructure**
0 *Pa* - 0 *Pa*	flat
printer	**printer_binder**
Voxeljet VX4000	Phenolic binder

mean_flat_vj_fu

date_measured	**date_processed**
synthetic	computed
temperature	**humidity**
20.0 °C - 20.0 °C	0 % - 0 %
pressure	**macrostructure**
0 *Pa* - 0 *Pa*	flat
printer	**printer_binder**
FDB	Furan binder

mean_flat_vj_ph

date_measured	**date_processed**
synthetic	computed
temperature	**humidity**
20.0 °C - 20.0 °C	0 % - 0 %
pressure	**macrostructure**
0 *Pa* - 0 *Pa*	flat
printer	**printer_binder**
PDB	Phenolic binder

mean_foam_1

date_measured	date_processed
synthetic	computed
temperature	**humidity**
20.0 °C - 20.0 °C	0 % - 0 %
pressure	**macrostructure**
0 *Pa* - 0 *Pa*	flat
printer	**printer_binder**
None	None

mean_foam_2

date_measured	date_processed
synthetic	computed
temperature	**humidity**
20.0 °C - 20.0 °C	0 % - 0 %
pressure	**macrostructure**
0 *Pa* - 0 *Pa*	flat
printer	**printer_binder**
None	None

mean_wood

date_measured	date_processed
synthetic	computed
temperature	**humidity**
20.0 °C - 20.0 °C	0 % - 0 %
pressure	**macrostructure**
0 *Pa* - 0 *Pa*	flat
printer	**printer_binder**
None	None

panel_0001_0

date_measured	date_processed
03-02-2020	03-02-2020
temperature	**humidity**
12.5 °C - 12.7 °C	64.2 % - 64.6 %
pressure	**macrostructure**
958.8 *Pa* - 958.8 *Pa*	panel_0015_0
printer	**printer_binder**
Voxeljet VX4000	Phenolic binder

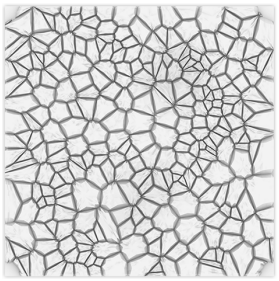

panel_0001_1

date_measured	**date_processed**
03-02-2020	04-02-2020
temperature	**humidity**
12.7 °C - 12.8 °C	65.3 % - 63.8 %
pressure	**macrostructure**
957.4 *Pa* - 957.4 *Pa*	panel_0015_1
printer	**printer_binder**
Voxeljet VX4000	Phenolic binder

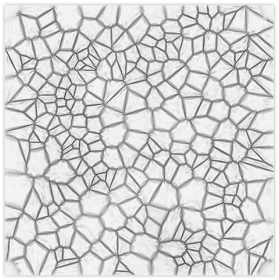


panel_0002_1

date_measured	**date_processed**
14-03-2020	26-03-2020
temperature	**humidity**
13.3 °C - 14.0 °C	50.4 % - 40.3 %
pressure	**macrostructure**
960.3 *Pa* - 960.3 *Pa*	panel_0015_1
printer	**printer_binder**
Voxeljet VX4000	Phenolic binder

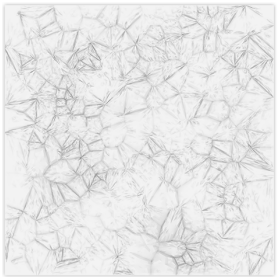
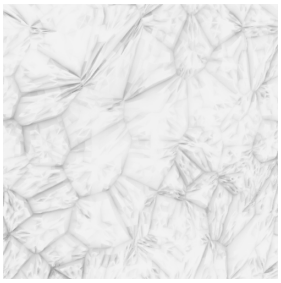

panel_0002reprint_0

date_measured	**date_processed**
29-07-2020	30-07-2020
temperature	**humidity**
22.3 °C - 22.5 °C	63.1 % - 61.1 %
pressure	**macrostructure**
958.7 *Pa* - 958.7 *Pa*	panel_0015_0
printer	**printer_binder**
ExOne S-Max	Furan binder

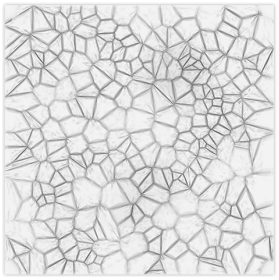
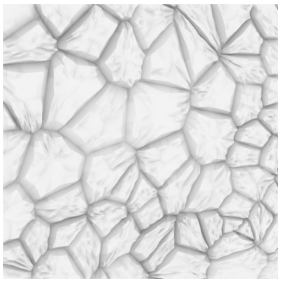

panel_0002reprint_1

date_measured	**date_processed**
30-07-2020	30-07-2020
temperature	**humidity**
22.4 °C - 22.6 °C	60.9 % - 60.7 %
pressure	**macrostructure**
961.1 *Pa* - 961.1 *Pa*	panel_0015_1
printer	**printer_binder**
ExOne S-Max	Furan binder

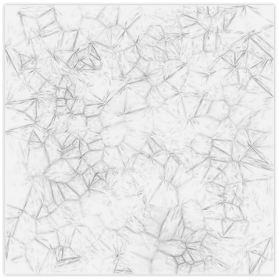
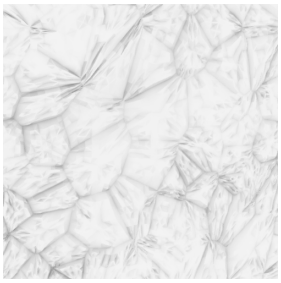

panel_0003_0

date_measured	date_processed
25-10-2019	27-10-2019
temperature	**humidity**
18.8 °C - 19.1 °C	63.6 % - 62.4 %
pressure	**macrostructure**
963.3 *Pa* - 963.3 *Pa*	panel_0015_0
printer	**printer_binder**
Voxeljet VX4000	Phenolic binder

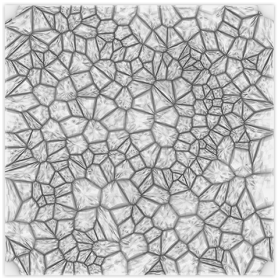

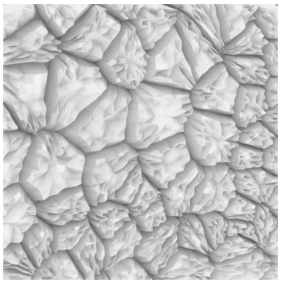

panel_0003_1

date_measured	date_processed
01-11-2019	04-11-2019
temperature	**humidity**
18.3 °C - 18.2 °C	57.8 % - 57.7 %
pressure	**macrostructure**
948.1 *Pa* - 948.0 *Pa*	panel_0015_1
printer	**printer_binder**
Voxeljet VX4000	Phenolic binder

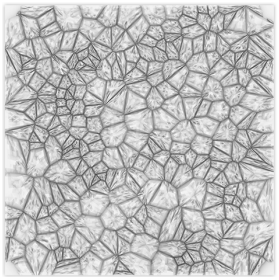

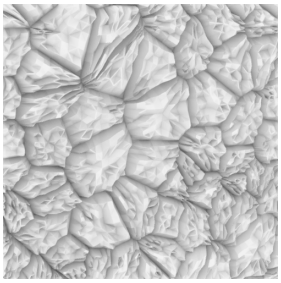

panel_0003rereprint_0

date_measured	date_processed
20-01-2021	21-01-2021
temperature	**humidity**
10.6 °C - 10.9 °C	46.6 % - 47.3 %
pressure	**macrostructure**
947.6 *Pa* - 947.6 *Pa*	panel_0015_0
printer	**printer_binder**
ExOne S-Max	Furan binder

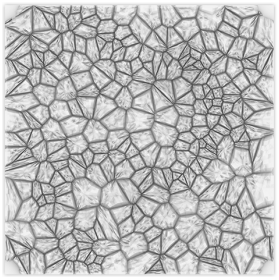

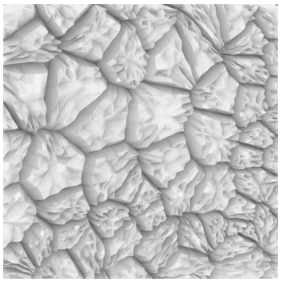

panel_0003rereprint_1

date_measured	date_processed
28-01-2021	29-01-2021
temperature	**humidity**
11.0 °C - 11.2 °C	49.1 % - 50.8 %
pressure	**macrostructure**
947.7 *Pa* - 947.7 *Pa*	panel_0015_1
printer	**printer_binder**
ExOne S-Max	Furan binder

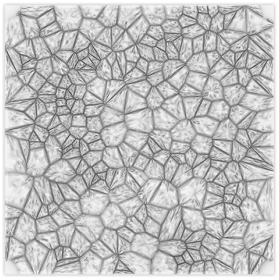

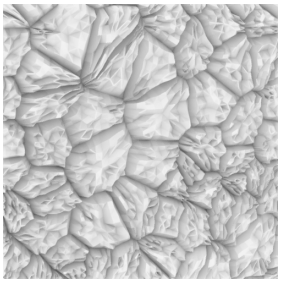

panel_0004_0

date_measured	date_processed
02-04-2020	06-04-2020
temperature	**humidity**
13.4 °C - 13.4 °C	40.1 % - 45.3 %
pressure	**macrostructure**
950.5 *Pa* - 950.5 *Pa*	panel_0015_0
printer	**printer_binder**
Voxeljet VX4000	Phenolic binder

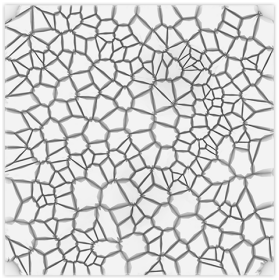

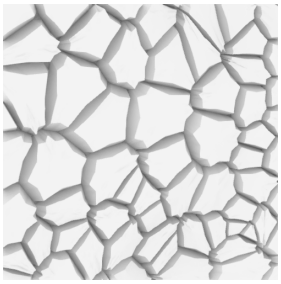

panel_0004_1

date_measured	date_processed
27-04-2020	27-04-2020
temperature	**humidity**
16.6 °C - 16.7 °C	55.3 % - 54.2 %
pressure	**macrostructure**
952.2 *Pa* - 952.2 *Pa*	panel_0015_1
printer	**printer_binder**
Voxeljet VX4000	Phenolic binder

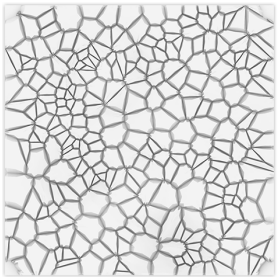

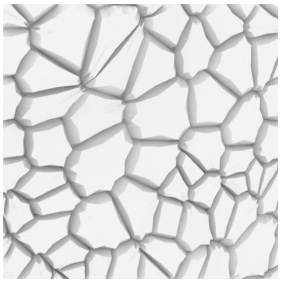

panel_0005_0

date_measured	date_processed
18-12-2019	19-12-2019
temperature	**humidity**
13.8 °C - 13.7 °C	55.7 % - 56.5 %
pressure	**macrostructure**
957.9 *Pa* - 957.9 *Pa*	panel_0015_0
printer	**printer_binder**
Voxeljet VX4000	Phenolic binder

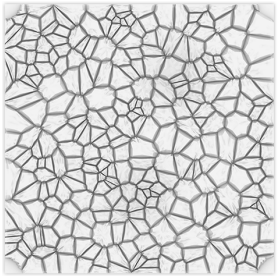

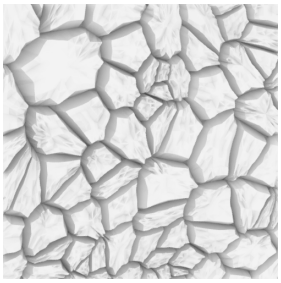

panel_0005_1

date_measured	date_processed
19-12-2019	20-12-2019
temperature	**humidity**
13.6 °C - 13.7 °C	57.0 % - 56.1 %
pressure	**macrostructure**
950.5 *Pa* - 950.5 *Pa*	panel_0015_1
printer	**printer_binder**
Voxeljet VX4000	Phenolic binder

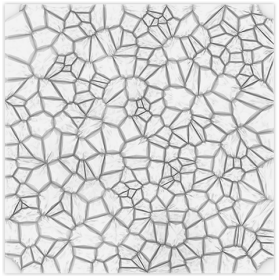

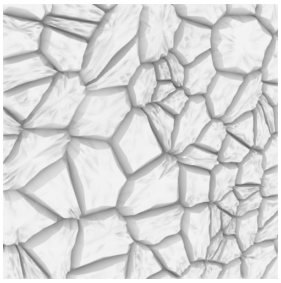

panel_0006_0

date_measured	**date_processed**
20-12-2019	21-12-2019
temperature	**humidity**
13.7 °C - 13.8 °C	56.2 % - 56.5 %
pressure	**macrostructure**
936.3 *Pa* - 936.3 *Pa*	panel_0015_0
printer	**printer_binder**
Voxeljet VX4000	Phenolic binder

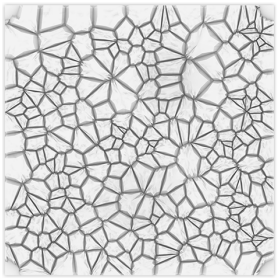
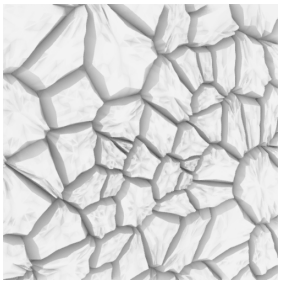

panel_0006_1

date_measured	**date_processed**
23-12-2019	23-12-2019
temperature	**humidity**
13.6 °C - 13.8 °C	56.6 % - 56.1 %
pressure	**macrostructure**
952.1 *Pa* - 952.1 *Pa*	panel_0015_1
printer	**printer_binder**
Voxeljet VX4000	Phenolic binder

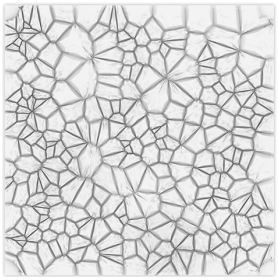
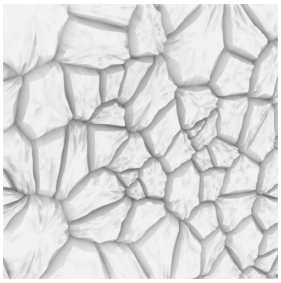

panel_0007_0

date_measured	**date_processed**
24-12-2019	24-12-2019
temperature	**humidity**
13.6 °C - 13.8 °C	55.5 % - 56.0 %
pressure	**macrostructure**
955.7 *Pa* - 955.7 *Pa*	panel_0015_0
printer	**printer_binder**
Voxeljet VX4000	Phenolic binder

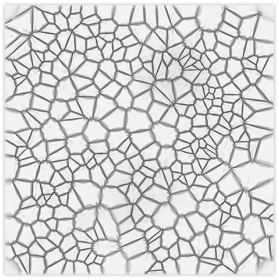
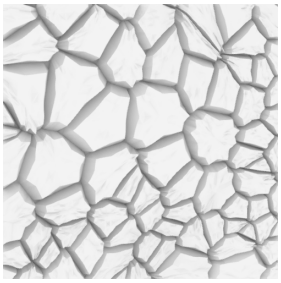

panel_0007_1

date_measured	**date_processed**
27-12-2019	30-12-2019
temperature	**humidity**
13.4 °C - 13.5 °C	55.9 % - 51.4 %
pressure	**macrostructure**
962.5 *Pa* - 962.6 *Pa*	panel_0015_1
printer	**printer_binder**
Voxeljet VX4000	Phenolic binder

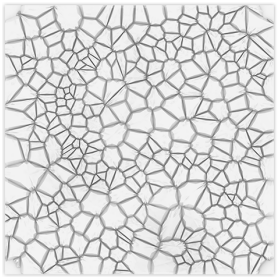
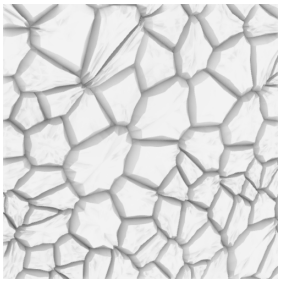

panel_0008_0

date_measured	date_processed
30-12-2019	31-12-2019
temperature	**humidity**
13.2 °C - 13.3 °C	49.9 % - 49.3 %
pressure	**macrostructure**
971.2 *Pa* - 971.2 *Pa*	panel_0015_0
printer	**printer_binder**
Voxeljet VX4000	Phenolic binder

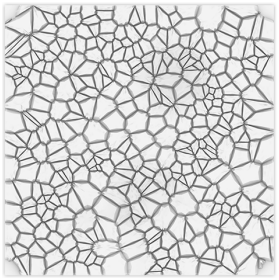
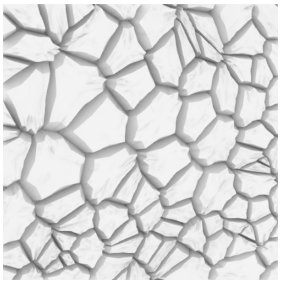

panel_0008_1

date_measured	date_processed
03-01-2020	06-01-2020
temperature	**humidity**
12.8 °C - 12.6 °C	48.6 % - 50.6 %
pressure	**macrostructure**
966.4 *Pa* - 966.4 *Pa*	panel_0015_1
printer	**printer_binder**
Voxeljet VX4000	Phenolic binder

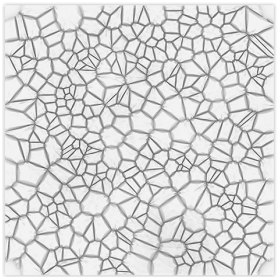


panel_0009_0

date_measured	date_processed
01-02-2020	02-02-2020
temperature	**humidity**
12.6 °C - 12.5 °C	60.1 % - 59.7 %
pressure	**macrostructure**
954.8 *Pa* - 954.8 *Pa*	panel_0015_0
printer	**printer_binder**
Voxeljet VX4000	Phenolic binder

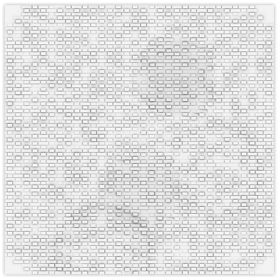
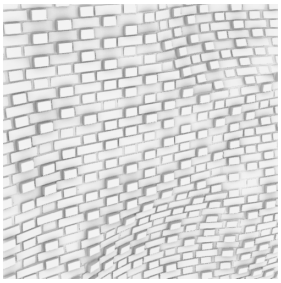

panel_0009_1

date_measured	date_processed
02-02-2020	02-02-2020
temperature	**humidity**
12.4 °C - 12.5 °C	61.4 % - 62.4 %
pressure	**macrostructure**
956.4 *Pa* - 956.4 *Pa*	panel_0015_1
printer	**printer_binder**
Voxeljet VX4000	Phenolic binder

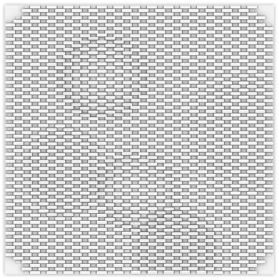
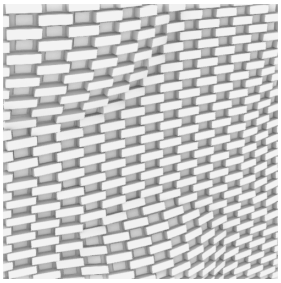

panel_0010_0

date_measured	**date_processed**
20-01-2020	20-01-2020
temperature	**humidity**
12.9 °C - 13.1 °C	48.3 % - 47.3 %
pressure	**macrostructure**
979.6 *Pa* - 979.6 *Pa*	panel_0015_0
printer	**printer_binder**
Voxeljet VX4000	Phenolic binder

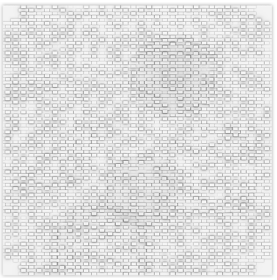

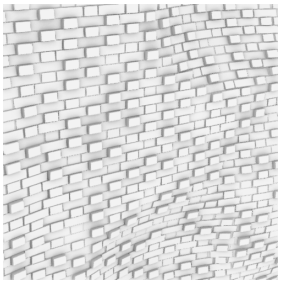

panel_0010_1

date_measured	**date_processed**
20-01-2020	21-01-2020
temperature	**humidity**
13.0 °C - 13.1 °C	46.8 % - 46.3 %
pressure	**macrostructure**
978.2 *Pa* - 978.2 *Pa*	panel_0015_1
printer	**printer_binder**
Voxeljet VX4000	Phenolic binder

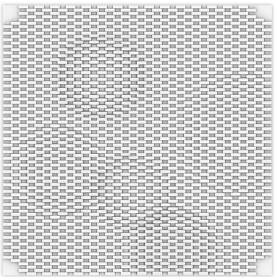

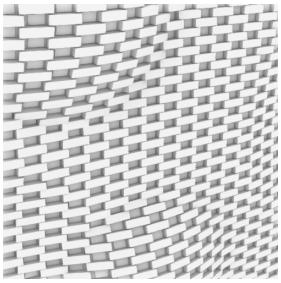

panel_0011_0

date_measured	**date_processed**
17-01-2020	18-01-2020
temperature	**humidity**
13.0 °C - 13.2 °C	51.3 % - 50.1 %
pressure	**macrostructure**
963.9 *Pa* - 963.9 *Pa*	panel_0015_0
printer	**printer_binder**
Voxeljet VX4000	Phenolic binder

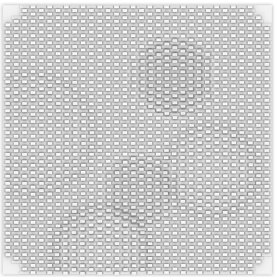

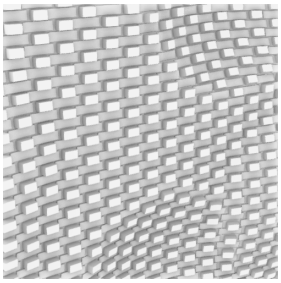

panel_0011_1

date_measured	**date_processed**
19-01-2020	19-01-2020
temperature	**humidity**
12.9 °C - 13.0 °C	48.8 % - 48.9 %
pressure	**macrostructure**
972.5 *Pa* - 972.5 *Pa*	panel_0015_1
printer	**printer_binder**
Voxeljet VX4000	Phenolic binder

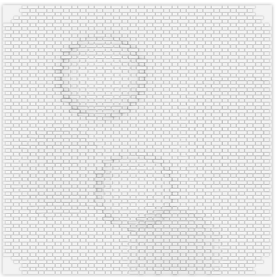

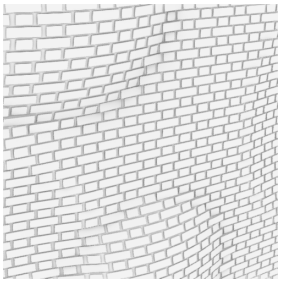

panel_0012_0

date_measured	date_processed
16-01-2020	17-01-2020
temperature	**humidity**
13.1 °C - 13.0 °C	49.2 % - 49.2 %
pressure	**macrostructure**
964.9 Pa - 964.9 Pa	panel_0015_0
printer	**printer_binder**
Voxeljet VX4000	Phenolic binder

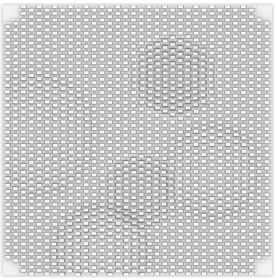
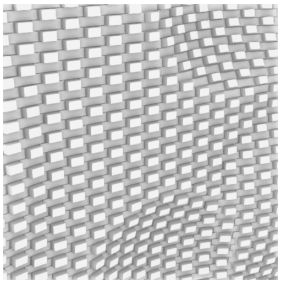

panel_0012_1

date_measured	date_processed
17-01-2020	17-01-2020
temperature	**humidity**
13.2 °C - 13.1 °C	49.2 % - 49.8 %
pressure	**macrostructure**
962.2 Pa - 962.2 Pa	panel_0015_1
printer	**printer_binder**
Voxeljet VX4000	Phenolic binder

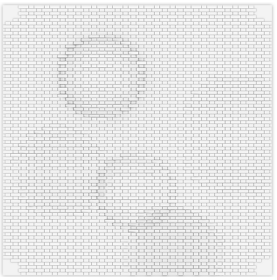
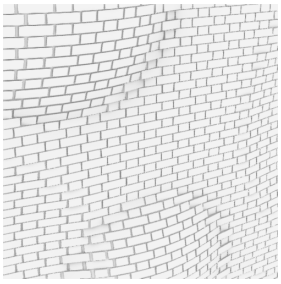

panel_0013_0

date_measured	date_processed
15-01-2020	16-01-2020
temperature	**humidity**
13.1 °C - 13.0 °C	47.8 % - 48.4 %
pressure	**macrostructure**
960.6 Pa - 960.6 Pa	panel_0015_0
printer	**printer_binder**
Voxeljet VX4000	Phenolic binder

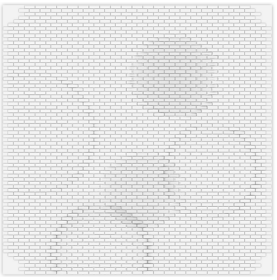
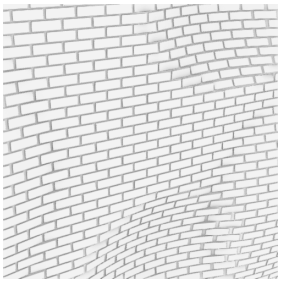

panel_0013_1

date_measured	date_processed
16-01-2020	16-01-2020
temperature	**humidity**
12.9 °C - 13.0 °C	48.8 % - 48.9 %
pressure	**macrostructure**
968.0 Pa - 968.0 Pa	panel_0015_1
printer	**printer_binder**
Voxeljet VX4000	Phenolic binder

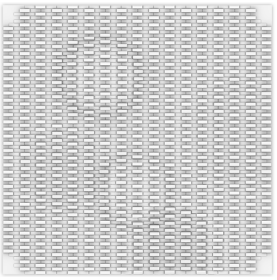
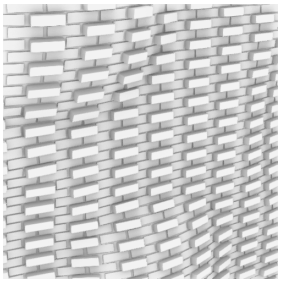

panel_0014_1

date_measured	date_processed
14-01-2020	15-01-2020
temperature	**humidity**
13.0 °C - 13.1 °C	48.1 % - 47.8 %
pressure	**macrostructure**
959.0 *Pa* - 959.0 *Pa*	panel_0015_1
printer	**printer_binder**
Voxeljet VX4000	Phenolic binder

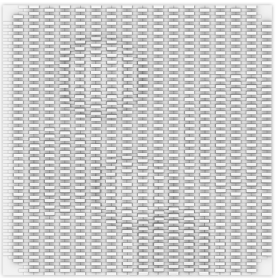

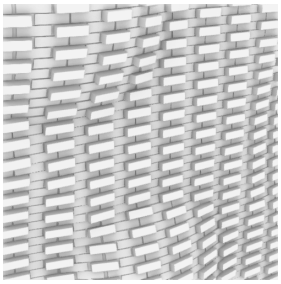

panel_0015_0

date_measured	date_processed
21-01-2020	21-01-2020
temperature	**humidity**
13.0 °C - 13.1 °C	46.0 % - 45.6 %
pressure	**macrostructure**
978.4 *Pa* - 978.4 *Pa*	macrostructure
printer	**printer_binder**
Voxeljet VX4000	Phenolic binder

panel_0015_1

date_measured	date_processed
21-01-2020	22-01-2020
temperature	**humidity**
13.0 °C - 13.0 °C	45.3 % - 45.0 %
pressure	**macrostructure**
974.9 *Pa* - 974.9 *Pa*	macrostructure
printer	**printer_binder**
Voxeljet VX4000	Phenolic binder

panel_0016_0

date_measured	date_processed
28-04-2020	28-04-2020
temperature	**humidity**
17.0 °C - 17.1 °C	57.5 % - 58.8 %
pressure	**macrostructure**
949.0 *Pa* - 949.0 *Pa*	panel_0015_0
printer	**printer_binder**
Voxeljet VX4000	Phenolic binder

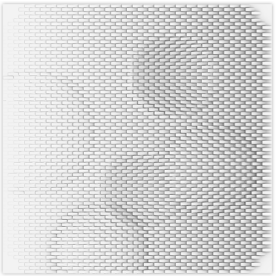

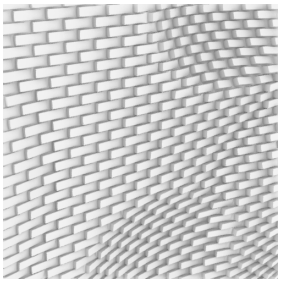

panel_0016_1

date_measured	**date_processed**
22-01-2020	23-01-2020
temperature	**humidity**
12.9 °C - 13.0 °C	44.5 % - 44.4 %
pressure	**macrostructure**
971.5 *Pa* - 971.5 *Pa*	panel_0015_1
printer	**printer_binder**
Voxeljet VX4000	Phenolic binder

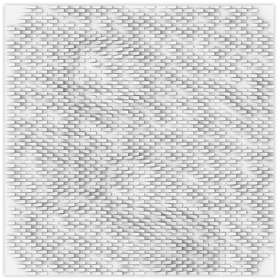
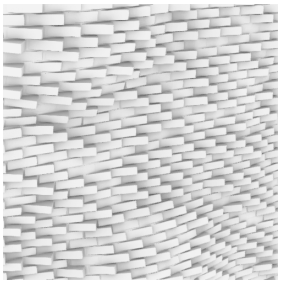

panel_0016_r180_0

date_measured	**date_processed**
28-04-2020	29-04-2020
temperature	**humidity**
17.0 °C - 17.2 °C	59.2 % - 58.1 %
pressure	**macrostructure**
950.6 *Pa* - 950.6 *Pa*	panel_0015_0
printer	**printer_binder**
Voxeljet VX4000	Phenolic binder

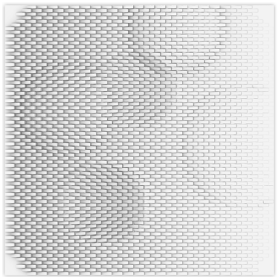
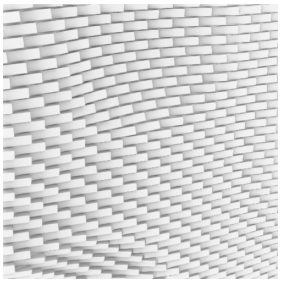

panel_0017_0

date_measured	**date_processed**
24-01-2020	25-01-2020
temperature	**humidity**
12.5 °C - 12.7 °C	44.7 % - 44.7 %
pressure	**macrostructure**
962.5 *Pa* - 962.5 *Pa*	panel_0015_0
printer	**printer_binder**
Voxeljet VX4000	Phenolic binder

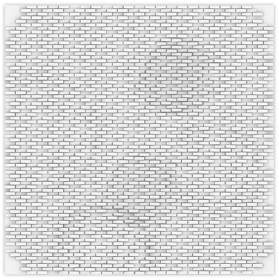
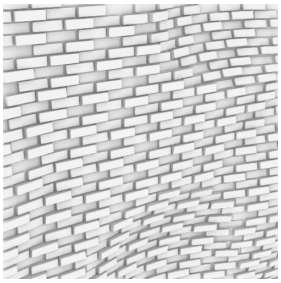

panel_0017_1

date_measured	**date_processed**
27-01-2020	28-01-2020
temperature	**humidity**
12.2 °C - 12.3 °C	51.0 % - 50.7 %
pressure	**macrostructure**
951.9 *Pa* - 951.9 *Pa*	panel_0015_1
printer	**printer_binder**
Voxeljet VX4000	Phenolic binder

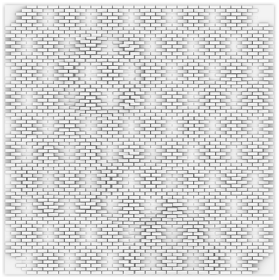


panel_0018_0

date_measured	**date_processed**
23-01-2020	23-01-2020
temperature	**humidity**
13.0 °C - 12.9 °C	43.3 % - 43.6 %
pressure	**macrostructure**
967.9 *Pa* - 967.9 *Pa*	panel_0015_0
printer	**printer_binder**
Voxeljet VX4000	Phenolic binder

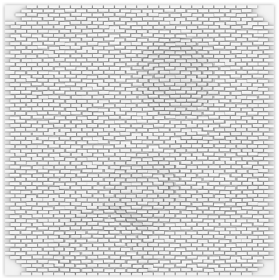
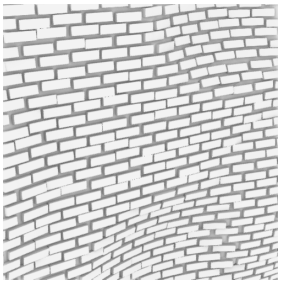

panel_0018_1

date_measured	**date_processed**
24-01-2020	24-01-2020
temperature	**humidity**
12.6 °C - 12.8 °C	44.2 % - 44.3 %
pressure	**macrostructure**
964.7 *Pa* - 964.7 *Pa*	panel_0015_1
printer	**printer_binder**
Voxeljet VX4000	Phenolic binder

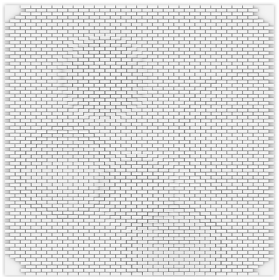
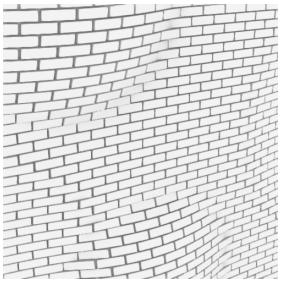

panel_0019_0

date_measured	**date_processed**
29-04-2020	29-04-2020
temperature	**humidity**
17.2 °C - 17.2 °C	58.8 % - 56.9 %
pressure	**macrostructure**
952.2 *Pa* - 952.2 *Pa*	panel_0015_0
printer	**printer_binder**
Voxeljet VX4000	Phenolic binder

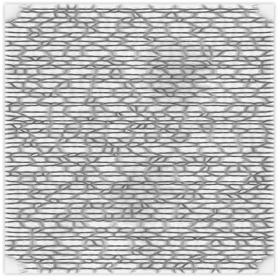
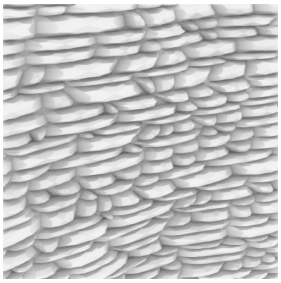

panel_0019_1

date_measured	**date_processed**
29-04-2020	30-04-2020
temperature	**humidity**
17.2 °C - 17.3 °C	57.0 % - 56.6 %
pressure	**macrostructure**
951.5 *Pa* - 951.5 *Pa*	panel_0015_1
printer	**printer_binder**
Voxeljet VX4000	Phenolic binder

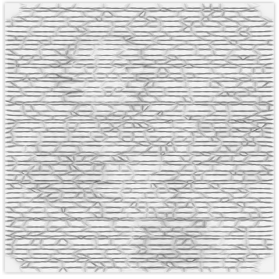
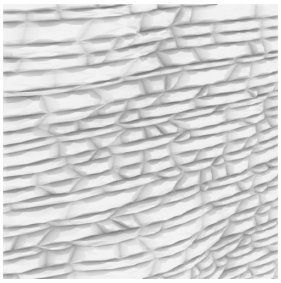

panel_0020_0

date_measured	**date_processed**
29-01-2020	29-01-2020
temperature	**humidity**
12.1 °C - 12.2 °C	51.8 % - 51.9 %
pressure	**macrostructure**
953.2 *Pa* - 953.1 *Pa*	panel_0015_0
printer	**printer_binder**
Voxeljet VX4000	Phenolic binder

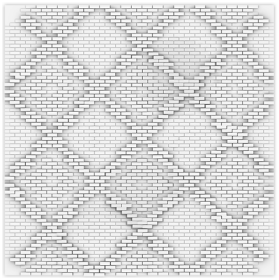
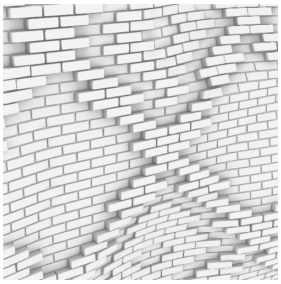

panel_0020_1

date_measured	**date_processed**
29-01-2020	30-01-2020
temperature	**humidity**
12.2 °C - 12.3 °C	52.3 % - 51.7 %
pressure	**macrostructure**
958.9 *Pa* - 958.9 *Pa*	panel_0015_1
printer	**printer_binder**
Voxeljet VX4000	Phenolic binder

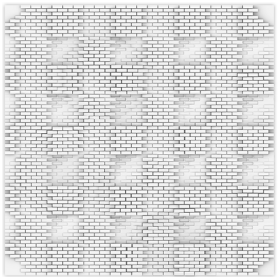
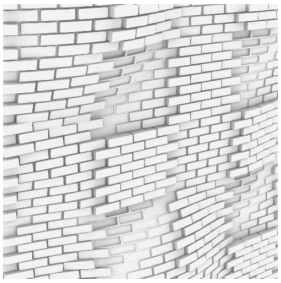

panel_0021_0

date_measured	**date_processed**
31-01-2020	31-01-2020
temperature	**humidity**
12.4 °C - 12.4 °C	55.1 % - 56.5 %
pressure	**macrostructure**
957.7 *Pa* - 957.7 *Pa*	panel_0015_0
printer	**printer_binder**
Voxeljet VX4000	Phenolic binder

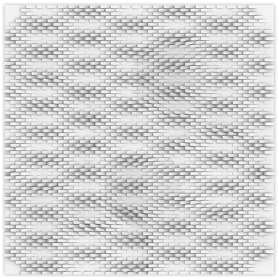
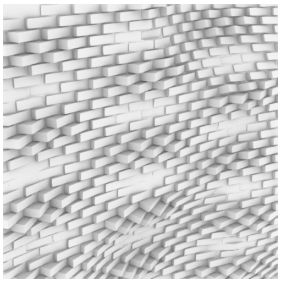

panel_0021_1

date_measured	**date_processed**
31-01-2020	01-02-2020
temperature	**humidity**
12.5 °C - 12.5 °C	57.3 % - 58.6 %
pressure	**macrostructure**
957.3 *Pa* - 957.3 *Pa*	panel_0015_1
printer	**printer_binder**
Voxeljet VX4000	Phenolic binder

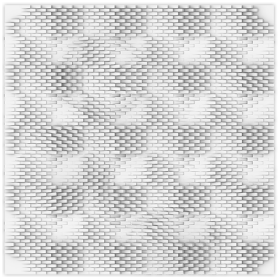
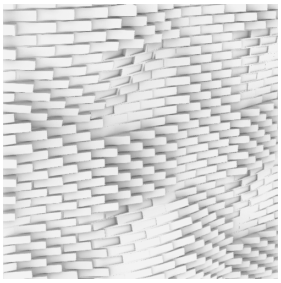

panel_0022_0

date_measured	**date_processed**
28-01-2020	28-01-2020
temperature	**humidity**
12.2 °C - 12.2 °C	52.5 % - 51.0 %
pressure	**macrostructure**
943.0 *Pa* - 943.0 *Pa*	panel_0015_0
printer	**printer_binder**
Voxeljet VX4000	Phenolic binder

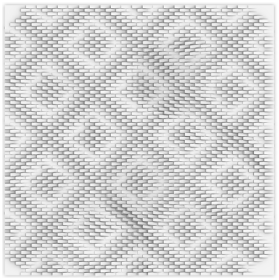
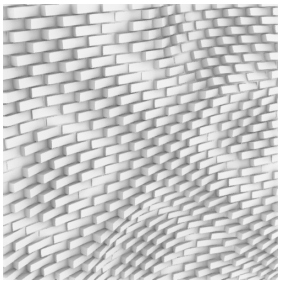

panel_0022_1

date_measured	**date_processed**
28-01-2020	29-01-2020
temperature	**humidity**
12.3 °C - 12.3 °C	51.1 % - 50.8 %
pressure	**macrostructure**
949.7 *Pa* - 949.7 *Pa*	panel_0015_1
printer	**printer_binder**
Voxeljet VX4000	Phenolic binder

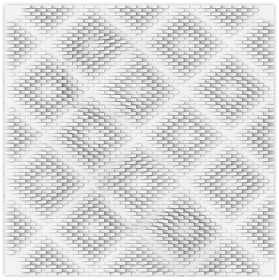


panel_0023_0

date_measured	**date_processed**
04-05-2020	04-05-2020
temperature	**humidity**
17.0 °C - 17.3 °C	57.3 % - 57.9 %
pressure	**macrostructure**
958.0 *Pa* - 958.0 *Pa*	panel_0031_0
printer	**printer_binder**
Voxeljet VX4000	Phenolic binder

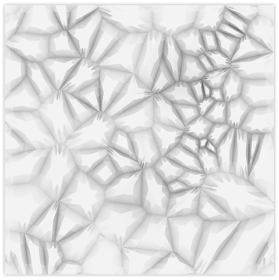
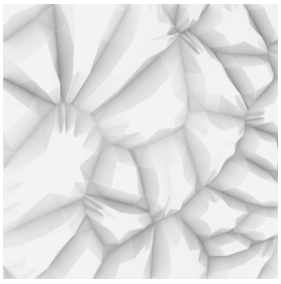

panel_0023_1

date_measured	**date_processed**
04-05-2020	05-05-2020
temperature	**humidity**
17.2 °C - 17.2 °C	58.4 % - 58.5 %
pressure	**macrostructure**
954.9 *Pa* - 954.9 *Pa*	panel_0031_1
printer	**printer_binder**
Voxeljet VX4000	Phenolic binder

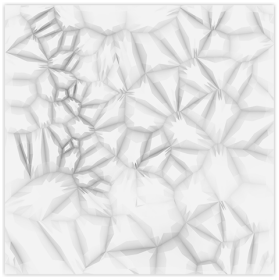
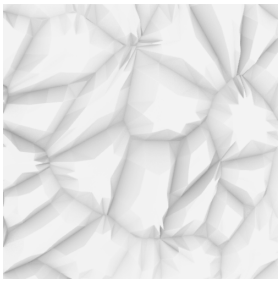

panel_0024_0

date_measured	date_processed
06-05-2020	06-05-2020
temperature	**humidity**
17.2 °C - 17.3 °C	59.7 % - 57.2 %
pressure	**macrostructure**
960.3 *Pa* - 960.3 *Pa*	panel_0015_0
printer	**printer_binder**
Voxeljet VX4000	Phenolic binder

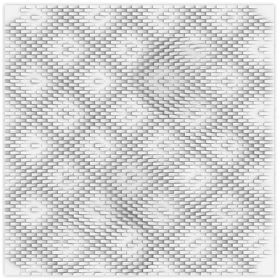


panel_0024_1

date_measured	date_processed
06-05-2020	07-05-2020
temperature	**humidity**
17.3 °C - 17.4 °C	56.5 % - 54.7 %
pressure	**macrostructure**
961.5 *Pa* - 961.5 *Pa*	panel_0015_1
printer	**printer_binder**
Voxeljet VX4000	Phenolic binder

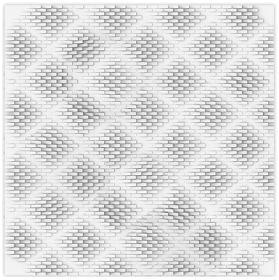
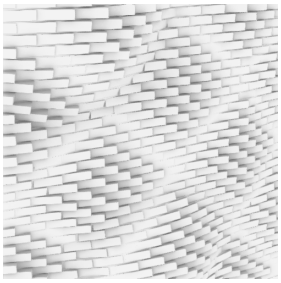

panel_0025_0

date_measured	date_processed
30-04-2020	30-04-2020
temperature	**humidity**
17.3 °C - 17.4 °C	57.4 % - 57.1 %
pressure	**macrostructure**
950.2 *Pa* - 950.2 *Pa*	panel_0015_0
printer	**printer_binder**
Voxeljet VX4000	Phenolic binder

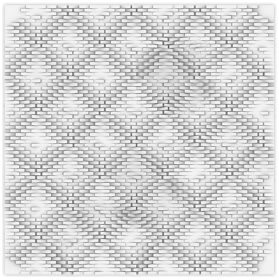


panel_0025_1

date_measured	date_processed
30-04-2020	01-05-2020
temperature	**humidity**
17.3 °C - 17.4 °C	57.3 % - 56.2 %
pressure	**macrostructure**
948.7 *Pa* - 948.7 *Pa*	panel_0015_1
printer	**printer_binder**
Voxeljet VX4000	Phenolic binder

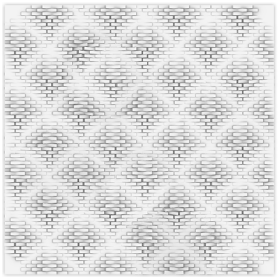


panel_0026_0

date_measured	date_processed
07-05-2020	07-05-2020
temperature	**humidity**
17.2 °C - 17.4 °C	53.8 % - 52.9 %
pressure	**macrostructure**
963.9 *Pa* - 963.9 *Pa*	panel_0031_0
printer	**printer_binder**
Voxeljet VX4000	Phenolic binder

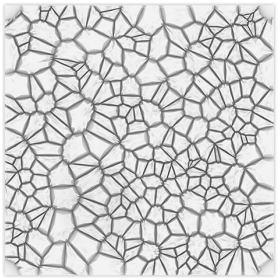
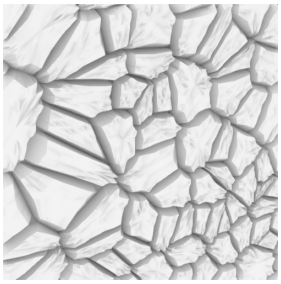

panel_0026_1

date_measured	date_processed
07-05-2020	08-05-2020
temperature	**humidity**
17.4 °C - 17.4 °C	52.2 % - 53.3 %
pressure	**macrostructure**
960.4 *Pa* - 960.4 *Pa*	panel_0031_1
printer	**printer_binder**
Voxeljet VX4000	Phenolic binder

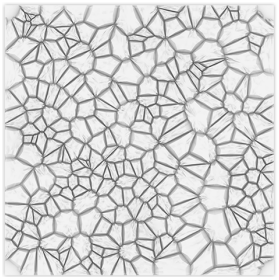
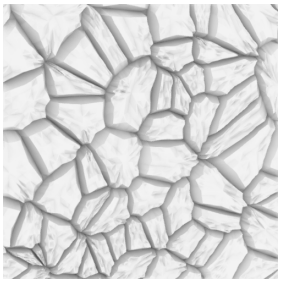

panel_0027_0

date_measured	date_processed
05-05-2020	05-05-2020
temperature	**humidity**
17.2 °C - 17.3 °C	59.0 % - 59.5 %
pressure	**macrostructure**
955.3 *Pa* - 955.3 *Pa*	panel_0031_0
printer	**printer_binder**
Voxeljet VX4000	Phenolic binder

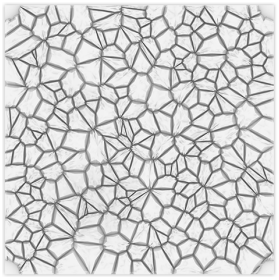
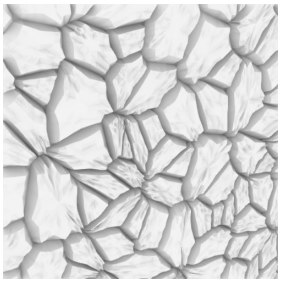

panel_0027_1

date_measured	date_processed
05-05-2020	06-05-2020
temperature	**humidity**
17.3 °C - 17.3 °C	60.1 % - 59.6 %
pressure	**macrostructure**
957.1 *Pa* - 957.1 *Pa*	panel_0031_1
printer	**printer_binder**
Voxeljet VX4000	Phenolic binder

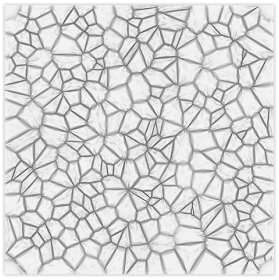
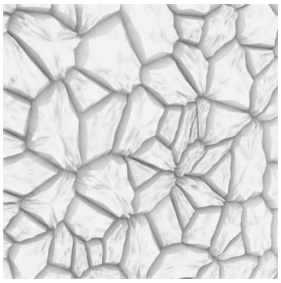

panel_0028_0

date_measured	**date_processed**
08-05-2020	08-05-2020
temperature	**humidity**
17.3 °C - 17.5 °C	54.2 % - 55.4 %
pressure	**macrostructure**
960.1 *Pa* - 960.1 *Pa*	panel_0015_0
printer	**printer_binder**
Voxeljet VX4000	Phenolic binder

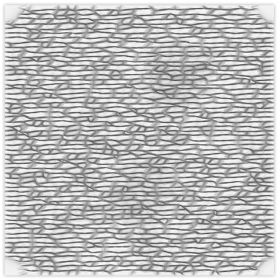
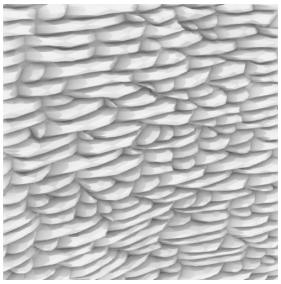

panel_0028_1

date_measured	**date_processed**
10-05-2020	11-05-2020
temperature	**humidity**
17.3 °C - 17.6 °C	63.5 % - 64.1 %
pressure	**macrostructure**
945.1 *Pa* - 945.1 *Pa*	panel_0015_1
printer	**printer_binder**
Voxeljet VX4000	Phenolic binder

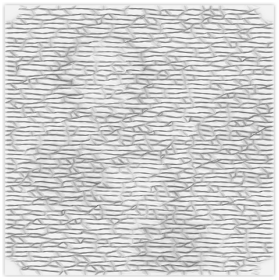
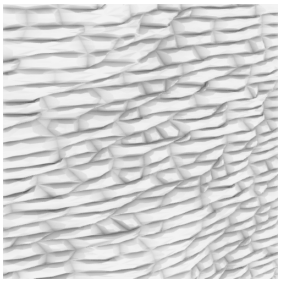

panel_0029_0

date_measured	**date_processed**
11-05-2020	11-05-2020
temperature	**humidity**
17.5 °C - 17.7 °C	65.4 % - 64.5 %
pressure	**macrostructure**
938.0 *Pa* - 938.0 *Pa*	panel_0015_0
printer	**printer_binder**
Voxeljet VX4000	Phenolic binder

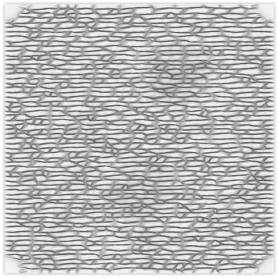
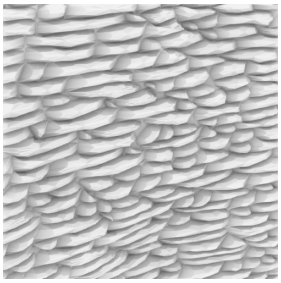

panel_0029_1

date_measured	**date_processed**
11-05-2020	12-05-2020
temperature	**humidity**
17.6 °C - 17.8 °C	64.2 % - 60.8 %
pressure	**macrostructure**
948.4 *Pa* - 948.4 *Pa*	panel_0015_1
printer	**printer_binder**
Voxeljet VX4000	Phenolic binder

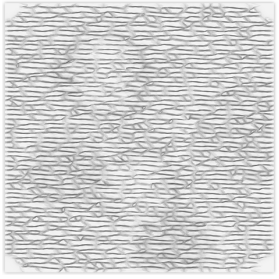
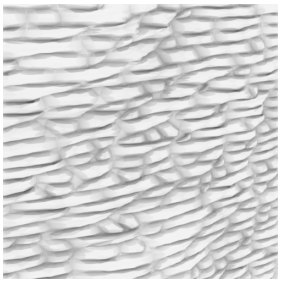

panel_0030_0

date_measured	date_processed
13-05-2020	13-05-2020
temperature	**humidity**
17.5 °C - 17.8 °C	56.5 % - 56.2 %
pressure	**macrostructure**
952.0 *Pa* - 952.0 *Pa*	panel_0015_0
printer	**printer_binder**
Voxeljet VX4000	Phenolic binder

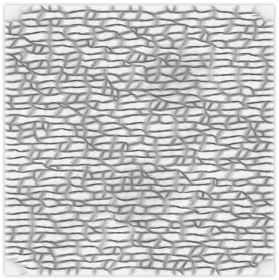
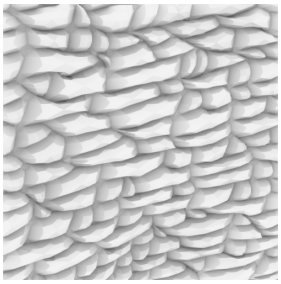

panel_0030_1

date_measured	date_processed
13-05-2020	14-05-2020
temperature	**humidity**
17.8 °C - 17.9 °C	56.6 % - 56.6 %
pressure	**macrostructure**
947.3 *Pa* - 947.3 *Pa*	panel_0015_1
printer	**printer_binder**
Voxeljet VX4000	Phenolic binder

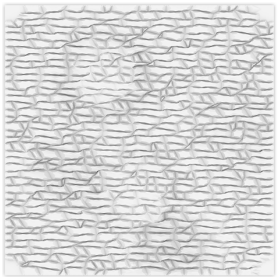
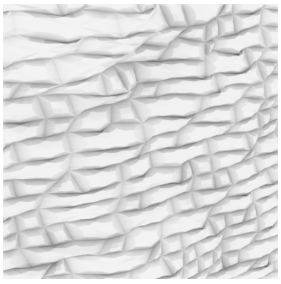

panel_0031_0

date_measured	date_processed
27-05-2020	28-05-2020
temperature	**humidity**
18.5 °C - 18.7 °C	52.0 % - 51.6 %
pressure	**macrostructure**
969.2 *Pa* - 969.2 *Pa*	macrostructure
printer	**printer_binder**
ExOne S-Max	Furan binder

panel_0031_1

date_measured	date_processed
28-05-2020	28-05-2020
temperature	**humidity**
18.6 °C - 18.7 °C	52.1 % - 51.8 %
pressure	**macrostructure**
967.8 *Pa* - 967.8 *Pa*	macrostructure
printer	**printer_binder**
ExOne S-Max	Furan binder

panel_0032_0

date_measured	**date_processed**
28-05-2020	29-05-2020
temperature	**humidity**
18.6 °C - 18.7 °C	53.3 % - 51.8 %
pressure	**macrostructure**
965.3 *Pa* - 965.3 *Pa*	panel_0015_0
printer	**printer_binder**
ExOne S-Max	Furan binder

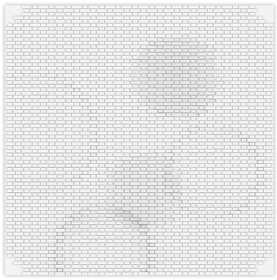
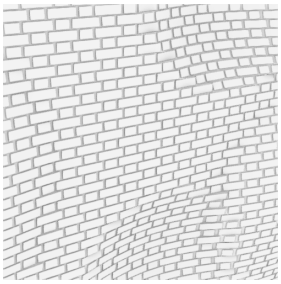

panel_0032_1

date_measured	**date_processed**
29-05-2020	30-05-2020
temperature	**humidity**
18.6 °C - 18.8 °C	51.4 % - 50.8 %
pressure	**macrostructure**
962.0 *Pa* - 962.0 *Pa*	panel_0015_1
printer	**printer_binder**
ExOne S-Max	Furan binder

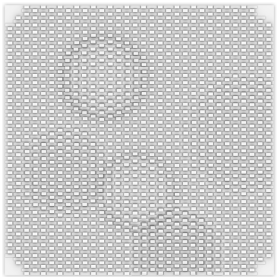
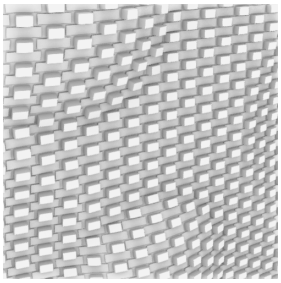

panel_0033_0

date_measured	**date_processed**
04-06-2020	05-06-2020
temperature	**humidity**
19.0 °C - 19.2 °C	58.4 % - 58.1 %
pressure	**macrostructure**
939.6 *Pa* - 939.6 *Pa*	panel_0015_0
printer	**printer_binder**
ExOne S-Max	Furan binder

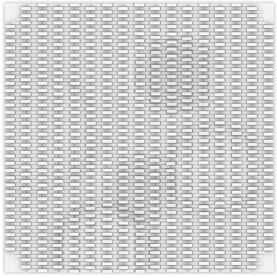
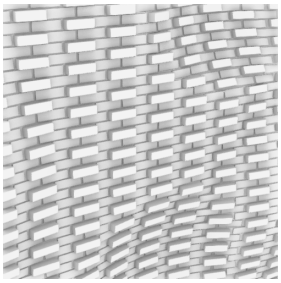

panel_0033_1

date_measured	**date_processed**
05-06-2020	05-06-2020
temperature	**humidity**
19.1 °C - 19.2 °C	58.2 % - 57.2 %
pressure	**macrostructure**
942.6 *Pa* - 942.6 *Pa*	panel_0015_1
printer	**printer_binder**
ExOne S-Max	Furan binder

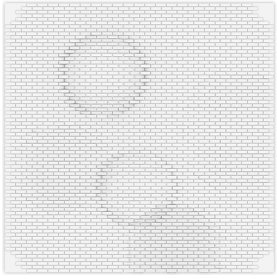
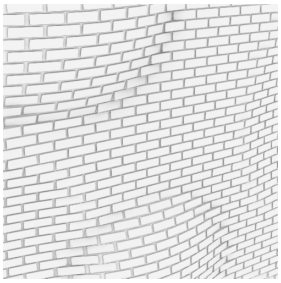

panel_0034_0

date_measured	**date_processed**
05-06-2020	06-06-2020
temperature	**humidity**
19.1 °C - 19.3 °C	57.3 % - 57.0 %
pressure	**macrostructure**
945.4 *Pa* - 945.4 *Pa*	panel_0015_0
printer	**printer_binder**
ExOne S-Max	Furan binder

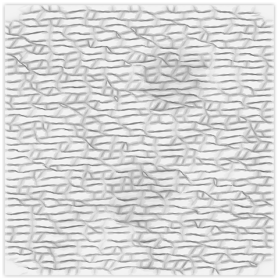
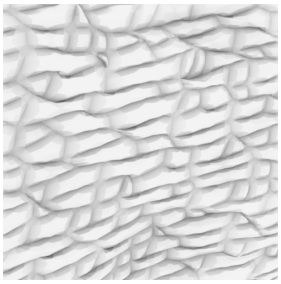

panel_0034_1

date_measured	**date_processed**
08-06-2020	08-06-2020
temperature	**humidity**
18.9 °C - 19.2 °C	58.6 % - 57.1 %
pressure	**macrostructure**
952.6 *Pa* - 952.5 *Pa*	panel_0015_1
printer	**printer_binder**
ExOne S-Max	Furan binder

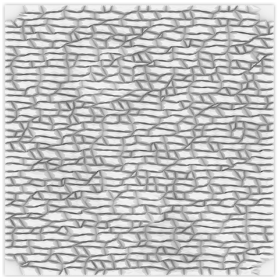
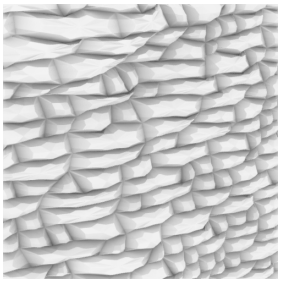

panel_0035_0

date_measured	**date_processed**
01-06-2020	02-06-2020
temperature	**humidity**
18.5 °C - 18.8 °C	50.3 % - 50.5 %
pressure	**macrostructure**
958.4 *Pa* - 958.4 *Pa*	panel_0015_0
printer	**printer_binder**
ExOne S-Max	Furan binder

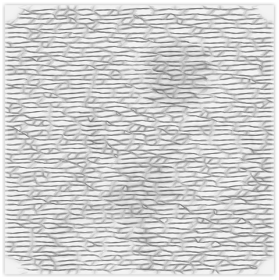
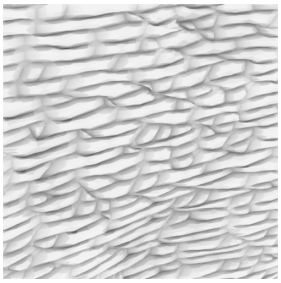

panel_0035_1

date_measured	**date_processed**
02-06-2020	02-06-2020
temperature	**humidity**
18.7 °C - 18.8 °C	51.1 % - 50.9 %
pressure	**macrostructure**
958.1 *Pa* - 958.1 *Pa*	panel_0015_1
printer	**printer_binder**
ExOne S-Max	Furan binder

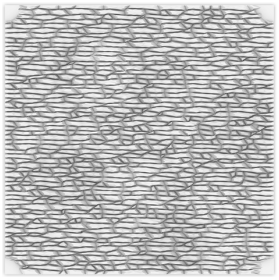
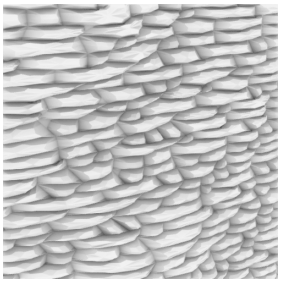

panel_0036_0

date_measured	**date_processed**
03-06-2020	04-06-2020
temperature	**humidity**
18.9 °C - 19.1 °C	53.4 % - 54.7 %
pressure	**macrostructure**
944.9 *Pa* - 944.9 *Pa*	panel_0031_0
printer	**printer_binder**
ExOne S-Max	Furan binder

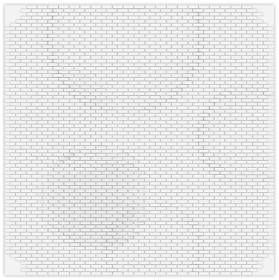
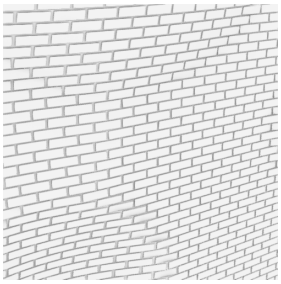

panel_0036_1

date_measured	**date_processed**
04-06-2020	04-06-2020
temperature	**humidity**
19.0 °C - 19.1 °C	55.8 % - 58.0 %
pressure	**macrostructure**
940.4 *Pa* - 940.4 *Pa*	panel_0031_1
printer	**printer_binder**
ExOne S-Max	Furan binder

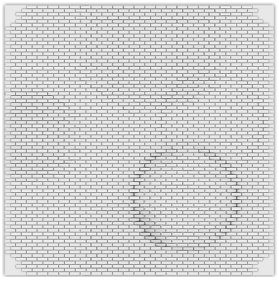
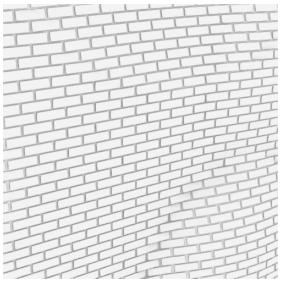

panel_0037_0

date_measured	**date_processed**
26-05-2020	27-05-2020
temperature	**humidity**
18.4 °C - 18.6 °C	55.1 % - 54.1 %
pressure	**macrostructure**
970.6 *Pa* - 970.6 *Pa*	flat
printer	**printer_binder**
ExOne S-Max	Furan binder

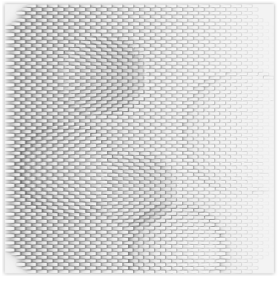


panel_0037_1

date_measured	**date_processed**
27-05-2020	27-05-2020
temperature	**humidity**
18.5 °C - 18.6 °C	54.4 % - 52.2 %
pressure	**macrostructure**
970.8 *Pa* - 970.8 *Pa*	flat
printer	**printer_binder**
ExOne S-Max	Furan binder

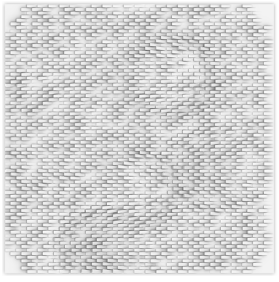
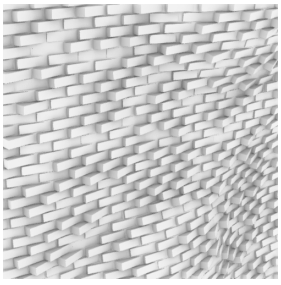

panel_0038_0

date_measured	date_processed
09-06-2020	10-06-2020
temperature	**humidity**
19.1 °C - 19.3 °C	59.2 % - 59.1 %
pressure	**macrostructure**
953.3 Pa - 953.3 Pa	flat
printer	**printer_binder**
ExOne S-Max	Furan binder

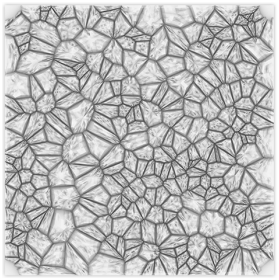
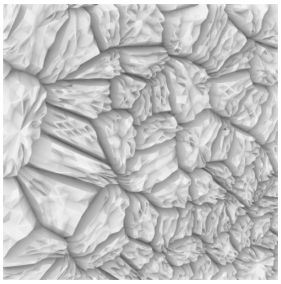

panel_0038_1

date_measured	date_processed
10-06-2020	10-06-2020
temperature	**humidity**
19.1 °C - 19.2 °C	59.7 % - 59.9 %
pressure	**macrostructure**
953.4 Pa - 953.4 Pa	flat
printer	**printer_binder**
ExOne S-Max	Furan binder

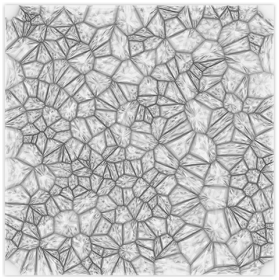
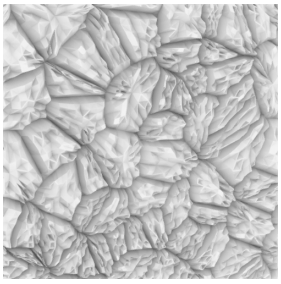

panel_0039_0

date_measured	date_processed
02-06-2020	03-06-2020
temperature	**humidity**
18.7 °C - 18.9 °C	51.2 % - 52.2 %
pressure	**macrostructure**
953.2 Pa - 953.2 Pa	flat
printer	**printer_binder**
ExOne S-Max	Furan binder

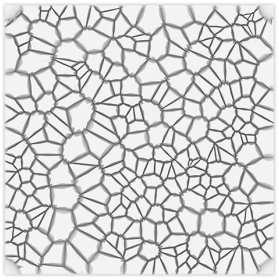
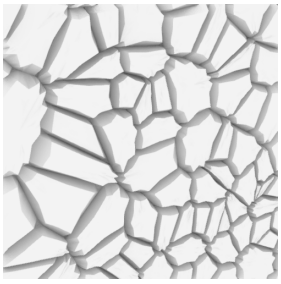

panel_0039_1

date_measured	date_processed
03-06-2020	03-06-2020
temperature	**humidity**
18.9 °C - 19.0 °C	52.6 % - 52.5 %
pressure	**macrostructure**
950.2 Pa - 950.2 Pa	flat
printer	**printer_binder**
ExOne S-Max	Furan binder

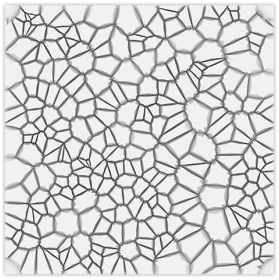
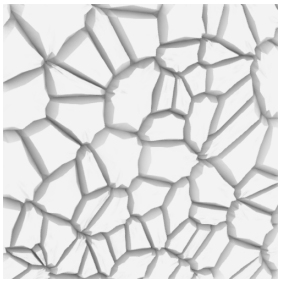

panel_0040_0

date_measured	date_processed
22-05-2020	23-05-2020
temperature	**humidity**
18.1 °C - 18.2 °C	61.2 % - 62.6 %
pressure	**macrostructure**
962.5 *Pa* - 962.5 *Pa*	flat
printer	**printer_binder**
ExOne S-Max	Furan binder

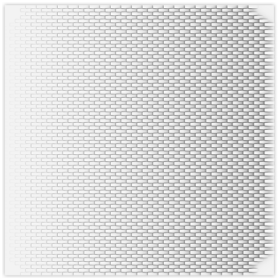
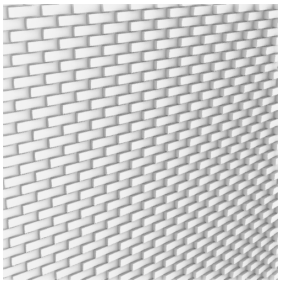

panel_0040_1

date_measured	date_processed
25-05-2020	25-05-2020
temperature	**humidity**
18.2 °C - 18.4 °C	58.2 % - 57.3 %
pressure	**macrostructure**
971.7 *Pa* - 971.7 *Pa*	flat
printer	**printer_binder**
ExOne S-Max	Furan binder

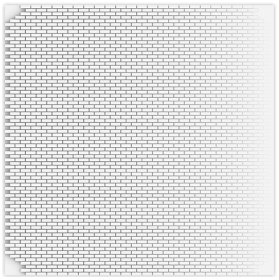
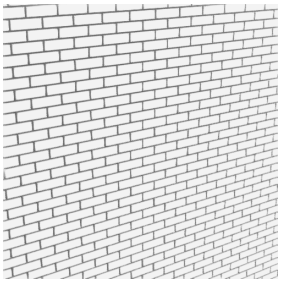

panel_0040_r180_0

date_measured	date_processed
02-12-2020	02-12-2020
temperature	**humidity**
15.1 °C - 15.2 °C	43.4 % - 43.2 %
pressure	**macrostructure**
954.2 *Pa* - 954.2 *Pa*	flat
printer	**printer_binder**
ExOne S-Max	Furan binder

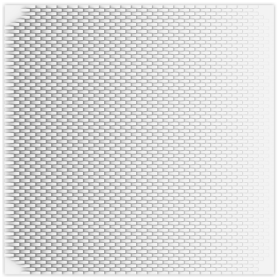
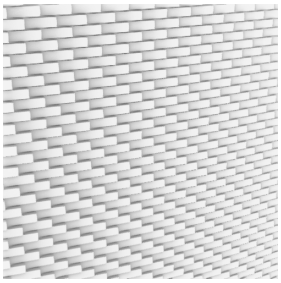

panel_0040_r180_1

date_measured	date_processed
02-12-2020	03-12-2020
temperature	**humidity**
15.1 °C - 15.2 °C	43.1 % - 42.9 %
pressure	**macrostructure**
952.7 *Pa* - 952.8 *Pa*	flat
printer	**printer_binder**
ExOne S-Max	Furan binder

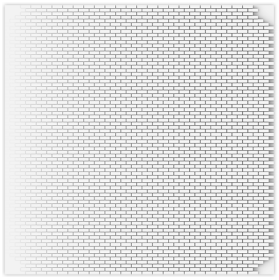
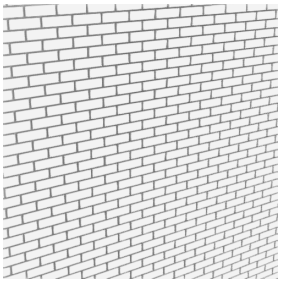

panel_0041_0

date_measured	**date_processed**
25-05-2020	26-05-2020
temperature	**humidity**
18.3 °C - 18.5 °C	57.5 % - 56.5 %
pressure	**macrostructure**
970.5 *Pa* - 970.5 *Pa*	flat
printer	**printer_binder**
ExOne S-Max	Furan binder

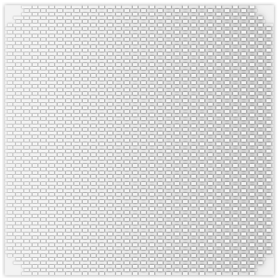
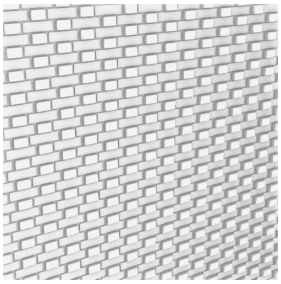

panel_0041_1

date_measured	**date_processed**
26-05-2020	26-05-2020
temperature	**humidity**
18.4 °C - 18.6 °C	56.8 % - 55.2 %
pressure	**macrostructure**
971.5 *Pa* - 971.5 *Pa*	flat
printer	**printer_binder**
ExOne S-Max	Furan binder

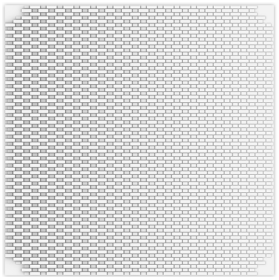
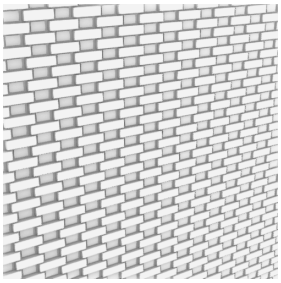

panel_0041_r180_0

date_measured	**date_processed**
03-12-2020	03-12-2020
temperature	**humidity**
14.8 °C - 15.1 °C	42.7 % - 42.2 %
pressure	**macrostructure**
948.8 *Pa* - 948.9 *Pa*	flat
printer	**printer_binder**
ExOne S-Max	Furan binder

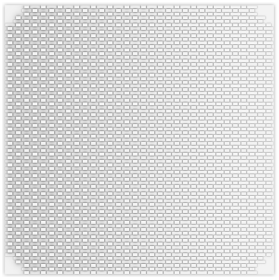
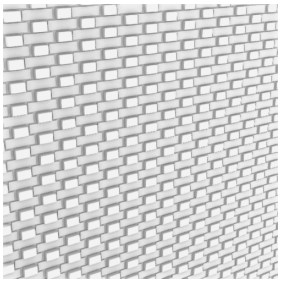

panel_0041_r180_1

date_measured	**date_processed**
03-12-2020	04-12-2020
temperature	**humidity**
14.9 °C - 15.0 °C	41.9 % - 42.0 %
pressure	**macrostructure**
938.3 *Pa* - 938.3 *Pa*	flat
printer	**printer_binder**
ExOne S-Max	Furan binder

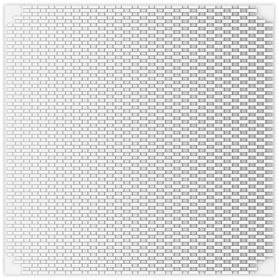
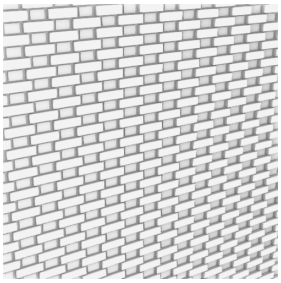

panel_0042_0

date_measured	date_processed
20-05-2020	20-05-2020
temperature	**humidity**
17.3 °C - 17.4 °C	59.0 % - 57.7 %
pressure	**macrostructure**
960.0 *Pa* - 960.0 *Pa*	flat
printer	**printer_binder**
ExOne S-Max	Furan binder

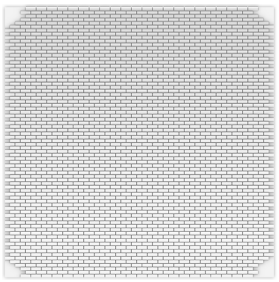
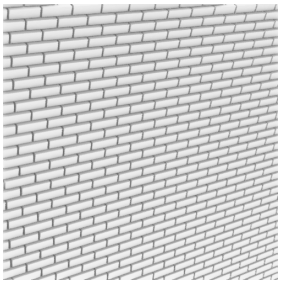

panel_0042_1

date_measured	date_processed
22-05-2020	22-05-2020
temperature	**humidity**
17.6 °C - 17.9 °C	61.1 % - 60.8 %
pressure	**macrostructure**
962.9 *Pa* - 962.9 *Pa*	flat
printer	**printer_binder**
ExOne S-Max	Furan binder

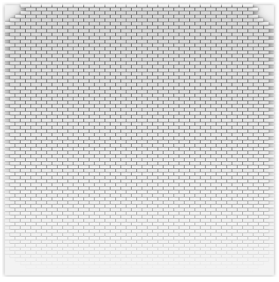
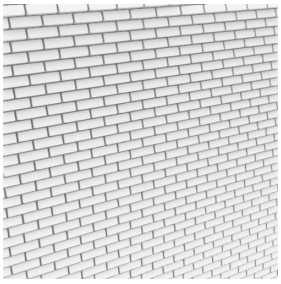

panel_0043_0

date_measured	date_processed
08-06-2020	09-06-2020
temperature	**humidity**
19.0 °C - 19.2 °C	56.1 % - 57.3 %
pressure	**macrostructure**
951.3 *Pa* - 951.2 *Pa*	panel_0015_0
printer	**printer_binder**
ExOne S-Max	Furan binder

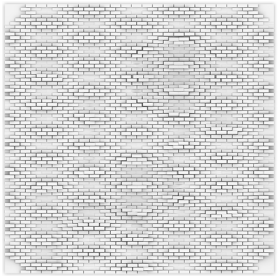
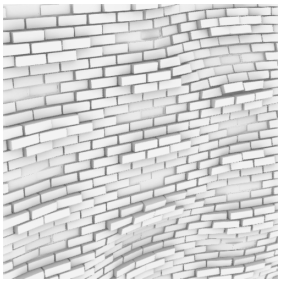

panel_0043_1

date_measured	date_processed
09-06-2020	09-06-2020
temperature	**humidity**
19.1 °C - 19.2 °C	58.0 % - 58.3 %
pressure	**macrostructure**
953.1 *Pa* - 953.1 *Pa*	panel_0015_1
printer	**printer_binder**
ExOne S-Max	Furan binder

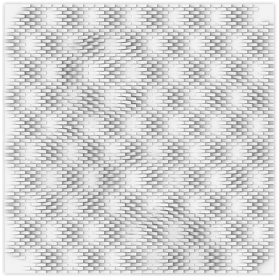
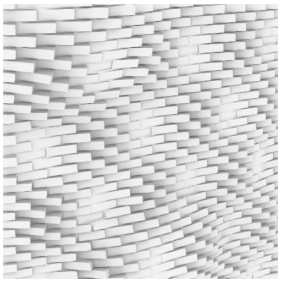

panel_0044_0

date_measured	**date_processed**
25-08-2020	25-08-2020
temperature	**humidity**
23.4 °C - 23.6 °C	55.9 % - 55.3 %
pressure	**macrostructure**
956.6 *Pa* - 956.5 *Pa*	panel_0015_0
printer	**printer_binder**
ExOne S-Max	Furan binder

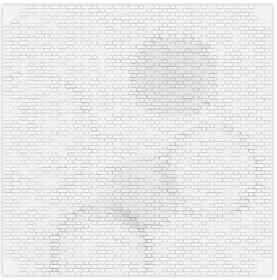
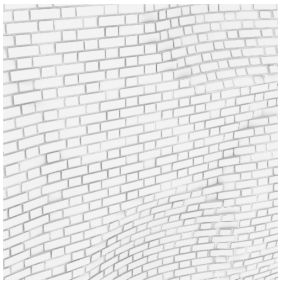

panel_0044_1

date_measured	**date_processed**
25-08-2020	26-08-2020
temperature	**humidity**
23.5 °C - 23.6 °C	55.0 % - 54.8 %
pressure	**macrostructure**
953.5 *Pa* - 953.5 *Pa*	panel_0015_1
printer	**printer_binder**
ExOne S-Max	Furan binder

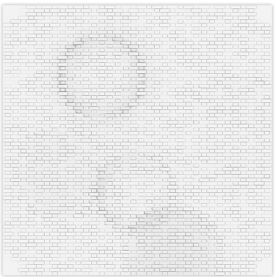
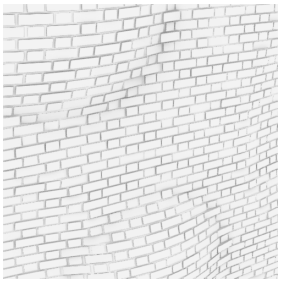

panel_0045_0

date_measured	**date_processed**
26-08-2020	26-08-2020
temperature	**humidity**
23.3 °C - 23.6 °C	55.5 % - 54.5 %
pressure	**macrostructure**
956.8 *Pa* - 956.8 *Pa*	panel_0015_0
printer	**printer_binder**
ExOne S-Max	Furan binder

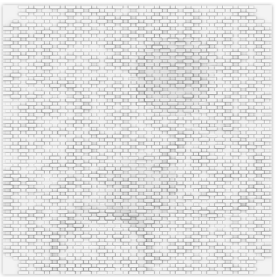
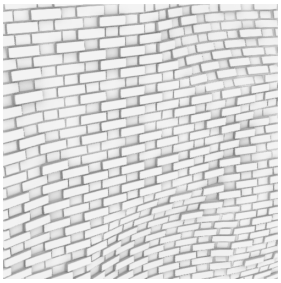

panel_0045_1

date_measured	**date_processed**
26-08-2020	27-08-2020
temperature	**humidity**
23.3 °C - 23.5 °C	53.5 % - 54.1 %
pressure	**macrostructure**
958.9 *Pa* - 958.9 *Pa*	panel_0015_1
printer	**printer_binder**
ExOne S-Max	Furan binder

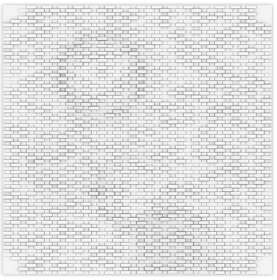
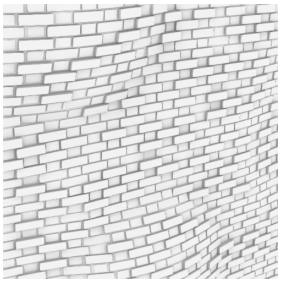

panel_0046_0

date_measured	**date_processed**
24-08-2020	24-08-2020
temperature	**humidity**
23.3 °C - 23.6 °C	59.4 % - 57.0 %
pressure	**macrostructure**
959.4 *Pa* - 959.4 *Pa*	panel_0015_0
printer	**printer_binder**
ExOne S-Max	Furan binder

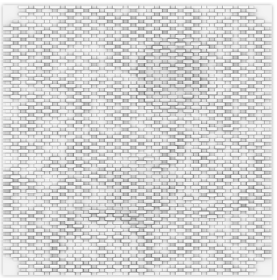
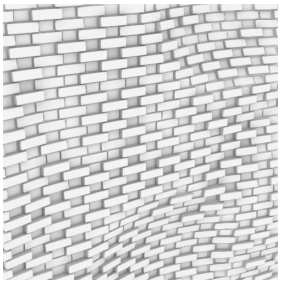

panel_0046_1

date_measured	**date_processed**
24-08-2020	25-08-2020
temperature	**humidity**
23.3 °C - 23.6 °C	55.8 % - 55.6 %
pressure	**macrostructure**
958.4 *Pa* - 958.4 *Pa*	panel_0015_1
printer	**printer_binder**
ExOne S-Max	Furan binder

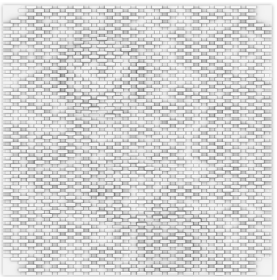
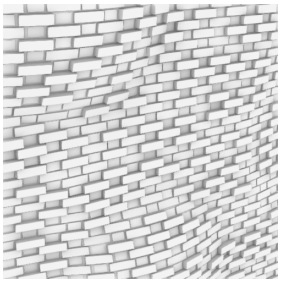

panel_0047_0

date_measured	**date_processed**
22-08-2020	23-08-2020
temperature	**humidity**
23.4 °C - 23.6 °C	64.7 % - 63.6 %
pressure	**macrostructure**
961.6 *Pa* - 961.6 *Pa*	panel_0015_0
printer	**printer_binder**
ExOne S-Max	Furan binder

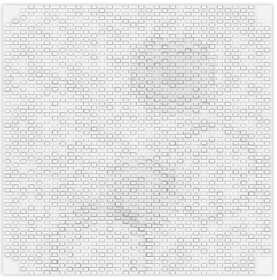
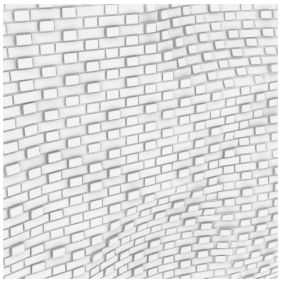

panel_0047_1

date_measured	**date_processed**
23-08-2020	24-08-2020
temperature	**humidity**
23.4 °C - 23.6 °C	63.1 % - 60.0 %
pressure	**macrostructure**
961.0 *Pa* - 961.0 *Pa*	panel_0015_1
printer	**printer_binder**
ExOne S-Max	Furan binder

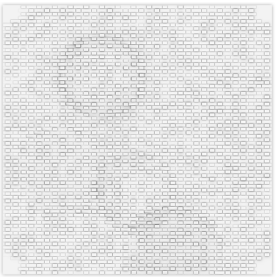
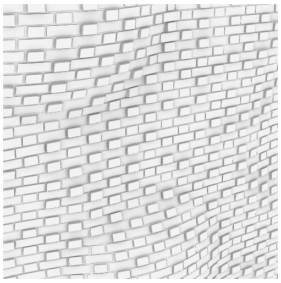

panel_0048_0

date_measured	**date_processed**
17-11-2020	17-11-2020
temperature	**humidity**
17.1 °C - 17.2 °C	53.9 % - 53.2 %
pressure	**macrostructure**
969.0 *Pa* - 969.0 *Pa*	panel_0015_0
printer	**printer_binder**
ExOne S-Max	Furan binder

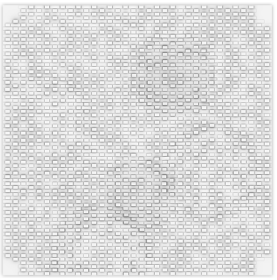
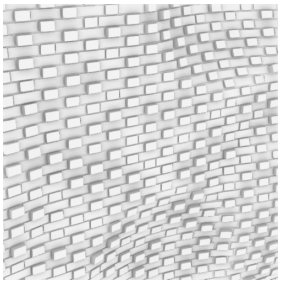

panel_0048_1

date_measured	**date_processed**
17-11-2020	18-11-2020
temperature	**humidity**
17.1 °C - 17.2 °C	53.2 % - 52.6 %
pressure	**macrostructure**
968.5 *Pa* - 968.5 *Pa*	panel_0015_1
printer	**printer_binder**
ExOne S-Max	Furan binder

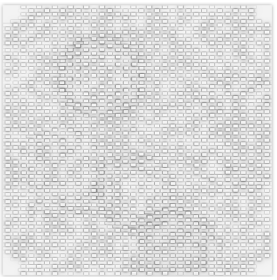
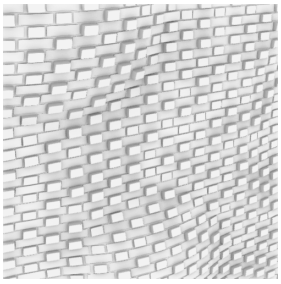

panel_0049_0

date_measured	**date_processed**
21-08-2020	22-08-2020
temperature	**humidity**
23.3 °C - 23.6 °C	63.8 % - 63.7 %
pressure	**macrostructure**
955.0 *Pa* - 954.9 *Pa*	panel_0015_0
printer	**printer_binder**
ExOne S-Max	Furan binder

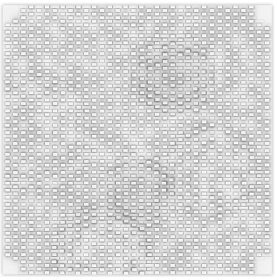
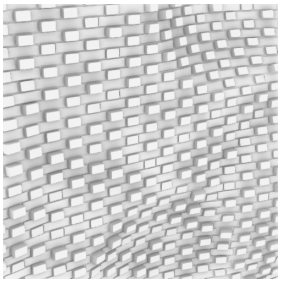

panel_0049_1

date_measured	**date_processed**
22-08-2020	22-08-2020
temperature	**humidity**
23.4 °C - 23.6 °C	64.7 % - 65.2 %
pressure	**macrostructure**
961.1 *Pa* - 961.1 *Pa*	panel_0015_1
printer	**printer_binder**
ExOne S-Max	Furan binder

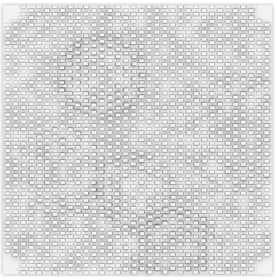
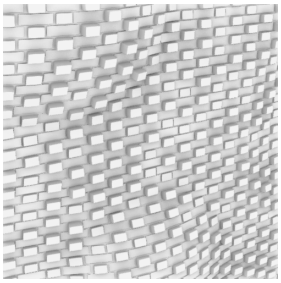

panel_0050_0

date_measured	date_processed
17-02-2021	18-02-2021
temperature	**humidity**
11.8 °C - 11.9 °C	47.3 % - 47.2 %
pressure	**macrostructure**
960.8 *Pa* - 960.8 *Pa*	panel_0015_0
printer	**printer_binder**
FDB	Furan binder

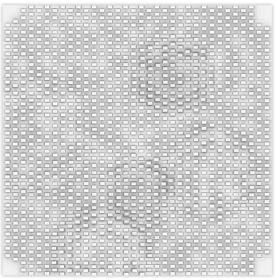

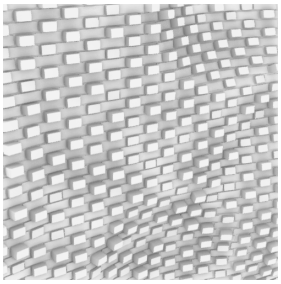

panel_0050_1

date_measured	date_processed
18-02-2021	18-02-2021
temperature	**humidity**
11.8 °C - 11.7 °C	47.8 % - 48.6 %
pressure	**macrostructure**
958.0 *Pa* - 958.0 *Pa*	panel_0015_1
printer	**printer_binder**
FDB	Furan binder

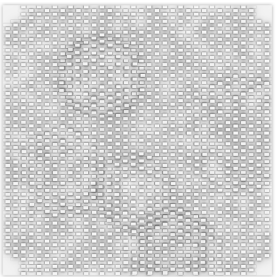

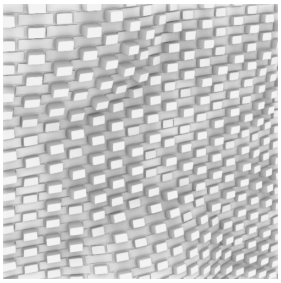

panel_0051_0

date_measured	date_processed
28-08-2020	28-08-2020
temperature	**humidity**
23.3 °C - 23.5 °C	56.0 % - 56.5 %
pressure	**macrostructure**
949.7 *Pa* - 949.7 *Pa*	panel_0015_0
printer	**printer_binder**
ExOne S-Max	Furan binder

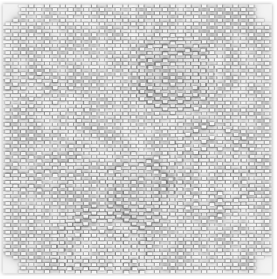

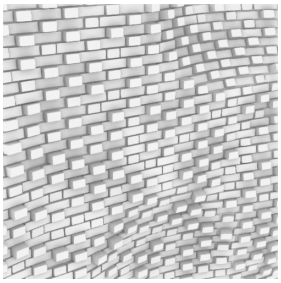

panel_0051_1

date_measured	date_processed
28-08-2020	29-08-2020
temperature	**humidity**
23.4 °C - 23.5 °C	57.3 % - 57.1 %
pressure	**macrostructure**
946.9 *Pa* - 946.8 *Pa*	panel_0015_1
printer	**printer_binder**
ExOne S-Max	Furan binder

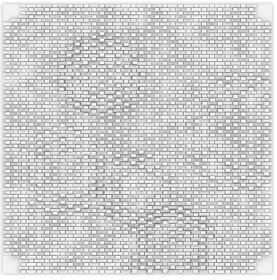

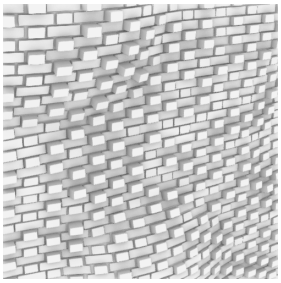

panel_0052_0

date_measured	**date_processed**
19-08-2020	19-08-2020
temperature	**humidity**
23.3 °C - 23.6 °C	64.0 % - 62.4 %
pressure	**macrostructure**
954.2 *Pa* - 954.2 *Pa*	panel_0015_0
printer	**printer_binder**
ExOne S-Max	Furan binder

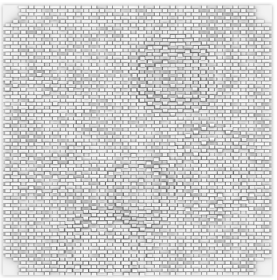
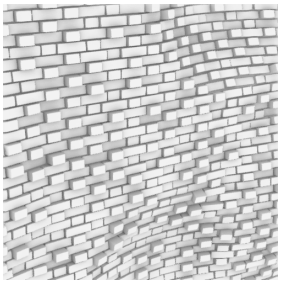

panel_0052_1

date_measured	**date_processed**
19-08-2020	20-08-2020
temperature	**humidity**
23.5 °C - 23.5 °C	62.6 % - 63.5 %
pressure	**macrostructure**
951.7 *Pa* - 951.7 *Pa*	panel_0015_1
printer	**printer_binder**
ExOne S-Max	Furan binder

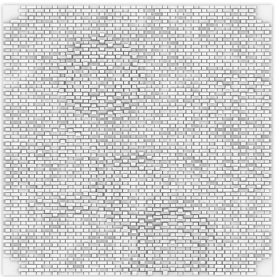
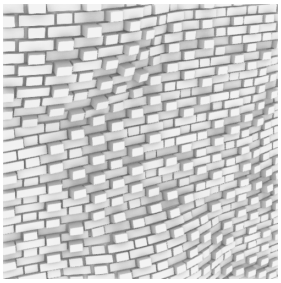

panel_0053_0

date_measured	**date_processed**
20-08-2020	21-08-2020
temperature	**humidity**
23.3 °C - 23.6 °C	63.4 % - 63.4 %
pressure	**macrostructure**
952.9 *Pa* - 952.9 *Pa*	panel_0015_0
printer	**printer_binder**
ExOne S-Max	Furan binder

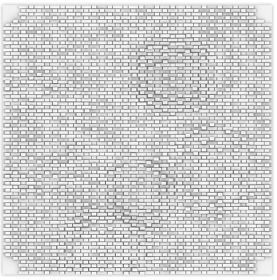
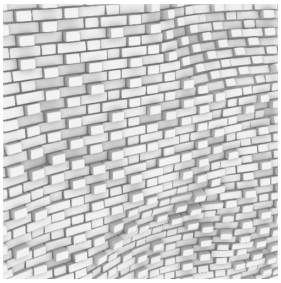

panel_0053_1

date_measured	**date_processed**
21-08-2020	21-08-2020
temperature	**humidity**
23.4 °C - 23.5 °C	64.6 % - 64.2 %
pressure	**macrostructure**
954.8 *Pa* - 954.8 *Pa*	panel_0015_1
printer	**printer_binder**
ExOne S-Max	Furan binder

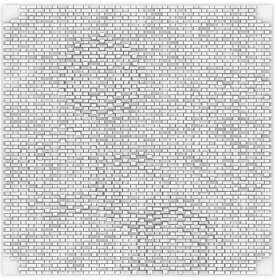
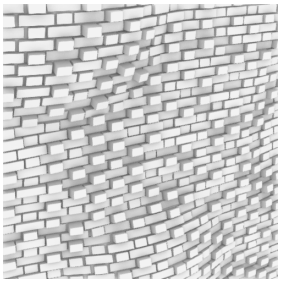

panel_0054_0

date_measured	date_processed
18-08-2020	18-08-2020
temperature	**humidity**
23.4 °C - 23.5 °C	64.5 % - 63.0 %
pressure	**macrostructure**
955.3 *Pa* - 955.3 *Pa*	panel_0015_0
printer	**printer_binder**
ExOne S-Max	Furan binder

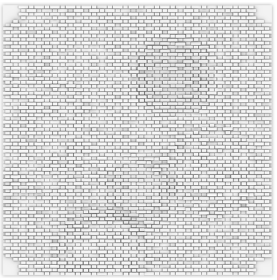
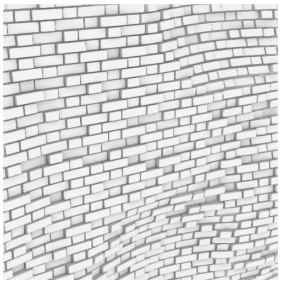

panel_0054_1

date_measured	date_processed
18-08-2020	19-08-2020
temperature	**humidity**
23.4 °C - 23.6 °C	62.9 % - 63.0 %
pressure	**macrostructure**
954.0 *Pa* - 954.0 *Pa*	panel_0015_1
printer	**printer_binder**
ExOne S-Max	Furan binder

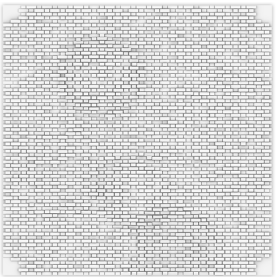
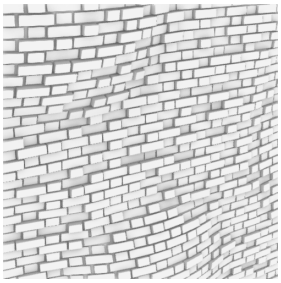

panel_0055_0

date_measured	date_processed
17-08-2020	17-08-2020
temperature	**humidity**
23.2 °C - 23.5 °C	66.6 % - 65.4 %
pressure	**macrostructure**
954.6 *Pa* - 954.6 *Pa*	panel_0015_0
printer	**printer_binder**
ExOne S-Max	Furan binder

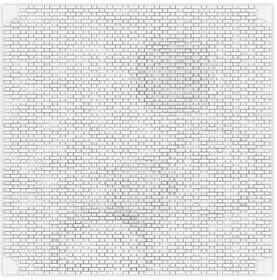
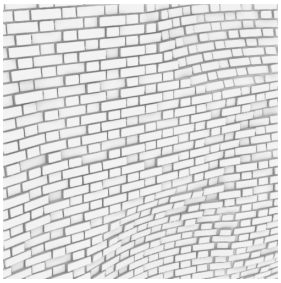

panel_0055_1

date_measured	date_processed
17-08-2020	18-08-2020
temperature	**humidity**
23.4 °C - 23.5 °C	65.3 % - 64.4 %
pressure	**macrostructure**
954.5 *Pa* - 954.5 *Pa*	panel_0015_1
printer	**printer_binder**
ExOne S-Max	Furan binder

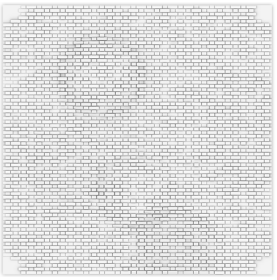
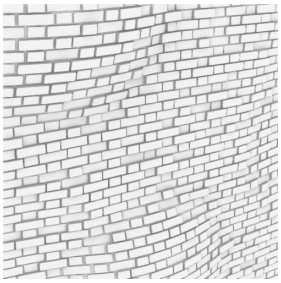

panel_0056_0

date_measured	**date_processed**
27-08-2020	27-08-2020
temperature	**humidity**
23.3 °C - 23.5 °C	54.7 % - 54.1 %
pressure	**macrostructure**
959.6 *Pa* - 959.5 *Pa*	panel_0015_0
printer	**printer_binder**
ExOne S-Max	Furan binder

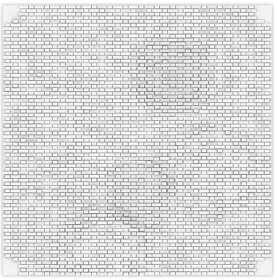
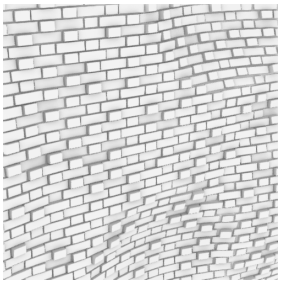

panel_0056_1

date_measured	**date_processed**
27-08-2020	28-08-2020
temperature	**humidity**
23.3 °C - 23.5 °C	53.8 % - 54.8 %
pressure	**macrostructure**
954.6 *Pa* - 954.6 *Pa*	panel_0015_1
printer	**printer_binder**
ExOne S-Max	Furan binder

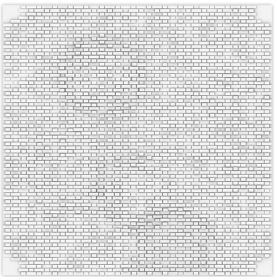
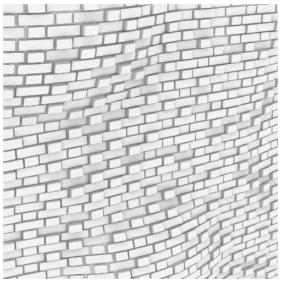

panel_0057_0

date_measured	**date_processed**
22-07-2020	23-07-2020
temperature	**humidity**
21.7 °C - 22.0 °C	64.0 % - 64.1 %
pressure	**macrostructure**
957.9 *Pa* - 957.9 *Pa*	panel_0015_0
printer	**printer_binder**
ExOne S-Max	Furan binder

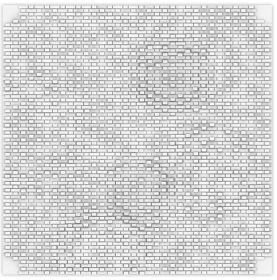
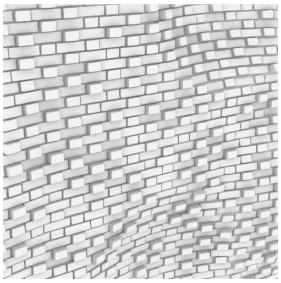

panel_0057_1

date_measured	**date_processed**
23-07-2020	23-07-2020
temperature	**humidity**
21.9 °C - 22.0 °C	64.2 % - 63.3 %
pressure	**macrostructure**
958.2 *Pa* - 958.2 *Pa*	panel_0015_1
printer	**printer_binder**
ExOne S-Max	Furan binder

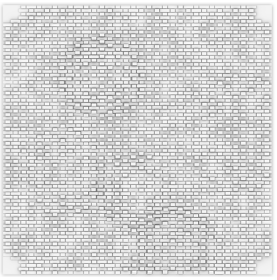
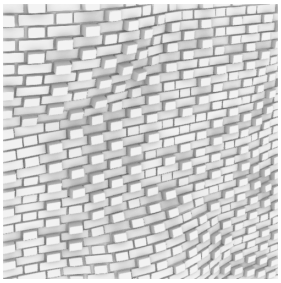

panel_0058_0

date_measured	date_processed
30-07-2020	31-07-2020
temperature	**humidity**
22.4 °C - 22.7 °C	61.5 % - 63.2 %
pressure	**macrostructure**
958.2 *Pa* - 958.2 *Pa*	panel_0015_0
printer	**printer_binder**
ExOne S-Max	Furan binder

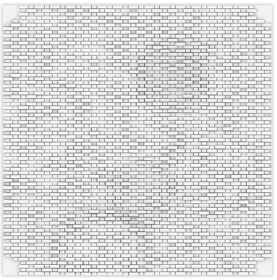

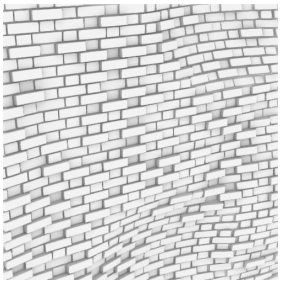

panel_0058_1

date_measured	date_processed
31-07-2020	31-07-2020
temperature	**humidity**
22.6 °C - 22.7 °C	64.0 % - 63.7 %
pressure	**macrostructure**
959.3 *Pa* - 959.3 *Pa*	panel_0015_1
printer	**printer_binder**
ExOne S-Max	Furan binder

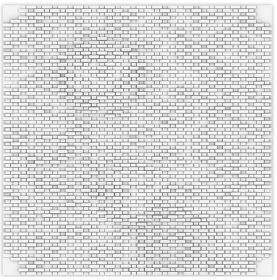

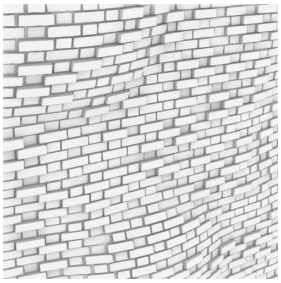

panel_0059_0

date_measured	date_processed
23-07-2020	24-07-2020
temperature	**humidity**
21.7 °C - 22.0 °C	62.7 % - 60.2 %
pressure	**macrostructure**
954.9 *Pa* - 954.9 *Pa*	panel_0015_0
printer	**printer_binder**
ExOne S-Max	Furan binder

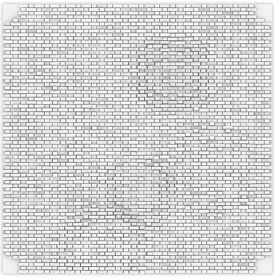

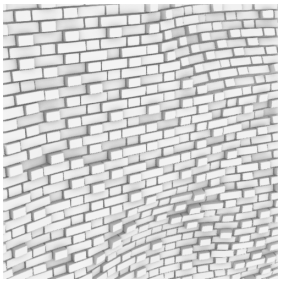

panel_0059_1

date_measured	date_processed
24-07-2020	24-07-2020
temperature	**humidity**
21.9 °C - 22.1 °C	60.7 % - 61.0 %
pressure	**macrostructure**
955.4 *Pa* - 955.4 *Pa*	panel_0015_1
printer	**printer_binder**
ExOne S-Max	Furan binder

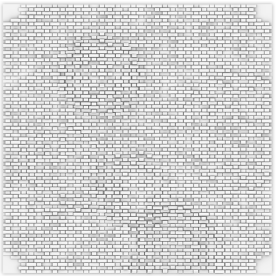

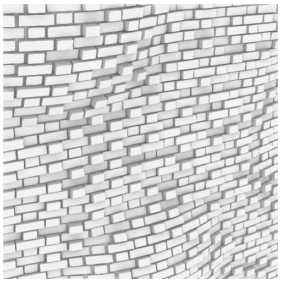

panel_0060_0

date_measured	**date_processed**
14-08-2020	15-08-2020
temperature	**humidity**
23.2 °C - 23.4 °C	66.5 % - 66.6 %
pressure	**macrostructure**
957.3 *Pa* - 957.3 *Pa*	panel_0015_0
printer	**printer_binder**
ExOne S-Max	Furan binder

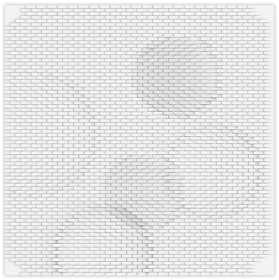
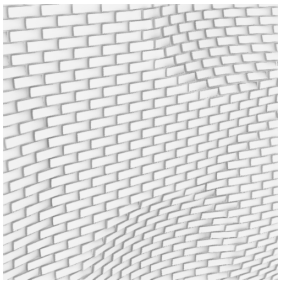

panel_0060_1

date_measured	**date_processed**
15-08-2020	15-08-2020
temperature	**humidity**
23.3 °C - 23.4 °C	66.9 % - 65.9 %
pressure	**macrostructure**
957.2 *Pa* - 957.2 *Pa*	panel_0015_1
printer	**printer_binder**
ExOne S-Max	Furan binder

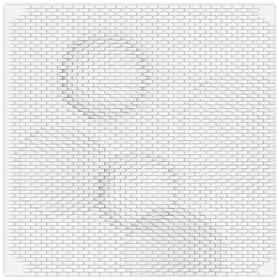


panel_0061_0

date_measured	**date_processed**
06-08-2020	06-08-2020
temperature	**humidity**
22.9 °C - 23.1 °C	59.3 % - 59.4 %
pressure	**macrostructure**
960.7 *Pa* - 960.7 *Pa*	panel_0015_0
printer	**printer_binder**
ExOne S-Max	Furan binder

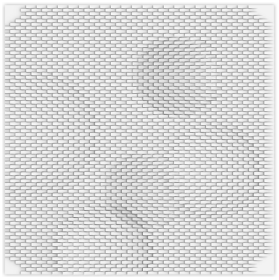
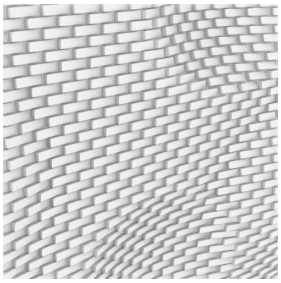

panel_0061_1

date_measured	**date_processed**
06-08-2020	07-08-2020
temperature	**humidity**
23.0 °C - 23.1 °C	59.7 % - 60.4 %
pressure	**macrostructure**
960.0 *Pa* - 960.0 *Pa*	panel_0015_1
printer	**printer_binder**
ExOne S-Max	Furan binder

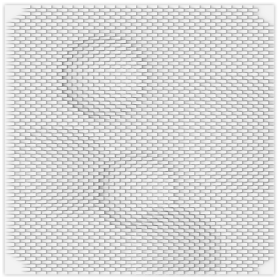
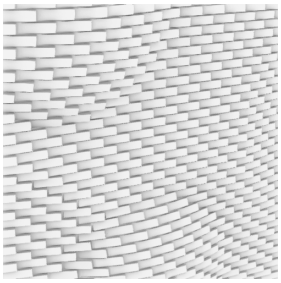

panel_0062_0

date_measured	date_processed
24-07-2020	25-07-2020
temperature	**humidity**
21.9 °C - 22.1 °C	61.7 % - 61.4 %
pressure	**macrostructure**
956.5 *Pa* - 956.5 *Pa*	panel_0015_0
printer	**printer_binder**
ExOne S-Max	Furan binder

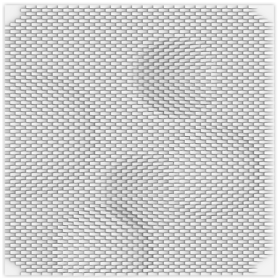
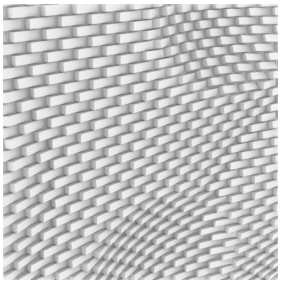

panel_0062_1

date_measured	date_processed
25-07-2020	25-07-2020
temperature	**humidity**
22.1 °C - 22.2 °C	61.6 % - 60.3 %
pressure	**macrostructure**
957.0 *Pa* - 957.0 *Pa*	panel_0015_1
printer	**printer_binder**
ExOne S-Max	Furan binder

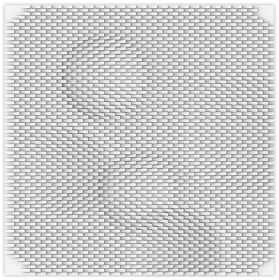
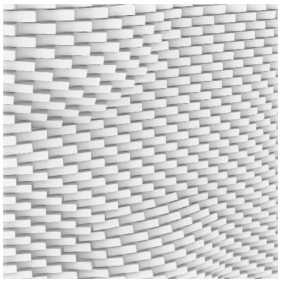

panel_0063_0

date_measured	date_processed
28-07-2020	29-07-2020
temperature	**humidity**
22.2 °C - 22.4 °C	66.0 % - 64.6 %
pressure	**macrostructure**
957.2 *Pa* - 957.2 *Pa*	panel_0015_0
printer	**printer_binder**
ExOne S-Max	Furan binder

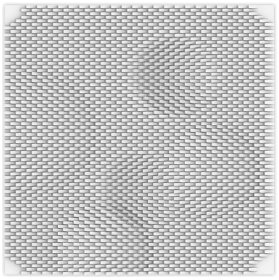
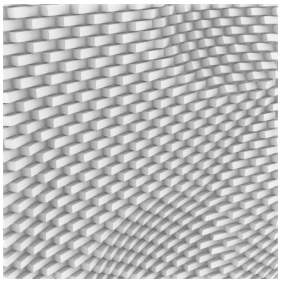

panel_0063_1

date_measured	date_processed
29-07-2020	29-07-2020
temperature	**humidity**
22.2 °C - 22.5 °C	64.1 % - 63.2 %
pressure	**macrostructure**
960.2 *Pa* - 960.2 *Pa*	panel_0015_1
printer	**printer_binder**
ExOne S-Max	Furan binder

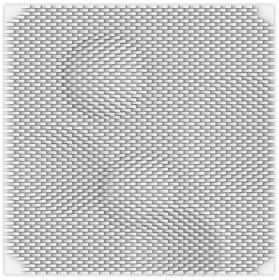
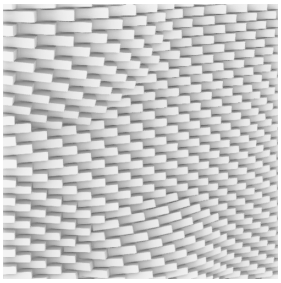

panel_0064_0

date_measured	date_processed
26-07-2020	26-07-2020
temperature	**humidity**
22.0 °C - 22.4 °C	62.1 % - 62.1 %
pressure	**macrostructure**
955.8 *Pa* - 955.8 *Pa*	panel_0015_0
printer	**printer_binder**
ExOne S-Max	Furan binder

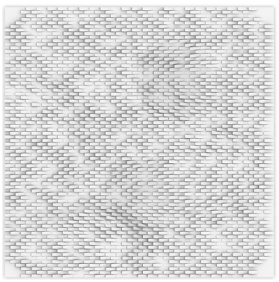


panel_0064_1

date_measured	date_processed
26-07-2020	27-07-2020
temperature	**humidity**
22.3 °C - 22.3 °C	62.3 % - 62.3 %
pressure	**macrostructure**
957.2 *Pa* - 957.2 *Pa*	panel_0015_1
printer	**printer_binder**
ExOne S-Max	Furan binder

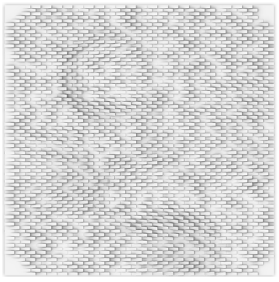
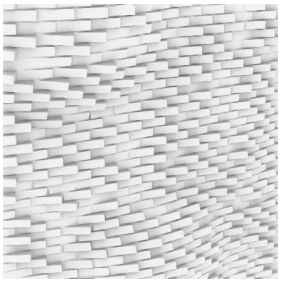

panel_0065_0

date_measured	date_processed
31-07-2020	01-08-2020
temperature	**humidity**
22.4 °C - 22.8 °C	65.1 % - 65.4 %
pressure	**macrostructure**
957.0 *Pa* - 957.0 *Pa*	panel_0015_0
printer	**printer_binder**
ExOne S-Max	Furan binder

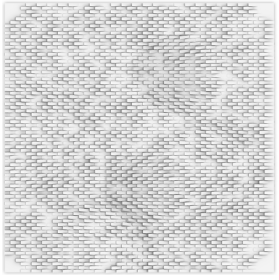
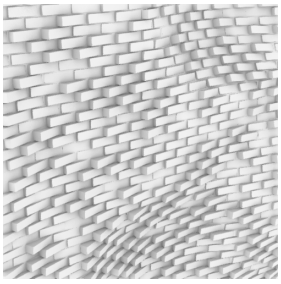

panel_0065_1

date_measured	date_processed
01-08-2020	03-08-2020
temperature	**humidity**
22.8 °C - 22.9 °C	65.5 % - 67.6 %
pressure	**macrostructure**
957.6 *Pa* - 957.6 *Pa*	panel_0015_1
printer	**printer_binder**
ExOne S-Max	Furan binder

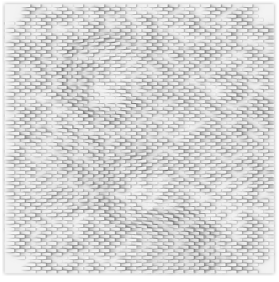


panel_0066_0

date_measured	date_processed
27-07-2020	27-07-2020
temperature	**humidity**
22.2 °C - 22.2 °C	63.1 % - 63.3 %
pressure	**macrostructure**
958.7 *Pa* - 958.7 *Pa*	panel_0015_0
printer	**printer_binder**
ExOne S-Max	Furan binder

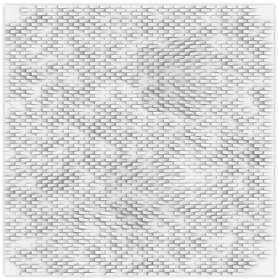
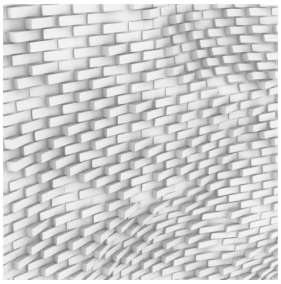

panel_0066_1

date_measured	date_processed
28-07-2020	28-07-2020
temperature	**humidity**
22.0 °C - 22.3 °C	64.1 % - 65.0 %
pressure	**macrostructure**
956.4 *Pa* - 956.4 *Pa*	panel_0015_1
printer	**printer_binder**
ExOne S-Max	Furan binder

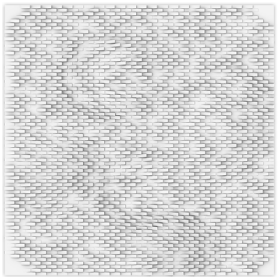


panel_0067_0

date_measured	date_processed
04-08-2020	04-08-2020
temperature	**humidity**
22.8 °C - 23.1 °C	64.7 % - 63.1 %
pressure	**macrostructure**
955.5 *Pa* - 955.4 *Pa*	flat
printer	**printer_binder**
ExOne S-Max	Furan binder

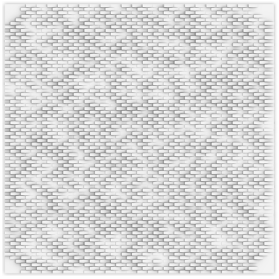


panel_0067_1

date_measured	date_processed
04-08-2020	05-08-2020
temperature	**humidity**
23.0 °C - 23.1 °C	63.2 % - 61.4 %
pressure	**macrostructure**
959.1 *Pa* - 959.1 *Pa*	flat
printer	**printer_binder**
ExOne S-Max	Furan binder

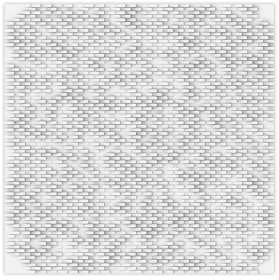


panel_0068_0

date_measured	date_processed
05-08-2020	05-08-2020
temperature	**humidity**
23.0 °C - 23.1 °C	61.5 % - 59.6 %
pressure	**macrostructure**
958.8 *Pa* - 958.8 *Pa*	flat
printer	**printer_binder**
ExOne S-Max	Furan binder

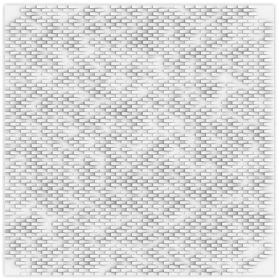
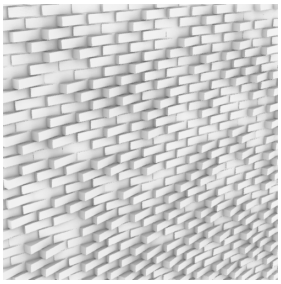

panel_0068_1

date_measured	date_processed
05-08-2020	06-08-2020
temperature	**humidity**
22.8 °C - 23.1 °C	60.0 % - 59.0 %
pressure	**macrostructure**
958.9 *Pa* - 958.9 *Pa*	flat
printer	**printer_binder**
ExOne S-Max	Furan binder

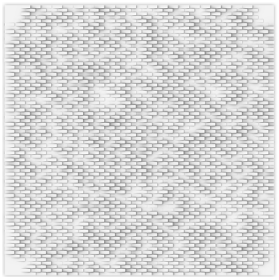


panel_0069_0

date_measured	date_processed
03-08-2020	03-08-2020
temperature	**humidity**
22.7 °C - 23.0 °C	68.2 % - 66.6 %
pressure	**macrostructure**
953.4 *Pa* - 953.4 *Pa*	flat
printer	**printer_binder**
ExOne S-Max	Furan binder

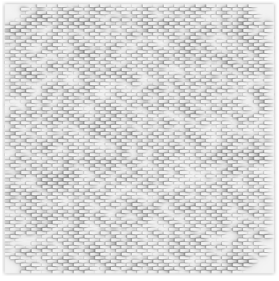


panel_0069_1

date_measured	date_processed
03-08-2020	04-08-2020
temperature	**humidity**
23.0 °C - 23.1 °C	66.5 % - 64.9 %
pressure	**macrostructure**
952.9 *Pa* - 952.9 *Pa*	flat
printer	**printer_binder**
ExOne S-Max	Furan binder

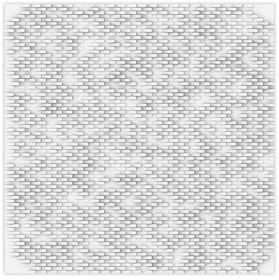


panel_0070_0

date_measured	**date_processed**
02-11-2020	02-11-2020
temperature	**humidity**
18.0 °C - 18.1 °C	57.3 % - 57.6 %
pressure	**macrostructure**
960.3 *Pa* - 960.2 *Pa*	panel_0031_0
printer	**printer_binder**
PDB	Phenolic binder

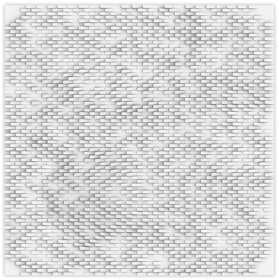
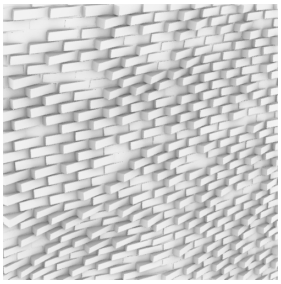

panel_0070_1

date_measured	**date_processed**
02-11-2020	03-11-2020
temperature	**humidity**
18.0 °C - 18.1 °C	58.2 % - 58.5 %
pressure	**macrostructure**
959.8 *Pa* - 959.8 *Pa*	panel_0031_1
printer	**printer_binder**
PDB	Phenolic binder

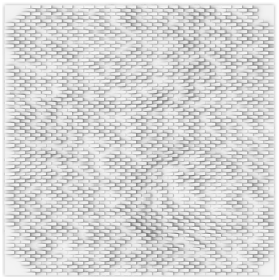


panel_0071_0

date_measured	**date_processed**
03-11-2020	03-11-2020
temperature	**humidity**
18.0 °C - 18.0 °C	59.8 % - 59.6 %
pressure	**macrostructure**
963.7 *Pa* - 963.7 *Pa*	panel_0031_0
printer	**printer_binder**
PDB	Phenolic binder

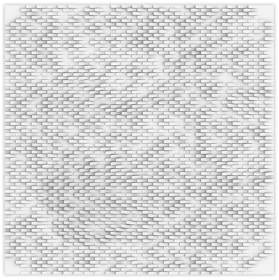
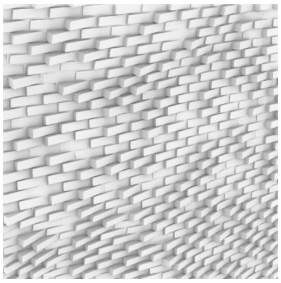

panel_0071_1

date_measured	**date_processed**
03-11-2020	04-11-2020
temperature	**humidity**
17.9 °C - 18.0 °C	59.8 % - 58.8 %
pressure	**macrostructure**
967.0 *Pa* - 967.0 *Pa*	panel_0031_1
printer	**printer_binder**
PDB	Phenolic binder

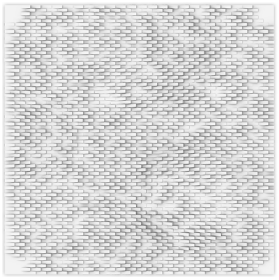


panel_0072_0

date_measured	date_processed
04-11-2020	04-11-2020
temperature	**humidity**
17.8 °C - 18.0 °C	58.7 % - 57.5 %
pressure	**macrostructure**
967.5 *Pa* - 967.5 *Pa*	panel_0031_0
printer	**printer_binder**
PDB	Phenolic binder

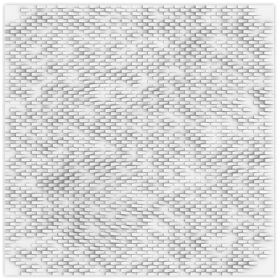

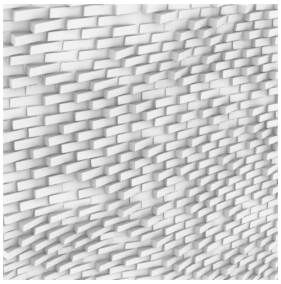

panel_0072_1

date_measured	date_processed
04-11-2020	05-11-2020
temperature	**humidity**
17.9 °C - 17.9 °C	57.3 % - 56.1 %
pressure	**macrostructure**
969.5 *Pa* - 969.6 *Pa*	panel_0031_1
printer	**printer_binder**
PDB	Phenolic binder

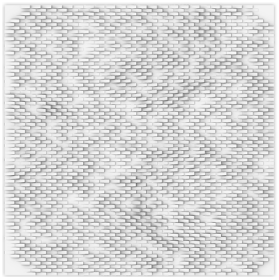

panel_0073_0

date_measured	date_processed
11-08-2020	11-08-2020
temperature	**humidity**
22.8 °C - 23.0 °C	65.1 % - 64.5 %
pressure	**macrostructure**
958.2 *Pa* - 958.2 *Pa*	flat
printer	**printer_binder**
PDB	Phenolic binder

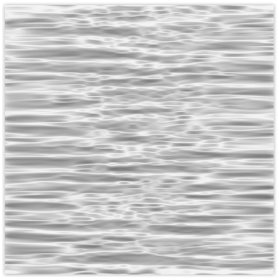

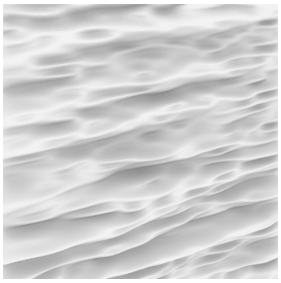

panel_0074_0

date_measured	date_processed
12-08-2020	12-08-2020
temperature	**humidity**
22.9 °C - 23.1 °C	67.3 % - 66.7 %
pressure	**macrostructure**
957.7 *Pa* - 957.7 *Pa*	flat
printer	**printer_binder**
PDB	Phenolic binder

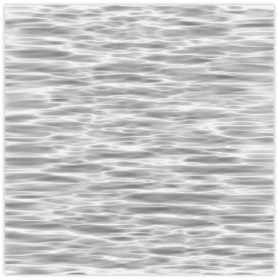

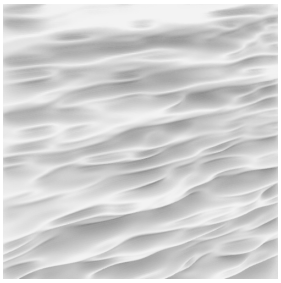

panel_0075_0

date_measured	date_processed
12-08-2020	13-08-2020
temperature	**humidity**
23.0 °C - 23.2 °C	67.2 % - 66.9 %
pressure	**macrostructure**
955.6 *Pa* - 955.6 *Pa*	flat
printer	**printer_binder**
PDB	Phenolic binder

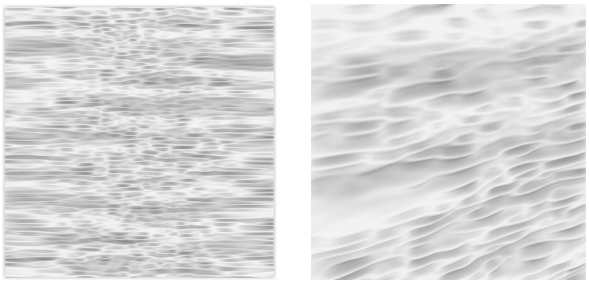

panel_0076_0

date_measured	date_processed
13-08-2020	13-08-2020
temperature	**humidity**
23.1 °C - 23.2 °C	67.3 % - 66.6 %
pressure	**macrostructure**
956.9 *Pa* - 956.9 *Pa*	flat
printer	**printer_binder**
PDB	Phenolic binder

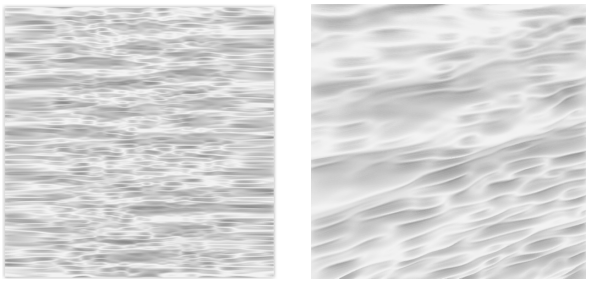

panel_0077_0

date_measured	date_processed
13-08-2020	14-08-2020
temperature	**humidity**
23.1 °C - 23.2 °C	66.8 % - 66.1 %
pressure	**macrostructure**
956.7 *Pa* - 956.7 *Pa*	flat
printer	**printer_binder**
PDB	Phenolic binder

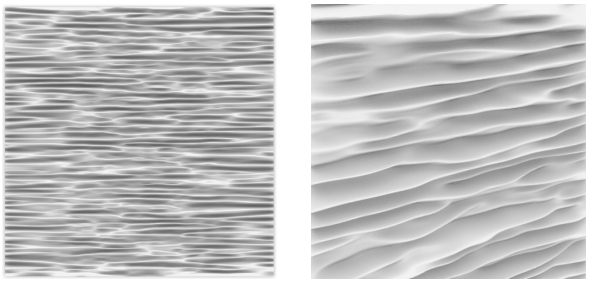

panel_0078_0

date_measured	date_processed
07-08-2020	07-08-2020
temperature	**humidity**
22.8 °C - 23.0 °C	62.0 % - 62.5 %
pressure	**macrostructure**
961.2 *Pa* - 961.2 *Pa*	flat
printer	**printer_binder**
PDB	Phenolic binder

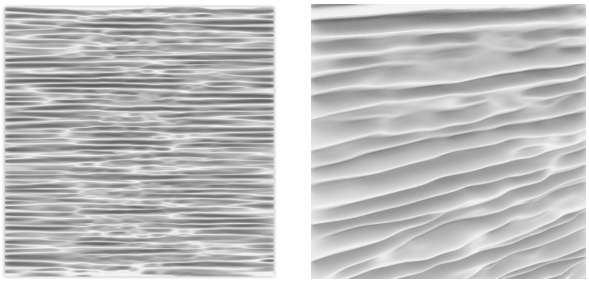

panel_0079_0

date_measured	date_processed
07-08-2020	08-08-2020
temperature	**humidity**
23.0 °C - 23.0 °C	63.0 % - 63.7 %
pressure	**macrostructure**
960.7 *Pa* - 960.7 *Pa*	flat
printer	**printer_binder**
PDB	Phenolic binder

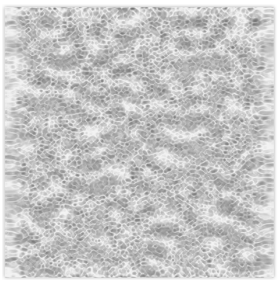
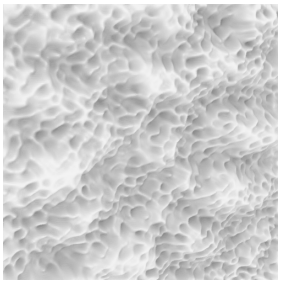

panel_0080_0

date_measured	date_processed
10-08-2020	10-08-2020
temperature	**humidity**
22.9 °C - 23.0 °C	64.6 % - 63.9 %
pressure	**macrostructure**
956.4 *Pa* - 956.4 *Pa*	flat
printer	**printer_binder**
PDB	Phenolic binder

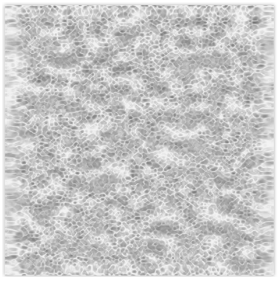
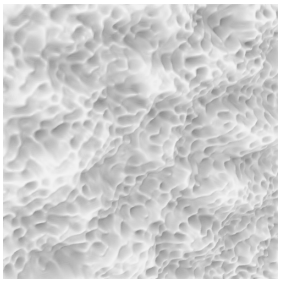

panel_0081_0

date_measured	date_processed
11-08-2020	12-08-2020
temperature	**humidity**
23.0 °C - 23.1 °C	64.9 % - 65.8 %
pressure	**macrostructure**
956.3 *Pa* - 956.2 *Pa*	flat
printer	**printer_binder**
PDB	Phenolic binder

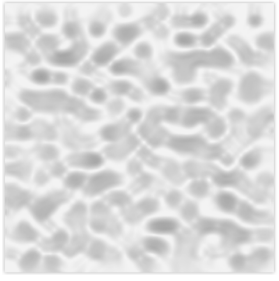
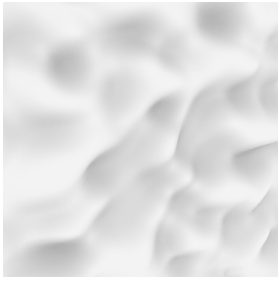

panel_0082_0

date_measured	date_processed
08-08-2020	08-08-2020
temperature	**humidity**
22.8 °C - 23.0 °C	64.0 % - 63.1 %
pressure	**macrostructure**
961.5 *Pa* - 961.5 *Pa*	flat
printer	**printer_binder**
PDB	Phenolic binder

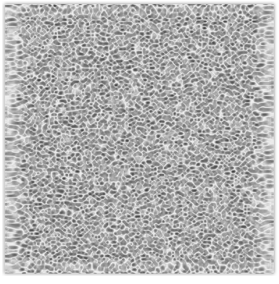
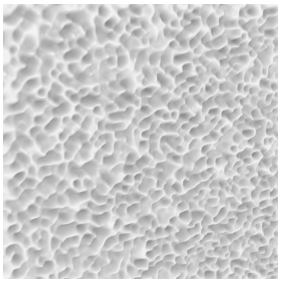

panel_0083_0

date_measured	date_processed
07-02-2021	08-02-2021
temperature	**humidity**
12.3 °C - 12.5 °C	61.8 % - 60.4 %
pressure	**macrostructure**
937.1 *Pa* - 937.1 *Pa*	macrostructure
printer	**printer_binder**
PDB	Phenolic binder

panel_0083_1

date_measured	date_processed
08-02-2021	09-02-2021
temperature	**humidity**
12.4 °C - 12.7 °C	59.5 % - 57.3 %
pressure	**macrostructure**
935.4 *Pa* - 935.4 *Pa*	macrostructure
printer	**printer_binder**
PDB	Phenolic binder

panel_0084_0

date_measured	date_processed
30-10-2020	31-10-2020
temperature	**humidity**
18.0 °C - 18.2 °C	55.4 % - 54.9 %
pressure	**macrostructure**
966.5 *Pa* - 966.5 *Pa*	panel_0083_0
printer	**printer_binder**
PDB	Phenolic binder

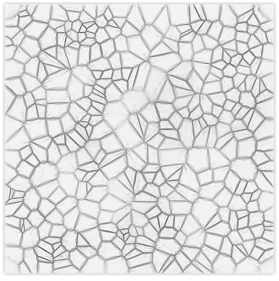

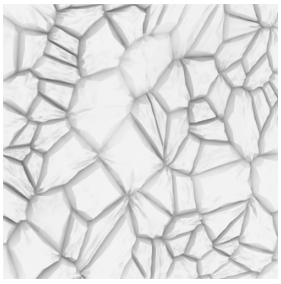

panel_0084_1

date_measured	date_processed
31-10-2020	31-10-2020
temperature	**humidity**
18.0 °C - 18.2 °C	55.0 % - 55.0 %
pressure	**macrostructure**
964.9 *Pa* - 964.9 *Pa*	panel_0083_1
printer	**printer_binder**
PDB	Phenolic binder

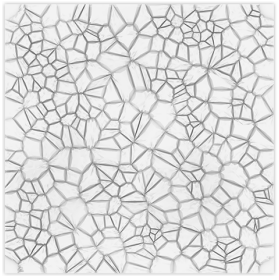

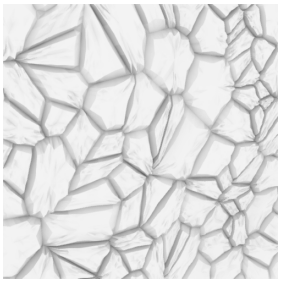

panel_0085_0

date_measured	date_processed
01-11-2020	01-11-2020
temperature	**humidity**
17.8 °C - 18.1 °C	55.5 % - 55.7 %
pressure	**macrostructure**
962.6 *Pa* - 962.6 *Pa*	panel_0083_0
printer	**printer_binder**
PDB	Phenolic binder

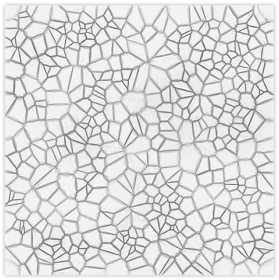
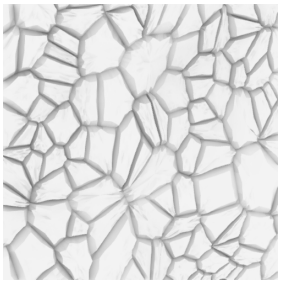

panel_0085_1

date_measured	date_processed
01-11-2020	02-11-2020
temperature	**humidity**
18.0 °C - 18.1 °C	55.9 % - 56.3 %
pressure	**macrostructure**
960.9 *Pa* - 960.9 *Pa*	panel_0083_1
printer	**printer_binder**
PDB	Phenolic binder

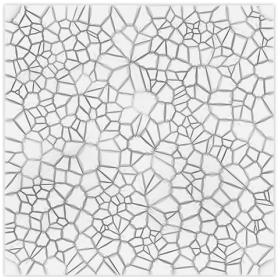
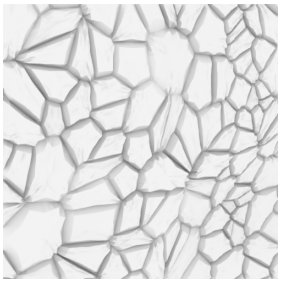

panel_0086_0

date_measured	date_processed
05-02-2021	06-02-2021
temperature	**humidity**
12.0 °C - 12.2 °C	61.6 % - 61.5 %
pressure	**macrostructure**
953.2 *Pa* - 953.2 *Pa*	panel_0083_0
printer	**printer_binder**
PDB	Phenolic binder

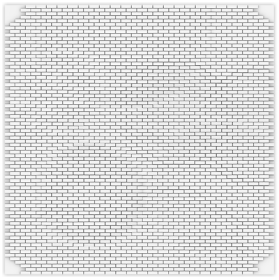
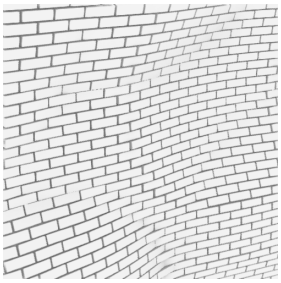

panel_0086_1

date_measured	date_processed
06-02-2021	07-02-2021
temperature	**humidity**
12.1 °C - 12.4 °C	62.3 % - 61.5 %
pressure	**macrostructure**
940.8 *Pa* - 940.8 *Pa*	panel_0083_1
printer	**printer_binder**
PDB	Phenolic binder

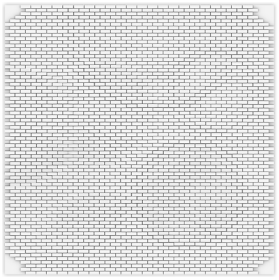
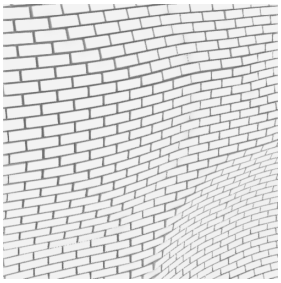

panel_0087_0

date_measured	date_processed
28-10-2020	28-10-2020
temperature	**humidity**
18.3 °C - 18.4 °C	52.2 % - 52.4 %
pressure	**macrostructure**
956.5 *Pa* - 956.5 *Pa*	panel_0083_0
printer	**printer_binder**
PDB	Phenolic binder

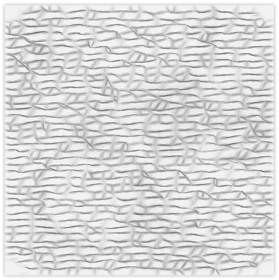
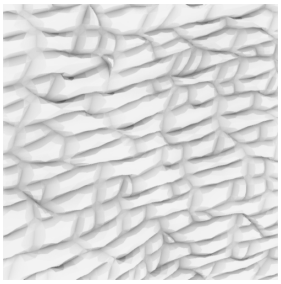

panel_0087_1

date_measured	date_processed
28-10-2020	29-10-2020
temperature	**humidity**
18.2 °C - 18.3 °C	52.6 % - 53.1 %
pressure	**macrostructure**
956.9 *Pa* - 956.9 *Pa*	panel_0083_1
printer	**printer_binder**
PDB	Phenolic binder

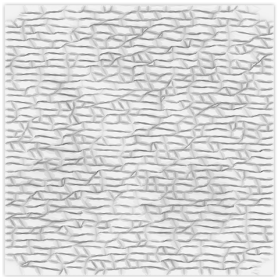
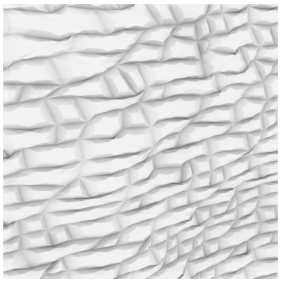

panel_0088_0

date_measured	date_processed
26-10-2020	26-10-2020
temperature	**humidity**
18.1 °C - 18.4 °C	56.6 % - 55.0 %
pressure	**macrostructure**
948.3 *Pa* - 948.3 *Pa*	panel_0083_0
printer	**printer_binder**
PDB	Phenolic binder

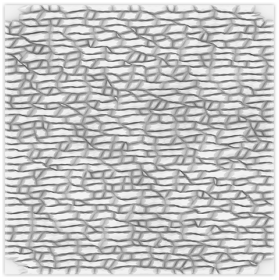
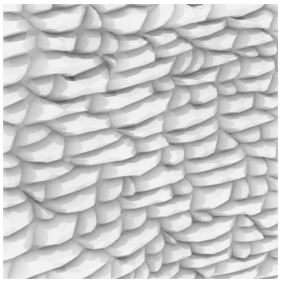

panel_0088_1

date_measured	date_processed
26-10-2020	27-10-2020
temperature	**humidity**
18.3 °C - 18.4 °C	54.7 % - 53.8 %
pressure	**macrostructure**
950.9 *Pa* - 950.9 *Pa*	panel_0083_1
printer	**printer_binder**
PDB	Phenolic binder

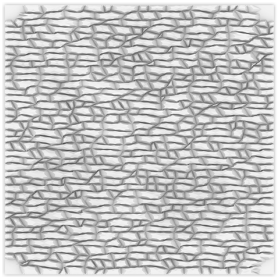


panel_0089_0

date_measured	date_processed
05-11-2020	05-11-2020
temperature	**humidity**
17.9 °C - 18.0 °C	56.0 % - 55.6 %
pressure	**macrostructure**
973.7 *Pa* - 973.7 *Pa*	panel_0031_0
printer	**printer_binder**
PDB	Phenolic binder

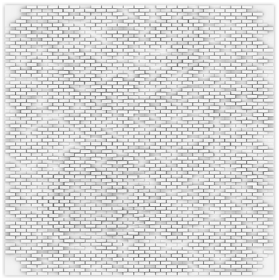
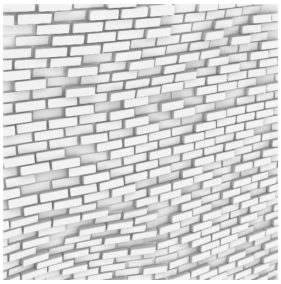

panel_0089_1

date_measured	date_processed
06-11-2020	06-11-2020
temperature	**humidity**
17.8 °C - 18.0 °C	55.3 % - 54.4 %
pressure	**macrostructure**
970.6 *Pa* - 970.6 *Pa*	panel_0031_1
printer	**printer_binder**
PDB	Phenolic binder

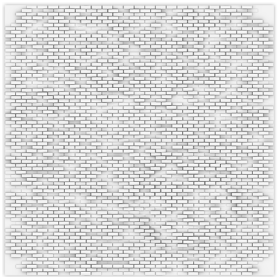
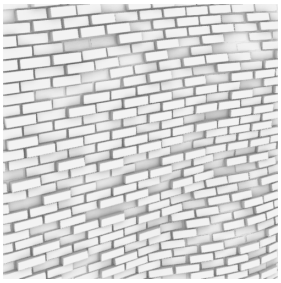

panel_0090_0

date_measured	date_processed
07-11-2020	08-11-2020
temperature	**humidity**
17.7 °C - 17.8 °C	54.2 % - 54.0 %
pressure	**macrostructure**
965.3 *Pa* - 965.3 *Pa*	panel_0083_0
printer	**printer_binder**
PDB	Phenolic binder

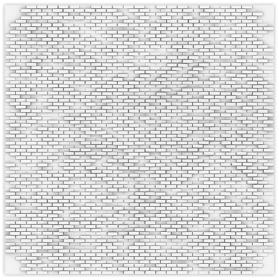
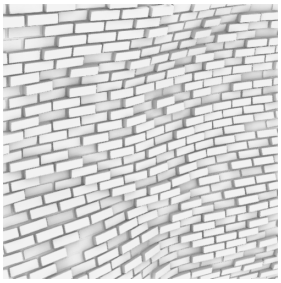

panel_0090_1

date_measured	date_processed
08-11-2020	08-11-2020
temperature	**humidity**
17.6 °C - 17.6 °C	54.1 % - 54.5 %
pressure	**macrostructure**
964.9 *Pa* - 964.9 *Pa*	panel_0083_1
printer	**printer_binder**
PDB	Phenolic binder

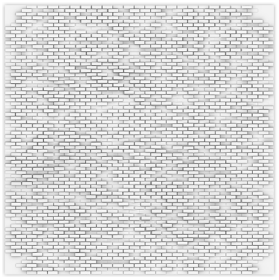


panel_0091_0

date_measured	date_processed
09-11-2020	09-11-2020
temperature	**humidity**
17.5 °C - 17.8 °C	54.0 % - 53.9 %
pressure	**macrostructure**
964.6 *Pa* - 964.6 *Pa*	flat
printer	**printer_binder**
PDB	Phenolic binder

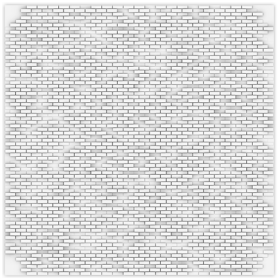
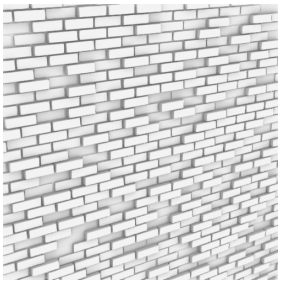

panel_0091_1

date_measured	date_processed
09-11-2020	10-11-2020
temperature	**humidity**
17.7 °C - 17.8 °C	54.1 % - 53.5 %
pressure	**macrostructure**
964.2 *Pa* - 964.2 *Pa*	flat
printer	**printer_binder**
PDB	Phenolic binder

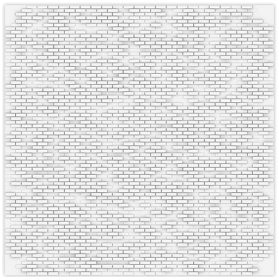
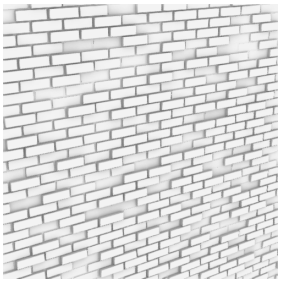

panel_0092_0

date_measured	date_processed
10-11-2020	10-11-2020
temperature	**humidity**
17.5 °C - 17.7 °C	53.4 % - 53.5 %
pressure	**macrostructure**
965.8 *Pa* - 965.8 *Pa*	flat
printer	**printer_binder**
PDB	Phenolic binder

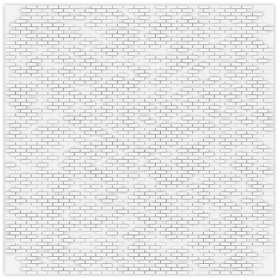
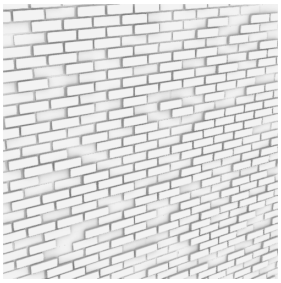

panel_0092_1

date_measured	date_processed
10-11-2020	11-11-2020
temperature	**humidity**
17.5 °C - 17.7 °C	53.7 % - 53.2 %
pressure	**macrostructure**
967.2 *Pa* - 967.2 *Pa*	flat
printer	**printer_binder**
PDB	Phenolic binder

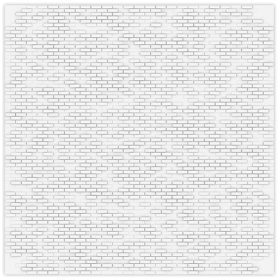
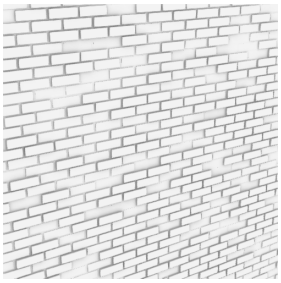

panel_0093_0

date_measured	date_processed
11-11-2020	11-11-2020
temperature	**humidity**
17.6 °C - 17.7 °C	53.2 % - 53.3 %
pressure	**macrostructure**
965.9 *Pa* - 965.9 *Pa*	flat
printer	**printer_binder**
PDB	Phenolic binder

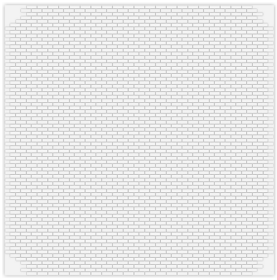

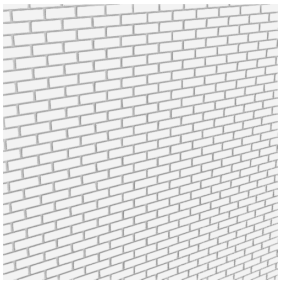

panel_0093_1

date_measured	date_processed
11-11-2020	12-11-2020
temperature	**humidity**
17.6 °C - 17.6 °C	53.4 % - 53.4 %
pressure	**macrostructure**
963.1 *Pa* - 963.1 *Pa*	flat
printer	**printer_binder**
PDB	Phenolic binder

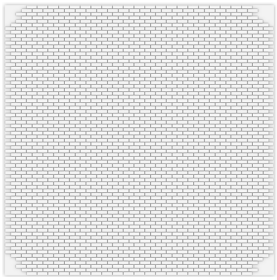

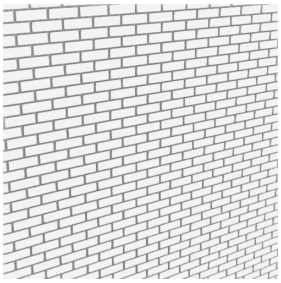

panel_0094_0

date_measured	date_processed
12-11-2020	12-11-2020
temperature	**humidity**
17.4 °C - 17.6 °C	53.8 % - 53.7 %
pressure	**macrostructure**
962.7 *Pa* - 962.7 *Pa*	flat
printer	**printer_binder**
PDB	Phenolic binder

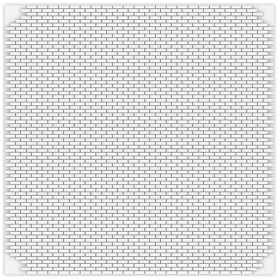

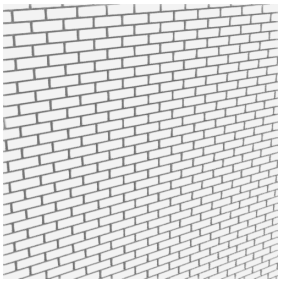

panel_0094_1

date_measured	date_processed
12-11-2020	13-11-2020
temperature	**humidity**
17.5 °C - 17.5 °C	54.0 % - 53.4 %
pressure	**macrostructure**
962.6 *Pa* - 962.5 *Pa*	flat
printer	**printer_binder**
PDB	Phenolic binder

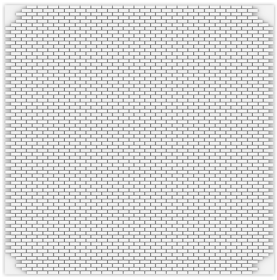

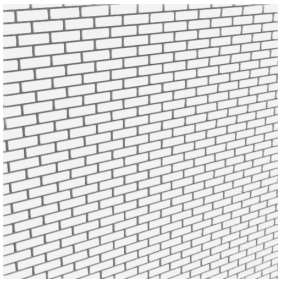

panel_0095_0

date_measured	date_processed
13-11-2020	13-11-2020
temperature	**humidity**
17.3 °C - 17.5 °C	53.6 % - 53.2 %
pressure	**macrostructure**
962.7 *Pa* - 962.7 *Pa*	panel_0031_0
printer	**printer_binder**
PDB	Phenolic binder

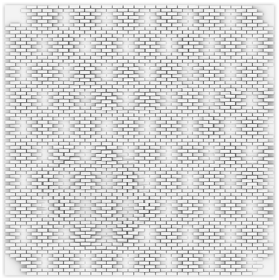
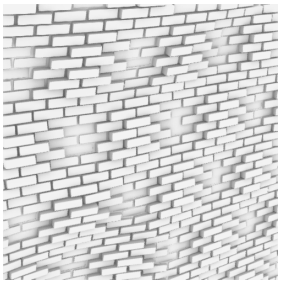

panel_0095_1

date_measured	date_processed
13-11-2020	14-11-2020
temperature	**humidity**
17.0 °C - 17.4 °C	53.3 % - 52.9 %
pressure	**macrostructure**
962.1 *Pa* - 962.1 *Pa*	panel_0031_1
printer	**printer_binder**
PDB	Phenolic binder

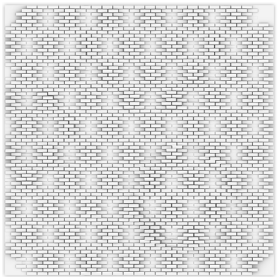
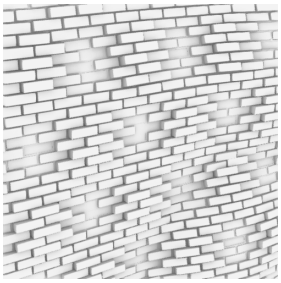

panel_0096_0

date_measured	date_processed
16-11-2020	16-11-2020
temperature	**humidity**
17.0 °C - 17.2 °C	54.5 % - 53.9 %
pressure	**macrostructure**
960.5 *Pa* - 960.5 *Pa*	panel_0083_0
printer	**printer_binder**
PDB	Phenolic binder

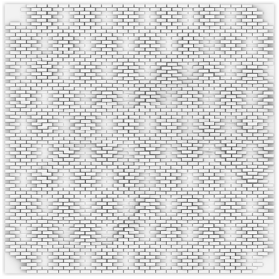


panel_0096_1

date_measured	date_processed
16-11-2020	17-11-2020
temperature	**humidity**
17.1 °C - 17.2 °C	54.0 % - 53.7 %
pressure	**macrostructure**
964.9 *Pa* - 964.9 *Pa*	panel_0083_1
printer	**printer_binder**
PDB	Phenolic binder

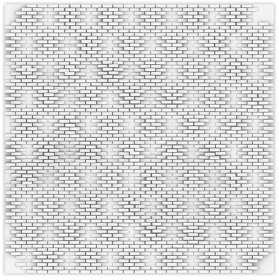
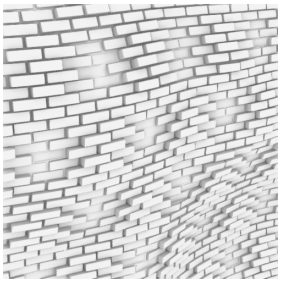

panel_0097_0

date_measured	date_processed
20-11-2020	21-11-2020
temperature	**humidity**
16.9 °C - 17.0 °C	49.2 % - 48.5 %
pressure	**macrostructure**
973.5 *Pa* - 973.5 *Pa*	flat
printer	**printer_binder**
PDB	Phenolic binder

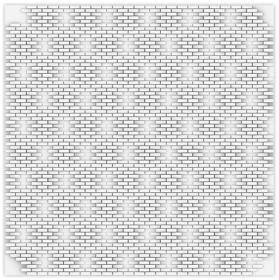
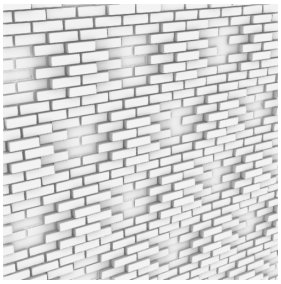

panel_0097_1

date_measured	date_processed
23-11-2020	24-11-2020
temperature	**humidity**
16.4 °C - 16.5 °C	45.8 % - 45.7 %
pressure	**macrostructure**
967.6 *Pa* - 967.6 *Pa*	flat
printer	**printer_binder**
PDB	Phenolic binder

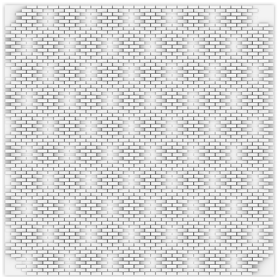
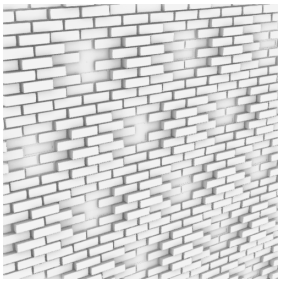

panel_0098_0

date_measured	date_processed
24-11-2020	24-11-2020
temperature	**humidity**
16.2 °C - 16.4 °C	45.9 % - 45.5 %
pressure	**macrostructure**
965.1 *Pa* - 965.2 *Pa*	panel_0031_0
printer	**printer_binder**
PDB	Phenolic binder

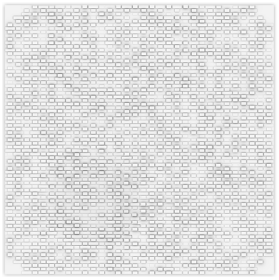
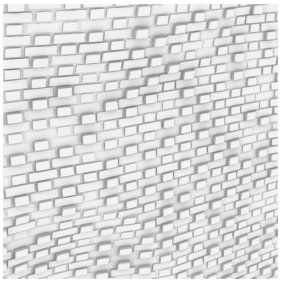

panel_0098_1

date_measured	date_processed
24-11-2020	25-11-2020
temperature	**humidity**
16.3 °C - 16.4 °C	45.2 % - 45.3 %
pressure	**macrostructure**
962.1 *Pa* - 962.1 *Pa*	panel_0031_1
printer	**printer_binder**
PDB	Phenolic binder

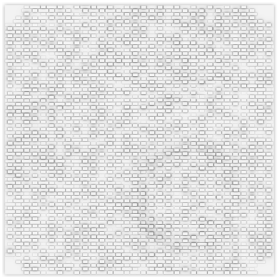
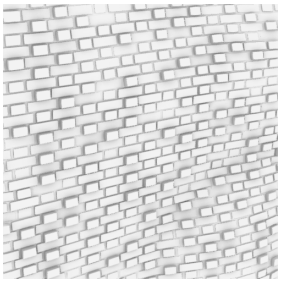

panel_0099_0

date_measured	date_processed
03-02-2021	03-02-2021
temperature	**humidity**
11.5 °C - 11.8 °C	61.6 % - 61.3 %
pressure	**macrostructure**
945.6 *Pa* - 945.6 *Pa*	panel_0083_0
printer	**printer_binder**
PDB	Phenolic binder

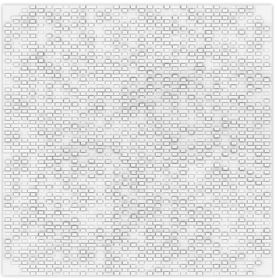

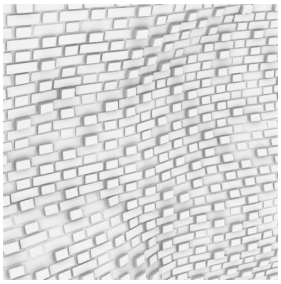

panel_0099_1

date_measured	date_processed
03-02-2021	04-02-2021
temperature	**humidity**
11.7 °C - 11.9 °C	61.7 % - 61.0 %
pressure	**macrostructure**
949.1 *Pa* - 949.1 *Pa*	panel_0083_1
printer	**printer_binder**
PDB	Phenolic binder

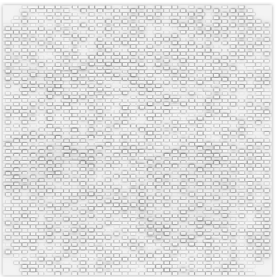

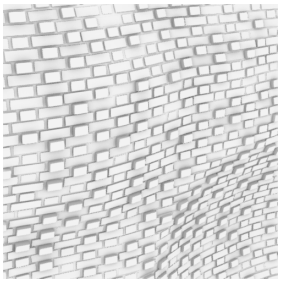

panel_0100_0

date_measured	date_processed
19-11-2020	20-11-2020
temperature	**humidity**
17.1 °C - 17.1 °C	52.2 % - 51.3 %
pressure	**macrostructure**
964.2 *Pa* - 964.3 *Pa*	flat
printer	**printer_binder**
PDB	Phenolic binder

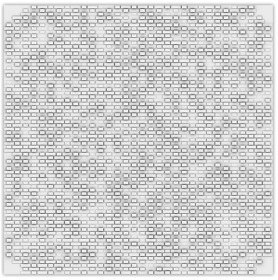

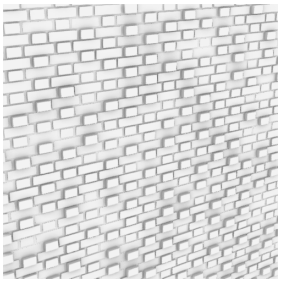

panel_0100_1

date_measured	date_processed
20-11-2020	20-11-2020
temperature	**humidity**
16.9 °C - 17.1 °C	51.4 % - 50.1 %
pressure	**macrostructure**
971.1 *Pa* - 971.2 *Pa*	flat
printer	**printer_binder**
PDB	Phenolic binder

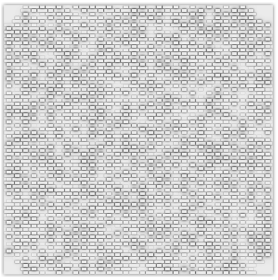

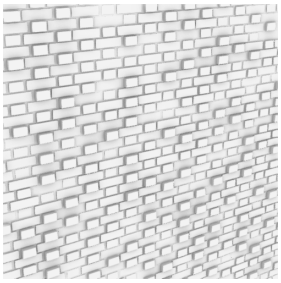

panel_0101_0

date_measured	**date_processed**
23-10-2020	24-10-2020
temperature	**humidity**
18.2 °C - 18.4 °C	59.0 % - 58.0 %
pressure	**macrostructure**
957.3 *Pa* - 957.3 *Pa*	panel_0031_0
printer	**printer_binder**
PDB	Phenolic binder

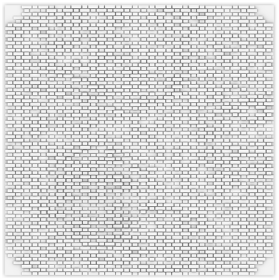

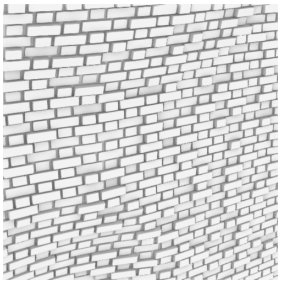

panel_0101_1

date_measured	**date_processed**
24-10-2020	24-10-2020
temperature	**humidity**
18.2 °C - 18.4 °C	58.7 % - 57.6 %
pressure	**macrostructure**
960.3 *Pa* - 960.3 *Pa*	panel_0031_1
printer	**printer_binder**
PDB	Phenolic binder

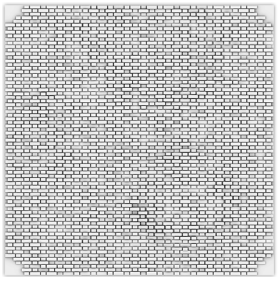

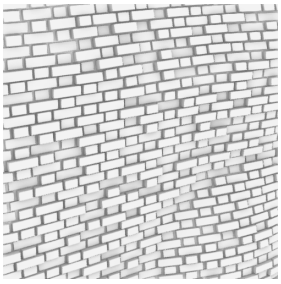

panel_0102_0

date_measured	**date_processed**
25-11-2020	25-11-2020
temperature	**humidity**
16.2 °C - 16.3 °C	45.3 % - 45.1 %
pressure	**macrostructure**
961.1 *Pa* - 961.1 *Pa*	panel_0083_0
printer	**printer_binder**
PDB	Phenolic binder

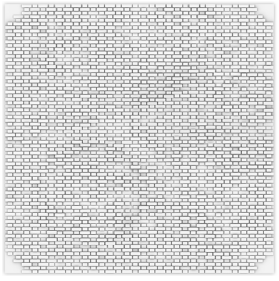

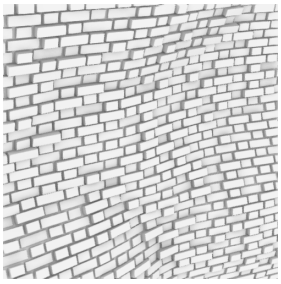

panel_0102_1

date_measured	**date_processed**
25-11-2020	26-11-2020
temperature	**humidity**
16.2 °C - 16.3 °C	44.8 % - 45.0 %
pressure	**macrostructure**
961.4 *Pa* - 961.4 *Pa*	panel_0083_1
printer	**printer_binder**
PDB	Phenolic binder

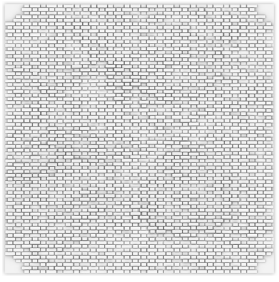

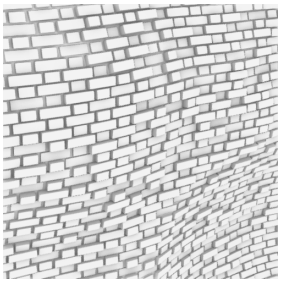

panel_0103_0

date_measured	date_processed
26-11-2020	26-11-2020
temperature	**humidity**
16.1 °C - 16.2 °C	44.9 % - 45.1 %
pressure	**macrostructure**
963.3 *Pa* - 963.3 *Pa*	flat
printer	**printer_binder**
PDB	Phenolic binder

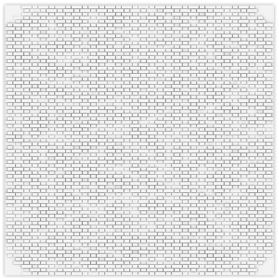
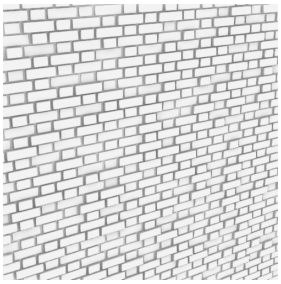

panel_0103_1

date_measured	date_processed
26-11-2020	27-11-2020
temperature	**humidity**
16.1 °C - 16.2 °C	45.1 % - 45.1 %
pressure	**macrostructure**
961.6 *Pa* - 961.6 *Pa*	flat
printer	**printer_binder**
PDB	Phenolic binder

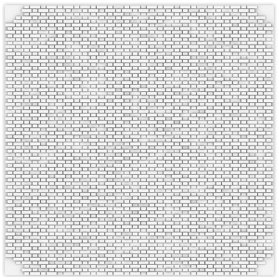
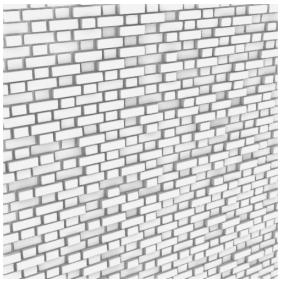

panel_0104_0

date_measured	date_processed
18-11-2020	18-11-2020
temperature	**humidity**
16.9 °C - 17.2 °C	52.3 % - 52.6 %
pressure	**macrostructure**
968.3 *Pa* - 968.3 *Pa*	panel_0031_0
printer	**printer_binder**
PDB	Phenolic binder

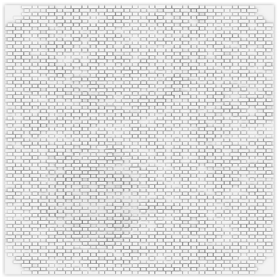
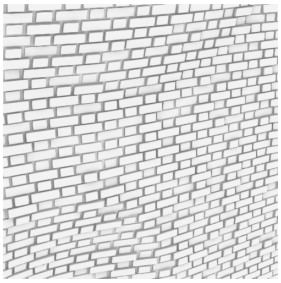

panel_0104_1

date_measured	date_processed
18-11-2020	19-11-2020
temperature	**humidity**
17.1 °C - 17.2 °C	52.4 % - 52.2 %
pressure	**macrostructure**
964.9 *Pa* - 964.9 *Pa*	panel_0031_1
printer	**printer_binder**
PDB	Phenolic binder

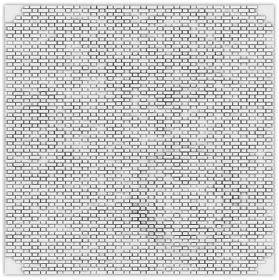
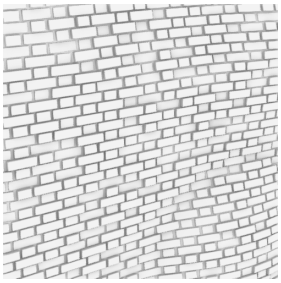

panel_0105_0

date_measured	**date_processed**
24-10-2020	25-10-2020
temperature	**humidity**
18.3 °C - 18.4 °C	57.8 % - 57.1 %
pressure	**macrostructure**
957.1 *Pa* - 957.1 *Pa*	panel_0083_0
printer	**printer_binder**
PDB	Phenolic binder

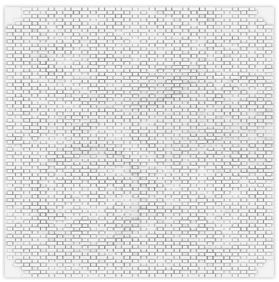

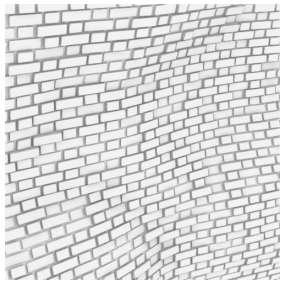

panel_0105_1

date_measured	**date_processed**
25-10-2020	25-10-2020
temperature	**humidity**
18.2 °C - 18.4 °C	57.2 % - 56.8 %
pressure	**macrostructure**
951.1 *Pa* - 951.1 *Pa*	panel_0083_1
printer	**printer_binder**
PDB	Phenolic binder

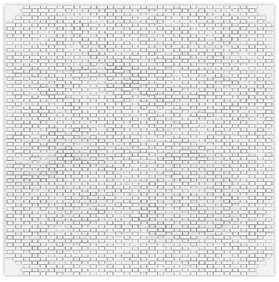

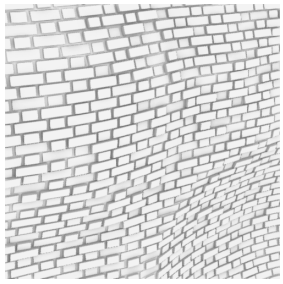

panel_0106_0

date_measured	**date_processed**
01-12-2020	01-12-2020
temperature	**humidity**
15.3 °C - 15.4 °C	42.5 % - 43.1 %
pressure	**macrostructure**
955.5 *Pa* - 955.4 *Pa*	panel_0031_0
printer	**printer_binder**
PDB	Phenolic binder

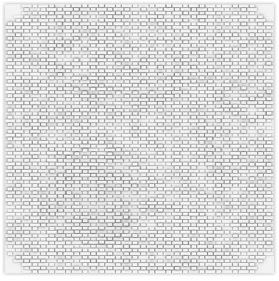

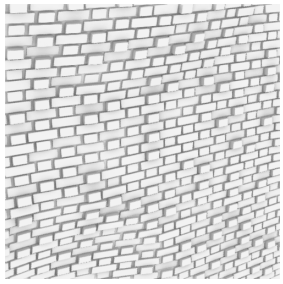

panel_0106_1

date_measured	**date_processed**
01-12-2020	02-12-2020
temperature	**humidity**
15.3 °C - 15.3 °C	43.2 % - 43.4 %
pressure	**macrostructure**
955.7 *Pa* - 955.7 *Pa*	panel_0031_1
printer	**printer_binder**
PDB	Phenolic binder

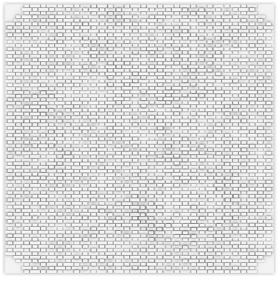

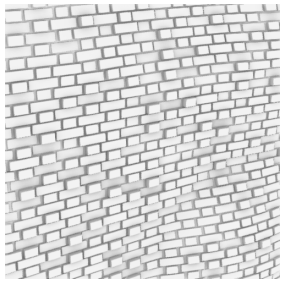

panel_0107_0

date_measured	date_processed
27-10-2020	27-10-2020
temperature	**humidity**
18.2 °C - 18.4 °C	53.2 % - 52.7 %
pressure	**macrostructure**
953.3 *Pa* - 953.3 *Pa*	panel_0083_0
printer	**printer_binder**
PDB	Phenolic binder

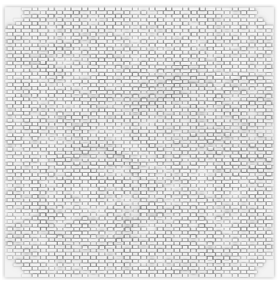

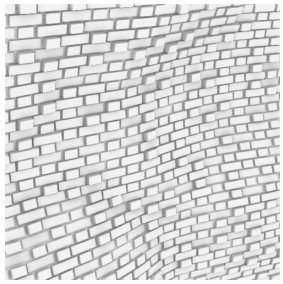

panel_0107_1

date_measured	date_processed
27-10-2020	28-10-2020
temperature	**humidity**
18.2 °C - 18.4 °C	52.2 % - 52.2 %
pressure	**macrostructure**
953.7 *Pa* - 953.7 *Pa*	panel_0083_1
printer	**printer_binder**
PDB	Phenolic binder

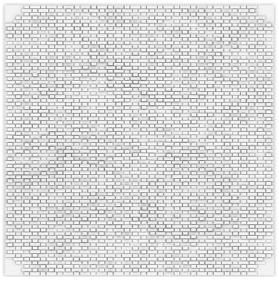

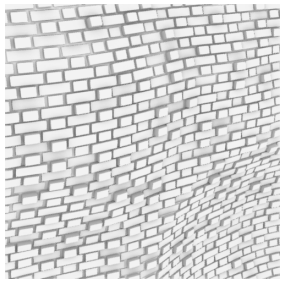

panel_0108_0

date_measured	date_processed
30-11-2020	30-11-2020
temperature	**humidity**
15.2 °C - 15.4 °C	43.8 % - 43.0 %
pressure	**macrostructure**
964.7 *Pa* - 964.7 *Pa*	flat
printer	**printer_binder**
PDB	Phenolic binder

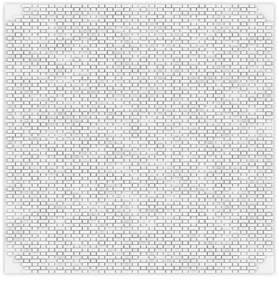

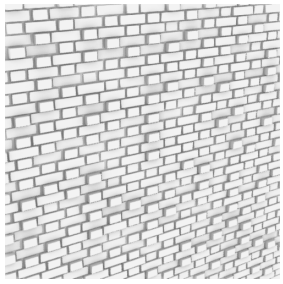

panel_0108_1

date_measured	date_processed
30-11-2020	01-12-2020
temperature	**humidity**
15.3 °C - 15.4 °C	42.9 % - 42.7 %
pressure	**macrostructure**
963.2 *Pa* - 963.2 *Pa*	flat
printer	**printer_binder**
PDB	Phenolic binder

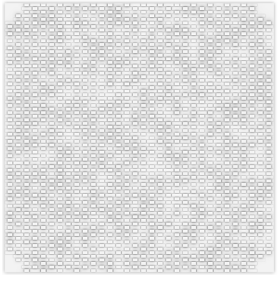

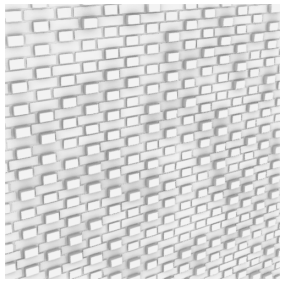

panel_0109_0

date_measured	date_processed
15-12-2020	16-12-2020
temperature	**humidity**
13.4 °C - 13.6 °C	50.2 % - 50.1 %
pressure	**macrostructure**
956.5 *Pa* - 956.5 *Pa*	flat
printer	**printer_binder**
FDB	Furan binder

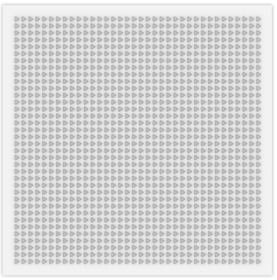

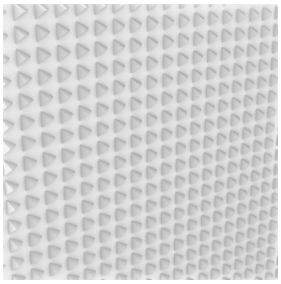

panel_0109_1

date_measured	date_processed
16-12-2020	16-12-2020
temperature	**humidity**
13.5 °C - 13.6 °C	50.5 % - 51.0 %
pressure	**macrostructure**
958.7 *Pa* - 958.7 *Pa*	flat
printer	**printer_binder**
FDB	Furan binder

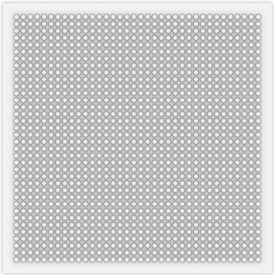

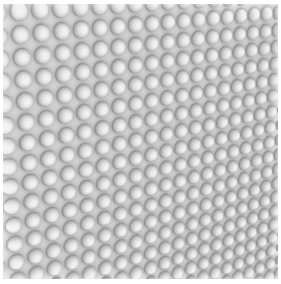

panel_0110_0

date_measured	date_processed
14-12-2020	14-12-2020
temperature	**humidity**
13.4 °C - 13.6 °C	48.4 % - 48.4 %
pressure	**macrostructure**
954.8 *Pa* - 954.8 *Pa*	flat
printer	**printer_binder**
FDB	Furan binder

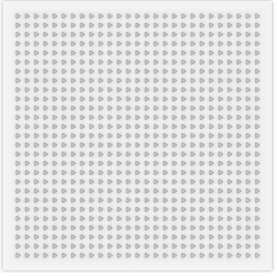

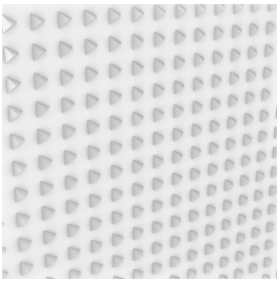

panel_0110_1

date_measured	date_processed
15-12-2020	15-12-2020
temperature	**humidity**
13.4 °C - 13.6 °C	49.0 % - 49.5 %
pressure	**macrostructure**
954.0 *Pa* - 954.0 *Pa*	flat
printer	**printer_binder**
FDB	Furan binder

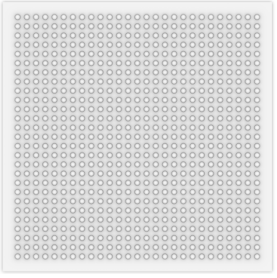

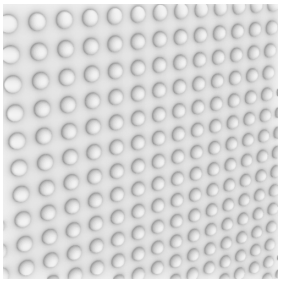

panel_0111_0

date_measured	date_processed
16-12-2020	17-12-2020
temperature	**humidity**
13.4 °C - 13.6 °C	51.7 % - 51.2 %
pressure	**macrostructure**
959.7 *Pa* - 959.7 *Pa*	flat
printer	**printer_binder**
FDB	Furan binder

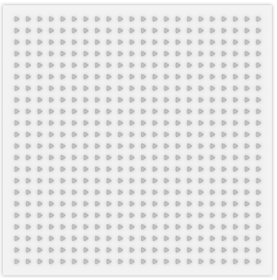

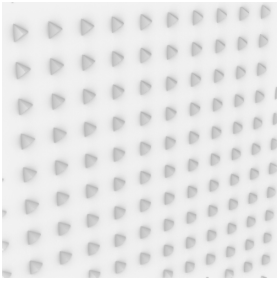

panel_0111_1

date_measured	date_processed
17-12-2020	17-12-2020
temperature	**humidity**
13.4 °C - 13.6 °C	51.5 % - 51.5 %
pressure	**macrostructure**
963.7 *Pa* - 963.7 *Pa*	flat
printer	**printer_binder**
FDB	Furan binder

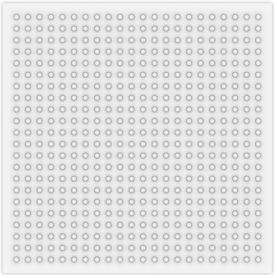

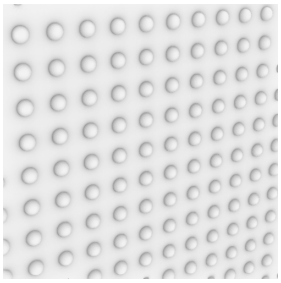

panel_0112_0

date_measured	date_processed
08-12-2020	09-12-2020
temperature	**humidity**
14.0 °C - 14.1 °C	44.6 % - 44.9 %
pressure	**macrostructure**
944.8 *Pa* - 944.8 *Pa*	flat
printer	**printer_binder**
FDB	Furan binder

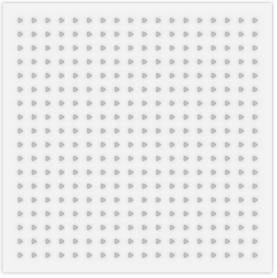

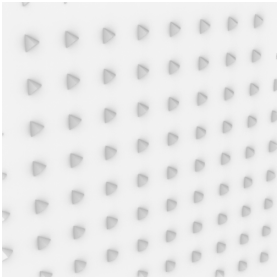

panel_0112_1

date_measured	date_processed
09-12-2020	10-12-2020
temperature	**humidity**
14.0 °C - 14.0 °C	44.9 % - 44.8 %
pressure	**macrostructure**
949.4 *Pa* - 949.4 *Pa*	flat
printer	**printer_binder**
FDB	Furan binder

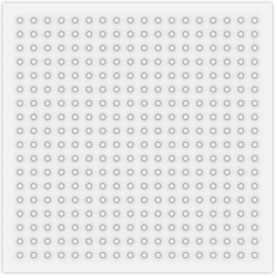

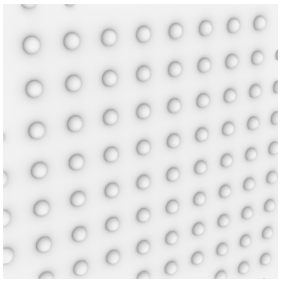

panel_0113_0

date_measured	date_processed
07-12-2020	08-12-2020
temperature	**humidity**
14.2 °C - 14.3 °C	45.1 % - 44.8 %
pressure	**macrostructure**
940.9 *Pa* - 940.9 *Pa*	flat
printer	**printer_binder**
FDB	Furan binder

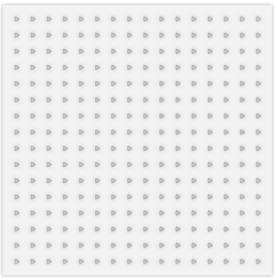

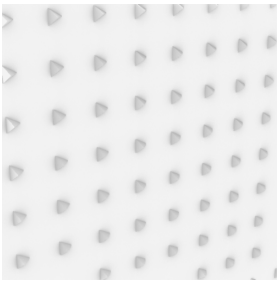

panel_0113_1

date_measured	date_processed
08-12-2020	08-12-2020
temperature	**humidity**
14.1 °C - 14.2 °C	44.7 % - 44.5 %
pressure	**macrostructure**
940.6 *Pa* - 940.6 *Pa*	flat
printer	**printer_binder**
FDB	Furan binder

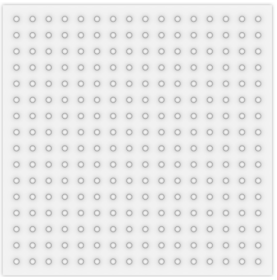

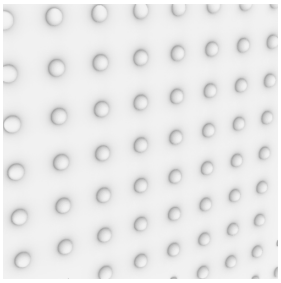

panel_0114_0

date_measured	date_processed
13-12-2020	13-12-2020
temperature	**humidity**
13.5 °C - 13.7 °C	47.6 % - 47.7 %
pressure	**macrostructure**
953.2 *Pa* - 953.2 *Pa*	flat
printer	**printer_binder**
FDB	Furan binder

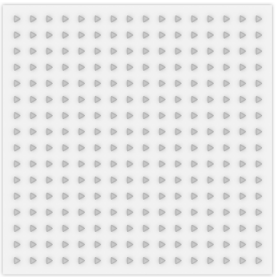

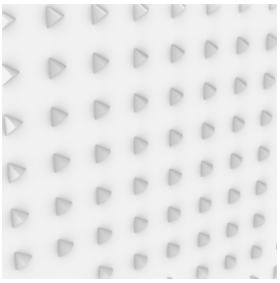

panel_0114_1

date_measured	date_processed
13-12-2020	14-12-2020
temperature	**humidity**
13.6 °C - 13.7 °C	48.1 % - 48.0 %
pressure	**macrostructure**
953.7 *Pa* - 953.7 *Pa*	flat
printer	**printer_binder**
FDB	Furan binder

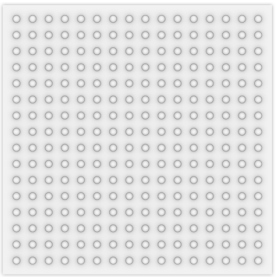

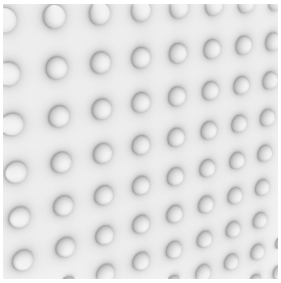

panel_0115_0

date_measured	date_processed
11-12-2020	12-12-2020
temperature	**humidity**
13.7 °C - 13.7 °C	44.2 % - 45.2 %
pressure	**macrostructure**
936.8 *Pa* - 936.8 *Pa*	flat
printer	**printer_binder**
FDB	Furan binder

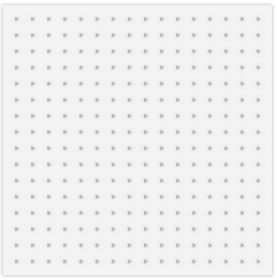

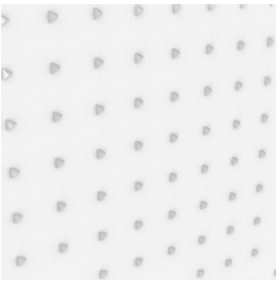

panel_0115_1

date_measured	date_processed
12-12-2020	13-12-2020
temperature	**humidity**
13.6 °C - 13.7 °C	45.8 % - 46.2 %
pressure	**macrostructure**
944.0 *Pa* - 944.0 *Pa*	flat
printer	**printer_binder**
FDB	Furan binder

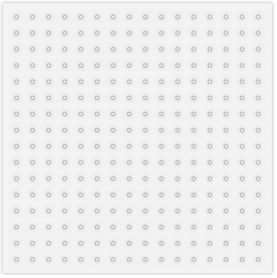

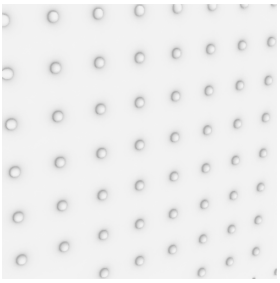

panel_0116_0

date_measured	date_processed
10-12-2020	10-12-2020
temperature	**humidity**
13.8 °C - 13.8 °C	44.9 % - 44.9 %
pressure	**macrostructure**
945.1 *Pa* - 945.1 *Pa*	flat
printer	**printer_binder**
FDB	Furan binder

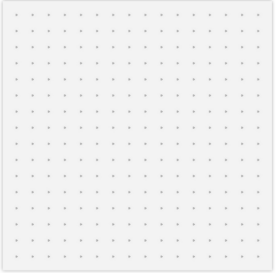

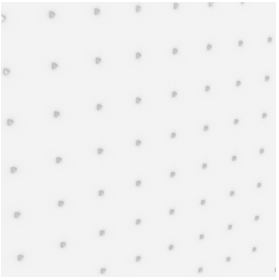

panel_0116_1

date_measured	date_processed
11-12-2020	11-12-2020
temperature	**humidity**
13.6 °C - 13.8 °C	44.2 % - 43.9 %
pressure	**macrostructure**
940.9 *Pa* - 940.9 *Pa*	flat
printer	**printer_binder**
FDB	Furan binder

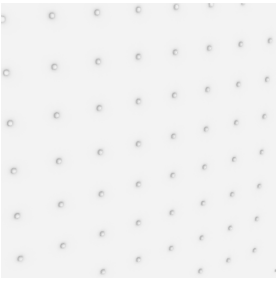

panel_0117_0

date_measured	date_processed
17-12-2020	18-12-2020
temperature	**humidity**
13.3 °C - 13.6 °C	52.4 % - 51.7 %
pressure	**macrostructure**
965.2 *Pa* - 965.2 *Pa*	flat
printer	**printer_binder**
FDB	Furan binder

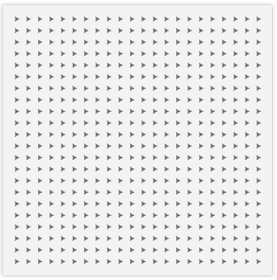

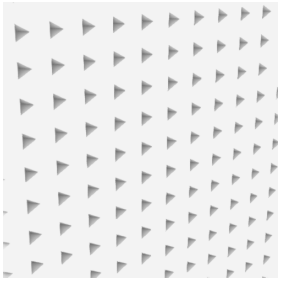

panel_0117_1

date_measured	date_processed
18-12-2020	18-12-2020
temperature	**humidity**
13.5 °C - 13.6 °C	51.9 % - 51.7 %
pressure	**macrostructure**
965.2 *Pa* - 965.2 *Pa*	flat
printer	**printer_binder**
FDB	Furan binder

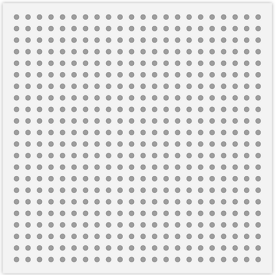

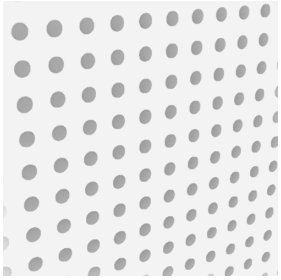

panel_0118_0

date_measured	date_processed
18-12-2020	19-12-2020
temperature	**humidity**
13.5 °C - 13.5 °C	52.0 % - 50.8 %
pressure	**macrostructure**
962.7 *Pa* - 962.6 *Pa*	flat
printer	**printer_binder**
FDB	Furan binder

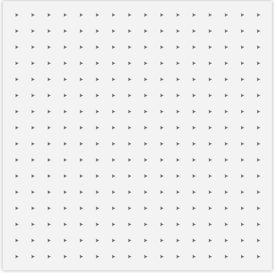

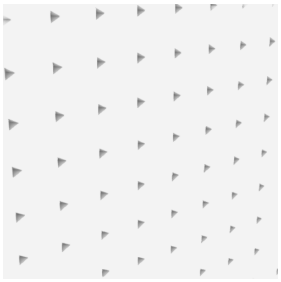

panel_0118_1

date_measured	date_processed
20-12-2020	22-12-2020
temperature	**humidity**
13.3 °C - 13.4 °C	51.5 % - 56.0 %
pressure	**macrostructure**
964.0 *Pa* - 964.0 *Pa*	flat
printer	**printer_binder**
FDB	Furan binder

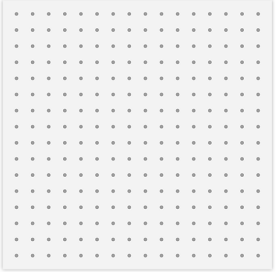

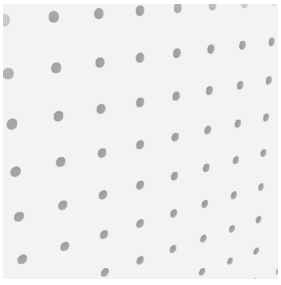

panel_0119_0

date_measured	date_processed
15-02-2021	16-02-2021
temperature	**humidity**
12.1 °C - 12.0 °C	39.7 % - 41.7 %
pressure	**macrostructure**
971.7 *Pa* - 971.7 *Pa*	flat
printer	**printer_binder**
FDB	Furan binder

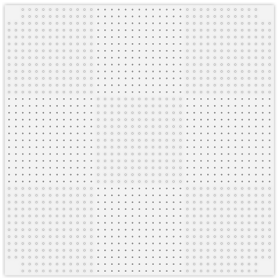

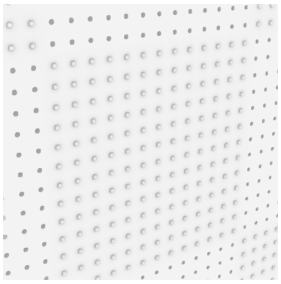

panel_0119_1

date_measured	date_processed
17-02-2021	17-02-2021
temperature	**humidity**
11.7 °C - 11.9 °C	46.3 % - 46.7 %
pressure	**macrostructure**
962.4 *Pa* - 962.4 *Pa*	flat
printer	**printer_binder**
FDB	Furan binder

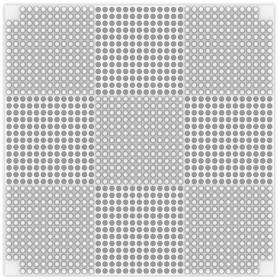

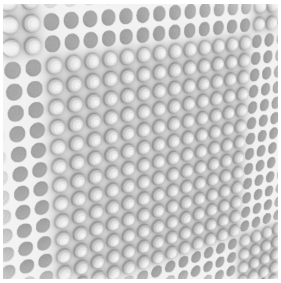

panel_0120_0

date_measured	date_processed
09-02-2021	10-02-2021
temperature	**humidity**
12.5 °C - 12.8 °C	54.5 % - 53.7 %
pressure	**macrostructure**
940.3 *Pa* - 940.3 *Pa*	flat
printer	**printer_binder**
FDB	Furan binder

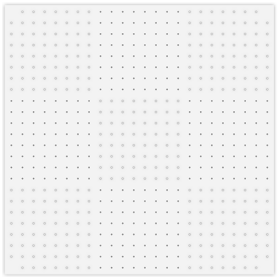

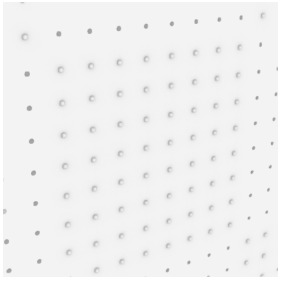

panel_0120_1

date_measured	date_processed
11-02-2021	11-02-2021
temperature	**humidity**
12.7 °C - 12.8 °C	50.9 % - 48.3 %
pressure	**macrostructure**
961.6 *Pa* - 961.6 *Pa*	flat
printer	**printer_binder**
FDB	Furan binder

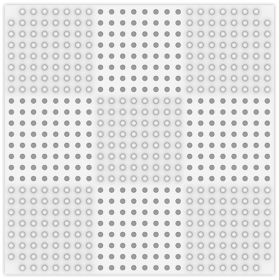

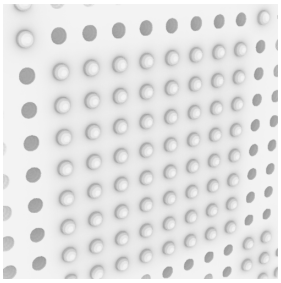

panel_0121_0

date_measured	date_processed
01-02-2021	02-02-2021
temperature	**humidity**
11.2 °C - 11.5 °C	58.6 % - 58.6 %
pressure	**macrostructure**
941.0 *Pa* - 941.0 *Pa*	flat
printer	**printer_binder**
FDB	Furan binder

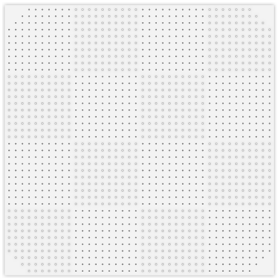

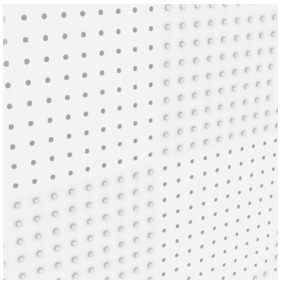

panel_0121_1

date_measured	date_processed
02-02-2021	02-02-2021
temperature	**humidity**
11.4 °C - 11.6 °C	59.2 % - 59.5 %
pressure	**macrostructure**
947.3 *Pa* - 947.3 *Pa*	flat
printer	**printer_binder**
FDB	Furan binder

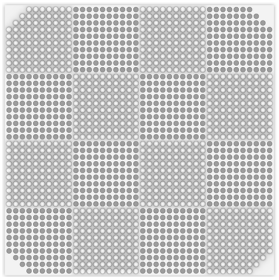

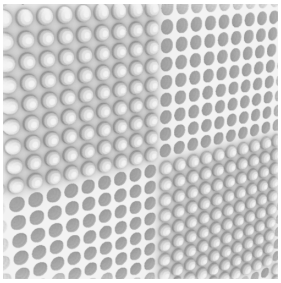

panel_0122_0

date_measured	date_processed
23-02-2021	23-02-2021
temperature	**humidity**
12.0 °C - 12.3 °C	54.2 % - 53.8 %
pressure	**macrostructure**
974.3 *Pa* - 974.3 *Pa*	flat
printer	**printer_binder**
FDB	Furan binder

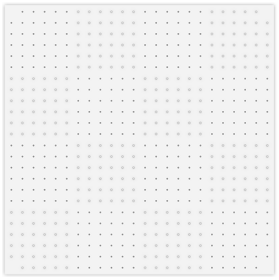

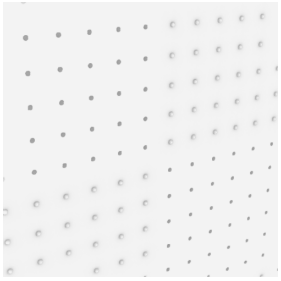

panel_0122_1

date_measured	date_processed
23-02-2021	24-02-2021
temperature	**humidity**
12.2 °C - 12.4 °C	54.2 % - 54.3 %
pressure	**macrostructure**
975.5 *Pa* - 975.5 *Pa*	flat
printer	**printer_binder**
FDB	Furan binder

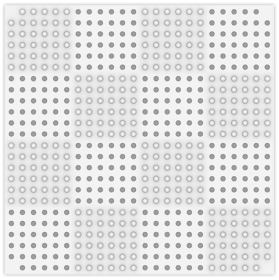

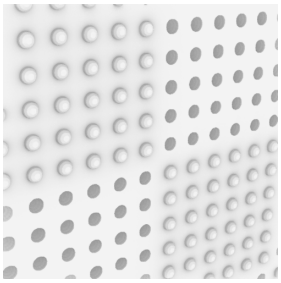

panel_0123_0

date_measured	date_processed
18-02-2021	19-02-2021
temperature	**humidity**
11.7 °C - 11.9 °C	49.2 % - 50.1 %
pressure	**macrostructure**
957.5 *Pa* - 957.5 *Pa*	flat
printer	**printer_binder**
FDB	Furan binder

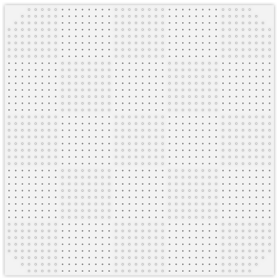

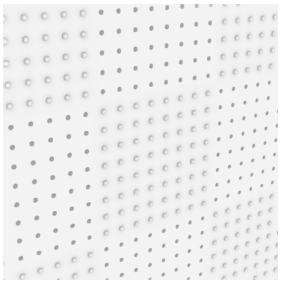

panel_0123_1

date_measured	date_processed
22-02-2021	23-02-2021
temperature	**humidity**
11.8 °C - 12.2 °C	54.0 % - 53.7 %
pressure	**macrostructure**
961.2 *Pa* - 961.2 *Pa*	flat
printer	**printer_binder**
FDB	Furan binder

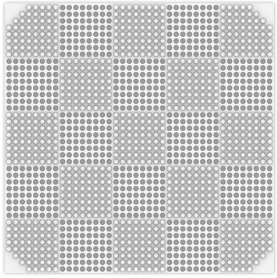

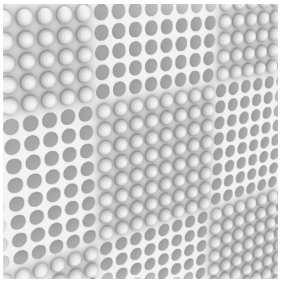

panel_0124_0

date_measured	date_processed
14-02-2021	14-02-2021
temperature	**humidity**
12.1 °C - 12.3 °C	40.0 % - 40.4 %
pressure	**macrostructure**
974.7 *Pa* - 974.6 *Pa*	flat
printer	**printer_binder**
FDB	Furan binder

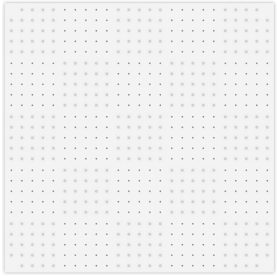

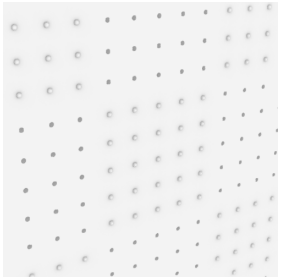

panel_0124_1

date_measured	date_processed
14-02-2021	15-02-2021
temperature	**humidity**
12.2 °C - 12.2 °C	40.0 % - 40.0 %
pressure	**macrostructure**
973.1 *Pa* - 973.1 *Pa*	flat
printer	**printer_binder**
FDB	Furan binder

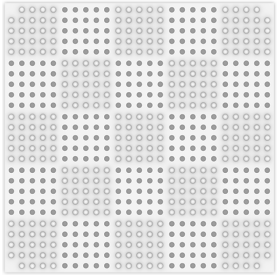

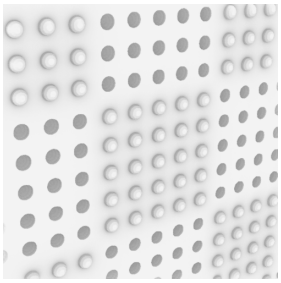

panel_0125_0

date_measured	date_processed
19-04-2021	20-04-2021
temperature	**humidity**
14.2 °C - 14.2 °C	43.7 % - 44.4 %
pressure	**macrostructure**
958.4 *Pa* - 958.4 *Pa*	flat
printer	**printer_binder**
FDB	Furan binder

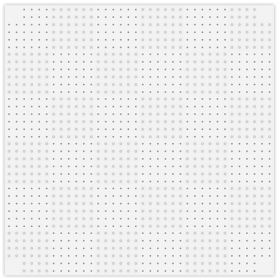

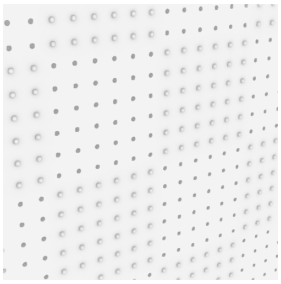

panel_0125_1

date_measured	date_processed
20-04-2021	21-04-2021
temperature	**humidity**
14.1 °C - 14.2 °C	44.7 % - 44.5 %
pressure	**macrostructure**
954.7 *Pa* - 954.7 *Pa*	flat
printer	**printer_binder**
FDB	Furan binder

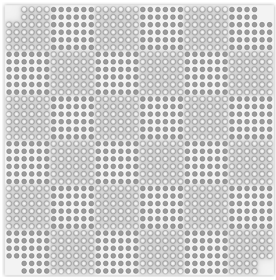

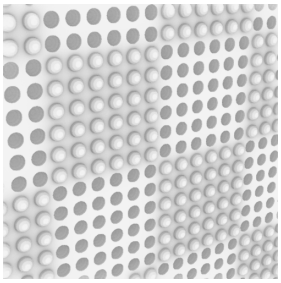

panel_0126_0

date_measured	date_processed
17-04-2021	18-04-2021
temperature	**humidity**
14.1 °C - 14.3 °C	41.6 % - 41.6 %
pressure	**macrostructure**
957.8 *Pa* - 957.8 *Pa*	flat
printer	**printer_binder**
FDB	Furan binder

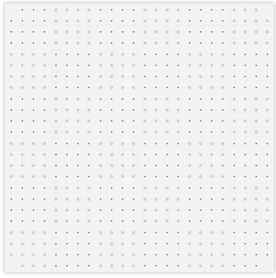

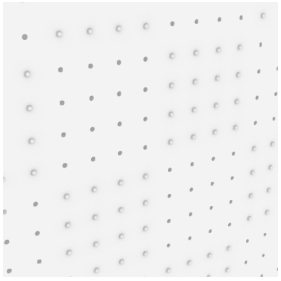

panel_0126_1

date_measured	date_processed
18-04-2021	19-04-2021
temperature	**humidity**
14.1 °C - 14.2 °C	43.0 % - 43.4 %
pressure	**macrostructure**
959.0 *Pa* - 959.0 *Pa*	flat
printer	**printer_binder**
FDB	Furan binder

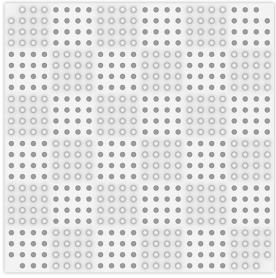

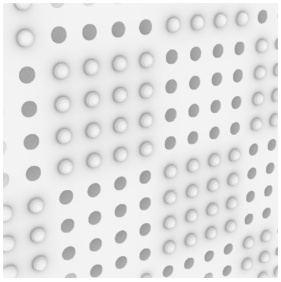

panel_0127_0

date_measured	date_processed
24-03-2021	25-03-2021
temperature	**humidity**
12.8 °C - 12.8 °C	44.0 % - 44.9 %
pressure	**macrostructure**
962.4 *Pa* - 962.3 *Pa*	flat
printer	**printer_binder**
FDB	Furan binder

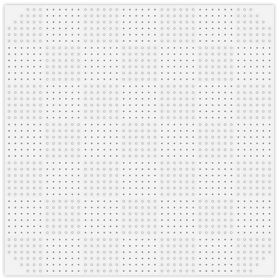

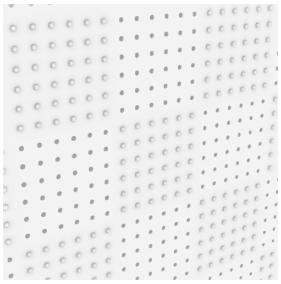

panel_0127_1

date_measured	date_processed
25-03-2021	26-03-2021
temperature	**humidity**
12.8 °C - 12.9 °C	45.1 % - 46.7 %
pressure	**macrostructure**
961.9 *Pa* - 961.9 *Pa*	flat
printer	**printer_binder**
FDB	Furan binder

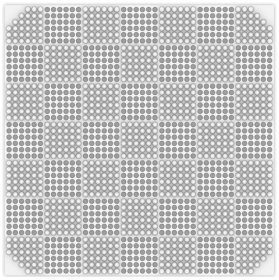

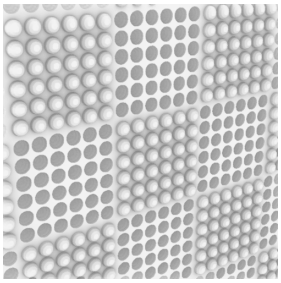

panel_0128_0

date_measured	date_processed
13-04-2021	14-04-2021
temperature	**humidity**
14.4 °C - 14.5 °C	45.1 % - 43.2 %
pressure	**macrostructure**
967.3 *Pa* - 967.3 *Pa*	flat
printer	**printer_binder**
FDB	Furan binder

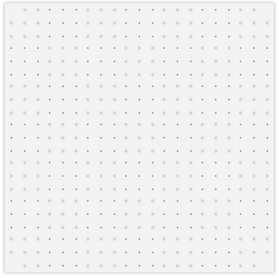

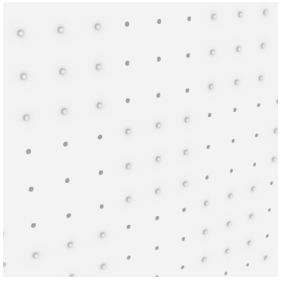

panel_0128_1

date_measured	date_processed
14-04-2021	15-04-2021
temperature	**humidity**
14.4 °C - 14.4 °C	43.1 % - 42.2 %
pressure	**macrostructure**
964.2 *Pa* - 964.2 *Pa*	flat
printer	**printer_binder**
FDB	Furan binder

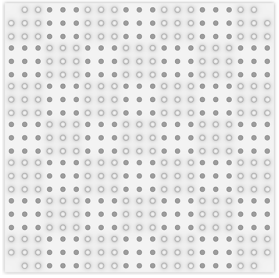

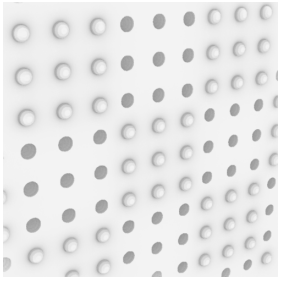

panel_0129_0

date_measured	date_processed
12-02-2021	13-02-2021
temperature	**humidity**
12.4 °C - 12.4 °C	45.4 % - 43.6 %
pressure	**macrostructure**
962.3 *Pa* - 962.3 *Pa*	flat
printer	**printer_binder**
FDB	Furan binder

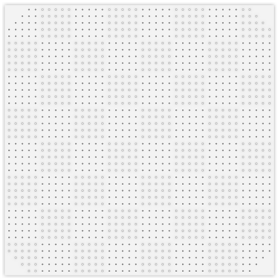

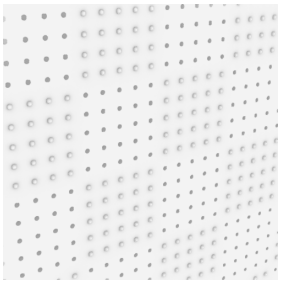

panel_0129_1

date_measured	date_processed
13-02-2021	14-02-2021
temperature	**humidity**
12.4 °C - 12.4 °C	42.9 % - 41.9 %
pressure	**macrostructure**
968.9 *Pa* - 968.9 *Pa*	flat
printer	**printer_binder**
FDB	Furan binder

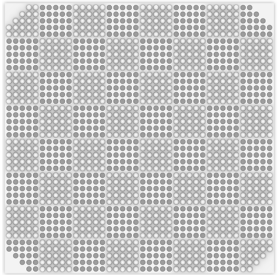

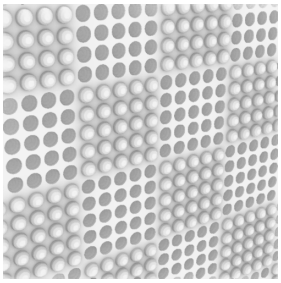

panel_0130_0

date_measured	date_processed
07-04-2021	07-04-2021
temperature	**humidity**
14.3 °C - 14.5 °C	43.0 % - 41.5 %
pressure	**macrostructure**
960.8 *Pa* - 960.9 *Pa*	flat
printer	**printer_binder**
FDB	Furan binder

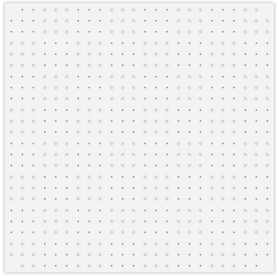

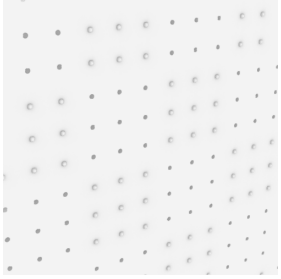

panel_0130_1

date_measured	date_processed
07-04-2021	08-04-2021
temperature	**humidity**
14.4 °C - 14.6 °C	42.0 % - 40.7 %
pressure	**macrostructure**
963.5 *Pa* - 963.5 *Pa*	flat
printer	**printer_binder**
FDB	Furan binder

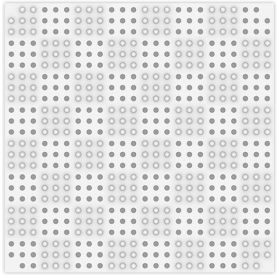

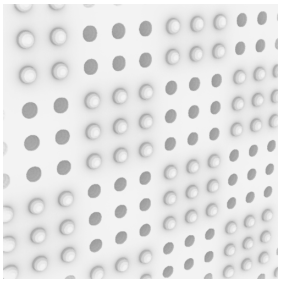

panel_0131_0

date_measured	date_processed
31-03-2021	01-04-2021
temperature	**humidity**
13.3 °C - 13.7 °C	50.2 % - 51.3 %
pressure	**macrostructure**
964.5 *Pa* - 964.4 *Pa*	flat
printer	**printer_binder**
FDB	Furan binder

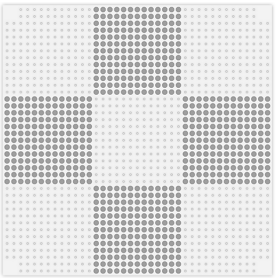

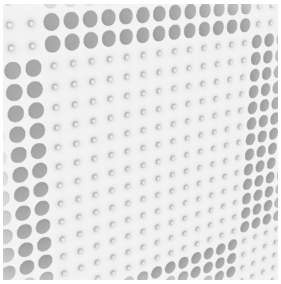

panel_0131_1

date_measured	date_processed
06-04-2021	07-04-2021
temperature	**humidity**
14.2 °C - 14.5 °C	44.2 % - 43.4 %
pressure	**macrostructure**
952.1 *Pa* - 952.1 *Pa*	flat
printer	**printer_binder**
FDB	Furan binder

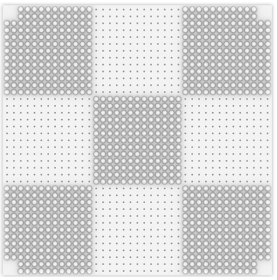

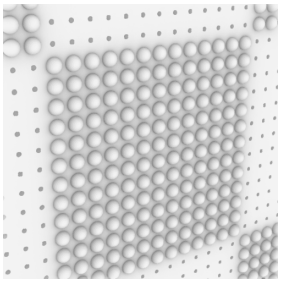

panel_0132_0

date_measured	date_processed
09-03-2021	10-03-2021
temperature	**humidity**
13.4 °C - 13.4 °C	46.4 % - 46.8 %
pressure	**macrostructure**
958.2 *Pa* - 958.2 *Pa*	flat
printer	**printer_binder**
FDB	Furan binder

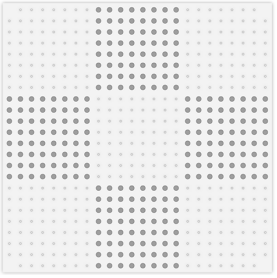

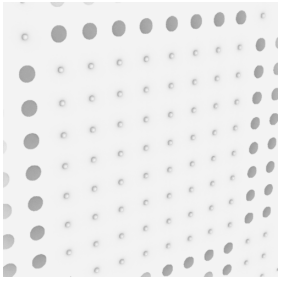

panel_0132_1

date_measured	date_processed
10-03-2021	11-03-2021
temperature	**humidity**
13.4 °C - 13.4 °C	46.9 % - 46.2 %
pressure	**macrostructure**
959.3 *Pa* - 959.2 *Pa*	flat
printer	**printer_binder**
FDB	Furan binder

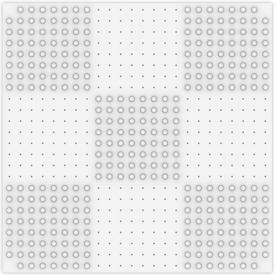

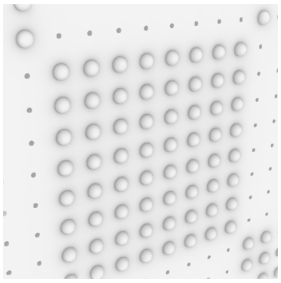

panel_0133_0

date_measured	date_processed
05-03-2021	07-03-2021
temperature	**humidity**
13.2 °C - 13.3 °C	52.1 % - 49.5 %
pressure	**macrostructure**
964.6 *Pa* - 964.6 *Pa*	flat
printer	**printer_binder**
FDB	Furan binder

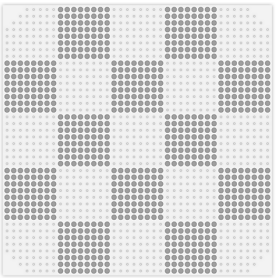

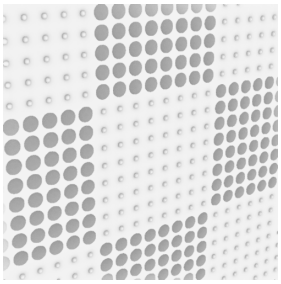

panel_0133_1

date_measured	date_processed
08-03-2021	08-03-2021
temperature	**humidity**
13.1 °C - 13.3 °C	49.7 % - 48.7 %
pressure	**macrostructure**
958.2 *Pa* - 958.2 *Pa*	flat
printer	**printer_binder**
FDB	Furan binder

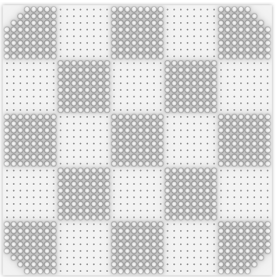

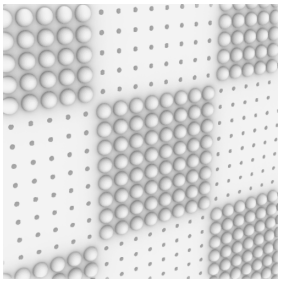

panel_0134_0

date_measured	date_processed
15-03-2021	15-03-2021
temperature	**humidity**
13.3 °C - 13.5 °C	48.7 % - 48.6 %
pressure	**macrostructure**
953.9 *Pa* - 953.9 *Pa*	flat
printer	**printer_binder**
FDB	Furan binder

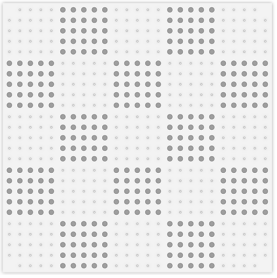

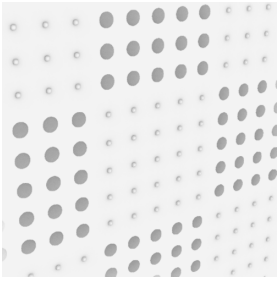

panel_0134_1

date_measured	date_processed
16-03-2021	24-03-2021
temperature	**humidity**
13.3 °C - 12.8 °C	48.9 % - 43.7 %
pressure	**macrostructure**
962.6 *Pa* - 962.6 *Pa*	flat
printer	**printer_binder**
FDB	Furan binder

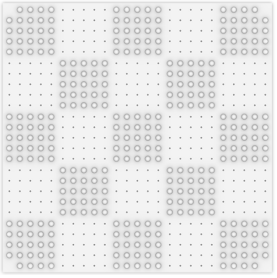

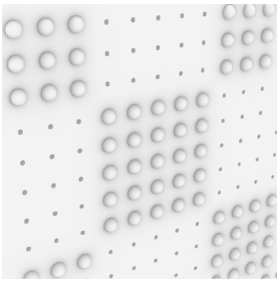

panel_0135_0

date_measured	date_processed
26-03-2021	27-03-2021
temperature	**humidity**
12.8 °C - 13.0 °C	47.6 % - 48.3 %
pressure	**macrostructure**
957.9 *Pa* - 957.8 *Pa*	flat
printer	**printer_binder**
FDB	Furan binder

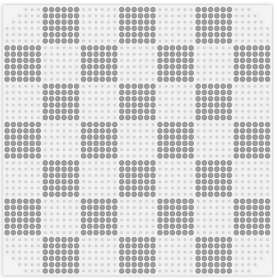

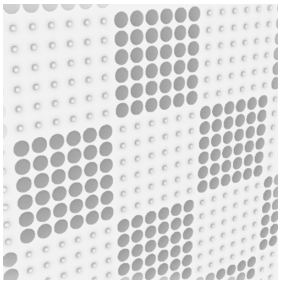

panel_0135_1

date_measured	date_processed
29-03-2021	29-03-2021
temperature	**humidity**
12.9 °C - 13.2 °C	48.5 % - 47.1 %
pressure	**macrostructure**
972.9 *Pa* - 972.9 *Pa*	flat
printer	**printer_binder**
FDB	Furan binder

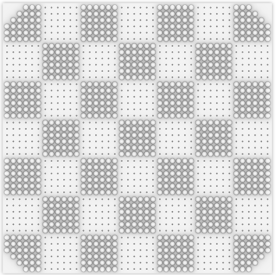

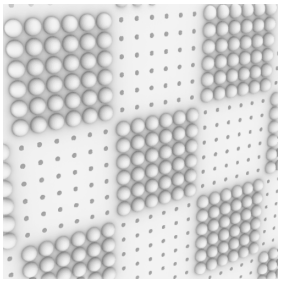

panel_0136_0

date_measured	date_processed
08-03-2021	09-03-2021
temperature	**humidity**
13.3 °C - 13.4 °C	48.6 % - 47.5 %
pressure	**macrostructure**
957.3 *Pa* - 957.3 *Pa*	flat
printer	**printer_binder**
FDB	Furan binder

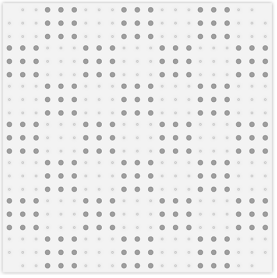

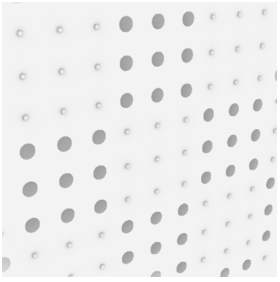

panel_0136_1

date_measured	date_processed
09-03-2021	09-03-2021
temperature	**humidity**
13.3 °C - 13.4 °C	47.3 % - 46.5 %
pressure	**macrostructure**
956.8 *Pa* - 956.8 *Pa*	flat
printer	**printer_binder**
FDB	Furan binder

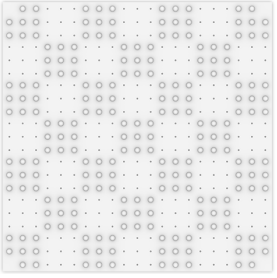

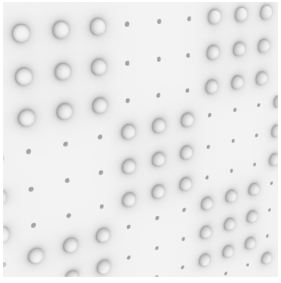

panel_0137_0

date_measured	date_processed
22-04-2021	22-04-2021
temperature	**humidity**
14.1 °C - 14.3 °C	47.7 % - 47.7 %
pressure	**macrostructure**
959.5 *Pa* - 959.5 *Pa*	flat
printer	**printer_binder**
FDB	Furan binder

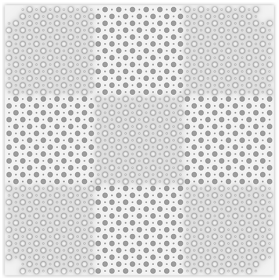

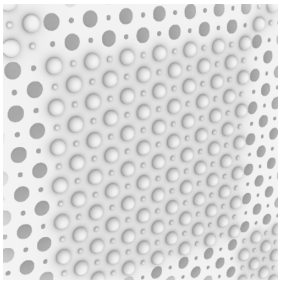

panel_0137_1

date_measured	date_processed
23-04-2021	24-04-2021
temperature	**humidity**
14.0 °C - 14.5 °C	45.0 % - 43.6 %
pressure	**macrostructure**
963.0 *Pa* - 963.0 *Pa*	flat
printer	**printer_binder**
FDB	Furan binder

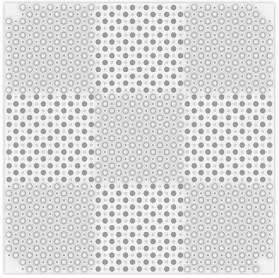

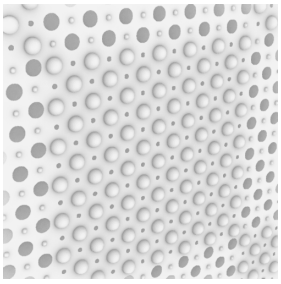

panel_0138_0

date_measured	date_processed
29-03-2021	30-03-2021
temperature	**humidity**
13.2 °C - 13.3 °C	47.2 % - 47.4 %
pressure	**macrostructure**
971.4 *Pa* - 971.4 *Pa*	flat
printer	**printer_binder**
FDB	Furan binder

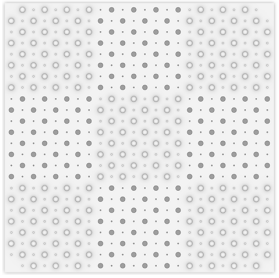

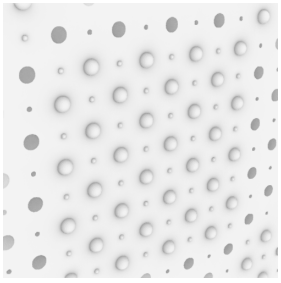

panel_0138_1

date_measured	date_processed
30-03-2021	30-03-2021
temperature	**humidity**
13.2 °C - 13.5 °C	47.9 % - 47.9 %
pressure	**macrostructure**
970.0 *Pa* - 970.0 *Pa*	flat
printer	**printer_binder**
FDB	Furan binder

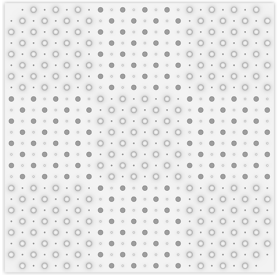

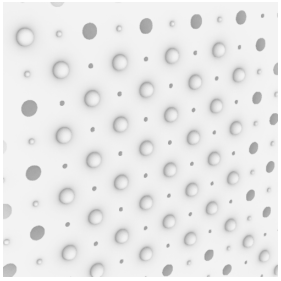

panel_0139_0

date_measured	date_processed
11-03-2021	11-03-2021
temperature	**humidity**
13.3 °C - 13.3 °C	46.4 % - 48.5 %
pressure	**macrostructure**
952.2 *Pa* - 952.2 *Pa*	flat
printer	**printer_binder**
FDB	Furan binder

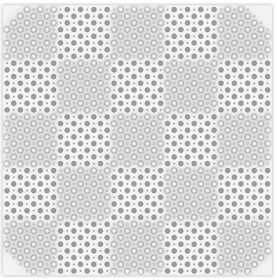

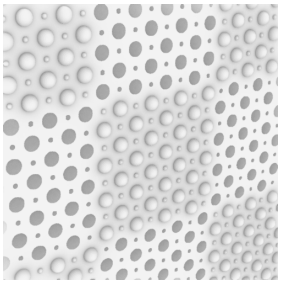

panel_0139_1

date_measured	date_processed
12-03-2021	13-03-2021
temperature	**humidity**
13.2 °C - 13.5 °C	48.5 % - 47.9 %
pressure	**macrostructure**
952.9 *Pa* - 952.9 *Pa*	flat
printer	**printer_binder**
FDB	Furan binder

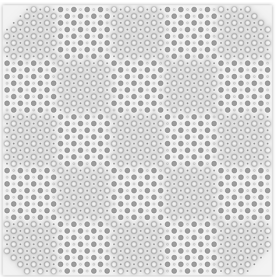

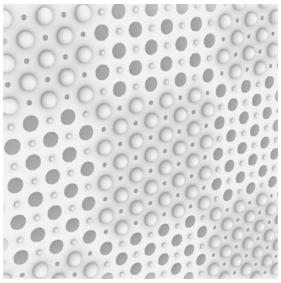

panel_0140_0

date_measured	date_processed
08-04-2021	09-04-2021
temperature	**humidity**
14.5 °C - 14.4 °C	40.6 % - 40.3 %
pressure	**macrostructure**
964.2 *Pa* - 964.2 *Pa*	flat
printer	**printer_binder**
FDB	Furan binder

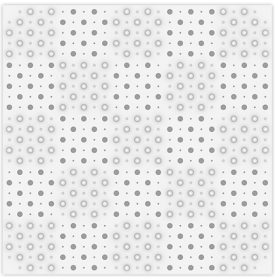

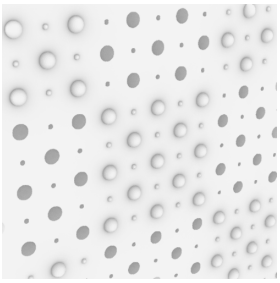

panel_0140_1

date_measured	date_processed
10-04-2021	11-04-2021
temperature	**humidity**
14.1 °C - 14.3 °C	42.6 % - 44.7 %
pressure	**macrostructure**
952.0 *Pa* - 952.0 *Pa*	flat
printer	**printer_binder**
FDB	Furan binder

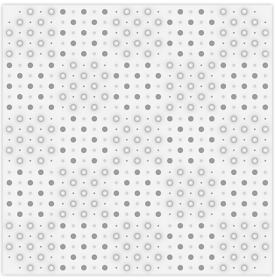

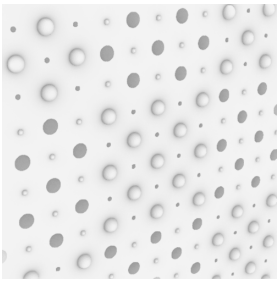

panel_0141_0

date_measured	date_processed
12-04-2021	12-04-2021
temperature	**humidity**
14.1 °C - 14.4 °C	46.8 % - 46.1 %
pressure	**macrostructure**
965.1 *Pa* - 965.1 *Pa*	flat
printer	**printer_binder**
FDB	Furan binder

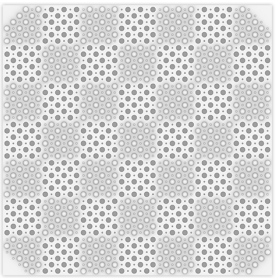
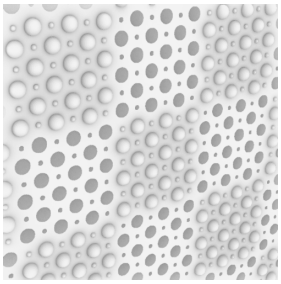

panel_0141_1

date_measured	date_processed
12-04-2021	13-04-2021
temperature	**humidity**
14.4 °C - 14.5 °C	46.2 % - 44.9 %
pressure	**macrostructure**
967.0 *Pa* - 967.0 *Pa*	flat
printer	**printer_binder**
FDB	Furan binder

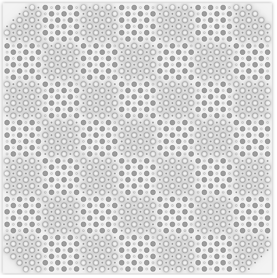
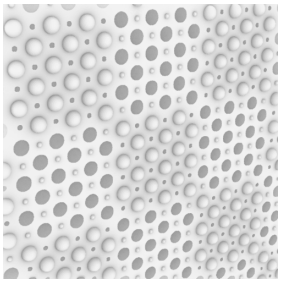

panel_0142_0

date_measured	date_processed
01-03-2021	01-03-2021
temperature	**humidity**
12.5 °C - 13.0 °C	52.2 % - 51.9 %
pressure	**macrostructure**
969.3 *Pa* - 969.3 *Pa*	flat
printer	**printer_binder**
FDB	Furan binder

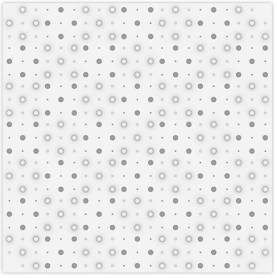
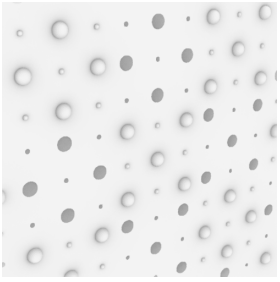

panel_0142_1

date_measured	date_processed
05-03-2021	05-03-2021
temperature	**humidity**
13.0 °C - 13.2 °C	51.6 % - 52.0 %
pressure	**macrostructure**
958.2 *Pa* - 958.2 *Pa*	flat
printer	**printer_binder**
FDB	Furan binder

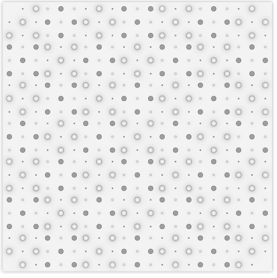
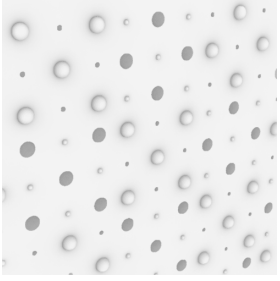

DISS. ETH NO. 29211